

SUDESHNA BORO SAIKIA

# MAGNETIC AND ACTIVITY CYCLES OF COOL STARS

DISSERTATION



# **Magnetic and activity cycles of cool stars**

Dissertation  
zur Erlangung des mathematisch-naturwissenschaftlichen  
Doktorgrades

“Doctor rerum naturalium”  
der Georg-August-Universität Göttingen

-

im Promotionsprogramm PROPHYS  
der Georg-August University School of Science (GAUSS)

vorgelegt von

**Sudeshna Boro Saikia**

aus Golaghat, Assam

Göttingen, 2016

### Betreuungsausschuss

Dr. Sandra V. Jeffers, Institut für Astrophysik, Universität Göttingen

Prof. Dr. Ansgar Reiners, Institut für Astrophysik, Universität Göttingen

### Mitglieder der Prüfungskommission

Referent: Dr. Sandra V. Jeffers, Institut für Astrophysik, Universität Göttingen

Korreferent: Prof. Dr. Stefan Dreizler, Institut für Astrophysik, Universität Göttingen

2. Korreferent: Prof. Dr. Jürgen Schmitt, Hamburger Sternwarte

Weitere Mitglieder der Prüfungskommission:

Prof. Dr. Ansgar Reiners, Institut für Astrophysik, Universität Göttingen

Prof. Dr. Angela Rizzi, IV. Physikalisches Institut, Universität Göttingen

Prof. Dr. Ariane Frey, II. Physikalisches Institut-Kern-und Teilchenphysik, Universität Göttingen

Prof. Dr. Jens Niemeyer, Institut für Astrophysik, Universität Göttingen

Tag der mündlichen Prüfung: 21.12.2016

# Abstract

Cool stars are known to exhibit weak to strong magnetic activity. Our nearest cool star, the Sun, is a middle aged and moderately active star with a cyclic generation of its magnetic field, which results in a 22 year magnetic cycle and a 11 year activity cycle. The physical process behind the solar cycles is called the dynamo. The aim of this thesis is to investigate the magnetic and activity cycles in cool stars over a range of stellar parameters, and to understand the dynamo mechanism and its dependence on basic stellar properties such as rotation and mass. The relationship between magnetic geometry and activity cycle was investigated. The large-scale magnetic field of three cool stars, HN Peg, 61 Cyg A and  $\epsilon$  Eridani is reconstructed using Zeeman Doppler imaging (ZDI). These stars vary in mass, rotation and age. The large-scale magnetic field of HN Peg is complex and highly variable, with a strong toroidal component, which is not seen in the Sun. The magnetic geometry of 61 Cyg A is strongly poloidal, which is a simple dipole during minimum activity and more complex during maximum activity, similar to the solar case. The large-scale field also flips polarity from one minimum to the next, indicating a solar-like magnetic cycle. This is the first detection of a solar-like magnetic cycle in any cool star other than the Sun.  $\epsilon$  Eridani shows a non axisymmetric complex magnetic field geometry during minimum chromospheric activity, with both poloidal and toroidal components. The toroidal percentage increases gradually in time, which is different from our Sun's axisymmetric poloidal dipolar magnetic geometry at activity minimum. Magnetic proxies such as chromospheric activity were also used to provide information on the activity cycles in cool stars, although they do not provide information about the magnetic field geometry evolution or the magnetic cycle of the star. A cool star chromospheric activity catalogue of Ca II H and K activity was developed. For the entire cool star range, we use a recently developed calibration to obtain accurate  $\log R'_{\text{HK}}$  measurements, the physical representation of chromospheric activity. For stars with long-term observations, the activity cycle periods were determined, using a period search algorithm, and their dependence on stellar rotation was investigated. For slowly rotating stars the chromospheric activity cycle periods show a possible dependence on rotation. This dependence has previously been shown and called the 'Inactive' branch of stellar cycles. On the other hand, and in contrast to previous work, we show that rapidly rotating stars exhibit a more random distribution on the cycle period-rotation plane, indicating an 'Active' region rather than an 'Active' branch. Furthermore, rapidly rotating stars also show the presence of multiple cycles. The multiple cycles might be caused by their complex magnetic field geometry, which can be completely different from the solar case. This thesis shows that cool stars exhibit a range of magnetic geometry variations during their activity cycle, which does not necessarily have to be solar-like. This result is important for understanding the dynamo processes acting in cool stars including our own Sun.



# Contents

<b>1. Introduction</b>	<b>1</b>
1.1. Cool stars . . . . .	1
1.2. Our Sun . . . . .	2
1.3. The 11 year solar cycle . . . . .	4
1.4. The 22 year solar magnetic cycle . . . . .	5
1.5. The solar dynamo . . . . .	5
1.6. Cool star magnetism . . . . .	7
1.6.1. Stellar activity cycles . . . . .	8
1.6.2. Stellar magnetic cycles . . . . .	10
1.7. Motivation . . . . .	11
<b>2. Methods of field detection</b>	<b>13</b>
2.1. Mechanisms for magnetic field detection . . . . .	14
2.1.1. Zeeman effect . . . . .	14
2.1.2. Polarisation of light and the Stokes parameters . . . . .	16
2.2. Instrumentation and data reduction . . . . .	19
2.2.1. An astronomical spectrograph . . . . .	19
2.2.2. Instrumentation to detect polarisation . . . . .	21
2.2.3. Least square deconvolution . . . . .	23
2.3. Magnetic field measurements using Stokes $V$ and $I$ . . . . .	25
2.3.1. Longitudinal magnetic field measurement . . . . .	25
2.3.2. Zeeman Doppler imaging (ZDI) . . . . .	26
2.4. Indirect proxies of magnetic activity . . . . .	31
2.4.1. Chromospheric activity . . . . .	31
2.4.2. Coronal activity . . . . .	34
2.5. Summary . . . . .	35
<b>3. Variable magnetic field geometry of the young Sun HN Pegasi (HD 206860)</b>	<b>37</b>
3.1. Abstract . . . . .	38
3.2. Introduction . . . . .	38
3.3. HN Peg . . . . .	39
3.4. Observations . . . . .	40
3.5. Mean longitudinal magnetic field ( $B_l$ ) . . . . .	41
3.6. Chromospheric activity indicators . . . . .	42
3.7. Large-scale magnetic field topology . . . . .	48
3.7.1. Radial velocity . . . . .	49
3.7.2. Inclination angle . . . . .	49
3.7.3. Differential rotation . . . . .	49

3.7.4. Magnetic topology . . . . .	50
3.8. Discussion . . . . .	55
3.8.1. Long-term magnetic variability . . . . .	55
3.8.2. Large scale magnetic topology . . . . .	57
3.8.3. Differential rotation . . . . .	59
3.9. Summary . . . . .	59
<b>4. A solar-like magnetic cycle on the mature K-dwarf 61 Cygni A (HD 201091)</b>	<b>61</b>
4.1. Abstract . . . . .	62
4.2. Introduction . . . . .	62
4.3. Physical properties of 61 Cyg A . . . . .	64
4.4. Instrumental setup and data reduction . . . . .	66
4.4.1. Optical data . . . . .	66
4.4.2. X-ray data . . . . .	67
4.5. Magnetic field detection: direct and indirect approach . . . . .	67
4.5.1. Mean longitudinal magnetic field . . . . .	67
4.5.2. Chromospheric activity as a proxy of magnetic activity . . . . .	68
4.6. Large-scale magnetic field geometry . . . . .	74
4.6.1. Vector magnetic field . . . . .	74
4.6.2. Evolution of the different multipolar modes over the magnetic cycle	80
4.6.3. Differential rotation . . . . .	82
4.7. Long-term evolution of the magnetic and activity cycle . . . . .	82
4.8. Discussion . . . . .	84
4.8.1. Large-scale magnetic field . . . . .	84
4.8.2. Chromospheric activity . . . . .	86
4.9. Summary . . . . .	87
<b>5. Göttingen chromospheric activity catalogue: questioning the Active branch of stellar activity cycles</b>	<b>89</b>
5.1. Abstract . . . . .	89
5.2. Introduction . . . . .	90
5.3. Data analysis . . . . .	92
5.4. Chromospheric activity . . . . .	94
5.4.1. S-index . . . . .	94
5.4.2. Chromospheric Ca II H and K . . . . .	96
5.4.3. Vaughan-Preston gap . . . . .	97
5.5. Long-term evolution of chromospheric activity vs rotation . . . . .	98
5.6. Conclusions . . . . .	104
<b>6. The relation between stellar magnetic field geometry and chromospheric activity cycles: the complex field of <math>\epsilon</math> Eridani at activity minimum</b>	<b>105</b>
6.1. Abstract . . . . .	105
6.2. Introduction . . . . .	106
6.3. Observations and Data Analysis . . . . .	106
6.3.1. Least Squares Deconvolution . . . . .	107

6.3.2.	Chromospheric emission - Ca II H&K . . . . .	107
6.4.	Large-scale magnetic field geometry . . . . .	107
6.4.1.	Magnetic maps . . . . .	108
6.4.2.	Magnetic energy . . . . .	109
6.5.	Discussion . . . . .	110
6.6.	Conclusions . . . . .	113
<b>7.</b>	<b>Summary and conclusions</b>	<b>115</b>
7.0.1.	Variable magnetic geometry of the young sun HN Pegasi (HD206860)	116
7.0.2.	A solar-like magnetic cycle on the mature K dwarf 61 Cygni A (HD201091) . . . . .	117
7.0.3.	Göttingen chromospheric activity catalogue: questioning the Active branch of stellar activity cycles . . . . .	117
7.0.4.	The relationship between stellar magnetic field geometry and chro- mospheric activity cycles: the complex field of $\epsilon$ Eridani at activity minimum . . . . .	119
7.1.	Ongoing and future work . . . . .	119
<b>A.</b>	<b>appendix</b>	<b>135</b>



# List of Figures

1.1. HR diagram . . . . .	2
1.2. Stellar structure . . . . .	2
1.3. Stellar atmospheric layers . . . . .	3
1.4. MDI image of the Sun . . . . .	4
1.5. Solar butterfly diagram . . . . .	5
1.6. Solar chromospheric activity . . . . .	5
1.7. Magnetic butterfly diagram of the Sun . . . . .	6
1.8. Cartoon of the $\alpha$ and $\Omega$ effect . . . . .	7
1.9. Ca II H and K lines . . . . .	8
1.10. Chromospheric activity cycle vs Rossby number . . . . .	9
1.11. Chromospheric activity cycle vs rotation period . . . . .	10
2.1. Zeeman effect . . . . .	15
2.2. Zeeman effect in polarised light . . . . .	17
2.3. Stokes vector . . . . .	18
2.4. Solar spectrum . . . . .	19
2.5. Example of a spectrograph . . . . .	20
2.6. Principles of a Wollaston prism . . . . .	21
2.7. A half-wave plate retarder . . . . .	22
2.8. Polarimetric unit of ESPaDOnS . . . . .	24
2.9. Least Square Deconvolution profile . . . . .	25
2.10. Principles of Zeeman Doppler imaging . . . . .	26
2.11. Principles of Zeeman Doppler imaging . . . . .	28
2.12. Temperature vs atmospheric height for a cool sun-like star . . . . .	31
2.13. Formation heights for different chromospheric lines . . . . .	32
2.14. X-ray luminosity vs magnetic flux . . . . .	35
3.1. HN Peg: rotational variability of $B_l$ . . . . .	42
3.2. HN Peg: rotational variability of chromospheric activity (S-index) . . . . .	43
3.3. HN Peg: long-term S-index measurements . . . . .	44
3.4. HN Peg: rotational variability of chromospheric activity ( $H\alpha$ ) . . . . .	45
3.5. HN Peg: rotational variability of chromospheric activity (CaIRT-index) . . . . .	46
3.6. HN Peg: temporal variability of average field and average chromospheric activity . . . . .	47
3.7. HN Peg: correlation between chromospheric activity tracers . . . . .	47
3.8. HN Peg: correlation between chromospheric activity tracers . . . . .	48
3.9. HN Peg: differential rotation. Best fit $B_{\text{mean}}$ map . . . . .	49
3.10. HN Peg: time series of Stokes V LSD profiles for six epochs . . . . .	51

3.11. HN Peg: magnetic field geometry reconstructed over six epochs . . . . .	52
3.12. HN Peg: magnetic energy distribution . . . . .	53
3.13. HN Peg: poloidal magnetic field distribution . . . . .	54
4.1. 61 Cyg A: rotational variability of $B_l$ and chromospheric activity (S-index) .	68
4.2. 61 Cyg A: long-term chromospheric activity (S-index) . . . . .	70
4.3. 61 Cyg A: rotational variability of chromospheric activity, $H\alpha$ and Ca II infrared triplet indices . . . . .	71
4.4. 61 Cyg A: coronal activity cycle . . . . .	72
4.5. 61 Cyg A: correlation between different magnetic field detection techniques	73
4.6. 61 Cyg A: time series of Stokes $V$ LSD spectra for six epochs . . . . .	75
4.7. 61 Cyg A: surface magnetic field geometry . . . . .	77
4.8. 61 Cyg A: poloidal magnetic field distribution for six epoch of observations.	80
4.9. 61 Cyg A: vector component of the average poloidal and toroidal magnetic field . . . . .	81
4.10. 61 Cyg A: radial magnetic field at different axisymmetric modes . . . . .	83
4.11. 61 Cyg A: magnetic field strength of the poloidal and toroidal component in $l=0$ mode . . . . .	83
4.12. 61 Cyg A: differential rotation. Best fit $B_{\text{mean}}$ map . . . . .	85
4.13. 61 Cyg A: long-term evolution of average chromospheric activity and mag- netic field . . . . .	87
5.1. HR diagram of the MS stars in the activity catalogue. . . . .	93
5.2. Chromospheric activity (S-index) vs $B - V$ for stars in the catalogue . . . .	95
5.3. Chromospheric flux ration $\log R'_{\text{HK}}$ vs $B - V$ . . . . .	96
5.4. Normalised distribution of chromospheric activity for different ranges of $B - V$	99
5.5. $\omega_{\text{cyc}}/\Omega$ vs $Ro^{-1}$ for stars with long-term activity data . . . . .	100
5.6. Activity cycle period vs rotation for stars with long-term activity data . . .	101
6.1. $\epsilon$ Eridani: Stokes $V$ profiles . . . . .	108
6.2. $\epsilon$ Eridani: magnetic field maps using ZDI . . . . .	110
6.3. Evolution of the magnetic field geometry at activity minimum . . . . .	112
7.1. Magnetic field geometry evolution of HN Peg . . . . .	116
7.2. Magnetic field geometry evolution of 61 Cyg A . . . . .	118
7.3. Latitudinal distribution of the the large-scale field of 61 Cyg A . . . . .	120
7.4. Latitudinal distribution of the large-scale field of the Sun . . . . .	121
A.1. Cool stars with clear solar-like cycles . . . . .	150
A.2. Cool stars with multiple cycles. The red fit to the data shows the strongest period in the periodogram. . . . .	151
A.3. Cool stars with probable solar-like cycles. . . . .	152

# List of Tables

2.1.	List of current and upcoming high-resolution spectropolarimeters . . . . .	23
3.1.	HN Peg: summary of the physical properties . . . . .	41
3.2.	HN Peg: magnetic properties extracted from the ZDI reconstructions . . . .	56
4.1.	61 Cyg A: summary of physical properties . . . . .	65
4.2.	61 Cyg A: magnetic properties extracted from ZDI . . . . .	79
5.1.	Total number of stars including their archival information . . . . .	93
5.2.	Common stars for HARPS S-index calibration to the Mount Wilson scale .	95
6.1.	Stellar Parameters . . . . .	106
6.2.	$\epsilon$ Eridani: magnetic properties extracted from the ZDI maps . . . . .	111
A.1.	HN Peg: journal of observations . . . . .	135
A.2.	HN Peg: chromospheric activity and magnetic field measurements . . . . .	138
A.3.	61 Cyg A: journal of observations . . . . .	141
A.4.	61 Cyg A: chromospheric activity and magnetic field measurements . . . .	144
A.5.	Chromospheric activity cycle and rotation periods . . . . .	147
A.6.	$\epsilon$ Eridani: journal of observations . . . . .	149



# 1. Introduction

## Contents

---

1.1. Cool stars . . . . .	1
1.2. Our Sun . . . . .	2
1.3. The 11 year solar cycle . . . . .	4
1.4. The 22 year solar magnetic cycle . . . . .	5
1.5. The solar dynamo . . . . .	5
1.6. Cool star magnetism . . . . .	7
1.6.1. Stellar activity cycles . . . . .	8
1.6.2. Stellar magnetic cycles . . . . .	10
1.7. Motivation . . . . .	11

---

## 1.1. Cool stars

A cool star is a low mass star with an convective outer envelope, which lies on the lower part of the main sequence (as shown in Fig. 1.1). The main sequence is the evolutionary stage where a star has a hydrogen burning core and is under hydrostatic equilibrium. Cool main sequence dwarfs have masses  $\leq 1.5 M_{\odot}$  and effective temperatures  $\leq 7500$  K (please refer to [Boehm-Vitense \(1989\)](#) for more details). Cool stars are also known as cool dwarfs and they belong to spectral types F, G, K and M. The inner core of a cool star can be either, radiative or fully convective, as shown in Fig. 1.2. Cool F, G, K and early M dwarfs consist of an inner radiative core and an outer convective zone, whereas mid to late M dwarfs are fully convective. One prominent example of a cool star is our own Sun (spectral type G2 V, where V stands for dwarf). Cool stars harbour strong to weak magnetic fields, which are responsible for their observed surface activity phenomena ( detailed review on cool stars' magnetic fields can be found in [Reiners \(2012\)](#)).

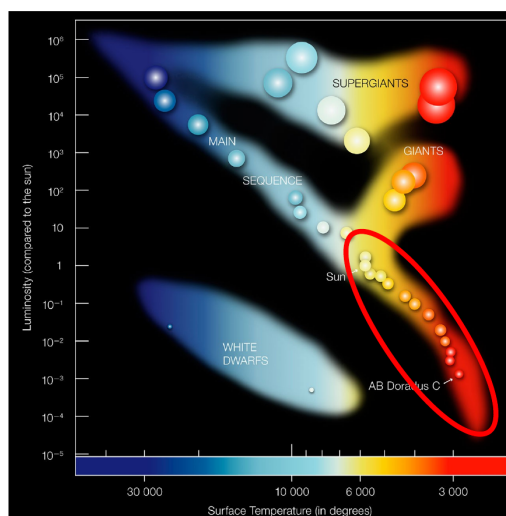


**Figure 1.1.:** HR diagram of stars, where the cool stars are circled in red on the main sequence. The effective temperature is shown on the x-axis and the luminosity is shown on the y-axis. Credit: ESO.

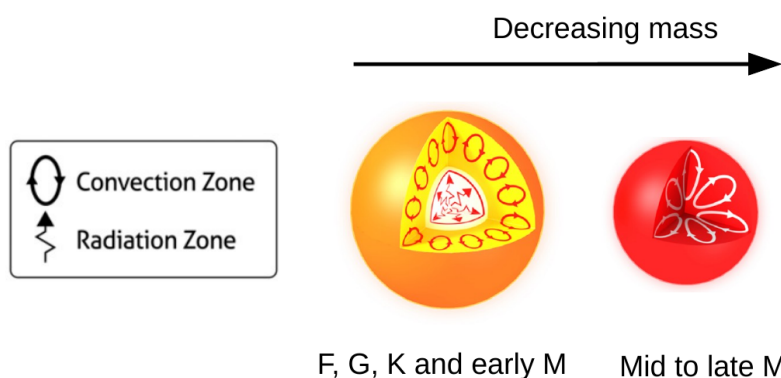


**Figure 1.2.:** Internal structure of cool main sequence stars. Credit: sun.org.

## 1.2. Our Sun

Our nearest cool star, the Sun, is a moderately active star. Its proximity to Earth makes it the most studied cool dwarf. Multiple observational campaigns, using both ground based and space based instruments <sup>1</sup>, have been carried out in different wavelengths to capture the full complexity of the solar magnetic field. Solar observations have revealed that the magnetic field manifests itself in different forms at different heights of the solar atmosphere. The solar

<sup>1</sup>Ground based observatories such as WSO (<http://wso.stanford.edu>) and space based instruments such as SOHO (<https://sohowww.nascom.nasa.gov>), SDO (<http://sdo.gsfc.nasa.gov>), STEREO (<https://stereo.gsfc.nasa.gov/>).

atmosphere can be divided into three main layers: the photosphere, the chromosphere and the corona, as shown in Fig. 1.3.

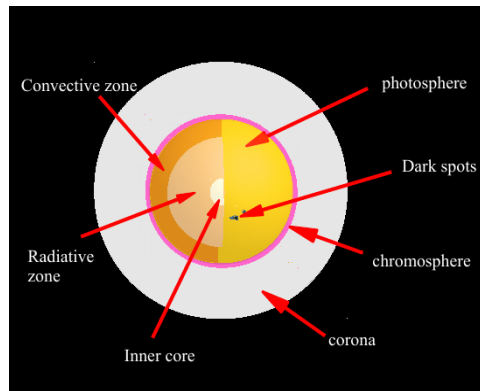


**Figure 1.3.:** Cartoon of a cool main sequence star similar to the Sun, where three main layers of the atmosphere are shown: the photosphere, the chromosphere and the corona.

**Photosphere** The photosphere is the lower part of the solar atmosphere. At the photosphere, the solar magnetic field manifests itself in the form of sunspots (dark spots) and faculae (bright spots), out of which sunspots are the most easily detected features of the solar magnetic field. The first detection of a magnetic field in sunspots was carried out in the early twentieth century by [Hale \(1908\)](#). Figure 1.4 (a) shows an image of the solar photosphere with sunspots and faculae. The corresponding magnetogram (taken from MDI/SOHO archive) in Fig. 1.4 (b) shows the distribution of the solar magnetic field on the same day. Direct observations of the photospheric magnetic field have been carried out over the past few decades using both ground and space based instruments (see [Solanki et al. \(2006\)](#) for a detailed review on solar magnetic activity), providing valuable information about magnetic field generation in the Sun.

**Chromosphere** The region of the solar atmosphere that lies above the photosphere is called the chromosphere. At the chromosphere the density of the plasma is thinner than the photosphere, but the temperature increases abruptly. The temperature rise in the chromosphere is attributed to the solar magnetic field (for more details please refer to Section 2.4.1 in this thesis). The magnetic activity of the chromosphere results in emission of the line cores of certain chromospheric lines. The connection between the solar magnetic field and chromospheric activity was first detected by [Schrijver et al. \(1989\)](#). Since then observations of chromospheric activity have been used as an indirect proxy of magnetic activity for the Sun and other cool stars ([Baliunas et al., 1995](#), [Duncan et al., 1991](#)).

**Corona** The solar corona is also heated by the magnetic field lines. The coronal magnetic fields are responsible for the release of highly energetic particles in the form of prominences, flares, coronal mass ejections and solar winds. The high-energy particles released by the Sun react with the magnetosphere of the Earth and produce the northern and southern lights. The correlation between coronal activity and magnetic flux of cool stars including the Sun was

detected by [Pevtsov et al. \(2003\)](#). The coronal activity of the Sun and other cool stars can be observed in X-ray wavelengths, which provides an indirect detection of the magnetic fields.

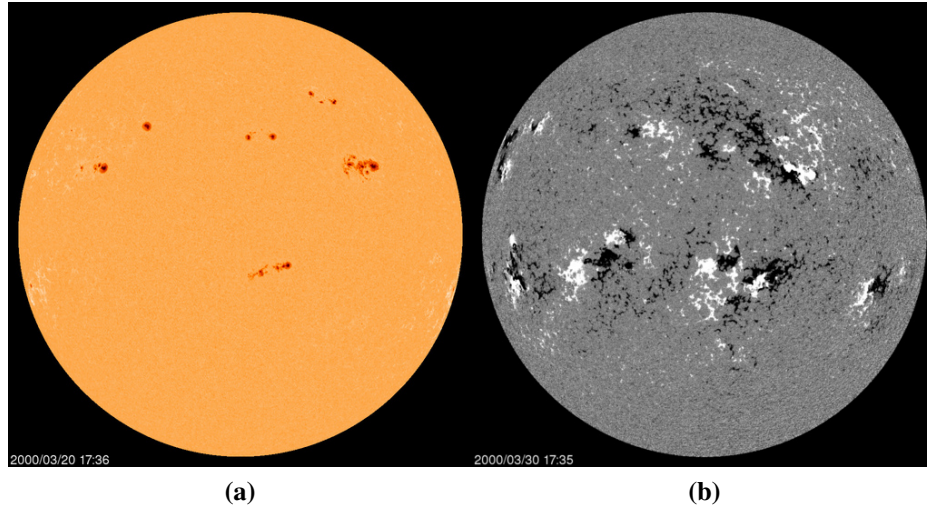


**Figure 1.4.:** (a) Sunspots (dark spots) and faculae (bright spots) on the solar surface. (b) Magnetogram of the Sun showing the bipolar magnetic regions on the surface. The two colours represent two different polarities of the field: one towards the observer and the other opposite. Both images were taken using the MDI instrument aboard SOHO. Credit: SOHO/-NASA

### 1.3. The 11 year solar cycle

The solar magnetic field undergoes cyclic variations, first detected in the form of the sunspot cycle by [Schwabe \(1844\)](#). Although individual sunspots have a lifetime ranging from a few days to weeks, the total number of sunspots vary periodically with a period of 11 years. The appearance of sunspots over the solar cycle is limited to a certain latitude range. As the cycle progresses the sunspots on both hemisphere migrate towards the equator. Long-term observations of the sunspot cycle has shown that the appearance of sunspots results in a characteristics “Butterfly” shape, which is known as the Butterfly diagram of the Sun ([Maunder, 1904](#)), as shown in Fig. 1.5.

The chromospheric and coronal activity of the Sun also undergo cyclic variations, which exhibit strong correlation with the sunspot cycle. Figure 1.6 shows the chromospheric cycle of the Sun ([Baliunas et al., 1995](#)) where the chromospheric activity index S-index shows cyclic variations over similar to the sunspot cycle. The S-index provides a measurement of the emission in the line cores of Ca II H and K lines normalised to the nearby continuum (Section 2.4.1 provides detailed description about the S-index). Observations of the Sun in soft X-rays have shown that the coronal activity of the Sun also varies in sync with the sunspot cycle ([Orlando et al., 2001](#)).

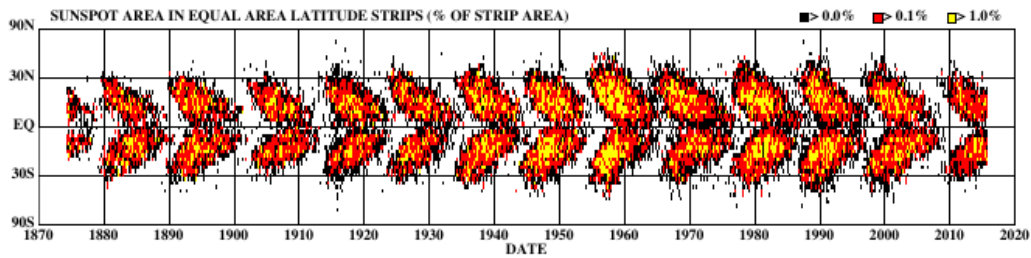


**Figure 1.5.:** The sunspot butterfly diagram with data taken from 1874 onward. Credit: David Hathaway, NASA Marshall space flight center.

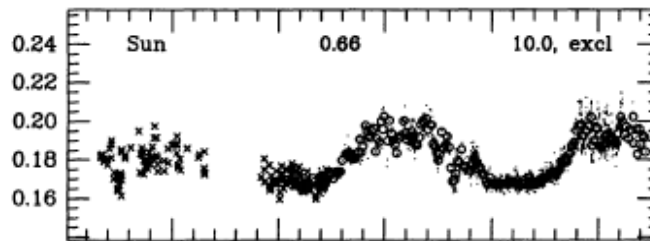


**Figure 1.6.:** Chromospheric activity (S-index) cycle of the Sun taken from [Baliunas et al. \(1995\)](#). The x-axis shows years of observations and the y-axis is the S-index. ©AAS. Reproduced with permission.

## 1.4. The 22 year solar magnetic cycle

Synoptic magnetic maps of the Sun, taken over 30 years, have shown that the global radial magnetic field of the Sun also changes cyclically which is the magnetic cycle of the Sun. The magnetic cycle of the Sun has a 2:1 ratio with its sunspot and activity cycle. During minimum activity when the number of sunspots is low, the magnetic field of the Sun is dipolar and concentrated at the polar regions. As the cycle progresses towards maximum activity the complexity of the radial field increases. The increased field complexity is caused by the appearance of bipolar magnetic regions on both hemispheres, as shown in Fig. 1.7. The bipolar regions appear with one polarity tilted towards the equator and the other towards the pole. The leading polarity of bipolar regions in the northern hemisphere is opposite in sign to the ones in the southern hemisphere. The opposite polarities cancel near the equator as the cycle progresses. The trailing polarity is transported by meridional flows to the poles, where they dominate over the existing opposite polarity magnetic field. This results in a change in polarity of the polar field at the next minimum of activity. It takes 22 years for the polar magnetic fields to revert back to the original polarity, resulting in a 22 year magnetic cycle.

## 1.5. The solar dynamo

The physical process behind the cyclic generation of the solar magnetic field is called the solar dynamo. The dynamo is believed to exist in an interface layer between the radiative

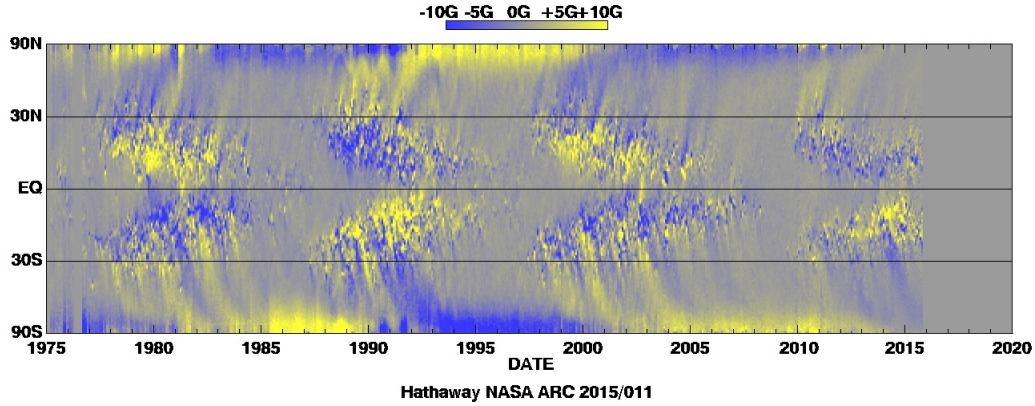


**Figure 1.7.:** The magnetic butterfly diagram which shows the evolution of the solar radial magnetic field. Credit: David Hathaway, NASA Marshall space flight center.

core and convection zone of the Sun known as the tachocline. The magnetic field of the Sun, generated by the dynamo, is responsible for the occurrence of the magnetic cycle. According to dynamo theory, the solar magnetic field consists of a toroidal and poloidal component which alternates as a function of time, resulting in the solar magnetic cycle. The poloidal to toroidal field conversion is caused by the differential rotation of the Sun ( $\Omega$  effect). The twisting of toroidal field to poloidal field is caused by the convective motions of the Sun ( $\alpha$  effect). The  $\alpha$  effect is also linked to the rotation of the star. In one of the most widely used dynamo theory, the mean-field dynamo theory, the  $\alpha$  and  $\Omega$  effect are the two key mechanisms driving the solar dynamo (Krause & Raedler, 1980). Figure 1.5 shows the conversion of poloidal to toroidal and toroidal to poloidal in a mean-field  $\alpha\Omega$  dynamo.

In recent years it has been also considered, that the  $\alpha$  and  $\Omega$  effect may not be the only key dynamo mechanism. Solar cycle observations have shown that the decay of magnetic regions during a magnetic cycle can trigger polarity reversals (Wang et al., 1989). This has triggered the resurgence of the Babcock-Leighton dynamo model, which was first suggested by Babcock (1961) and further developed by Leighton (1964, 1969). In this model, active regions are considered an essential ingredient for the dynamo process. However, there is still no general scientific consensus whether active regions play a direct role or if they are just by products of the dynamo process. Despite the tremendous advances made in dynamo theory over the past few decades, we still lack a uniform model that successfully reproduces all features of solar and stellar magnetic field observations.

The dynamo process in cool stars other than the Sun is poorly understood when compared to the solar dynamo. It is assumed that cool stars with a radiative core and a convective envelope can sustain a dynamo operating from the tachocline. But fully convective cool stars lack an interface layer to support a solar type  $\alpha\Omega$  dynamo. Observations of cool stars show that they might harbour a distributed dynamo that does not require a tachocline to operate (Donati & Collier Cameron, 1997). Such strong azimuthal component is not seen in the case of the

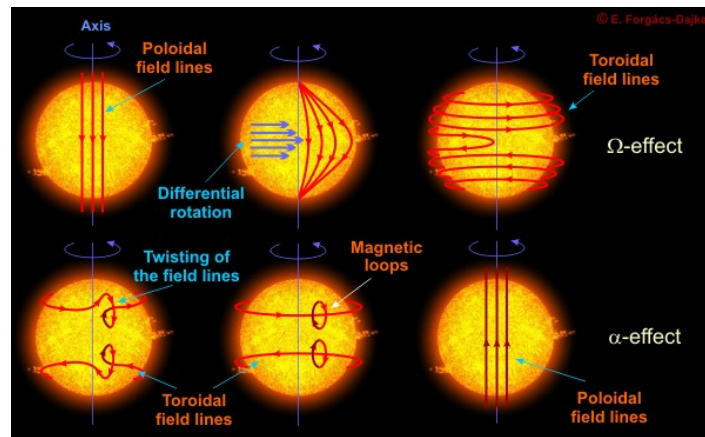


**Figure 1.8.:** Cartoon of the  $\alpha$  and  $\Omega$  effect of the solar dynamo. Credit: E. Forgács Dajka.

Sun. Theoretical models of [Brown et al. \(2010\)](#) shows that a dynamo distributed throughout the convection zone can operate in rapidly rotating cool stars, producing azimuthal magnetic fields.

## 1.6. Cool star magnetism

Solar observations over multiple decades have provided much needed constraints for dynamo theory. On the downside, only one star as a reference is not enough to understand the full complexity of solar and stellar magnetism. Complementary stellar observations over a wide range of parameter can provide valuable information that will improve our knowledge of the physical processes behind magnetic activity in cool stars like the Sun. Apart from dynamo theory, a detailed understanding of magnetic field generation is also necessary for planet detection and habitability studies. During the course of the Sun's cycle, highly energetic events such as strong stellar winds and flares interact with the magnetosphere of the Earth. This interaction is usually harmless and can be seen in the form of northern and southern lights. However, strong eruptive events can cause failures of the orbiting satellites, causing communication disruptions and power blackouts on Earth. The early Sun's strong magnetic field might also have been responsible for the loss of liquid water on Mars' atmosphere ([Lundin et al., 2007](#)).

Cool stars are point sources, and they lack the spatial and temporal resolution of the Sun. Under such conditions, we cannot directly observe individual magnetic features such as spots and plages but only observe integrated light from the visible stellar disk. Magnetic activity in cool stars is observed in the form of chromospheric emission of certain spectral lines ([Baliunas et al., 1995](#), [Duncan et al., 1991](#), [Wilson, 1978](#)) (as shown in Fig. 1.9), coronal emission in X ray observations ([Güdel, 2004](#), [Pevtsov et al., 2003](#)) and photometric variability ([Basri et al., 2013](#)). Direct detection of magnetic fields in cool stars depends on the Zeeman effect on both polarised ([Semel, 1989](#)) and unpolarised ([Reiners & Basri, 2006](#), [Robinson, 1980](#), [Saar, 1996](#)) spectral lines. These different techniques of field detection probe different aspects of stellar magnetic fields. No technique alone can unravel the full complexity of stellar

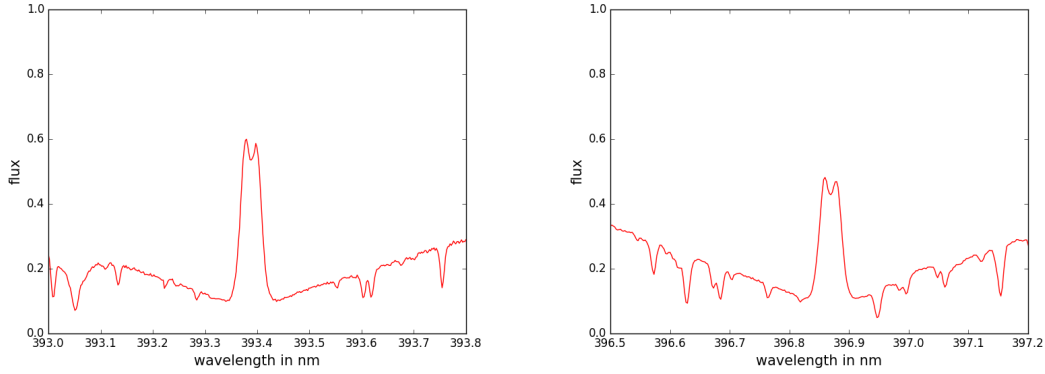


**Figure 1.9.:** Chromospheric Ca II H and K lines for an active sun-like star, where the emission in the K and H lines are shown.

magnetism. By combining these different techniques, more detailed information on stellar magnetic fields can be obtained.

### 1.6.1. Stellar activity cycles

Chromospheric activity is the most widely used proxy of magnetic activity. The first direct relation between chromospheric emission and the solar magnetic field was determined by [Schrijver et al. \(1989\)](#). For cool stars, the long-term Mount Wilson program is arguably the most famous monitoring program of chromospheric activity. Almost half a century's worth of observations made during this project resulted in the first sun-like activity cycles in other stars ([Baliunas et al., 1995](#)). Based on these observations [Baliunas et al. \(1995\)](#) reported that solar-type cool stars tend to exhibit different levels of cyclic/non-cyclic activity variations which is probably governed by their stellar properties. Cyclic variations of coronal activity, on the other hand, is not as widely monitored as its chromospheric counterpart. Since the first statistical evidence of coronal activity ([Hempelmann et al., 1996](#)), coronal cycles have been detected in X-ray observations for a few cool stars in the past decade ([Favata et al., 2008](#), [Robrade et al., 2012](#), [Sanz-Forcada et al., 2013](#)).

With the detection of chromospheric activity cycles in cool stars numerous authors also investigated the relationship between cycle periods and stellar rotation ([Baliunas et al., 1985](#), [Brandenburg et al., 1998](#), [Noyes et al., 1984b](#), [Saar & Brandenburg, 1999](#)). The key motivation behind carrying out such studies was to investigate the relationship between activity cycle and rotation. For old stars with cyclic chromospheric activity, [Noyes et al. \(1984b\)](#) reported a possible correlation between activity cycle period  $P_{cyc}$  and Rossby number  $Ro$ , where  $Ro$  is the ratio of the rotation period to the convective overturn time ( $P_{rot}/\tau$ ). Surprisingly [Baliunas et al. \(1985\)](#) did not find any correlation between activity cycle period  $P_{cyc}$ , rotation period  $P_{rot}$ , Rossby number  $Ro$  and other stellar properties. The Mount Wilson sample was re-investigated by [Brandenburg et al. \(1998\)](#), where they used the ratio of activity cycle and rotation frequencies ( $\omega_{cyc}/\Omega = P_{rot}/P_{cyc}$ ) instead of  $P_{cyc}$  and defined  $Ro$  as  $1/2\Omega\tau = P_{rot}/4\pi\tau$ . The motivation behind using  $\omega_{cyc}/\Omega$  is that in mean field dynamo theory

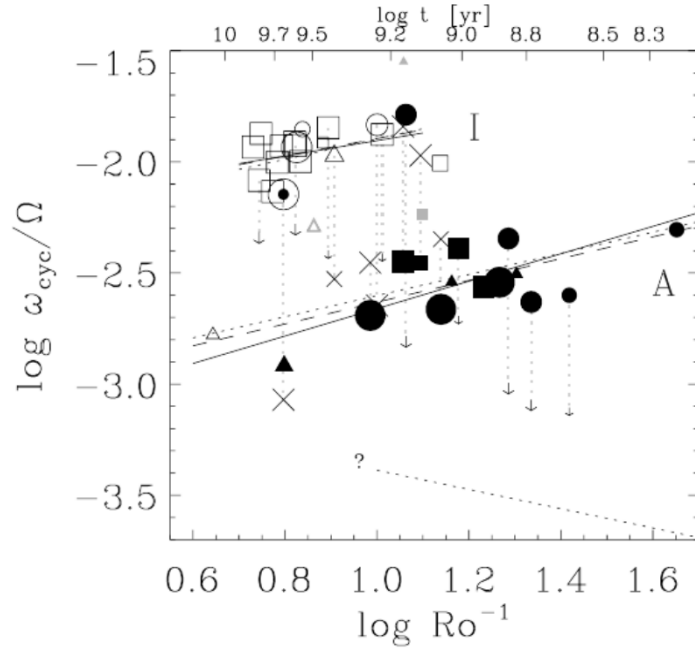


**Figure 1.10.:** Plot showing the Active (A) and Inactive (I) branch classification of chromospheric activity cycle periods, taken from Saar & Brandenburg (1999). Both x and y axis are in logarithmic scale. The x-axis plots the inverse Rossby number which represents stellar rotation. The y-axis is  $\omega_c/\Omega$  which is equivalent to rotation period/activity cycle period. The open symbols are inactive stars with low chromospheric activity ( $\log R'_{HK} > -4.75$ ) and the filled symbols are active stars. The different symbols represent different spectral types (F, G, K). ©AAS. Reproduced with permission.

the ratio is proportional to the  $\alpha$  effect. One of the most noteworthy results of Brandenburg et al. (1998) was the increase of  $\alpha$  with magnetic activity. Brandenburg et al. (1998) also reported the presence of two distinct branches of stars separated in  $\omega_{cyc}/\Omega$ . The presence of these two separate branches was first reported by Saar & Baliunas (1992) where they classified the two branches as Active (young) and Inactive (old) branch, further reconfirmed by Saar & Brandenburg (1999) as shown in Fig. 1.10.

The Rossby number is inversely proportional to the convective overturn time  $\tau_c$  ( $Ro \propto \frac{1}{\tau_c}$ ). However, the  $\tau_c$  used in previous work is empirically determined and is a function of  $B - V$  colour. It is also heavily dependent on the model used to calculate it. Additionally,  $\tau_c$  might have a dependence on other stellar properties such as metallicity or age (Landin et al., 2010), which have not been fully explored. Hence, to investigate the activity cycle period-rotation relation independently, Böhm-Vitense (2007) investigated cycle periods as a function of rotation periods. The author also report the presence of the Inactive and Active branch as shown in Fig. 1.11, with the Sun in the middle of the two branches.

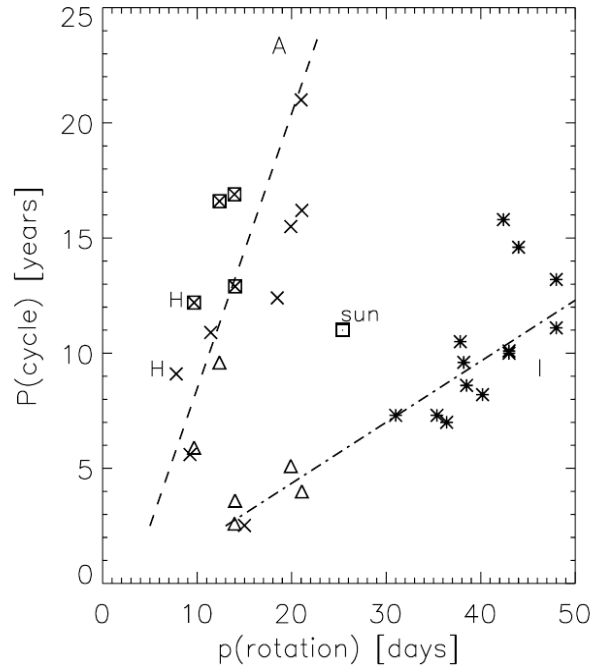


**Figure 1.11.:** Chromospheric activity cycles as a function of rotation period, taken from [Böhm-Vitense \(2007\)](#). ©AAS. Reproduced with permission.

### 1.6.2. Stellar magnetic cycles

As previously mentioned, chromospheric activity is an indirect proxy of magnetic activity. As a result of which the activity cycles determined from the Mount Wilson project and any other subsequent long-term chromospheric activity monitoring provides indirect information about the star's dynamo operated magnetic cycle. Information about the large-scale magnetic field and the resulting magnetic cycle of cool stars can be obtained by using Zeeman Doppler imaging (ZDI) ([Brown et al., 1991](#), [Donati et al., 1997](#), [Semel, 1989](#)) on spectropolarimetric observations (see Section 2.3.2 for a detailed description of the ZDI technique). ZDI is a tomographic technique that reconstructs the large-scale surface magnetic field geometry of stars using circularly polarised spectra. The magnetic cycle is determined from polarity reversals of the large-scale field of the star, which indicates the presence of a magnetic cycle.

Magnetic cycle in cool stars other than the Sun was first detected for the F star  $\tau$  Boo ([Fares et al., 2009](#), [Mengel et al., 2016](#)), where the large-scale geometry flipped polarity on a yearly basis resulting in a magnetic cycle which is shorter than 2 years. [Mengel et al. \(2016\)](#) also reports that the magnetic cycle of  $\tau$  Boo has a 3:1 relation with the activity cycle of the star. A magnetic cycle was also detected for the G0 dwarf HD 78366 ([Morgenthaler et al., 2011](#)), where the radial component of the magnetic field reverses polarity indicating a possible 3-year cycle. Polarity reversals were observed in the large-scale field of the G2 dwarf HD 190771 ([Morgenthaler et al., 2011](#), [Petit et al., 2009](#)). However, the variability of the large-scale field of HD 190771 is more complex. The polarity reversal in the azimuthal field

reported by [Petit et al. \(2009\)](#) is not detected in subsequent epochs. Instead, a polarity reversal is reported in the radial component of the magnetic field in the following epochs as shown by [Morgenthaler et al. \(2011\)](#). Polarity reversals of the large-scale field have been detected only for a few cool stars, out of which none exhibit a magnetic/activity cycle relationship similar to the solar case.

## 1.7. Motivation

The motivation behind this thesis is to investigate magnetic and activity cycles in cool stars belonging to a wide range of stellar properties. Observations of magnetic and activity cycles in cool stars can provide valuable information about the stellar dynamo and its dependence on basic stellar properties such as rotation. In this thesis, the magnetic and activity cycle of cool stars are investigated using both spectropolarimetric and spectroscopic observations. Detailed investigation of cool stellar magnetic field geometry is carried out for three stars, HN Peg, 61 Cyg A and  $\epsilon$  Eridani. HN Peg is a young G dwarf (rotation period of 4.6 days), 61 Cyg A is an older K dwarf (rotation period of 35.7 days)<sup>2</sup> and  $\epsilon$  Eridani is a young K dwarf (rotation period of 11.68 days)<sup>3</sup>. The magnetic field geometry was reconstructed using ZDI on long-term spectropolarimetric observations, and the chromospheric activity variations were determined from three chromospheric tracers namely, Ca II H & K, H $\alpha$  and the Ca II infrared triplet. The relation between chromospheric activity cycle period and rotation was also investigated for a wide range of F,G,K stars, which are part of the Göttingen chromospheric activity catalogue<sup>4</sup>. The catalogue was developed by Sudeshna Boro Saikia in collaboration with another PhD student Christopher J. Marvin.

The thesis is structured into the following sections. Chapter 2 describes the methodology of stellar magnetic field detection including the magnetic field geometry reconstruction using ZDI. Chapter 3 describes the spectropolarimetric observations and magnetic field geometry reconstructions of HN Peg, followed by the results of 61 Cyg A in Chapter 4<sup>5</sup>. Chapter 5 discusses the Göttingen chromospheric activity catalogue and the cycle period-rotation relation for F,G,K stars<sup>6</sup>. Chapter 6 describes the magnetic geometry evolution of Epsilon Eridani at its chromospheric activity minimum. Finally, Chapter 7 summarises the results and their implication on current stellar magnetic field research and outlook for the future.

---

<sup>1</sup>The spectropolarimetric and spectroscopic data of 61 Cyg A and HN Peg were obtained as part of the international BCooll collaboration. [http://bcool.ast.obs-mip.fr/Bcool/Bcool\\_\\_\\_cool\\_magnetic\\_stars.html](http://bcool.ast.obs-mip.fr/Bcool/Bcool___cool_magnetic_stars.html)

<sup>2</sup>An article containing the results of  $\epsilon$  Eridani will be submitted to the journal MNRAS in November 2016

<sup>3</sup>The chromospheric database included in this thesis was carried out as a collaborative work between Sudeshna Boro Saikia and Christopher J. Marvin. More details in Chapter 5

<sup>4</sup>Both Chapters 3 and Chapter 4 were published in the peer-reviewed journal *Astronomy & Astrophysics*, [Boro Saikia et al. \(2015\)](#), [Boro Saikia et al. \(2016a\)](#)

<sup>5</sup>Chapter 5 has been submitted to *Astronomy & Astrophysics* ([Boro Saikia et al., 2016b](#))



## 2. Methods of field detection

### Contents

---

<b>2.1. Mechanisms for magnetic field detection . . . . .</b>	<b>14</b>
2.1.1. Zeeman effect . . . . .	14
2.1.2. Polarisation of light and the Stokes parameters . . . . .	16
<b>2.2. Instrumentation and data reduction . . . . .</b>	<b>19</b>
2.2.1. An astronomical spectrograph . . . . .	19
2.2.2. Instrumentation to detect polarisation . . . . .	21
2.2.3. Least square deconvolution . . . . .	23
<b>2.3. Magnetic field measurements using Stokes <math>V</math> and <math>I</math> . . . . .</b>	<b>25</b>
2.3.1. Longitudinal magnetic field measurement . . . . .	25
2.3.2. Zeeman Doppler imaging (ZDI) . . . . .	26
<b>2.4. Indirect proxies of magnetic activity . . . . .</b>	<b>31</b>
2.4.1. Chromospheric activity . . . . .	31
2.4.2. Coronal activity . . . . .	34
<b>2.5. Summary . . . . .</b>	<b>35</b>

---

The presence of magnetic fields in cool stars can be detected by observing the Zeeman effect in spectral lines or by using indirect proxies of magnetic activity. To determine the large-scale magnetic geometry of cool stars, observations of the Zeeman effect in polarised spectra is required. High-resolution spectropolarimeters (a polarimetric unit coupled with a spectrograph) are necessary to detect the faint Zeeman signatures in polarised spectral lines. ZDI is used to reconstruct the large-scale magnetic field geometry of stars, which requires high-resolution circularly polarised spectra sampled over the rotational cycle of the star. ZDI reconstructions of cool stars have been possible only recently with the development of high-resolution spectropolarimeters such as NARVAL, ESPaDOnS and HARPS-pol. On the other hand, indirect proxies, such as chromospheric activity, can be determined from the emission of certain chromospheric spectral lines. Details about stellar magnetic field detection, including ZDI reconstructions and indirect proxies, can be found below.

## 2.1. Mechanisms for magnetic field detection

### 2.1.1. Zeeman effect

When electrons in an atom or a molecule transition from one energy level to another it results in emission or absorption of photons. In the presence of a magnetic field the energy levels are split into different components, detected as split in the emission or absorption line, resulting in the Zeeman effect (Zeeman, 1897). This splitting of the energy levels is dependent on the spin ( $S$ ) and orbital ( $L$ ) momentum of the electron together with the magnetic moment of the field.

In classical theory, the Zeeman effect can be simply explained by the Lorentz triplet as shown in Fig 2.1. Although splitting of a spectral line into a triplet is most commonly accepted as the *normal* Zeeman effect, we now know that it is not the general case. Under normal circumstances the splitting is more complicated with multiple lines, which is now known as the *anomalous* Zeeman effect. The *normal* Zeeman effect comes into play when the electron spin effect is absent, which can be seen in the case of singlets (a more detailed overview on the Zeeman effect can be obtained from Condon & Shortley (1963)).

In the presence of an applied magnetic field the Hamiltonian of an atom is described by the unperturbed Hamiltonian  $H_0$  and the magnetic Hamiltonian  $H_B$  (Condon & Shortley, 1963, Landi Degl'Innocenti & Landolfi, 2004). For stars  $H_B$  can be expressed without the diamagnetic term as shown in equation 2.1. The diamagnetic term is negligible for the weak magnetic fields in stars.

$$H_B = \mu_0(L + 2S) \cdot B \quad (2.1)$$

where  $\mu_0$  is the Bohr magneton,  $L$  and  $S$  are the orbital and spin angular momenta of the atom, and  $B$  is the weak field applied to the atom. For weak fields, the magnetic energy is comparatively smaller than the spacing between the energy levels. In such cases the total spin and orbital momenta of the atom can be considered to be a summation of the individual spin and orbital momenta of the electrons. As a result of which the total angular momentum ( $J$ ) is described as  $J=L+S$  (also known as  $LS$  coupling). When such a weak magnetic field is applied, each energy level with an unperturbed total angular momentum of  $J$ , splits into  $2J+1$  states. The change in energies is given by,

$$\Delta E = \mu_0 g B M \quad (2.2)$$

where  $\Delta E = E_f - E_i$  ( $E_f$  is the final and  $E_i$  is the initial energy),  $M$  is the magnetic quantum number that ranges from  $-J \leq M \leq J$ , and  $g$  is the dimensionless Landé factor. The Landé factor describes the magnetic moment of the electron and is dependent on its orbital and spin momentum. Under the conditions of  $LS$  coupling, which is applicable for lightweight atoms,  $g$  can be expressed as,

$$g(SLJ) = \frac{3}{2} + \frac{S(S+1) - L(L+1)}{2J(J+1)} \quad (2.3)$$

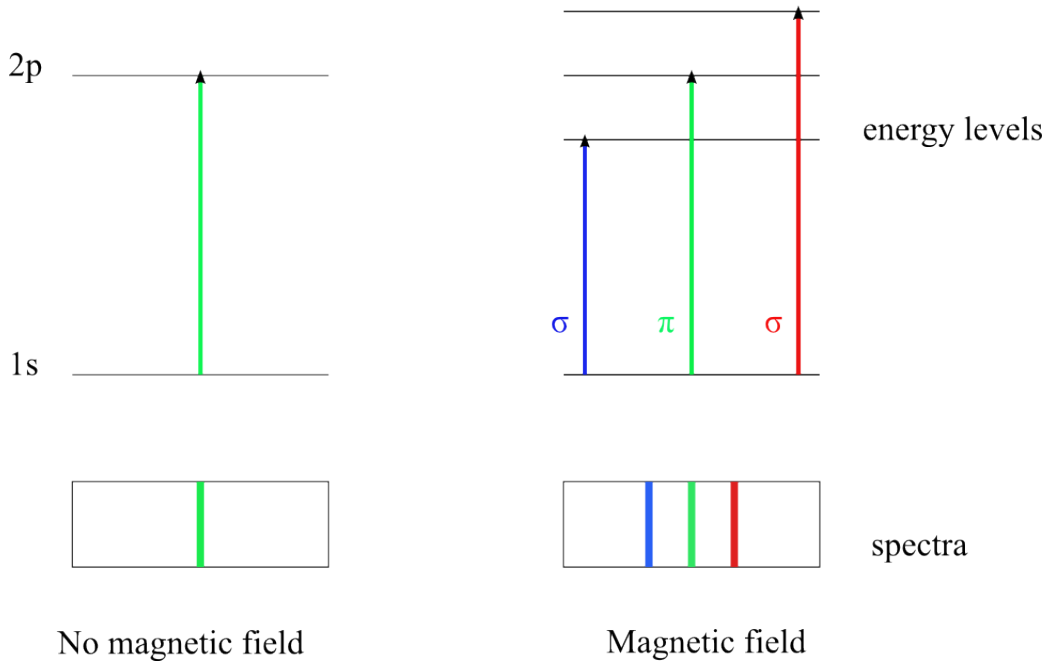


**Figure 2.1.:** Zeeman effect where splitting of a line into three components ( $\pi$ ,  $\sigma_{red}$ ,  $\sigma_{blue}$ ) is shown.

The splitting of spectral line into multiple lines is determined by the Landé factor  $g$ . In the case of a simple dipole transition between two energy levels  $E_i$  and  $E_f$  obeys the selection rule  $\Delta M = 0, \pm 1$  ( $\Delta M = M_f - M_i$ ) and results in the formation of three groups of lines. The lines formed due to  $\Delta M = 0$  are called the  $\pi$  components and the group of lines formed due to  $\Delta M = \pm 1$  are called the  $\sigma$  components ( $\sigma_{red}$ ,  $\sigma_{blue}$ ). The  $\pi$  components are formed around the unperturbed line and the  $\sigma$  components are formed symmetrically on either side of the unperturbed line as shown in Fig 2.1. The  $\pi$  and  $\sigma$  groups usually consists of several components but for the *normal* Zeeman effect only three components are formed resulting in a triplet. The triplet is formed when both energy states  $E_i$  and  $E_f$  have  $g$  equal to unity ( $g_i = g_f = 1$ ). In fact as long as the Landé factor is equal between the two energy states the resulting split will consist of a triplet. The triplet is also formed for cases where  $J=0$  for one of the energy levels. The shift in the two  $\sigma$  components are always equal and it depends on the Landé factor and the strength of the external magnetic field  $B$ .

The shift of a  $\sigma$  component can also be expressed in terms of wavelengths as shown by equation 2.4, which is used for magnetic field measurements in stars. Under such circumstances the wavelength shift is a function of the initial unperturbed wavelength.

$$\Delta\lambda(\text{nm}) = 4.67 \times 10^{-12} \bar{g} \lambda_0^2 B \quad (2.4)$$

where  $\lambda_0$  is the unperturbed wavelength in nm,  $B$  is the field strength in Gauss, and  $\bar{g}$  is the effective Landé factor. The effective Landé factor ( $\bar{g}$ ) is a special term to characterise the average shift of the  $\sigma$  components with respect to the unperturbed line center in the presence of a magnetic field.  $\bar{g}$  can be expressed in terms of the Landé factor of the initial and final

energy levels  $g_i$  and  $g_f$  as shown,

$$\bar{g} = \frac{1}{2}(g_i + g_f) + \frac{1}{4}(g_i - g_f)(J_i - J_f)(J_i + J_f + 1) \quad (2.5)$$

where  $g_i$  and  $g_f$  are the Landé factors, and  $J_i$  and  $J_f$  are the angular momenta of the initial and final energy levels.

### **Zeeman effect in unpolarised spectra**

Cool star magnetic fields are generally in the order of a few kG, which is extremely difficult to detect in optical wavelengths using unpolarised spectroscopy. For example, in the case of Na D lines in a 1 kG field the splitting caused at  $\lambda_0 = 500$  nm is roughly 0.001 nm or less than  $1 \text{ km s}^{-1}$  in velocity space. Such small displacement are beyond the detection limit of current astronomical instrumentation. But equation 2.4 tells us that, for the same  $B$  and effective Landé factor  $\bar{g}$ ,  $\Delta\lambda$  is directly proportional to  $\lambda_0$ . As a result of which if we go to longer wavelengths such as the infra-red, the displacement gets bigger and easier to detect. Additionally, in the absence of any splitting the broadening of spectral lines can be also used to measure the field strength. However, care should be taken as the broadening due to Zeeman effect can be masked by other effects such as rotation.

Broadening due to the Zeeman effect can be determined from spectral lines that are highly sensitive to the magnetic field, providing measurements of the average field intensities (Saar, 1988). On the other hand if we go to the infrared or near infrared wavelength, weaker field strengths in cool stars specially M dwarfs can be easily determined. M dwarfs have more flux in longer wavelengths as a result of which not only average field intensities but Zeeman splitting can also be directly determined for some stars (Saar & Linsky, 1985). However, when it comes to F, G, K stars this technique is not as effective as their magnetic field can be much weaker than M dwarfs.

### **2.1.2. Polarisation of light and the Stokes parameters**

Zeeman effect can also be detected as polarised signatures in spectral lines. One advantage of investigating the polarised signatures of spectral lines is the detection of weaker field strengths, as fields as weak as a few G can be detected. Another advantage is that by analysing the polarisation state of spectral lines information can also be gained on the orientation of the magnetic field (Donati & Landstreet, 2009, Landi Degl'Innocenti & Landolfi, 2004).

In the presence of an external magnetic field, the three components  $\pi$ ,  $\sigma_{\text{red}}$ , and  $\sigma_{\text{blue}}$  exhibit their own specific polarisation states as shown in Fig 2.2. Depending on the angle between the line-of-sight and the magnetic field vector, the observed polarisation state changes. The linearly polarised  $\pi$  component is visible only if the line-of-sight is perpendicular to the magnetic field vector as shown in Fig 2.2. If the magnetic field is in the same direction as the line-of-sight then the  $\pi$  component is non existent in that direction. On the other hand

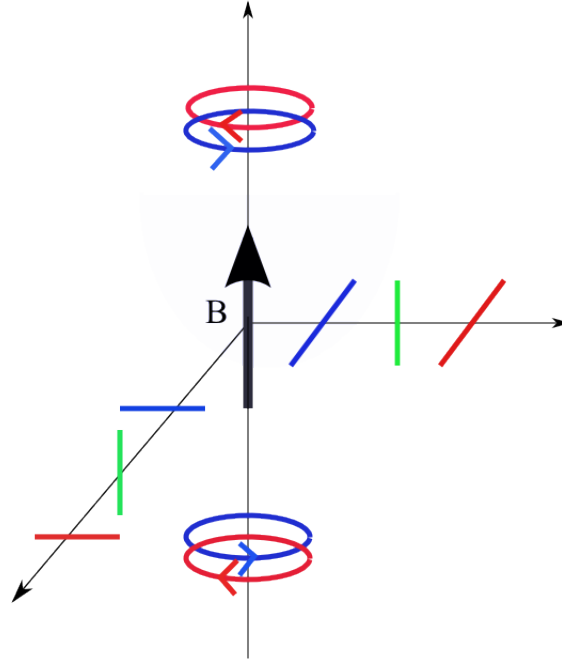


**Figure 2.2.:** Polarisation states of the  $\pi$  and  $\sigma$  components in the presence of a magnetic field  $B$ . The colours used are same as Fig 2.1

the  $\sigma$  components can be both linearly and circularly polarised depending on the orientation of the observer with respect to the magnetic field vector. If the line-of-sight is perpendicular to the magnetic field vector, the  $\sigma$  components are linearly polarised and perpendicular to the  $\pi$  component as shown in Fig. 2.2. On the other hand, if the line-of-sight is in the same direction as the magnetic field vector then the two  $\sigma$  components ( $\sigma_{red}$ ,  $\sigma_{blue}$ ) are circularly polarised with opposite signs. The different polarisation states of the  $\pi$  and  $\sigma$  components can be characterised by using the Stokes parameters (Stokes, 1852).

### Stokes parameters

The Stokes parameters are used to describe polarised stellar spectra and can be represented by using Mueller calculus, where the four parameters are grouped into a column vector known as Stokes vector. There are four Stokes parameters  $I, Q, U$  and  $V$ , where  $I$  represents the intensity of the light and  $Q, U$  and  $V$  are the different polarisation states as shown in Fig 2.3. Stokes  $Q$  is defined by subtracting two orthogonal linearly polarised beam. Stokes  $U$  also represent linear polarisation but is shifted by  $45^\circ$  with respect to  $Q$ . Stokes  $V$  is the circular polarisation state defined by subtracting a right and a left circularly polarised beam. The four Stokes parameters can be determined experimentally but only  $Q, U$  and  $V$  are independent, since  $I^2 = Q^2 + U^2 + V^2$  for a perfectly polarised spectrum. Hence  $I$  can always be deduced

from the other three parameters but the other three Stokes parameters cannot be deduced by knowing  $I$  as it results in ambiguity in sign.

Stokes parameters provide a relatively straightforward technique to measure linear and circular polarisation. However, in order to apply it to stellar magnetic fields certain key points have to be considered. If our knowledge of the solar magnetic field applies to other solar-type stars, then they will also exhibit group of spots with opposite polarity. In circularly polarised Stokes  $V$ , the spots with opposite polarity will cancel each other resulting in no magnetic field detection. Where as with linearly polarised Stokes  $Q$  and  $U$ , opposite polarity spots perpendicular to each other will cancel. But in reality stars are rotating bodies with complex magnetic field geometry. In spite of the cancellation effect in circularly polarised spectra a “net” or large-scale magnetic field can be still measured.

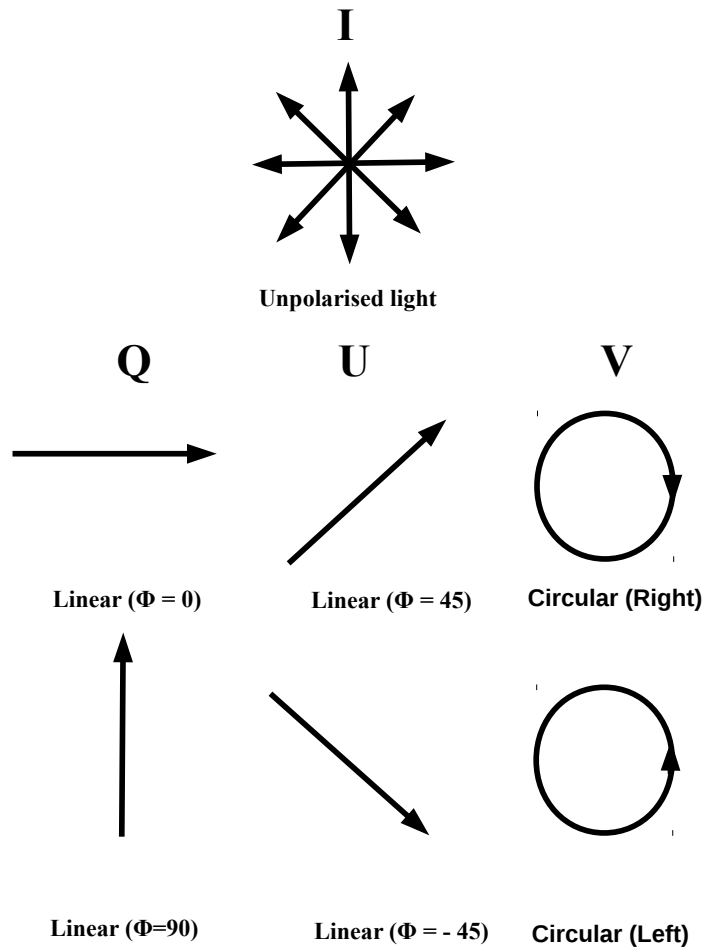


**Figure 2.3.:** Stokes parameters that represent the different polarisation states.

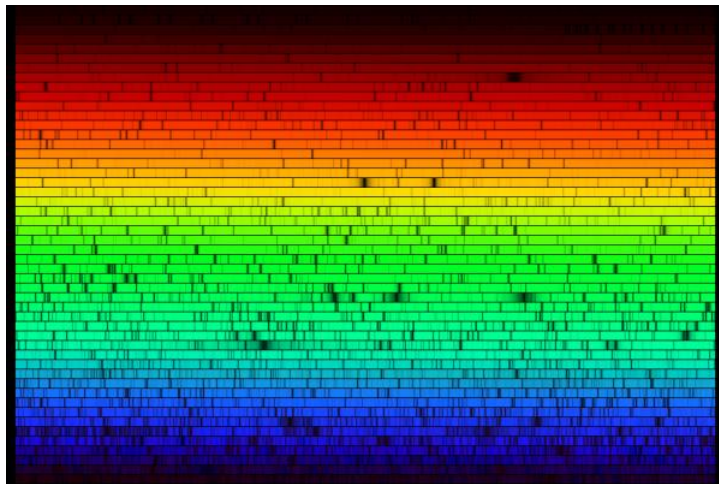


**Figure 2.4.:** Solar spectrum taken using a Fourier Transform Spectrometer (FTS) at the National solar Observatory, Kitt peak. The image is created to mimic an echelle spectrum with complete coverage in the visual wavelength. Credit: N.A.Sharp, NOAO/NSO/Kitt Peak FTS/AURA/NSF

In the past decade, circularly polarised Stokes  $V$  observations have been very successful in detecting cool star magnetic fields thanks to high-resolution spectropolarimeters such as NARVAL, ESPaDOnS, HARPS-pol (description of a high-resolution spectropolarimeter can be found in the next Section). A previous study of cool star magnetic fields using stellar models (Piskunov & Kochukhov, 2002) has shown that linear polarisation (Stokes  $Q$  and  $U$ ) is extremely difficult to detect and requires very strong magnetic fields. Linear polarisation signatures in stellar spectral lines are weaker than circular polarisation by at least a factor of 10. Apart from magnetic field measurements in all Stokes parameters for Ap and Bp stars by Wade et al. (2000), all Stokes measurements have only been possible for a RS CVn star II Peg Rosén et al. (2015). As a result of which only circularly polarised Stokes  $V$  is currently used to measure magnetic fields in cool stars using techniques such as Zeeman Doppler Imaging (ZDI) (Brown et al., 1991, Donati & Brown, 1997, Semel, 1989). Section 2.3.2 provides a detailed description of the ZDI technique.

## 2.2. Instrumentation and data reduction

### 2.2.1. An astronomical spectrograph

Spectroscopy is used as a fundamental tool to detect stellar magnetic fields, stellar activity, exoplanets and to determine physical properties, chemical composition of astronomical sources. It is the technique of dispersing light as a function of its wavelength into a spectrum. To record stellar spectrum a spectrograph has to be used. Figure 2.4 shows the solar spectrum, where the image was created to mimic an echelle spectrum (brief description of an echelle spectrograph can be found below) covering the full visible wavelength range. The dark spaces in the spectrum are absorption lines.

Astronomical spectrographs disperse light collected by a telescope onto a detector to record the spectrum. They consist of at least four optical elements: a slit, a collimator, a dispersing element and a detector. In case of an echelle spectrograph one extra optical element known as a cross-disperser is added after the dispersing element. Figure 2.5 provides an illustration of a basic slit spectrograph, where light collected by the telescope passes through the different optical elements.

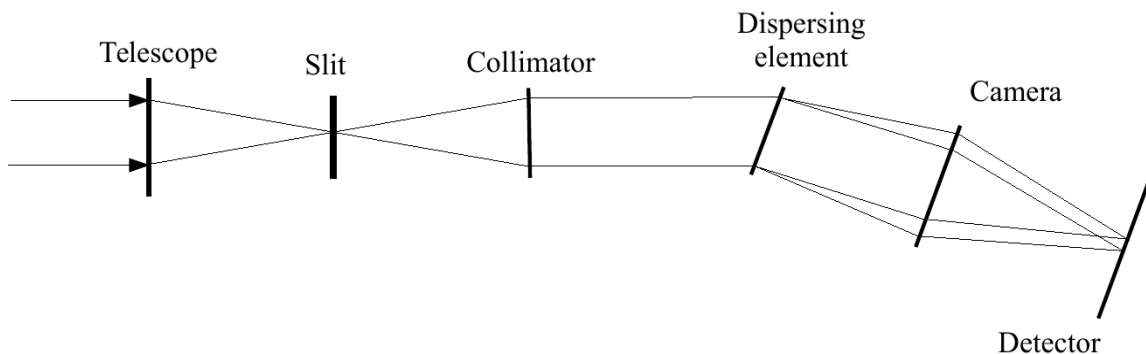


**Figure 2.5.:** Illustration showing the basic components of a spectrograph.

The slit of a spectrograph sits on the focal plane of the telescope, where the beam of light from the telescope is passed. The diverging light beam from the slit passes through a collimator (a mirror or a lens). The collimator is used to convert the diverging beam of light into a parallel beam directed towards the disperser. The collimated beam of light is dispersed by a diffraction grating or a prism. Grating spectrographs have a better angular dispersion compared to prisms which makes them very attractive for optical spectroscopy. The most widely used dispersing element in modern spectrographs is an echelle grating (Bingham, 1979). The echelle grating is a diffraction grating operating at high angle of diffraction and high diffraction orders. This allows the use of small number of grooves on the grating. The higher orders is required to perform high-resolution spectroscopy. However, one disadvantage of using higher orders is the overlap in wavelength. Echelle spectrographs use of a cross-disperser to reduce this wavelength overlap. Either a prism or a grating can be used as a cross-disperser. Once the dispersed beam leaves the echelle grating it is projected onto a detector that produces the spectrum. Photographic plates were the detector of choice before the arrival of electronic devices. The detector used in most modern astronomical spectrographs is a CCD (charge-coupled device). The CCD consists of a 2D array of photon-sensitive elements known as pixels. The photons collected by the pixels result in the release of electrons, which are collected in a read-out device to record the spectrum (for detailed description of astronomical spectrographs please refer to Massey & Hanson (2013)). To detect Stokes *V* signatures in stellar spectral lines high resolution spectrographs equipped with state of the art polarimeters are required. The basic principles of an astronomical polarimetric instrument is discussed below.

### 2.2.2. Instrumentation to detect polarisation

A conventional polarimetric instrumental setup consists of a polariser and a retarder. A polariser is an optical element which only allows linearly polarised light to pass by blocking all other polarisation states of the emerging beam. For a simple single beam polariser, any state of vibration orthogonal to the polariser's axis is rejected. On the other hand a double-beam polariser allows both orthogonally linear polarised wave to pass. An example of a polariser is a birefringent crystal such a Wollaston prism. Fig 2.6 shows a Wollaston prism that consists of two prisms (either calcite or quartz) joined together such that the optical axis of the two prisms are orthogonal to each other. When the unpolarised beam of light is orthogonally incident on the two optical axis, the birefringent nature of the prisms separates the beam into two orthogonal linearly polarised states.

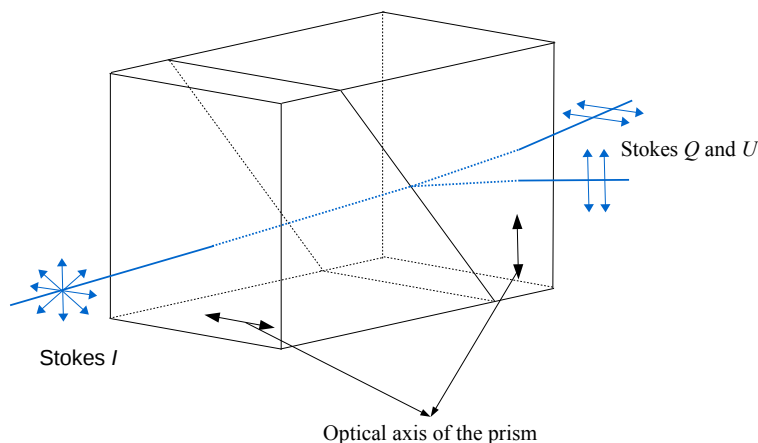


**Figure 2.6.:** Figure showing the principles of a Wollaston prism.

A retarder is used to change the polarisation state of the emerging beam of light. Two of the most commonly used retarders are half-wave and quarter-wave retarders. Quarter-wave retarders are used to convert linear polarisation to circular polarisation and vice versa, where as half-wave retarders are used to change the direction of vibration of the linearly polarised beam. When a linearly polarised light is incident orthogonal to the optical axis of a birefringent wave-plate, it introduces a phase delay between the two perpendicular components of the linearly polarised beam. The phase delay between these two components depends on the thickness of the wave-plate, the material used, the difference in refractive indices of the material and the wavelength of the light. Fig 2.7 shows a half wave-plate which is made of a birefringent crystal. The component of the polarised light parallel to the optical axis is

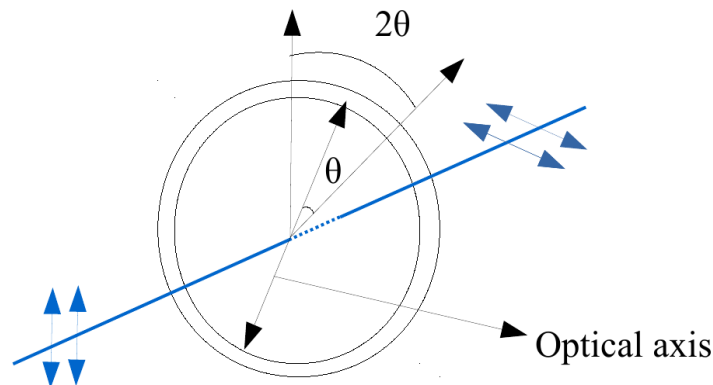


**Figure 2.7.:** Half wave plate made of a birefringent crystal that transforms one linear polarisation state to another.

retarded relative to the perpendicular component. This results in a phase delay which is in the order of half a wavelength, causing a change in direction of polarisation of the linearly polarised beam.

The same principles described above are used in astronomical polarimeters. However, to be able to detect polarised signatures in spectral lines high-resolution spectropolarimeters covering a wide wavelength range are essential. Modern spectropolarimeters usually consists of a polarimeter coupled with a high-resolution spectrograph. Fig 2.8 shows the layout of the ESPaDOnS spectropolarimeter which consists of a retarder, a polariser and several other optical elements. ESPaDOnS is a high-resolution echelle spectrograph with a polarimetric unit. The polarimeter is installed at the Cassegrain module of the telescope and fibre-fed to the spectrograph. Fresnel rhombs are used as retarders, where one quarter-wave retarder is flanked by two half-wave retarders followed by a Wollaston prism. Linear or circularly polarised spectra can be obtained by rotating the half-wave Fresnel rhombs with respect to the quarter-wave rhomb and the Wollaston prism (Donati, 2003). When the polarimetric unit is not required the Wollaston prism can be replaced by a wedged plate. Full spectropolarimetry to obtain all Stokes parameters (Stokes  $I$ ,  $U$ ,  $V$  and  $Q$ ) can also be performed using this setup. The spectropolarimetric data used in this thesis is taken using the NARVAL spectropolarimeter which is a twin of the ESPaDOnS spectropolarimeter. A list of current and upcoming high-resolution spectropolarimeters can be found in Table 2.1.

**Table 2.1.:** List of current and upcoming high-resolution spectropolarimeters

Spectropolarimeter	Resolution	Wavelength coverage (in nm)	status
NARVAL	65000	350 to 1000	current
ESPaDOnS	65000	350 to 1000	current
HARPS-pol	110,000	380 to 690	current
PEPSI	120,000	450 to 1100	upcoming
SPIRou	70000	980 to 2350	upcoming

### 2.2.3. Least square deconvolution

For active cool stars, circular polarisation induced Zeeman signature has too low an amplitude to be detected in individual spectral lines. Direct detection of circular polarisation (Stokes  $V$  signatures) in individual stellar spectral lines require a signal-to-noise (S/N) of at least 1000 (Donati et al., 1992) which is extremely difficult to achieve for cool stars. To detect Zeeman effect induced circular polarisation in stellar spectra a multiline technique called least squares deconvolution (LSD) is used (Donati et al., 1997, Kochukhov et al., 2010). It is safe to assume that under the weak field regime the magnetic field affects all magnetically sensitive stellar lines in a similar way. LSD reconstructs a single averaged line profile with improved S/N by averaging multiple spectral lines. It has been shown that for cool stars with weak magnetic field of a few kG such assumptions for Stokes  $V$  are perfectly applicable (Kochukhov et al., 2010). In this technique the circularly polarised spectrum of a rotating cool star is assumed to be a convolution of a line mask and an averaged Stokes  $V$  line profile. The averaged Stokes  $V$  line profile is then obtained by deconvolving the line mask from the polarised spectrum.

If we consider that the local line profile of all lines are similar in shape and scale up in depth with the local central line depth, then the entire spectrum can be considered as a sum of the scaled and shifted line profiles as shown,

$$V(v) = \sum_i w_i \delta(v - v_i) Z(v) \quad (2.6)$$

where  $V(v)$  is the normalised Stokes  $V$  spectrum,  $v$  is the velocity ( $v = c\Delta\lambda/\lambda$ ),  $w_i$  is the weight of each spectral line,  $v_i$  is the associated position of each line in velocity space and  $Z(v)$  is the mean line profile. Equation 2.6 can also be written as,

$$\begin{aligned} V(v) &= M(v) * Z(v) \\ M(v) &= \sum_i w_i \delta(v - v_i) \end{aligned} \quad (2.7)$$

where  $M(v)$  is the line mask or the line pattern function, (See Donati et al., 1997, for more details). Equation 2.7 can be further simplified as a matrix multiplication where,

$$V = M.Z \quad (2.8)$$

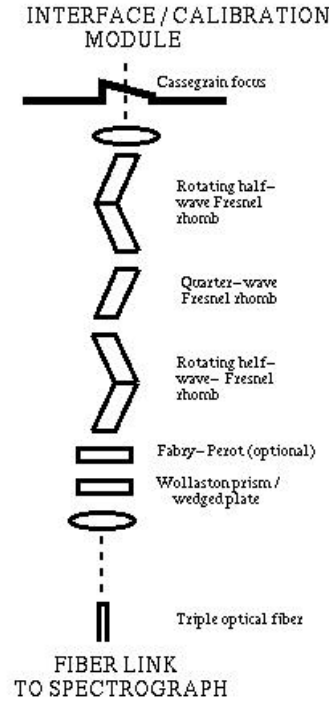


**Figure 2.8.:** Polarimetric unit of the high resolution spectropolarimeter ESPaDOnS. Credit goes to E.P. Jacobs

Under the assumption that all lines add up linearly we can now solve for the mean line profile  $Z$  for a given line mask  $M$  for the input spectrum  $V$ . The least-squares solution of  $Z$  is given by,

$$Z = (M^T \cdot S^2 \cdot M)^{-1} \cdot M^T \cdot S^2 \cdot V \quad (2.9)$$

where  $S$  is a square diagonal matrix consisting of inverse error bars for individual pixels in the spectrum. The term  $M^T \cdot S^2 \cdot V$  in equation 2.9 represents the weighted cross correlation between the spectrum  $V$  and the line mask  $M$ , and the term  $(M^T \cdot S^2 \cdot M)^{-1}$  is the inverse of the auto-correlation matrix which provides the uncertainties associated with the mean line profile  $Z$  and removes effects caused by line blends. The same technique can also be applied to the intensity spectrum to obtain mean LSD Stokes  $I$  profiles. The implementation of LSD on linearly polarised Stokes  $Q$  and  $U$  can be found in [Wade et al. \(2000\)](#). Since LSD assumes a similar line profile for all spectral lines it is needless to say that for very fast rotating stars this assumption does not hold. But for solar-type stars these assumptions are appropriate, provided we ignore lines such as the Ca II H&K,  $H\alpha$ , and other strong lines. Fig 2.9 shows the Stokes  $V$  LSD profile of 61 Cyg A (Chapter 4 discusses the results of 61 Cyg A in details). A total of 12467 lines were used to generate the LSD profile, resulting in the detection of a clear polarisation signature in Stokes  $V$ .

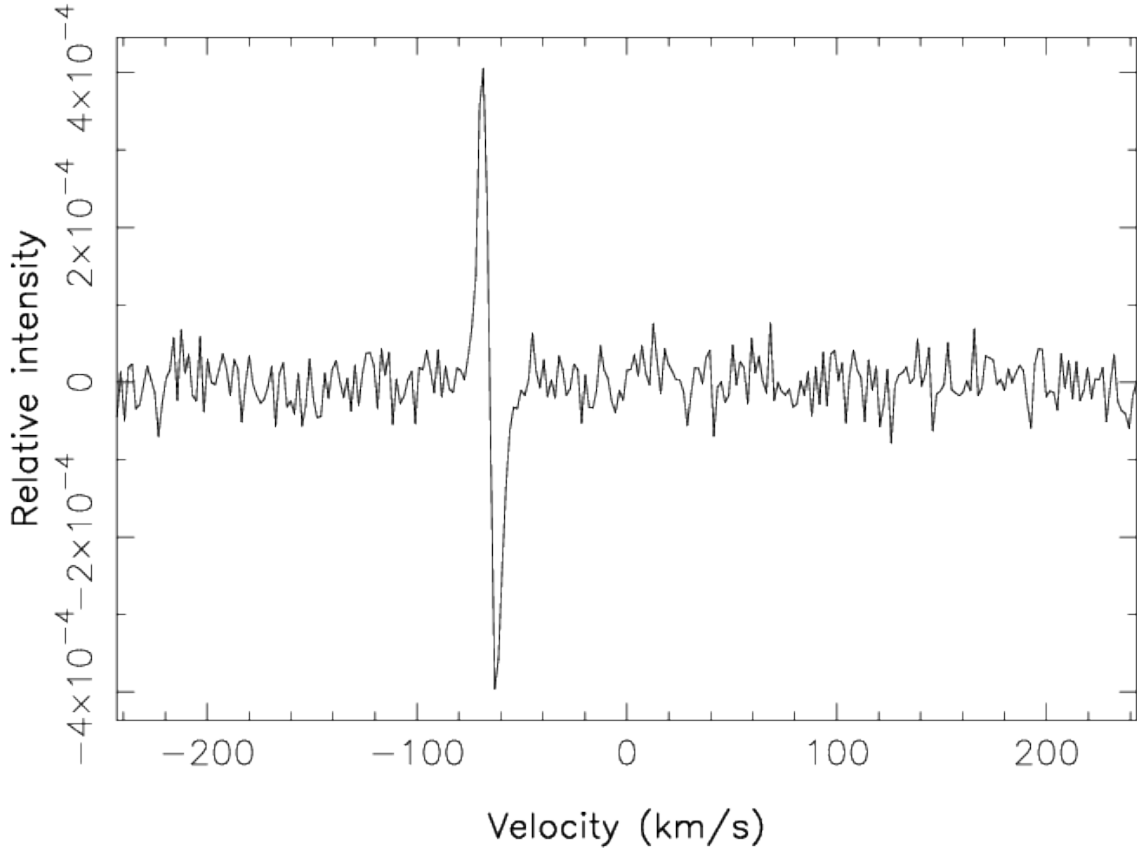


**Figure 2.9.:** An example LSD profile for the K dwarf 61 Cyg A, which shows a clear signature in the Stokes  $V$  LSD profile (12467 lines were used).

## 2.3. Magnetic field measurements using Stokes $V$ and $I$

### 2.3.1. Longitudinal magnetic field measurement

Using circularly polarised Stokes  $V$  LSD profiles together with Stokes  $I$  LSD profiles, the surface averaged magnetic field in the line-of-sight can be measured as shown by [Donati et al. \(1997\)](#),

$$B_l(\text{G}) = -2.14 \times 10^{11} \frac{\int vV(v)dv}{\lambda_0 g c \int (I_c - I(v))dv} \quad (2.10)$$

where  $B_l$  is the longitudinal field in Gauss integrated over the stellar surface,  $c$  is the speed of light,  $v$  is the radial velocity in  $\text{kms}^{-1}$ ,  $g$  is the average Landé factor,  $\lambda_0$  is the central wavelength of the LSD line profile and  $I_c$  is the normalised continuum. The longitudinal magnetic field represents the first-order moment of the Stokes  $V$  LSD profiles. This provides a first estimate on the surface magnetic field strength. Due to the use of Stokes  $V$ ,  $B_l$  only measures the large-scale magnetic field strength.

### 2.3.2. Zeeman Doppler imaging (ZDI)

Using tomographic techniques such as Zeeman Doppler imaging (ZDI) (Brown et al., 1991, Donati & Brown, 1997, Semel, 1989) on circularly polarised spectra, the large-scale magnetic field geometry of cool stars can be reconstructed. The ZDI technique used in this work was first developed by Semel (1989), where he demonstrated how circular polarisation in spectral lines can be used for direct measurements of magnetic field in active stars.

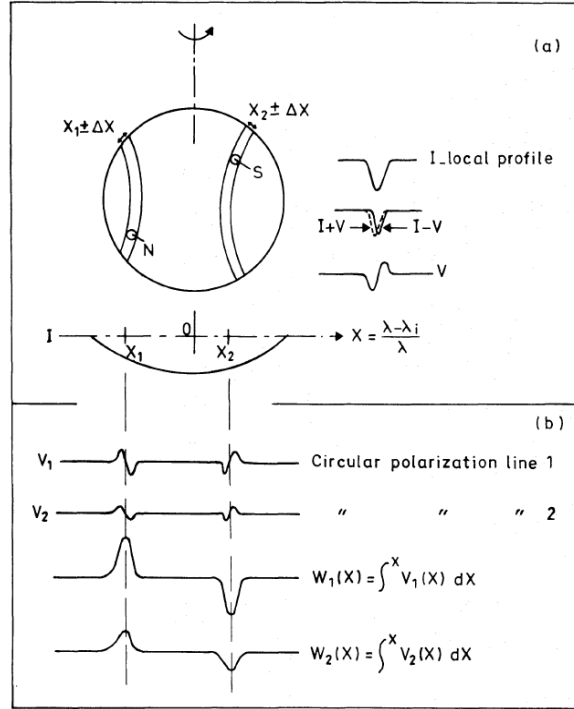


**Figure 2.10.:** Two spots of opposite polarity on two different zones of a rotating stellar surface. The Top Figure on the Right shows the local stokes  $I$  profile due to the presence of a single spot. The lines  $I + V$  and  $I - V$  correspond to the two different circular polarisation states which when subtracted from each other results in the Stokes  $V$  profile. The bottom Figure shows the Stokes  $V$  profile in two lines and their integrals. This Figure is taken from Semel (1989). Credit: Semel 1989, A&A, 225, 456, 1989, ©ESO. Reproduced with permission.

The basic principles of reconstructing the surface magnetic field geometry using Stokes  $V$  observations can be explained by using a model star with two magnetic spots. If the magnetic spots are of equal strength but opposite polarity on a non rotating stellar surface, then the two spots will cancel each other when observed in Stokes  $V$ . In the case of a rotating stellar surface, due to Doppler effect (Vogt & Penrod, 1983) the rotating spots will have different local radial velocities. This will result in a net polarisation signal. Figure 2.10 shows an example of a rotating star with magnetic spots at two different latitudes on the stellar surface. The Stokes  $V$  signature due to the presence of these two spots is separated in wavelength and their contribution can be seen in individual spectral lines as shown in Fig

2.10.

The shape and direction of a Stokes  $V$  profile from the magnetic star changes based on the direction of the magnetic field and the rotational phase of the star. Figure 2.11 (a) shows a model star with a magnetic spot with only the radial field at three different rotational phases and the corresponding Stokes  $V$  signatures. As the star rotates the Stokes  $V$  signal changes in amplitude, where the signal is strongest when the spot is in the line-of-sight. Fig 2.11 (b) also shows a stellar spot on the surface and the corresponding Stokes  $V$  profiles, but with the field directing towards the azimuth at three different rotational phases. In this case as the star rotates, the Stokes  $V$  signature changes its orientation. The signal becomes almost axisymmetric in the line-of-sight. Depending on the orientation of the magnetic field and the rotational phase at which the star was observed, both the amplitude and signature of the Stokes  $V$  profile changes. By obtaining multiple observations of the stellar surface covering a minimum of one rotational cycle, information on the stellar magnetic field configuration can be obtained from Stokes  $V$ . Using inverse techniques such as ZDI the circularly polarised Stokes  $V$  spectra can be utilised to reconstruct surface magnetic geometry of cool stars.

ZDI is a powerful tool that reconstructs the large-scale surface geometry (radial, azimuthal and meridional) of cool stars from a time series of Stokes  $V$  profiles, covering at least one rotation cycle of the star. The observed Stokes  $V$  profiles are compared to synthetic Stokes  $V$  profiles to reconstruct the surface magnetic geometry. It is to be noted that this technique is applied under the weak field assumption, where all forms of spectral line broadening is ignored except rotational broadening. ZDI tackles an inverse problem as it "inverts" the line profiles into surface distribution of the vector magnetic field. One has to be careful while tackling this problem as there is always an "uniqueness" issue while looking for a solution. It means that there can be infinite surface magnetic field reconstructions that might fit the observed spectra. To deal with this issue a regularisation technique is used to select the best fit solution. In this version of ZDI maximum entropy (Skilling & Bryan, 1984) is used as a regularisation technique, which selects the surface reconstruction that contains the least information. One disadvantage of using ZDI is that, due to use of only circularly polarised light it is insensitive to small-scale magnetic features and only reconstructs the large-scale magnetic field. As previously mentioned the use of the complete Stokes parameters will provide a clearer view on cool star magnetism but it is difficult to obtain for solar-type stars as the linear polarisation signature is very weak. A brief description of the ZDI code used in this work is provided below.

### **Stellar model**

The synthetic Stokes  $V$  profiles are computed for the same rotational phases as the observed Stokes  $V$  profiles from a simple stellar model, where the stellar surface is divided into a grid of pixels (Donati & Brown, 1997, Folsom et al., 2016). The local Stokes  $I$  line profile associated with each of these pixels are assumed to be Gaussian in nature and the depth and width of the profiles are adjusted to match the observed Stokes  $I$  profiles. This simple assumption is a good approximation for the line averaged LSD profiles (Donati & Brown,

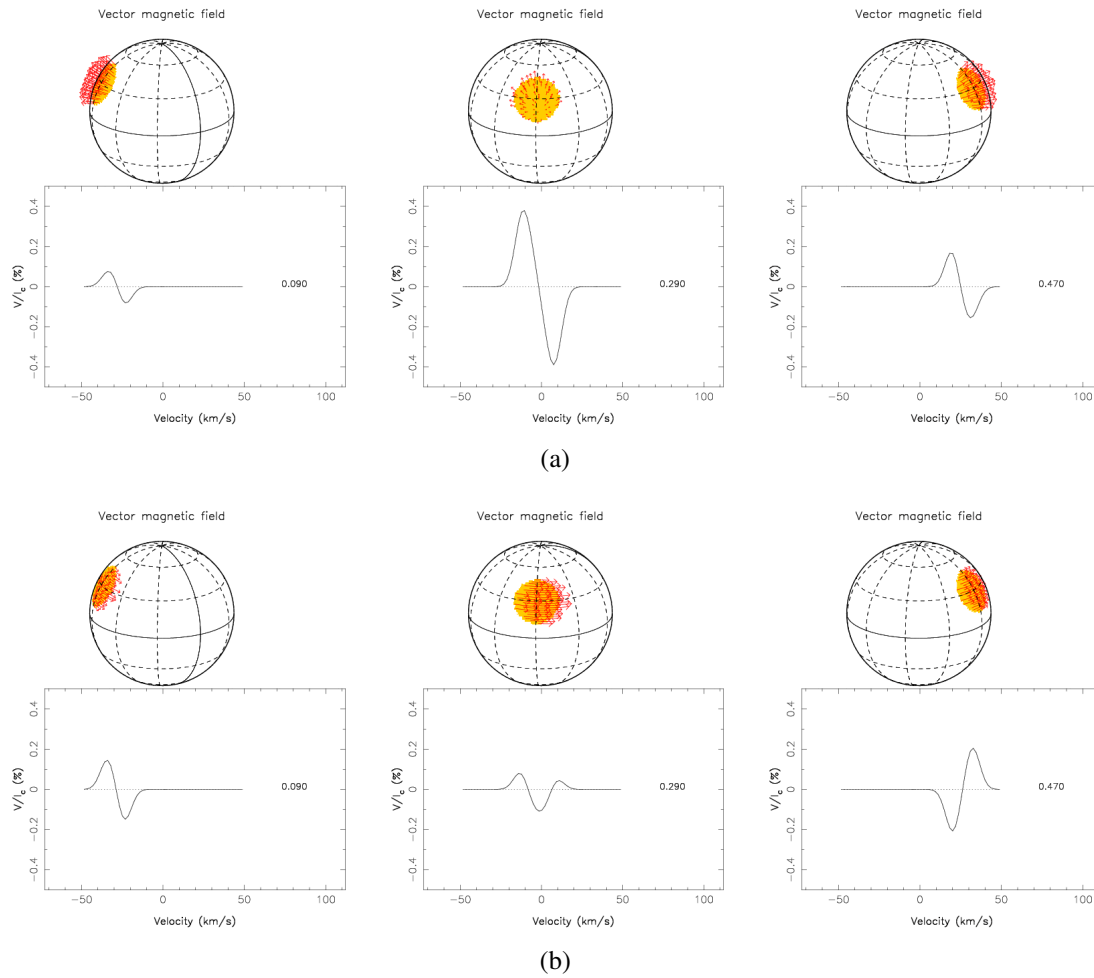


**Figure 2.11.:** Illustration showing the rotational evolution of a Stokes  $V$  LSD profile due to the presence of a surface magnetic field region in (a) the radial direction (b) azimuthal direction. Credit: J. F. Donati

1997, Donati et al., 1997). The local Stokes  $V$  profile associated with the stellar surface is calculated under the weak field assumption,

$$V(\lambda) = -\lambda_0^2 B_l \frac{ge}{4\pi m_e c} \frac{dI}{d\lambda} \quad (2.11)$$

where  $\lambda_0$  is the central wavelength of the line,  $g$  is the Landé factor of the line and  $B_l$  is the line of sight component of the magnetic field. The central wavelength and the Landé factor of the line are set to the values used while generating the observed LSD Stokes  $V$  profiles. For the local line profiles, a linear limb-darkening law is applied and the surface brightness is assumed to be homogeneous through out the stellar disk.

### Spherical harmonics decomposition

The version of ZDI used in this work reconstructs the surface magnetic field into its poloidal and toroidal components expressed as spherical harmonics expansions (Donati et al., 2006). The use of spherical harmonics expansion allows the code to be more robust in reconstructing both simple and complex magnetic field structure. Lower order spherical harmonics modes can be recovered reliably for even slowly rotating stars providing a large-scale reconstruction of their surface magnetic geometry. Another advantage of using spherical harmonics decomposition is that the code also calculates fraction of the poloidal and toroidal field together with the percentage of axisymmetry and other quantities that can be used for direct comparisons with theoretical results. Previous versions of the ZDI code reconstructed the surface magnetic field as three independent magnetic image pixels (radial, azimuthal and meridional field) corresponding to the three vector components in spherical coordinates (Donati & Brown, 1997). Although the previous versions of the code were very successful in reconstructing complex field structure, the code was incapable of reconstructing simple dipolar field.

Under the spherical harmonics frame the three surface magnetic field components (radial, meridional and azimuthal) can be formalised as (Donati et al., 2006),

$$B_r(\theta, \phi) = - \sum_{l,m} \alpha_{l,m} Y_{l,m}(\theta, \phi) \quad (2.12)$$

$$B_\theta(\theta, \phi) = - \sum_{l,m} [\beta_{l,m} Z_{l,m}(\theta, \phi) + \gamma_{l,m} X_{l,m}(\theta, \phi)] \quad (2.13)$$

$$B_\phi(\theta, \phi) = - \sum_{l,m} [\beta_{l,m} X_{l,m}(\theta, \phi) - \gamma_{l,m} Z_{l,m}(\theta, \phi)] \quad (2.14)$$

where  $B_r$  is the radial magnetic field,  $B_\theta$  is the meridional field and  $B_\phi$  is the azimuthal field.  $l$  and  $m$  represents the order and degree of the spherical harmonics modes where  $\theta$  and  $\phi$  are the co-latitude and longitude respectively.  $\alpha_{l,m}$ ,  $\beta_{l,m}$  and  $\gamma_{l,m}$  are the set of complex spherical harmonics coefficients that characterises the magnetic field.  $\alpha_{l,m}$  represents the radial component of the poloidal field,  $\beta_{l,m}$  characterises the azimuthal and meridional component of the poloidal field and  $\gamma_{l,m}$  is the azimuthal and meridional component of the toroidal field. Furthermore  $Y_{l,m}$ ,  $Z_{l,m}$  and  $X_{l,m}$  are expressed in terms of the Legendre polynomial  $P_{l,m}$  as follows,

$$Y_{l,m}(\theta, \phi) = c_{l,m} P_{l,m}(\cos \theta) e^{im\phi} \quad (2.15)$$

$$Z_{l,m}(\theta, \phi) = \frac{c_{l,m}}{l+1} \frac{\partial P_{l,m}(\cos \theta)}{\partial \theta} e^{im\phi} \quad (2.16)$$

$$X_{l,m}(\theta, \phi) = \frac{c_{l,m}}{l+1} \frac{P_{l,m}(\cos \theta)}{\sin \theta} i m e^{im\phi} \quad (2.17)$$

$$(2.18)$$

and

$$c_{l,m} = \sqrt{\frac{2l+1}{4\pi} \frac{(l-m)!}{(l+m)!}} \quad (2.19)$$

The spherical harmonics coefficients are then reconstructed by iteratively fitting synthetic Stokes  $V$  profiles to the observed Stokes  $V$  profiles using maximum entropy as a regularisation technique.

### Inversion process and maximum entropy solution

The inversion technique of ZDI aims at reconstructing the coefficients  $\alpha_{l,m}$ ,  $\beta_{l,m}$  and  $\gamma_{l,m}$  that form the image vector  $I$ . If the observed Stokes  $V$  profiles form the vector  $D$  with the associated error bars in vector  $\sigma$ , then the relationship between the image and the spectra can be given by,

$$D = R(I) + \sigma \quad (2.20)$$

where  $R$  corresponds to the stellar model used to generate the synthetic profiles. This problem is formally ill-posed, since there are potentially multiple images  $I$ , that can produce the same spectra  $R(I)$ . This potential degeneracy can be removed by using a form of regularisation as an additional constraint. This is usually done by using the maximum entropy algorithm (Skilling & Bryan, 1984), where an entropy function  $S(I)$  is included in the fitting procedure and the goodness of fit is determined by a  $\chi^2$ .

The maximum entropy algorithm sets up a Lagrange function  $Q(I)$  such that the final solution maximises  $Q(I)$ ,

$$Q(I) = S(I) - \lambda \chi^2 \quad (2.21)$$

where  $S(I)$  is the entropy and  $\lambda$  is the Lagrange multiplier. The Skilling & Bryan (1984) regularisation is carried out by specifying a target  $\chi_{aim}^2$  which is a finite number. The target  $\chi_{aim}^2$  is used to set the weighting between the  $\chi^2$  and entropy  $S$ . The routine modifies  $\lambda$  on each iteration such that the  $\chi^2$  converges towards the target value  $\chi_{aim}^2$ , without strongly decreasing the entropy  $S$ . As the  $\chi^2$  reaches its target value ( $\chi^2 = \chi_{aim}^2$ ), the routine starts increasing the entropy until entropy is at its maximum.

### Zeeman Doppler imaging of cool stars

Over the past decade the large-scale magnetic field geometry of cool stars have been successfully reconstructed using ZDI. The large-scale magnetic field of several solar-type stars reconstructed using ZDI over multiple epochs, has revealed their strongly varying magnetic geometry. In the recent years, long time-baseline observations of cool stars have also resulted in detection of cyclic magnetic activity in some cool stars. For the G7 dwarf  $\xi$  Bootis A ( $0.86 M_{\odot}$ ,  $T_{\text{eff}} = 5551$  K) (Morgenthaler et al., 2012), the K2 dwarf  $\epsilon$  Eridani ( $0.856 M_{\odot}$ ,  $T_{\text{eff}} = 5146$  K) (Jeffers et al., 2014) strong azimuthal fields were reconstructed with a rapidly varying field geometry. A two year magnetic cycle was revealed for the planet hosting F7 dwarf  $\tau$  Bootis ( $1.42 M_{\odot}$ ,  $T_{\text{eff}} = 6360$  K) (Donati et al., 2008, Fares et al., 2009). A recent study by Mengel et al. (2016) reveals the magnetic cycle of  $\tau$  Boo could be even shorter, with possible yearly polarity reversals. Magnetic cycle was also detected for the G0 dwarf HD 78366 ( $1.34 M_{\odot}$ ,  $T_{\text{eff}} = 6014$  K) (Morgenthaler et al., 2011), where the radial component

of the magnetic field exhibits polarity reversals indicating a possible 3-year cycle. Polarity reversals were observed in the large-scale field of the G2 dwarf HD 190771 ( $0.96 M_{\odot}$ ,  $T_{\text{eff}} = 5834 \text{ K}$ ) (Morgenthaler et al., 2011, Petit et al., 2009). However, the variability of the large-scale field of HD 190771 is more complex as the polarity reversal in the azimuthal field reported by Petit et al. (2009) is not detected in subsequent epochs. Instead polarity reversal is reported in the radial component of the magnetic field in the following epochs as shown by Morgenthaler et al. (2011).

## 2.4. Indirect proxies of magnetic activity

Non-thermal emission in certain chromospheric lines is associated with stellar magnetic fields (Hall, 2008). The flux in these lines provide a measurement of stellar chromospheric activity, which is an indirect diagnostics of the surface magnetic field. Surface magnetic activity can also be inferred from coronal activity, UV and radio emissions but for cool stars these indirect proxies are not as well studied as chromospheric activity.

### 2.4.1. Chromospheric activity

Chromosphere is the part of the stellar atmosphere that lies above the photosphere and below the corona, as shown in Fig. 1.3. It is the part of the atmosphere where we detect emission in excess of what we would expect in a radiative equilibrium and much higher temperatures compared to the underlying photosphere. Figure 2.12 shows an illustration of the rise in temperature vs atmospheric height for different layers of the stellar atmosphere. In the photosphere the temperature decreases with increase in height. However, the temperature rises abruptly once the chromosphere is reached.

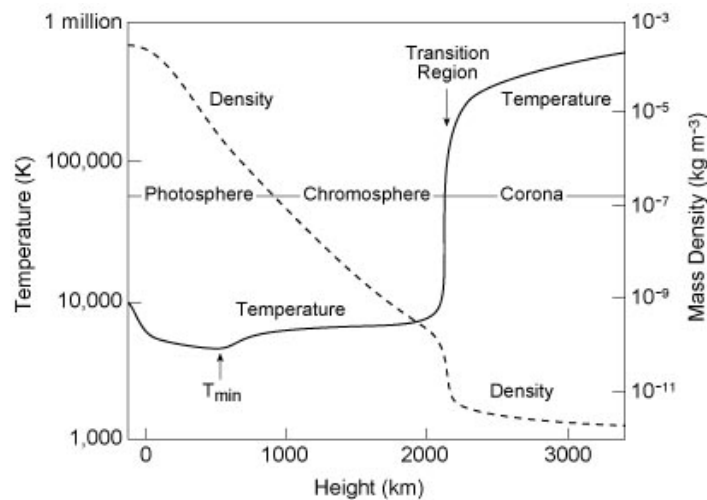


**Figure 2.12.:** Illustration showing the formation heights vs temperature and density for different layers of a stellar atmosphere for a sun-like star. The temperature is shown by the black curve and the density is shown by the dashed line. Credit: Eugene Avrett, Smithsonian Astrophysical Observatory.

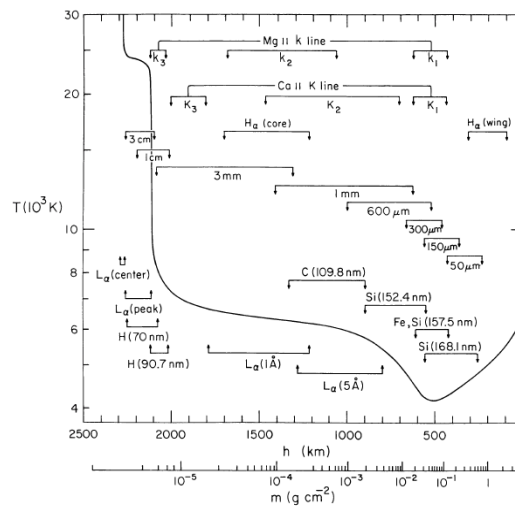


**Figure 2.13.:** Illustration showing the formation heights for different chromospheric lines, taken from Vernazza et al. (1981). ©AAS. Reproduced with permission.

Stellar magnetic fields are widely accepted as the primary mechanism responsible for the chromospheric temperature rise. It was Babcock (1961) who first described a model where a dynamo generated magnetic field could explain the excess emission in certain chromospheric lines. Observations of the Sun as a star by Schrijver et al. (1989) has also revealed a clear correlation between the variation of the chromospheric Ca II H and K line and sunspot numbers.

Since the first successful use of emission in the line cores of Ca II H&K lines by Wilson (1978), the H and K lines have been widely used as a tool to study stellar activity. Apart from the H and K lines other chromospheric lines such as the H $\alpha$ , Ca II IRT (infrared triplet), Mg II, Na D lines are used as activity tracers. These lines are formed at different heights of the chromosphere as shown in Fig. 2.13. Furthermore, the formation mechanism is different for different lines. For example, the Ca II H&K lines are resonance lines which are dependent on the local chromospheric temperature and electron density (Jefferies & Thomas, 1959). Contrary to the Ca II H&K lines, the H $\alpha$  line is a Balmer line which is insensitive to the local chromospheric conditions but more sensitive to the radiation temperature (Jefferies & Thomas, 1959).

The chromospheric activity of a cool star is widely defined in terms of the S-index (or  $S_{MW}$ ), which is a dimensionless quantity that defines the ratio of the flux in the H and K line cores to two nearby band passes. This index was first introduced by (Duncan et al., 1991) for observations taken at the Mount Wilson observatory. Since then it is one of the standards used to define cool star chromospheric activity. The Mount Wilson  $S_{MW}$  is defined by taking a triangular band pass at the core of K and H lines at 393.3663 nm and 396.8469 nm and two 2 nm wide rectangular band passes to measure the nearby continuum at 390.107 nm and

400.107 nm respectively as shown,

$$S_{\text{MW}} = \alpha \frac{N_H + N_K}{N_R + N_V} \quad (2.22)$$

where,  $\alpha$  is the calibration factor,  $N_H$  and  $N_K$  represents the flux in H and K lines and,  $N_R$  and  $N_V$  represents the flux in the continuum band passes. The Mount Wilson project (Baliunas et al., 1995, Duncan et al., 1991) determined  $S_{\text{MW}}$  for a large sample of cool stars over a long time baseline from 1966 to early 2000s. From this long time series of  $S_{\text{MW}}$  a wide range of stellar activity classes were discovered. Cool stars exhibit different levels of activity variation: irregular activity variations in fast rotating stars, cyclic activity in comparatively slowly rotating solar-type stars and Maunder minimum like flat activity in some stars (Baliunas et al., 1995). A further analysis on the Maunder-minimum candidates from the Mount Wilson survey by Schröder et al. (2013) reveals them to be slightly more evolved than the Sun. Multiple other surveys have been carried out in the past few decades, providing a huge pool of stellar activity data (Gray et al., 2006, Hall et al., 2007, Henry et al., 1996). However, care should be taken when using  $S_{\text{MW}}$  to compare stellar activity over a wide range of stellar parameters. Since  $S_{\text{MW}}$  depends on the continuum band passes on either side of the H&K lines, any change in the continuum level will influence  $S_{\text{MW}}$ . When we go from hotter to more cooler stars the continuum level decreases, resulting in an increase in  $S_{\text{MW}}$ . This makes comparison of  $S_{\text{MW}}$  difficult for stars of different spectral types. The line cores in the H and K lines are also sensitive to the photospheric contribution in the pass bands, as a result of which  $S_{\text{MW}}$  is not purely chromospheric in nature.

To correct for spectral types Middelkoop (1982) introduced a new index called  $R_{\text{HK}}$  which corrects for stellar colour as shown below,

$$R_{\text{HK}} = C_{\text{cf}} \times S_{\text{MW}} \quad (2.23)$$

$$\log C_{\text{cf}} = 1.13(B - V)^3 - 3.91(B - V)^2 + 2.84(B - V) - 0.47 \quad (2.24)$$

where  $C_{\text{cf}}(B - V)$  is the correction factor applied to the S-index to correct for variations with stellar colour and  $R_{\text{HK}} = F_{\text{HK}}/T_{\text{eff}}^4$ , where  $F_{\text{MW}}$  is the flux in the H and K lines per unit area of the stellar surface.

In order to correct for photospheric contribution, Noyes et al. (1984a) devised a new term called  $R'_{\text{HK}}$ . This correction accounts for the photospheric contribution in the emission cores of H and K lines, resulting in an index which is purely chromospheric in nature. The  $R'_{\text{HK}}$  index is defined as follows,

$$R'_{\text{HK}} = R_{\text{HK}} - R_{\text{phot}} \quad (2.25)$$

where  $R_{\text{HK}}$  is the correction defined by Middelkoop (1982) and  $R_{\text{phot}}$  is the photospheric contribution in the H and K line cores. Noyes et al. (1984a) determined  $R_{\text{phot}}$  analytically from the K lines of six of their least active dwarfs, under the assumption that  $R_{\text{phot}}$  varies only with  $B - V$  and is independent of any chromospheric activity. They derived equation 2.26 by using the description by Hartmann et al. (1984),

$$\log R_{\text{phot}} = -4.898 + 1.918(B - V)^2 - 2.893(B - V)^3 \quad (2.26)$$

It is worth noting that the calibration of [Noyes et al. \(1984a\)](#) only holds for cool stars with  $B - V$  range that lies between 0.45 and 0.82.

Apart from the widely used Ca II H&K lines two other chromospheric lines  $H\alpha$  and Ca II IRT lines are also used in this Thesis work. The  $H\alpha$ -index is determined by the technique specified by [Gizis et al. \(2002\)](#), where a rectangular band pass of 0.36 nm width is used at the  $H\alpha$  line at 656.285 nm. Two rectangular band passes  $N_{H\alpha\text{blue}}$  and  $N_{H\alpha\text{red}}$  of 0.22 nm width are used to measure the nearby continuum,

$$H\alpha\text{-index} = \frac{N_{H\alpha}}{N_{H\alpha\text{blue}} + N_{H\alpha\text{red}}} \quad (2.27)$$

where  $N_{H\alpha}$ ,  $N_{H\alpha\text{blue}}$  and  $N_{H\alpha\text{red}}$  refers to different band passes used.

The CaIRT-index is measured by taking 0.2 nm wide rectangular band passes centred at the Ca II triplet lines at 849.8023 nm, 854.2091 nm, and 866.241 nm respectively. The nearby continuum is measured by taking two 0.5 nm band passes  $N_{\text{IRred}}$  and  $N_{\text{IRblue}}$  at 870.49 nm, and 847.58 nm respectively ([Marsden et al., 2014](#)), as shown in equation ??,

$$\text{CaIRT-index} = \frac{N_{\text{IR1}} + N_{\text{IR2}} + N_{\text{IR3}}}{N_{\text{IRred}} + N_{\text{IRblue}}} \quad (2.28)$$

where  $N_{\text{IR1}}$ ,  $N_{\text{IR2}}$ , and  $N_{\text{IR3}}$  represent flux in the Ca II infrared triplet lines. The continuum flux is represented by  $N_{\text{IRred}}$  and  $N_{\text{IRblue}}$  respectively.

### 2.4.2. Coronal activity

The linear relationship between X-ray luminosity and magnetic flux was determined by [Pevtsov et al. \(2003\)](#) from observations of the Sun and active cool stars as shown in Fig. 2.14. Observations of the solar corona in soft X-rays have revealed that its coronal activity cycle is also in good agreement with its sunspot and activity cycle ([Orlando et al., 2001](#)). The Sun exhibits stronger X-ray emission during activity maximum and the X-ray emission goes down at activity minimum.

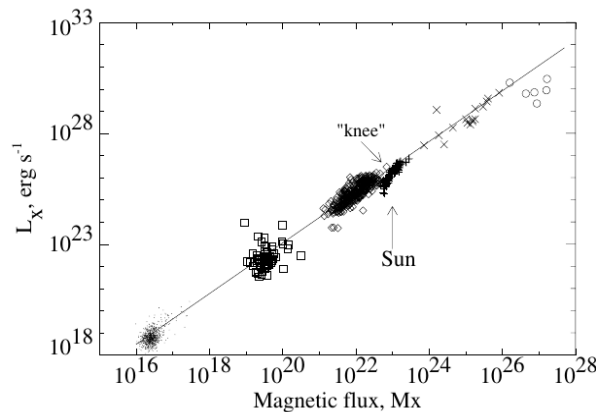


**Figure 2.14.:** X-ray luminosity  $L_X$  vs magnetic flux taken from [Pevtsov et al. \(2003\)](#). The different symbols represent observations taken of the Sun and other cool stars. The fit to the data results in a power law of  $L_X = \phi^{1.15}$ . ©AAS. Reproduced with permission.

X-ray observations have been carried out only for a few cool stars other than the Sun over their activity cycle. Weak statistical evidence of coronal activity cycles in cool stars were first detected by [Hempelmann et al. \(1996\)](#). Coronal activity cycles have been also detected for a few G and K dwarfs. [Favata et al. \(2008\)](#) reported the presence of a coronal activity cycle for the binary system HD81809. Cyclic coronal activity was also detected for the star 61 Cyg A and the K1 dwarf  $\alpha$  Cen B ([Robrade et al., 2012](#)). The shortest coronal activity cycle of 1.6 years was reported for the young active Sun  $\iota$  Horologii ([Sanz-Forcada et al., 2013](#)), where the coronal activity cycle is in phase with its short chromospheric activity cycle.

## 2.5. Summary

In this thesis, the large-scale magnetic field geometry reconstruction technique ZDI and chromospheric activity is used to detect magnetic and activity cycles of stars. The ZDI technique is used to monitor the magnetic field geometry evolution of three stars, HN Peg, 61 Cyg A and  $\epsilon$  Eridani, with simultaneous monitoring of their chromospheric activity. Three chromospheric activity tracers (Ca II H and K, H $\alpha$  and Ca II IRT) are used to monitor their chromospheric activity. Additionally, a chromospheric activity catalogue (Ca II H and K) is developed for the entire cool star spectral range. For stars with multi-year observations, chromospheric activity cycles are determined and their dependence on basic stellar properties, such as rotation, is investigated. The results are presented and discussed in the next four Chapters.



# 3. Variable magnetic field geometry of the young Sun HN Peg (HD 206860)\*

## Contents

<b>3.1. Abstract</b>	<b>38</b>
<b>3.2. Introduction</b>	<b>38</b>
<b>3.3. HN Peg</b>	<b>39</b>
<b>3.4. Observations</b>	<b>40</b>
<b>3.5. Mean longitudinal magnetic field (<math>B_l</math>)</b>	<b>41</b>
<b>3.6. Chromospheric activity indicators</b>	<b>42</b>
<b>3.7. Large-scale magnetic field topology</b>	<b>48</b>
3.7.1. Radial velocity	49
3.7.2. Inclination angle	49
3.7.3. Differential rotation	49
3.7.4. Magnetic topology	50
<b>3.8. Discussion</b>	<b>55</b>
3.8.1. Long-term magnetic variability	55
3.8.2. Large scale magnetic topology	57
3.8.3. Differential rotation	59
<b>3.9. Summary</b>	<b>59</b>

\*This Chapter was previously published in the journal *Astronomy & Astrophysics* (**Boro Saikia, S.**, Jeffers, S.V., Petit, P., Marsden, S., Morin, J., Folsom, C. P., A&A, 2015, 573,17). The data analysis was carried by Sudeshna Boro Saikia (S.B.S). The text in the paper was written by S.B.S (University of Goettingen). S. V. Jeffers (S.V.J) (University of Goettingen) supervised the project and the other co-authors (P. Petit (CNRS, IRAP Toulouse, France), S. Marsden (University of Southern Queensland, Australia), J. Morin (Université Montpellier, France) and C.P. Folsom (CNRS, IRAP Toulouse, France)) provided the data, their expert insight and helped in the interpretation of the results. This work was carried out as part of the project A16, supported by SFB 963/DFG. Part of this work was also supported by the COST Action MP1104 "Polarisation as a tool to study the Solar System and beyond". The word 'paper' has been replace by the word 'chapter' to conform with the Thesis format. Credit: Boro Saikia, S et al., A&A, 573, 17, 2015, reproduced with permission ©ESO.

### 3.1. Abstract

The large-scale magnetic field of solar-type stars reconstructed from their spectropolarimetric observations provide important insight into their underlying dynamo processes. We aim to investigate the temporal variability of the large-scale surface magnetic field and chromospheric activity of a young solar analogue, the G0 dwarf HN Peg. The large-scale surface magnetic field topology is reconstructed using Zeeman Doppler imaging at six observational epochs covering seven years. We also investigated the chromospheric activity variations by measuring the flux in the line cores of the three chromospheric activity indicators: Ca II H&K, H $\alpha$ , and the Ca II IRT lines. The magnetic topology of HN Peg shows a complex and variable geometry. While the radial field exhibits a stable positive polarity magnetic region at the poles at each observational epoch, the azimuthal field is strongly variable in strength, where a strong band of positive polarity magnetic field is present at equatorial latitudes. This field disappears during the middle of our timespan, reappearing again during the last two epochs of observations. The mean magnetic field derived from the magnetic maps also follow a similar trend to the toroidal field, with the field strength at a minimum in epoch 2009.54. Summing the line of sight magnetic field over the visible surface at each observation, HN Peg exhibits a weak longitudinal magnetic field (B<sub>l</sub>) ranging from -14G to 13G, with no significant long-term trend, although there is significant rotational variability within each epoch. Those chromospheric activity indicators exhibit more long-term variations over the time span of observations, where the minimal is observed in Epoch 2008.71.

### 3.2. Introduction

Solar dynamo models suggest that the regeneration of the solar magnetic field results from the interplay between convection and differential rotation (Brandenburg & Subramanian, 2005, Charbonneau, 2010, Parker, 1955). These cyclic dynamo processes are responsible for the different manifestations of solar activity such as prominences, flares, solar winds. Observations of surface activity features of young solar type stars provide an important insight into the underlying dynamo processes that operate in stars other than the Sun (see Donati & Landstreet, 2009). In general, solar-type cool stars all have a similar internal structure to the Sun, with a radiative core surrounded by a convective envelope. This would suggest that, as in the case of the Sun, their magnetic activity is generated by a  $\alpha$ - $\Omega$  dynamo. Although, the exact mechanism of the dynamo processes is still not completely understood, observations of significant azimuthal field in rapidly rotating solar type stars indicate the presence of dynamo distributed throughout the convective zone (Donati et al., 2003, Petit et al., 2008). The possibility that such a distributed dynamo operates in rapidly-rotating solar-type stars is supported by detailed numerical modelling (Brown et al., 2010).

The presence of the magnetic field can result in emission in the line cores of certain chromospheric lines, such as Ca II H&K, H $\alpha$ , Ca II IRT lines. The Mount Wilson survey was the first long term monitoring of Ca II H&K to investigate the surface magnetic variability of stars with an outer convective envelope (Duncan et al., 1991). This survey observed a wide range of variability ranging from cyclic to non-cyclic and irregular variability. Since

the Mount Wilson project, a host of other activity surveys were carried out in the last few decades (Hall et al., 2007, Wright et al., 2004). While monitoring Ca II H&K can provide a long-term indication of the magnetic variability, the disadvantage of using this method is that this tracer does not provide any direct measurement of the field strength or information about the large-scale geometry of the star’s magnetic field.

In recent years, with the arrival of spectropolarimeters such as ESPaDOnS, NARVAL and HARPSpol, the magnetic field observations of other solar type stars have provided an important insight in understanding the dynamo processes that drive the different manifestations of surface activity (Marsden et al., 2014, Petit et al., 2008). For example, magnetic cycles have been observed on the F7 dwarf  $\tau$  Bootis ( $1.42 \pm 0.05 M_{\odot}$ ,  $T_{\text{eff}}=6360 \pm 80$  K (Catala et al., 2007)), where the large-scale magnetic field is observed to exhibit cycles over a two year period (Fares et al., 2009). Recent observations of  $\tau$  Boo by Mengel et al. (2016) suggests that, the magnetic cycle of the star might be even shorter than the current 2 year period. Magnetic cycles have also been observed on HD 78366 (Morgenthaler et al., 2011), with a mass of  $1.34 \pm 0.13 M_{\odot}$  and  $T_{\text{eff}}$  of  $6014 \pm 50$  K, which shows two polarity reversals with a probable cycle of approximately three years. More complex variability has been observed on HD 190771 (Petit et al., 2009, 2008), which is similar in mass to the Sun ( $0.96 \pm 0.13 M_{\odot}$ ) with  $T_{\text{eff}}$  of  $5834 \pm 50$  K, where polarity reversals are observed in its radial and azimuthal field but over the time span of the observations, they do not return to the initial field configuration. These results indicate that the 22 year magnetic cycle of the Sun is not an exception but that cyclic activity is also present in other solar-type stars with ages close to the Sun’s.

In this chapter we determine the large-scale magnetic field geometry of the young Solar analogue HN Peg using the technique of Zeeman-Doppler Imaging. We also measure HN Peg’s chromospheric activity using the core emission in Calcium II H&K, H $\alpha$  and Calcium II IR triplet lines. In Section 3.2 we review the literature on HN Peg, followed by a description of the observations in Section 3.3. The longitudinal magnetic field and chromospheric activity measurements are presented in Section 3.4. The large-scale magnetic field reconstructions are presented in Section 3.5. The results are discussed in Section 3.6.

### 3.3. HN Peg

HN Peg is a G0 dwarf, with a mass of  $1.085 \pm 0.091 M_{\odot}$ , and a radius of  $1.002 \pm 0.018 R_{\odot}$  (Valenti & Fischer, 2005) as shown in Table 3.1, which is part of the Her-Lyr association. HN Peg’s association with the Her-Lyr moving group was discovered by Gaidos (1998), when he detected a group of stars (V439 And, MN UMa, DX Leo, NQ UMa and HN Peg) with similar kinematics (Fuhrmann, 2004, López-Santiago et al., 2006). The age of Her-Lyr was established to be approximately 200 Myr, by gyrochronology and also by comparing the Li and H $\alpha$  lines of Her-Lyr with the UMa group (Eisenbeiss et al., 2013, Fuhrmann, 2004). A separate gyrochronology study carried out on the Mount Wilson sample also provided an age of HN Peg of  $237 \pm 33$  Myr (Barnes, 2007).

The Mount Wilson survey estimated a period of  $6.2 \pm 0.2$  years for HN Peg, with high chromospheric variability (Baliunas et al., 1995, Schröder et al., 2013). Photometric measurements carried out by Messina & Guinan (2002) claimed the presence of a solar-type star spot cycle of HN Peg with a period of  $5.5 \pm 0.3$  years. Both spectroscopic and photometric observations of HN Peg were observed by Frasca et al. (2000), where rotational modulation in both Ca II H&K and H $\alpha$  were observed. Power spectrum analysis of the spectra of HN Peg (Baliunas et al., 1985) suggested the presence of surface differential rotation. Differential rotation of HN Peg was also investigated by observing variations in the rotational period (Messina & Guinan, 2003), where the evolution of the average rotation of HN Peg along the activity cycle was observed to be anti-solar.

From direct imaging using the Spitzer Space Telescope, HN Peg also has also been shown to have an early T-dwarf companion HN Peg b at a distance of approximately 794 AU (Leggett et al., 2008, Luhman et al., 2007). Photometric observations of HN Peg have indicated that it also harbours a debris disk (Ertel et al., 2012).

## 3.4. Observations

The data were collected as part of the international BCool collaboration <sup>1</sup> (Marsden et al., 2014), using the NARVAL spectropolarimeter at the 2 m Telescope Bernard Lyot (TBL) at Pic du Midi Observatory. NARVAL is a new generation spectropolarimeter which is a twin of the ESPaDOnS stellar spectropolarimeter <sup>2</sup>. NARVAL is a cross dispersed echelle spectrograph with minimum instrumental polarisation (Aurière, 2003, Petit et al., 2008). NARVAL has a resolution of approximately 65,000 and covers the full optical domain from 370 nm to 1000 nm, ranging over 40 grating orders.

The data were extracted using Libre-ESPRIT (Donati et al., 1997), which is a fully automated data reduction package installed at TBL. The observations were taken to maximise rotational phase coverage. Seven sets of data were obtained for the observational epochs 2007.67, 2008.71, 2009.54, 2010.62, 2011.67, 2012.61 and 2013.68 (the journal of observations is shown in Table A.1). Each of these seven epochs contains 8 to 14 polarised Stokes V observations.

Because the signal-to-noise ratio (S/N) ratio in individual spectral lines is not high enough to detect Zeeman signatures in polarised light, we apply the technique of Least Square Deconvolution (LSD) on the spectra (Donati et al., 1997, Kochukhov et al., 2010). LSD is a multi-line technique which considers a similar local profile for each line and obtains an averaged line profile by deconvolving the stellar spectra to a line mask <sup>3</sup>. A G2 line mask consisting of approximately 4800 lines, matching a stellar photosphere model for HN Peg, was used to generate the averaged line profile for Stokes I and Stokes V, resulting in huge

---

<sup>1</sup><http://bcool.ast.obs-mip.fr/Bcool>

<sup>2</sup>Fig 2.8 shows a schematic diagram of the ESPaDOnS spectropolarimeter

<sup>3</sup>For a more detailed description on the LSD technique please refer to Section 2.2.3 of this thesis

**Table 3.1.:** Summary of the physical parameters of HN Peg.

Object	HD 206860	References
Effective temperature, $T_{\text{eff}}$	5974 K	1
Radius	$1.002 \pm 0.018 R_{\odot}$	1
Mass	$1.085 \pm 0.091 M_{\odot}$	1
Rotational period, $P_{\text{rot}}$	4.6 days	this work
Rotational velocity, $v \sin i$	$10.6 \text{ kms}^{-1}$	1
Age	$\sim 200 \text{ Myr}$	2

**References** (1) [Valenti & Fischer \(2005\)](#); (2) [Zuckerman & Song \(2009\)](#) and [Eisenbeiss et al. \(2013\)](#).

multiplex gain in the S/N ratio of the polarised Stokes  $V$  profile as shown in Table A.1. The mask covers a wavelength range of 370 nm to 900 nm and the LSD profiles are normalised by using a mean Landé factor of 1.21 and a mean wavelength of 550 nm from the line list.

The polarised Stokes  $V$  spectra from 2012 and part of 2011 were discarded because of instrumental defects of NARVAL. The reference point for one of the polarisation rhombs was incorrect. This resulted in incorrect polarisation signatures for HN Peg in the last two observations in 2011 (Table A.1) and sudden polarisation changes in 2012. However the unpolarised spectra in 2011 and 2012 are not affected, and can be used to measure the chromospheric proxies of magnetic activity. Subsequent tests have confirmed that the polarised data collected in 2013 is reliable.<sup>4</sup>

### 3.5. Mean longitudinal magnetic field ( $B_l$ )

The longitudinal magnetic field is measured using the LSD Stokes  $V$  and Stokes  $I$  profiles, where the field measured is the mean magnetic field (line of sight component) integrated over the entire visible stellar surface. The center-of-gravity method ([Rees & Semel, 1979](#)) was used on the LSD profile of HN Peg to measure its longitudinal magnetic field, as shown in equation 3.1,

$$B_l(\text{G}) = -2.14 \times 10^{11} \frac{\int vV(v)dv}{\lambda_0 g c \int (I_c - I(v))dv} \quad (3.1)$$

where  $B_l$  is the longitudinal magnetic field in Gauss,  $\lambda_0 = 550 \text{ nm}$  is the central wavelength of the LSD profile,  $g = 1.21$  is the Landé factor of the line list,  $c$  is the speed of light in  $\text{kms}^{-1}$ ,  $v$  is the radial velocity in  $\text{kms}^{-1}$  and  $I_c$  is the normalised continuum. The velocity range covered by the integration window is  $\pm 17 \text{ kms}^{-1}$  around the line centre. The uncertainty in each of the  $B_l$  measurements are obtained by propagating the errors computed by the reduction pipeline in equation 2.10 as described by [Marsden et al. \(2014\)](#). The magnetic field from

<sup>4</sup>A detailed description of the polarisation defects and the correction technique used can be found here: <http://spiptbl.bagn.obs-mip.fr/Actualites/Anomalies-de-mesures>

the LSD Null profiles were also calculated for each observations where the magnetic field is approximately zero, indicating negligible spurious polarisation affect on the longitudinal field measurements. The errors in the longitudinal magnetic field of HN Peg is higher than the null profiles except in a few cases where the SN is weak compared to the rest of the observations. The magnetic field of HN Peg ( $B_l$ ) and the magnetic field from the Null profile ( $N_l$ ) and their related uncertainties are recorded in Table A.2.

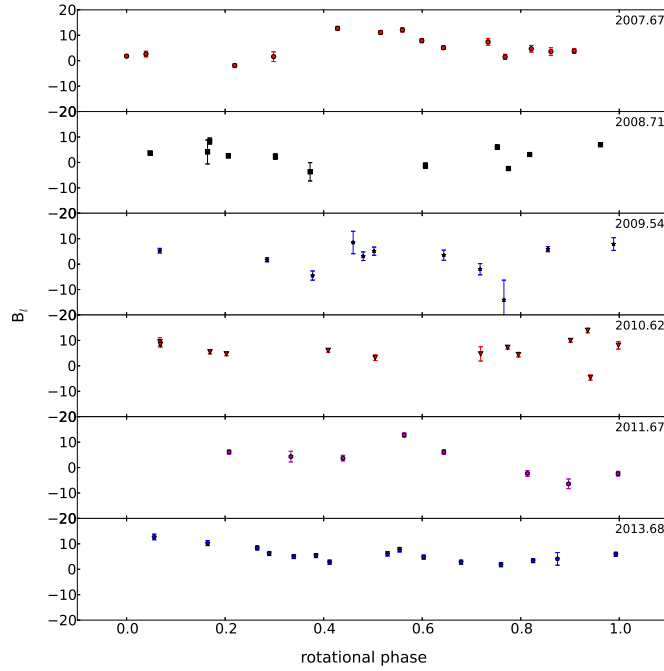


**Figure 3.1.:** Variability of longitudinal field ( $B_l$ ) as a function of the rotational phase. Each of the sub plots from top to bottom correspond to six different epochs (2007.67, 2008.71, 2009.54, 2010.62, 2011.67 and 2013.68).

The variability of the longitudinal magnetic field of HN Peg as a function of rotational phase is shown in Fig 3.1. The phase dependence of the longitudinal magnetic field indicates a complex surface magnetic field geometry. No long-term trend in mean longitudinal field measurements was observed for HN Peg as shown in Fig 3.6, where  $B_l$  exhibits no significant long-term variations through out the observational timespan. The mean  $B_l$  value of 5.3 G with a dispersion of 4.2 G in epoch 2007.67 goes down to its lowest value of 1.9 G with a dispersion of 6.3 G in epoch 2009.54. The mean value is the highest in epoch 2010.62.

### 3.6. Chromospheric activity indicators

Chromospheric activity has been widely observed in solar type stars, which is manifested as emission in the line cores of the chromospheric lines, such as: Ca II H&K, H $\alpha$ , Ca II IRT

lines. The varying flux in these line cores can be used as a proxy to investigate magnetic cycles.

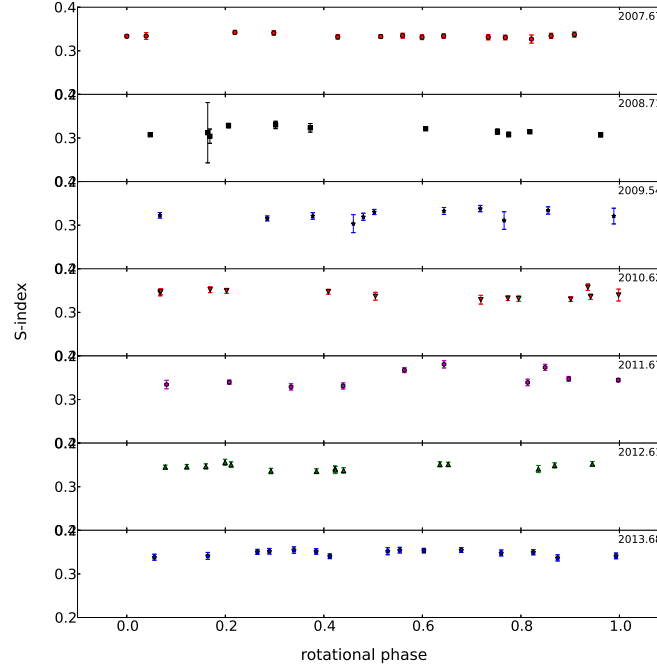


**Figure 3.2.:** Variability of S-index as a function of the rotational phase. Each of the subplots from top to bottom correspond to seven different epochs (2007.67, 2008.71, 2009.54, 2010.62, 2011.67, 2012.61 and 2013.68).

### S-index

we detect strong emission lines in the Ca II H&K line cores of HN Peg as a function of its rotational phase. The S-index is calculated using two triangular band passes centered at Ca II H and K lines (Duncan et al., 1991) at 396.8469 and 393.3663 nm respectively with a FWHM of 0.1 nm. The flux in the continuum at the red and blue sides of the line is measured by using two 2 nm wide rectangular band passes R and V at 400.107 and 390.107 nm respectively. Equation 3.2 is used to calibrate our index with the Mount Wilson values,

$$\text{S-index} = \frac{\alpha F_H + \beta F_K}{\gamma F_R + \delta F_V} + \Phi \quad (3.2)$$

where  $F_H$ ,  $F_K$ ,  $F_R$  and  $F_V$  are the flux in the band passes H, K, R and V. The NARVAL coefficients used to match our S-index values to the Mt Wilson values (Marsden et al., 2014) are  $\alpha = 12.873$ ,  $\beta = 2.502$ ,  $\gamma = 8.877$ ,  $\delta = 4.271$  and  $\Phi = 1.183\text{e-}03$ . We do not carry out the renormalisation procedure used by Morgenthaler et al. (2012) and carry out the continuum check following the procedure in Waite et al. (2014), where it was determined that removal of the overlapping orders is as efficient as renormalisation of the spectra.

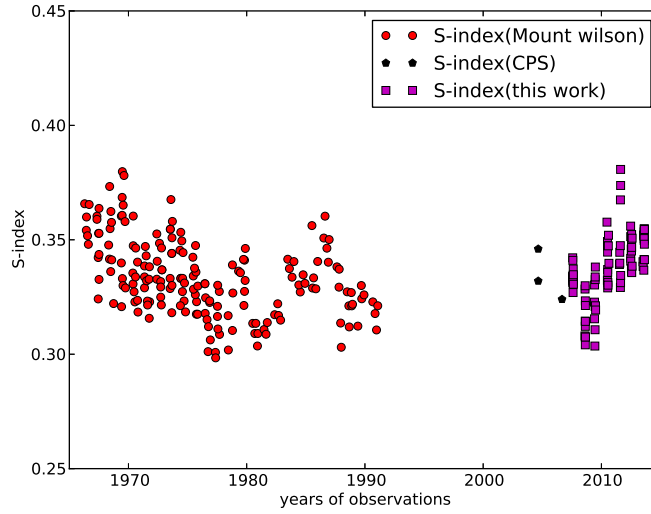


**Figure 3.3.:** S-index measurements of HN Peg from the combined data sets.

The variability of HN Peg’s S-index for each of the seven epochs is shown as a function of rotational phase in Fig 3.2. The error in the S-index for each measurement was calculated using error propagation. The S-index and related uncertainty for each observation is shown in Table A.2.

We also included S-index measurements of HN Peg from the Mount Wilson survey, where the data was collected from 1966 to 1991 (Baliunas et al., 1995). There are no published S-index measurements of HN Peg from 1991 to 2004. Additional S-index values were obtained from the California Planet Search Program(CPS) Isaacson & Fischer (2010), two in 2004 and one in 2006. No error bars are available for the S-index measurements taken from literature. The long term S-index measurements from the combined data are shown in Fig 3.3.

### H $\alpha$ -index

The rotational variation of the H $\alpha$  line profile was also determined. A rectangular band pass of 0.36 nm width, centered at the H $\alpha$  line at 656.285 nm (Gizis et al., 2002) and two 0.22 nm wide rectangular band passes  $N_{H\alpha\text{blue}}$  and  $N_{H\alpha\text{red}}$  at 655.77 and 656.0 nm respectively were used to measure the H $\alpha$ -index. We corrected the order overlap in the NARVAL spectra and used the order containing the complete H $\alpha$  line core. We then calculated the H $\alpha$ -index using equation 3.3.

$$\text{H}\alpha\text{-index} = \frac{F_{\text{H}\alpha}}{F_{\text{blue}} + F_{\text{red}}} \quad (3.3)$$

where  $F_{\text{H}\alpha}$  represents the flux in the H $\alpha$  line core and  $F_{\text{blue}}$  and  $F_{\text{red}}$  represent the flux in the continuum band pass filters  $H_{\text{blue}}$  and  $H_{\text{red}}$  respectively. The variability of H $\alpha$  as a function of HN Peg’s rotational phase is shown in Fig 3.4. The uncertainty in H $\alpha$ -index measurements

were calculated using error propagation. The  $H\alpha$ -index and related uncertainty for each observations are shown in Table A.2.

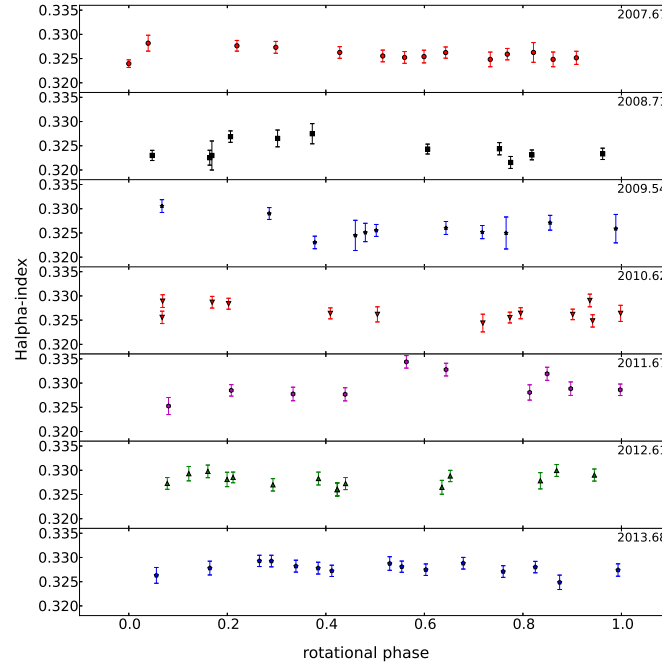


**Figure 3.4.:** Variability of the  $H\alpha$ -index as a function of rotational phase. Each of the sub plots from top to bottom correspond to seven different epochs (2007.67, 2008.71, 2009.54, 2010.62, 2011.67, 2012.61 and 2013.68).

### CaIRT-index

Since NARVAL covers a wide wavelength range from 350 nm up to 1000 nm, we can also observe the Ca II IR triplet lines. We take 0.2 nm wide rectangular band passes in the cores of each of the triplet lines at 849.8023 nm, 854.2091 nm and 866.241 nm. Two continuum band passes of the width of 0.5 nm are also taken,  $IR_{red}$  at 870.49 nm and  $IR_{blue}$  at 847.58 nm for the flux at the red and blue sides of the IR lines (Petit et al., 2013). We calculate the CaIRT-index using equation 3.4,

$$\text{CaIRT-index} = \frac{F_{Ca1} + F_{Ca2} + F_{Ca3}}{F_{IRTblue} + F_{IRTred}} \quad (3.4)$$

where the flux in the three line cores are represented by  $F_{Ca1}$ ,  $F_{Ca2}$  and  $F_{Ca3}$  respectively and the continuum fluxes are defined by  $F_{IRTblue}$  and  $F_{IRTred}$  respectively. The error bars for individual observations were calculated using error propagation. The variability of the CaIRT-index as a function of HN Peg's rotational phase is shown in Fig 3.5.

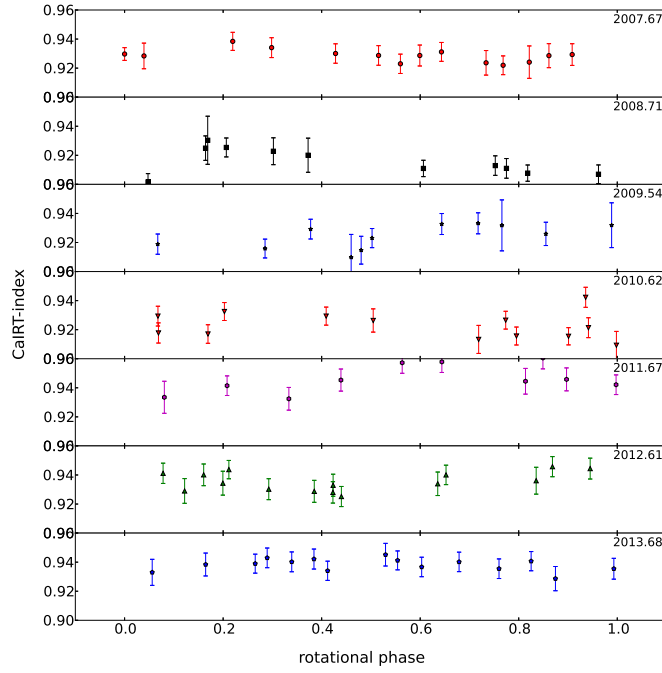


**Figure 3.5.:** Variability of CaIRT-index with the rotational phase. Each of the sub plots from top to bottom correspond to seven different epochs (2007.67, 2008.71, 2009.54, 2010.62, 2011.67, 2012.61 and 2013.68)

The long-term variability over the observational epochs of this analysis for the three activity indicators: Ca II H&K, H $\alpha$ , Ca II IRT lines are shown in Fig 3.6, where the mean values of each index is plotted as a function of the observational epochs. The error bars represent the standard deviation of the activity proxies for each epoch of observation. The long-term S-index variations are prominent than the rotationally induced variations. The long-term S-index and H $\alpha$  index show visible correlation over the entire time span of the observations. The two indices show a decreasing trend from 2007.67 to 2008.71 and show an increasing trend from 2008.71 to 2011.67 and then exhibits a flat trend. The long-term Ca II IRT measurements show global correlation with the S-index but shows more small-scale variations on a year to year basis.

The correlation between the different activity proxies is prominent in some epochs but not clearly visible in other epochs. The correlation between S-index and H $\alpha$ -index throughout the entire observational timespan is shown in Fig 3.7, where the correlation is more clearly visible. Correlation between S-index and Ca IRT is shown in Fig 3.8. The activity index measurements and their related uncertainties of HN Peg is tabulated in Table A.2.

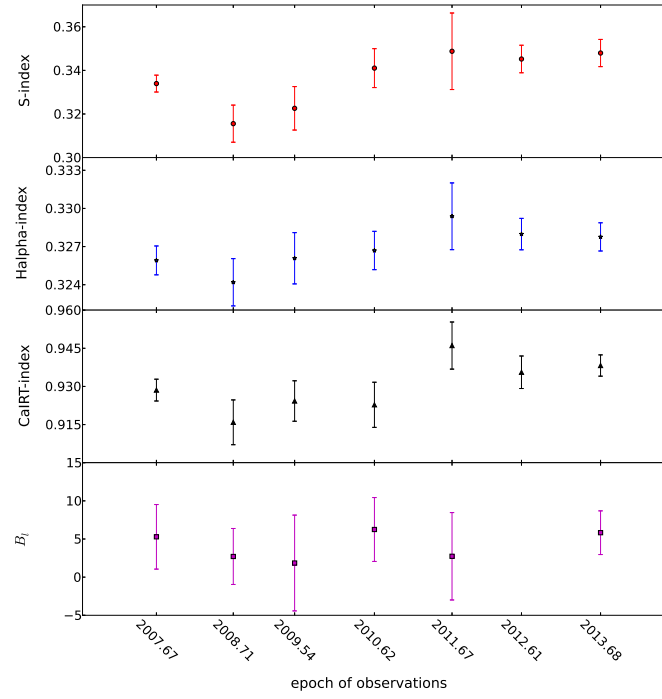


**Figure 3.6.:** Average value of the three different indices with the vertical bars showing the dispersion in each epoch of observations. Top to Bottom: Average values of S-index (red full circles), H $\alpha$ -index (blue stars), CaIRT-index (black triangle) and  $B_I$  (magenta squares) plotted against the epochs (2007-2013) in average Julian dates.

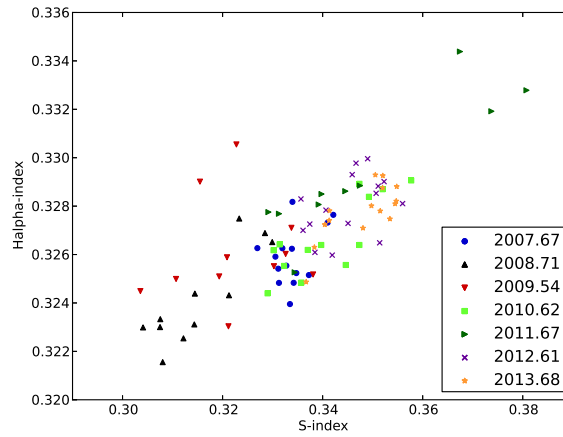


**Figure 3.7.:** Correlation between the S-index and H $\alpha$ -index for each epoch of observations.

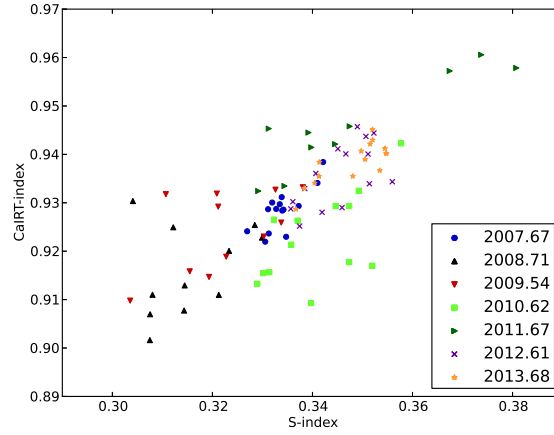


**Figure 3.8.:** Correlation between the S-index and CaIRT-index for each epoch of observations.

### 3.7. Large-scale magnetic field topology

The large-scale surface magnetic topology of HN Peg was reconstructed by using the Zeeman Doppler Imaging (ZDI) tomographic technique, developed by [Brown et al. \(1991\)](#), [Donati & Brown \(1997\)](#), [Semel \(1989\)](#). ZDI technique involves solving an inverse problem and reconstructing the large-scale surface magnetic geometry by iteratively comparing the Stokes  $V$  profile to the synthetically generated profiles, which are generated from a synthetic stellar model.

The large-scale field geometry of HN Peg was reconstructed by using the version of ZDI that reconstructs the field into its toroidal and poloidal components, expressed as spherical harmonics expansion ([Donati et al., 2006](#)). A synthetic stellar model of HN Peg was constructed using 5000 grid points, where the local Stokes  $I$  profile in each grid cell was assumed to have a Gaussian shape and was adjusted to match the observed Stokes  $I$  profile. The synthetic local Stokes  $V$  profiles were computed under the weak field assumption and iteratively compared to the observed Stokes  $V$  profile. The maximum entropy approach adopted by the ZDI code is based on the algorithm of [Skilling & Bryan \(1984\)](#). In this implementation of the maximum entropy principle, a target value of the reduced  $\chi^2$  is set by the user, where we define the reduced  $\chi^2$  as the  $\chi^2$  divided by the number of data points [Skilling & Bryan \(1984\)](#). In its first series of iterations, the ZDI code produces magnetic models with associated synthetic profiles that progressively get closer to the target  $\chi^2$  value. When the required reduced  $\chi^2$  value is reached, new iterations increase the entropy of the model (at fixed  $\chi^2$ ), converging step by step towards the magnetic model that minimises the total information of the magnetic map.

### 3.7.1. Radial velocity

The radial velocity of HN Peg was determined by fitting a Gaussian directly to the Stokes  $I$  profile to determine the centroid of the profile. This method was applied to each epoch of HN Peg. Additionally the radial velocity in the ZDI code was varied in  $0.1 \text{ km s}^{-1}$  steps. The radial velocity which results in the minimum information content was chosen which was comparable to the radial velocity obtained by the Gaussian fit. The radial velocity and the associated uncertainty for each observational epoch is shown in Table 3.2.

### 3.7.2. Inclination angle

The inclination angle of  $75^\circ$  was inferred using the stellar parameters of HN Peg shown in Table 3.1, which was tested within its error range by using as an input to the ZDI code. The inclination angle was increased in  $5^\circ$  steps and the inclination angle which resulted in minimum information content was used to generate the magnetic maps.

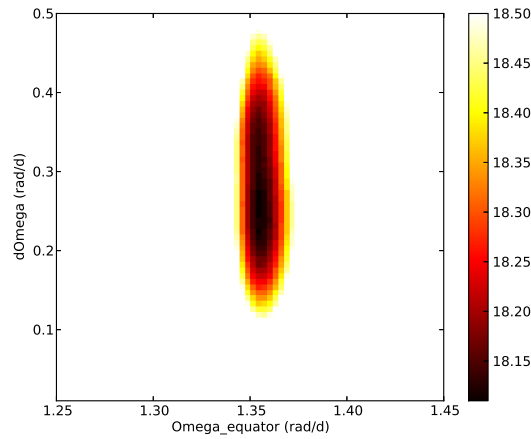


**Figure 3.9.:** Best fit map <sup>5</sup>obtained by varying the parameters for 2007 data . The  $\Omega_{\text{eq}}$  and  $d\Omega$  values obtained from this map are  $1.36 \text{ rad d}^{-1}$  and  $0.22 \text{ rad d}^{-1}$  respectively.

### 3.7.3. Differential rotation

The data used to reconstruct the magnetic field topology were collected over a span of several weeks, which might result into the introduction of latitudinal differential rotation during the timespan of observation. Differential rotation of HN Peg was measured by determining the difference in equatorial and polar shear incorporating a simplified solar-like differential rotation law into the imaging process,

$$\Omega(l) = \Omega_{\text{eq}} - d\Omega \sin^2 l \quad (3.5)$$

<sup>5</sup> $B_{\text{mean}}$  map obtained at unit  $\chi^2$  and minimising the information (minimising the field strength) where the colour bar represents  $B_{\text{mean}}$

where  $\Omega(l)$  is the rotation rate at latitude  $l$ ,  $\Omega_{\text{eq}}$  is the equatorial rotation and  $d\Omega$  is the difference in rotation between the equator and the poles.

For a given set of  $\Omega_{\text{eq}}$  and  $d\Omega$  the large-scale magnetic field geometry was reconstructed, following the method of [Petit et al. \(2002\)](#). Approximately 15 observations with good phase coverage ([Morgenthaler et al., 2012](#)) is required to retrieve the parameters of the surface differential law. As good phase coverage is important to perform differential rotation calculations, the two epochs 2007.67 (14 observations) and 2013.68 (13 observations) were selected and individual differential rotation parameters were calculated. As shown in Fig 3.9 the  $\Omega$  and  $d\Omega$  values for 2007.67 epoch are  $1.36 \pm 0.01 \text{ rad d}^{-1}$  and  $0.22 \pm 0.03 \text{ rad d}^{-1}$  and for 2013.68 epoch are  $1.27 \pm 0.01 \text{ rad d}^{-1}$  and  $0.22 \pm 0.02 \text{ rad d}^{-1}$  respectively. For the other epochs with less dense phase coverage the differential rotation values measured for 2007.67 are used for 2008.71, 2009.52 and values from 2013.68 are used for 2010.62 and 2011.67. The rotational period of HN Peg was also measured from the calculated differential rotational parameters.

The uncertainty in the differential rotation measurements were evaluated by obtaining  $\Omega_{\text{eq}}$  and  $d\Omega$  values by varying the input stellar parameters, within the error bars of the individual parameters. The dispersion in the resulting values was considered as the error bar.

#### 3.7.4. Magnetic topology

The large-scale magnetic field topology of HN Peg was reconstructed using ZDI, for the epochs 2007.67, 2008.71, 2009.54, 2010.62, 2011.67 and 2013.68. The stellar parameters used to reconstruct the magnetic field topology are a  $v \sin i$  of  $10.6 \text{ kms}^{-1}$  and an inclination angle of  $75^\circ$ . The number of spherical harmonics  $l$  used in our ZDI code is  $l_{\text{max}}=8$ .

##### Epoch 2007.67

For the epoch 2007.67, the modelled Stokes  $V$  LSD profile and the corresponding fit to the observed Stokes  $V$  LSD profile is shown in Fig 3.10 (Top left). The observed fit was achieved with a reduced  $\chi^2$  of 1.0. The number of degree of freedom is 152. In the radial field component of the magnetic field as shown in Fig 3.11, a strong positive field region is reconstructed at the equator along with a cap of positive polarity magnetic field encircling the pole. The azimuthal component is reconstructed as a band of positive magnetic field at equatorial latitudes as shown in Fig 3.11. The percentage of the total magnetic energy distributed into its poloidal and toroidal configuration for the epoch 2007.67 is shown in Fig 3.12. The magnetic energy is 57% poloidal and 43% toroidal as shown in Table 3.2. The percentage of the poloidal field reconstructed into its different components is shown in Fig 3.13. The mean magnetic field strength of HN Peg is  $18 \pm 0.5 \text{ G}$  (Table 3.2).

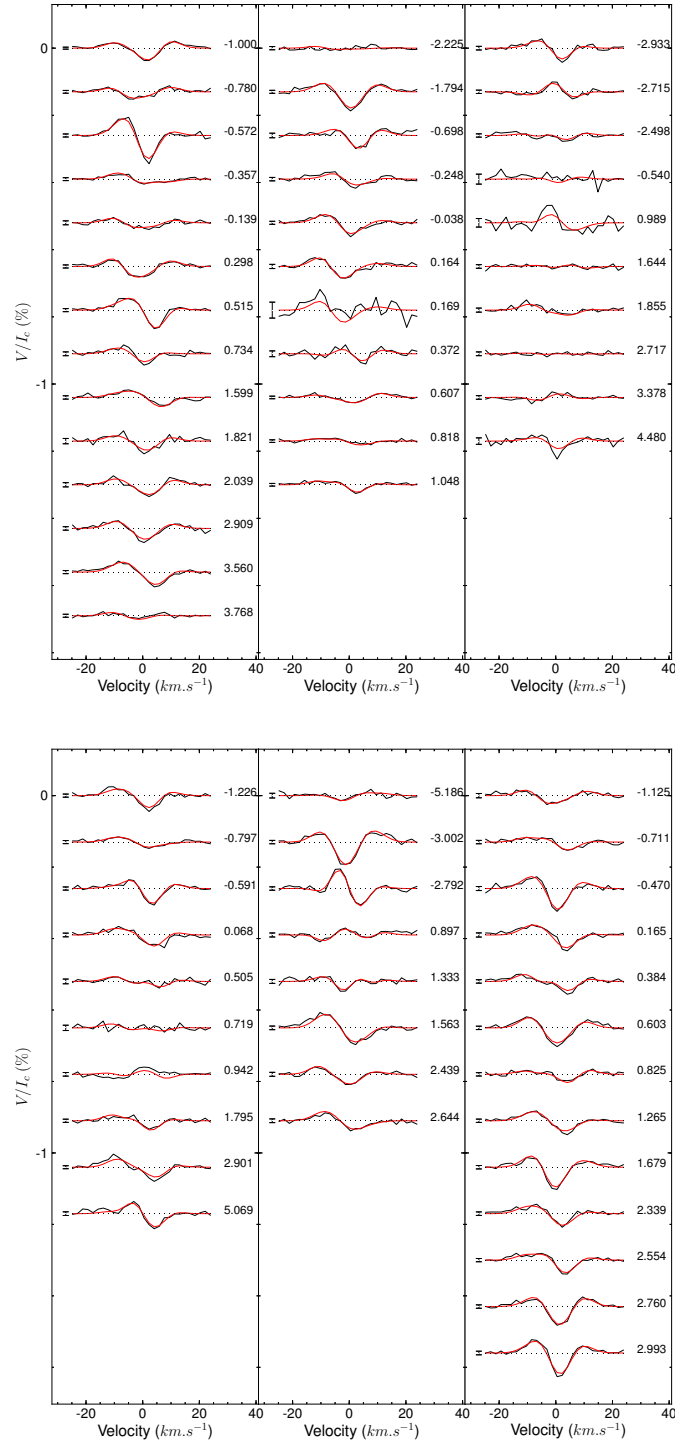


**Figure 3.10.:** *Top row:* The time series of the LSD Stokes  $V$  profiles from 2007.67, 2008.71 and 2009.54. *Bottom row:* Time series of the LSD Stokes  $V$  profiles for the epochs 2010.62, 2011.67 and 2013.68. The black line represents the observed Stokes  $V$  spectra and the red line represents the fit to the spectra. Rotational cycle is shown to the right and  $1\sigma$  error bars for each observations is shown to the left for each plot.

### 3. Variable magnetic field geometry of the young Sun HN Pegasi (HD 206860)

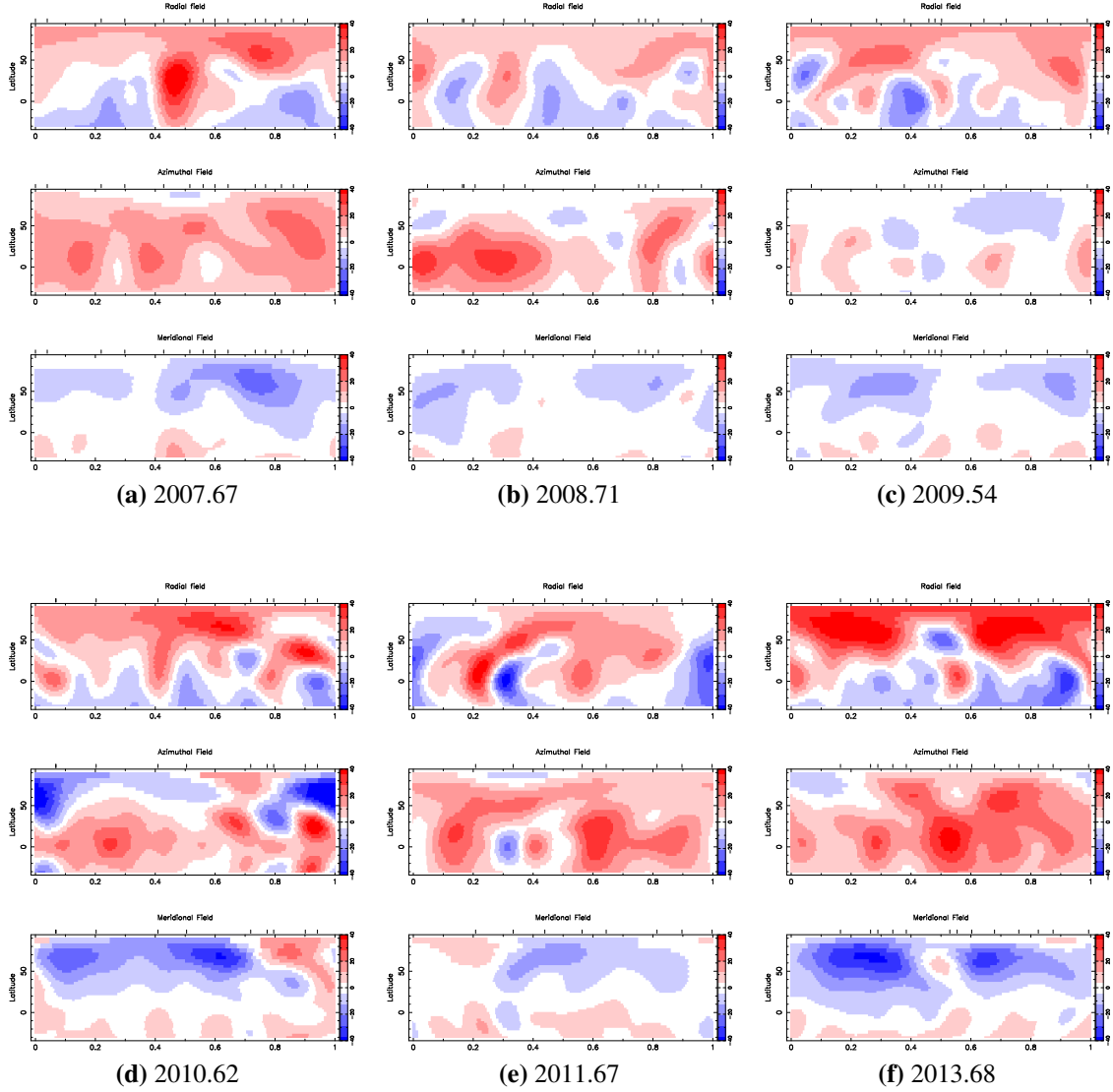


**Figure 3.11.:** Surface magnetic field geometry of HN Peg for six epochs as reconstructed using Zeeman Doppler Imaging. *Top row:* (a) 2007.67, (b) 2008.71, (c) 2009.54. *Bottom row :* (d) 2010.62, (e) 2011.67, (f) 2013.68. For each epoch, the magnetic field components are shown as projection onto one axis of the spherical coordinate frame, where from Top to Bottom: radial, azimuthal and meridional magnetic field components are shown. The field strength is shown in Gauss, where red represents positive polarity and blue represents negative polarity.

#### Epoch 2008.71

The LSD Stokes  $V$  profile and the corresponding fit for the epoch 2008.71 is shown in Fig 3.10 (Top middle). The observed fit was achieved with a  $\chi^2$  minimised to 1.0 and the number of degree of freedom is 68. The radial field geometry is dominated by a positive magnetic region over the poles as shown in Fig 3.11, where the strong positive field at the equator in epoch 2007.67 is not visible one year later in epoch 2008.71. The azimuthal field

geometry is dominated by two regions of positive polarity at the equator. The meridional field geometry is also shown in Fig 3.11. The percentage of the total magnetic energy distributed into the poloidal and toroidal components is shown in Fig 3.12. The majority of the magnetic energy is reconstructed as toroidal field component as shown in Table 3.2. The percentage of fraction of the poloidal magnetic field reconstructed into its different components is shown in Fig 3.13. The mean magnetic field strength decreases to  $14 \pm 0.3$  G (Table 3.2).

### Epoch 2009.54

The Stokes  $V$  profile in 2009.54 is shown in Fig 3.10 (Top right), where some of the Stokes  $V$  profile have a lower S/N ratio. The Stokes  $V$  profiles are fitted to the reconstructed profile with a  $\chi^2$  level of 1.0 and the number of degree of freedom is 40. The positive polarity magnetic region around the pole in the previous epochs is also present in 2009.54 as shown in Fig 3.11. The band of positive polarity azimuthal field observed in the previous epochs is surprisingly absent in this epoch as shown in Fig 3.11, with only 11% of the magnetic energy being toroidal. The percentage of magnetic energy reconstructed as poloidal component is 89% as shown in Fig 3.12. The percentage of the fraction of the poloidal magnetic energy distributed into its different field configurations is shown in Fig 3.13. The mean magnetic field strength is at its lowest at  $11 \pm 0.2$  G. (Table 3.2).

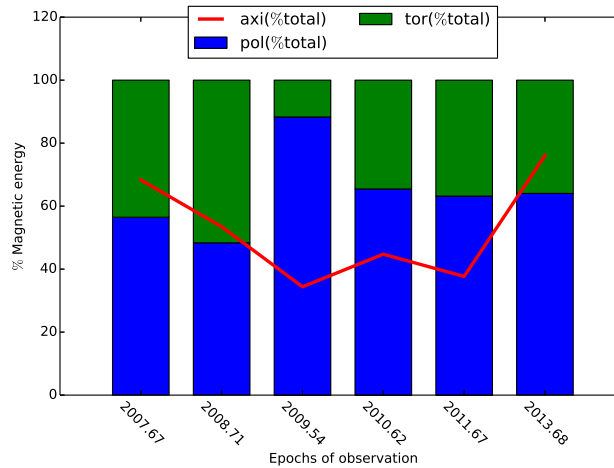


**Figure 3.12.:** Magnetic energy distribution throughout the six epochs (2007.67, 2008.71, 2009.54, 2010.62, 2011.67, 2013.68). The fraction of magnetic field stored in poloidal component is shown in blue and toroidal component in green. The red line represents the fraction of the energy stored in the axisymmetric component. The error bars associated with each epoch are shown in Table 3.2.

### Epoch 2010.62

The Stokes  $V$  profile and magnetic maps of HN Peg for epoch 2010.62 are shown in Fig 3.10 (Bottom left) and Fig 3.11 respectively. The best fit to the observed Stokes  $V$  profiles were obtained with a  $\chi^2$  level of 1.4, which might be a result of some intrinsic behaviour that could not be accounted for. The number of degree of freedom is 40. The radial field component is

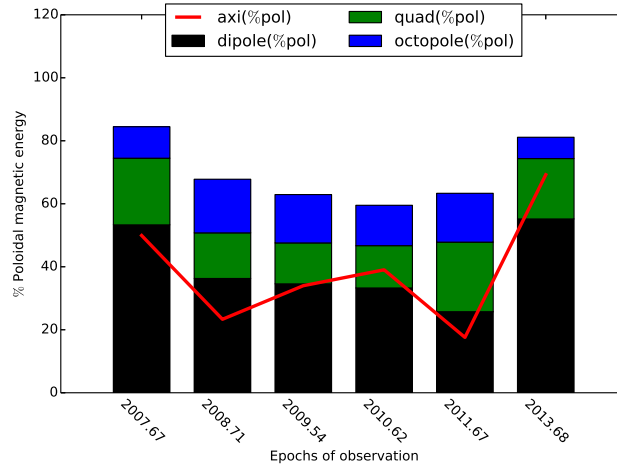


**Figure 3.13.:** Poloidal magnetic field distributed into different configurations throughout the six epochs(2007.67, 2008.71, 2009.54, 2010.62, 2011.67, 2013.68). The fraction of the poloidal magnetic energy stored as dipole is shown in black, quadrupole in green and octopole in blue. The red line represents the fraction of the poloidal energy stored in the axisymmetric component. The error bars associated with each epoch are shown in Table 3.2.

still mostly positive around the poles as shown in Fig 3.11. The azimuthal field is stronger than in epoch 2009.54, with the presence of both positive and negative polarity regions. The meridional field component is also shown in Fig 3.11. The percentage of the magnetic energy distribution into its poloidal and toroidal component is shown in Fig 3.12. 65% of the magnetic energy is reconstructed in the poloidal component and 35% of the energy is stored in the toroidal component as shown in Table 3.2. The percentage of the fraction of the poloidal component reconstructed into its different components is shown in Fig 3.13. The mean magnetic field strength of HN Peg has increased from  $11 \pm 0.2$  G in 2009.54 to  $19 \pm 0.8$  G (Table 3.2).

#### Epoch 2011.67

For the epoch 2011.67, the reconstructed Stokes  $V$  profile and its fit to the observed Stokes  $V$  profile is shown in Fig 3.10 (Bottom middle). The observed fit was obtained with a  $\chi^2$  minimised to 1.1. The formal computation of the number of degree of freedom for this epoch results in a negative value, which means for this particular case the problem is underdetermined. The magnetic field geometry in the radial field is more complex than in the previous epochs, with the presence of both positive and negative magnetic regions as shown in Fig 3.11. However, the phase coverage is not sufficient to reliably confirm the negative polarity regions. The azimuthal field is mostly positive with regions of positive polarity around the equator. The meridional field is also shown in Fig 3.11. The percentage of the magnetic energy distributed into the poloidal and toroidal components is shown in Fig 3.12. The percentage of the fraction of the poloidal component reconstructed into its different field configurations is shown in Fig 3.13. 61% of the magnetic energy is reconstructed into its poloidal component as shown in Table 3.2, where the mean magnetic field strength of HN

Peg is  $19 \pm 0.7$  G.

### Epoch 2013.68

The observed and reconstructed Stokes  $V$  profiles for the epoch 2013.68 is shown in Fig 3.10 (Bottom right). The best fit to the observed Stokes  $V$  profiles was obtained with a  $\chi^2$  of 1.0. The number of degree of freedom is 124. The magnetic field in the radial component is shown in Fig 3.11, where the pole is dominated with a ring of positive polarity magnetic field. The azimuthal field component is dominated by a band of positive polarity magnetic field at the equator as shown in Fig 3.11. The percentage of the magnetic energy distributed into different field configurations is shown in Fig 3.12. The magnetic energy is mostly poloidal (62%) as shown in Table 3.2. The percentage of the fraction of poloidal field reconstructed into its different configurations is shown in Fig 3.13. The mean magnetic field is at its highest at  $24 \pm 0.7$  G, where 77% of the total field is axisymmetric (Table 3.2).

The uncertainties associated with the magnetic maps for each epoch of observations were obtained by using different values for the input stellar parameters into the ZDI code (see [Petit et al., 2002](#)), where the individual parameters were varied within their error bars. The dispersion in the resulting values was considered as error bars.

## 3.8. Discussion

HN Peg was observed for seven epochs from 2007.67 to 2013.68, providing new insights into its magnetic field variations and the associated geometry.

### 3.8.1. Long-term magnetic variability

The longitudinal magnetic field ( $B_l$ ) for each observation of HN Peg was derived using Stokes  $V$  profile and Stokes  $I$  profile integrated over the entire visible stellar surface. The longitudinal field varies as a function of the rotational phase during each observational epoch, which indicates a non-axisymmetric magnetic geometry. Over the epochs of this analysis no significant long-term  $B_l$  variations are apparent as shown in Fig 3.6, where the mean  $B_l$  values exhibit variability over the observational timespan but the overall trend with dispersion is flat. HN Peg exhibits a strong longitudinal magnetic field strength when compared to the other solar type stars included in [Marsden et al. \(2014\)](#).  $B_l$  ranges from -14 G up to 13 G

The long term chromospheric variability of HN Peg was monitored using three different chromospheric lines: Ca II H&K, H $\alpha$  and Ca II IRT. The three chromospheric tracers exhibit weak rotational dependence during each observational epoch. Periodic analysis of HN Peg carried out by the Mount Wilson survey categorised HN Peg as a variable star with a period of  $6.2 \pm 0.2$  years. The chromospheric activity of HN Peg was also measured as part of the Bcool snapshot survey ([Marsden et al., 2014](#)), where the measured S-index are compatible with our S-index measurements.

**Table 3.2.:** Magnetic properties of HN Peg extracted from the ZDI maps.

Dates (frac.years)	no of obs	$v_r$ km s <sup>-1</sup>	$B_{mean}$ (G)	pol (%tot)	dipole (%pol)	quad (%pol)	oct (%pol)	axi (%tot)	$\Omega_{eq}$ rad d <sup>-1</sup>	$d\Omega$ rad d <sup>-1</sup>
2007.67	14	-16.60±0.17	18±0.5	57±4	54±4	22±4	9±1	69±15	1.36±0.01	0.22±0.03
2008.71	10	-16.67±0.04	14±0.3	49±12	35±3	15±2	17±1	54±21	–	–
2009.54	11	-16.63±0.20	11±0.2	89±23	42±4	11±3	14±1	45±21	–	–
2010.62	11	-16.65±0.02	19±0.8	65±13	33±4	13±3	12±2	44±20	–	–
2011.67	8	-16.66±0.08	19±0.7	61±22	25±4	19±3	16±1	38±21	–	–
2013.68	13	-16.66±0.03	24±0.7	62±4	57±4	17±4	6±1	77±10	1.27±0.01	0.22±0.02

Correlations were observed for the three chromospheric tracers for individual epochs with visible scatter, which might be due to the effect of different temperature and pressure conditions associated with the chromospheric lines, Ca II H&K, H $\alpha$  and Ca II IRT. Correlations between S-index and H $\alpha$ -index were also observed for  $\xi$  Bootis A by Morgenthaler et al. (2012). The observed scatter in the correlation between S-index and H $\alpha$ -index for each epoch might be also explained by the contribution of plage variation in Ca II H&K and filament variation in H $\alpha$  flux (Meunier & Delfosse, 2009), where increase in filament contribution might result in decrease in correlation between the two chromospheric tracers. Apart from the contribution of filament and plage, Meunier & Delfosse (2009) also concluded that stellar inclination angle and phase coverage might also effect the correlation between these two tracers.

In their long-term evolution, the chromospheric tracers exhibit a similar trend, with visible correlation between the S-index and H $\alpha$ -index. In the long-term mean S-index and H $\alpha$ -index exhibit correlation in cool stars, which might be due to the effect of stellar colour (Cincunegui et al., 2007). The long-term Ca II H&K and H $\alpha$  correlation is clearly observed in the Sun (Livingston et al., 2007), where the two activity proxies follow the solar magnetic cycle. This long-term correlation between these two tracers have also been observed in other cool stars with high activity index (Gomes da Silva et al., 2013).

For each observational epoch no visible correlation is observed between the variability of the longitudinal magnetic field and the chromospheric tracers. Correlations between the direct field measurements and the magnetic activity proxies were also not observed for the solar analogue  $\xi$  Bootis A (Morgenthaler et al., 2012). This lack of correlation can be explained by the contribution of small scale magnetic features in chromospheric activity measurements which are lost in the polarised Stokes V magnetic field calculations due to magnetic flux cancellations.

### 3.8.2. Large scale magnetic topology

The large-scale magnetic topology of HN Peg was reconstructed for six observational epochs (2007.67, 2008.71, 2009.54, 2010.62, 2011.67 and 2013.68), where the mean magnetic field strength ( $B_{\text{mean}}$ ) changes with the geometry of the field from epoch to epoch. The mean magnetic field strength determined from the ZDI maps (Table 3.2) is in the order of a few G, which is considerably smaller when compared to the mean magnetic field of other solar analogues HD 189733 ( $1.34 \pm 0.13 M_{\odot}$ ,  $T_{\text{eff}}=6014$  K) (Fares et al., 2010) and  $\xi$  Bootis A ( $0.86 \pm 0.07 M_{\odot}$ ,  $T_{\text{eff}}=5551 \pm 20$ ) (Morgenthaler et al., 2012). The mean magnetic field strength of HN Peg is higher than HD 190771, which has a mass of  $0.96 \pm 0.13 M_{\odot}$  and  $T_{\text{eff}}$  of  $5834 \pm 50$  (Morgenthaler et al., 2011, Petit et al., 2009). When compared to solar-type stars of similar spectral type HN Peg exhibits higher mean field strength than the mean field strength of  $\tau$  Boo(F7) with a mass of  $1.33 \pm 0.11 M_{\odot}$  (Fares et al., 2009), HD 179949(F8) (Fares et al., 2012), where  $\tau$  Boo and HD 179949 are both planet hosting stars.

The radial field component of HN Peg exhibits a variable field geometry, where the field strength varies from epoch to epoch as shown in Fig 3.11. A positive polarity region at the pole is observed in epoch 2007.67, where a strong positive polarity magnetic region is also observed near the equator. The positive region at the pole is present throughout the observational epoch, without exhibiting any polarity switch. The magnetic field energy is stored into its poloidal and toroidal components. The poloidal field of HN Peg is not a simple dipole. HN Peg shows a significant toroidal magnetic field. Toroidal component is prominent in solar type stars with rotation periods as short as a few days (Petit et al., 2008) and stars with longer rotational periods show more prominent poloidal component, which is clearly observed in the Sun. The fraction of energy stored into the different components of the poloidal field exhibits variations from epoch to epoch as shown in Fig 3.13.

The azimuthal field component of HN Peg exhibits a more variable geometry compared to the radial field geometry. The azimuthal field component exhibits the presence of a significant positive polarity magnetic regions, which undergoes variations from epoch to epoch as shown in Fig 3.11. A strong positive polarity band of magnetic field encircling the star is observed in epoch 2007.67. In 2008.71 two strong positive polarity magnetic regions were observed near the equator. The azimuthal component becomes negligible in the epoch 2009.54. The toroidal field percentage is minimum in epoch 2009.54. The azimuthal field reappears in 2010.62, where opposite polarity magnetic field regions are observed. In 2011.67 stronger positive polarity regions are observed, which finally appears as an azimuthal ring in epoch 2013.68.

Prominent toroidal features have been observed in a wide range of stars belonging to different spectral class, such as HD 190771 (Petit et al., 2009),  $\xi$  Bootis A (Morgenthaler et al., 2012),  $\tau$  Boo (Fares et al., 2009) and HD 189733 (Fares et al., 2010). The sudden disappearance of the toroidal field was also observed in  $\xi$  Boo (Morgenthaler et al., 2012). The toroidal component is prominent in solar-type stars with rotation periods as short as a few days (Petit et al., 2008) and stars with longer rotation periods show more prominent poloidal component, which is clearly observed in the Sun. Toroidal band was also not observed in the F8 dwarf HD 179949 (Fares et al., 2012), where only two epochs of observations were available. The presence of significant global-scale toroidal field has also been observed in numerical simulations of rapidly rotating Suns (Brown et al., 2010), where the surface field topology becomes predominantly toroidal for stars with rotation periods of a few days.

No polarity switches have been observed for HN Peg, although it showed significant evolution of its magnetic field geometry over the span of six observational epochs. Magnetic cycles were also not observed for  $\xi$  Bootis A and HD 189733, which are slower rotators when compared to HN Peg. Polarity switches were observed in HD 190771,  $\tau$  Boo and HD 78366 over their observational time span. Magnetic cycles shorter than the magnetic cycle of the Sun were observed for  $\tau$  Boo and HD 78366.

The variability of the mean magnetic field of HN Peg follows a similar trend as that of the toroidal field component (Table 3.2). The mean magnetic field ( $B_{\text{mean}}$ ) of HN Peg show

a gradual decrease in its field strength from 2007.67 to 2009.54, with minimum  $B_{\text{mean}}$  in 2009.54. The mean field starts increasing from 2009.54 till it reaches a maximum strength in 2013.68. This indicates strong dependence of the mean field strength on the toroidal component of the magnetic field.

### 3.8.3. Differential rotation

HN Peg has a low  $v \sin i$  of  $10.6 \text{ km s}^{-1}$ , which makes it unsuitable for differential rotation calculations using other conventional studies such as line profile studies using Fourier Transform method (Reiners & Schmitt, 2003). Photometric observations of HN Peg were used to measure its differential rotation by Messina & Guinan (2003), where the evolution of the rotation of the star along the star spot cycle was measured with inconclusive results.

The differential rotation of HN Peg was calculated using Stokes  $V$  and  $I$  profiles in the ZDI technique. Two epochs with the best phase coverage were used (2007.67 and 2013.68) in the differential rotation calculations. The  $\Omega$  and  $d\Omega$  values for 2007.67 epoch were  $1.36 \pm 0.01 \text{ rad d}^{-1}$  and  $0.22 \pm 0.03 \text{ rad d}^{-1}$  and for 2013.68 epoch were  $1.27 \pm 0.01 \text{ rad d}^{-1}$  and  $0.22 \pm 0.02 \text{ rad d}^{-1}$  respectively.

HN Peg exhibits weak differential rotation compared to other dwarfs of similar spectral types such as HD 171488 (G0) (Stokes  $I$ /Stokes  $V$ :  $\Omega_{\text{eq}} = 4.93 \pm 0.05 / 4.85 \pm 0.05 \text{ rad d}^{-1}$ ,  $d\Omega = 0.52 \pm 0.04 / 0.47 \pm 0.04 \text{ rad d}^{-1}$ ) (Jeffers & Donati, 2008) and  $\tau$ Boo (F7) (2008 June:  $\Omega_{\text{eq}} = 2.05 \pm 0.04 \text{ rad d}^{-1}$  and  $d\Omega = 0.42 \pm 0.10 \text{ rad d}^{-1}$ , 2008 July:  $\Omega_{\text{eq}} = 2.12 \pm 0.12 \text{ rad d}^{-1}$  and  $d\Omega = 0.50 \pm 0.15 \text{ rad d}^{-1}$ ) (Fares et al., 2009). HD 171488 is the closest to HN Peg in terms of spectral type, stellar radius and age. The  $d\Omega$  values of HN Peg is higher than the other young early G dwarfs such as LQ Lup ( $\Omega_{\text{eq}} = 20.28 \pm 0.01 \text{ rad d}^{-1}$ ,  $d\Omega = 0.12 \pm 0.02 \text{ rad d}^{-1}$ ) (Donati et al., 2000) and R58 (2000 January:  $\Omega_{\text{eq}} = 11.14 \pm 0.01$  and  $d\Omega = 0.03 \pm 0.02$ , 2003 March:  $\Omega_{\text{eq}} = 11.19 \pm 0.01$  and  $d\Omega = 0.14 \pm 0.01$ ) (Marsden et al., 2004). When compared to HD 179949 ( $\Omega_{\text{eq}} = 0.82 \pm 0.01 \text{ rad d}^{-1}$ ,  $d\Omega = 0.22 \pm 0.06 \text{ rad d}^{-1}$ ) (Fares et al., 2012), HN Peg exhibits comparable  $d\Omega$  values. Although, when compared to other fast rotators such as  $\xi$ Boo ( $P_{\text{rot}} = 6.43 \text{ days}$ ) (Morgenthaler et al., 2012), HN Peg exhibits weaker differential rotation. No direct correlation between differential rotation of HN Peg and solar analogues of similar stellar parameters such as age, spectral type,  $P_{\text{rot}}$  have been observed so far.

## 3.9. Summary

In this chapter we presented the large-scale magnetic geometry of the young solar analogue HN Peg. HN Peg is a variable young dwarf with a complex magnetic geometry, where the radial field exhibits stable positive polarity magnetic field region throughout our observational epochs. In contrast, the azimuthal field exhibits a highly variable geometry where a band of positive polarity field is observed in the first epoch of observation, followed by a negligible toroidal field two years later in epoch 2009.54. The toroidal band emerges again one year later in epoch 2010.62 which is stable in the later epochs 2011.67 and 2013.68. The long-term longitudinal magnetic field variations were also calculated where in the long-term

### *3. Variable magnetic field geometry of the young Sun HN Pegasi (HD 206860)*

---

the longitudinal magnetic field exhibits a flat trend. The chromospheric activity was also measured where the chromospheric activity indicators exhibit a long-term correlation.

# 4. A solar-like magnetic cycle on the mature K-dwarf 61 Cygni A (HD 201091) \*

## Contents

<b>4.1. Abstract</b>	<b>62</b>
<b>4.2. Introduction</b>	<b>62</b>
<b>4.3. Physical properties of 61 Cyg A</b>	<b>64</b>
<b>4.4. Instrumental setup and data reduction</b>	<b>66</b>
4.4.1. Optical data	66
4.4.2. X-ray data	67
<b>4.5. Magnetic field detection: direct and indirect approach</b>	<b>67</b>
4.5.1. Mean longitudinal magnetic field	67
4.5.2. Chromospheric activity as a proxy of magnetic activity	68
<b>4.6. Large-scale magnetic field geometry</b>	<b>74</b>
4.6.1. Vector magnetic field	74
4.6.2. Evolution of the different multipolar modes over the magnetic cycle	80
4.6.3. Differential rotation	82
<b>4.7. Long-term evolution of the magnetic and activity cycle</b>	<b>82</b>

\*This Chapter was previously published in the peer-reviewed journal *Astronomy & Astrophysics* (**Boro Saikia, S.**, Jeffers, S. V., Morin, J., Petit, P., Folsom, C. P., Marsden, S. C., Donati, J. F., Cameron, R., Hall, J. C., Pedrelwitz, V., Reiners, A., Vidotto, A., 2016, A&A, 594, 29). The chromospheric and ZDI analysis was carried out by Sudeshna Boro Saikia (S.B.S) (University of Goettingen). The text in the paper was written by S.B.S. S. V. Jeffers (University of Goettingen) supervised S.B.S. J. F. Donati (CNRS, IRAP Toulouse and Université de Toulouse, France) determined the stellar properties used here. R.Cameron (Max Plank Institutue for Solar System Research Goettingen, Germany) helped in the interpretation of the results in the context of the Sun. J. C. Hall (Lowell Observatory, USA) provided the Lowell observatory chromospheric data. The X-ray data of 61 Cyg A was analysed by V. Pedrelwitz (Hamburger Sternwarte, Germany), who collaborated in this project and provided the X-ray luminosity data used here. The other co-authors (J. Morin (LUPM, Université Montpellier, France), P.Petit (CNRS, IRAP Toulouse and Université de Toulouse, France), C. P. Folsom (IPAG, UJF-Grenoble 1/CNRS-INSU, France), S. C. Marsden (University of Southern Queensland, Australia), A. Reiners (University of Goettingen), A. Vidotto (Université de Genève, Switzerland and Trinity College Dublin, Ireland)) provided the data, their expert insight and helped in interpreting the results. The work was supported by the project A16 SFB 963/DFG. Part of the work was also funded by the COST Action MP1104. The word ‘paper’ is replaced by the word ‘chapter’ to conform with the format of the Thesis. Credit: Boro Saikia et al., A&A, 594, 29, 2016, reproduced with permission ©ESO.

<b>4.8. Discussion</b>	<b>84</b>
4.8.1. Large-scale magnetic field	84
4.8.2. Chromospheric activity	86
<b>4.9. Summary</b>	<b>87</b>

---

## 4.1. Abstract

The long-term monitoring of magnetic cycles in cool stars is a key diagnostic in understanding how dynamo generation and amplification of magnetic fields occur in stars similar in structure to the Sun. We investigated the temporal evolution of a possible magnetic cycle of 61 Cyg A. The magnetic cycle is determined from 61 Cyg A's large-scale field over its activity cycle using spectropolarimetric observations and compared to the solar large-scale magnetic field. We used the tomographic technique of Zeeman Doppler imaging (ZDI) to reconstruct the large-scale magnetic geometry of 61 Cyg A over multiple observational epochs spread over a time span of nine years. We investigated the time evolution of the different components of the large-scale field and compared it with the evolution of the star's chromospheric activity by measuring the flux in three different chromospheric indicators: Ca II H&K, H $\alpha$  and Ca II infrared triplet lines. We also compared our results with the star's coronal activity using XMM-Newton observations. The large-scale magnetic geometry of 61 Cyg A exhibits polarity reversals in both poloidal and toroidal field components, in phase with its chromospheric activity cycle. We also detect weak solar-like differential rotation with a shear level similar to that of the Sun. During our observational time span of nine years, 61 Cyg A exhibits solar-like variations in its large-scale field geometry as it evolves from minimum activity to maximum activity and vice versa. During its activity minimum in epoch 2007.59, ZDI reconstructs a simple dipolar geometry which becomes more complex when it approaches activity maximum in epoch 2010.55. The radial field flips polarity and reverts back to a simple geometry in epoch 2013.61. The field is strongly dipolar and the evolution of the dipole component of the field is reminiscent of solar behaviour. The polarity reversal of the large-scale field indicates a magnetic cycle that is in phase with the chromospheric and coronal cycle.

## 4.2. Introduction

High resolution observations of the Sun, including over 30 years of synoptic magnetic field maps, have revealed a coherent picture of the way in which the large-scale magnetic field evolves over the course of the 22-year solar magnetic cycle. At minimum, the field is concentrated at the polar regions and is mostly axisymmetric with respect to the rotation axis. At activity maximum, the field is no longer concentrated at the polar regions and is restricted to lower latitudes (Hathaway, 2010). When the next minimum occurs, the polar field reappears but with the opposite sign to that observed in the previous minimum at the start of the cycle. This cyclic process repeats every 11 years and it takes 22 years for the polar magnetic fields to revert back to the same polarity, forming a 22-year magnetic cycle. During the course of

the solar magnetic cycle the geometry of the large-scale field of the Sun also changes dramatically. The Sun varies from an almost dipolar geometry during cycle minimum to a more complex geometry during cycle maximum (DeRosa et al., 2012, Sanderson et al., 2003). A recent study by DeRosa et al. (2012) has revealed that during cycle minimum the dipolar component of the large-scale solar field dominates the other components. During polarity reversals the quadrupolar and octopolar component of the large-scale field dominates the dipolar component.

When it comes to other solar-type stars, observations do not have even a fraction of the spatial and temporal resolution of the solar observations. Magnetic cycles in other cool stars have been investigated by using two well known proxies of magnetic activity: chromospheric activity (Baliunas et al., 1995, Hall, 2008) and coronal activity (Güdel, 2004, Pevtsov et al., 2003). The first long-term monitoring of chromospheric activity in solar-type dwarfs was carried out at the Mount Wilson observatory (Baliunas et al., 1995, Duncan et al., 1991, Wilson, 1978), where emission in the line cores of Ca II H&K lines was measured. These observations revealed that different solar-type stars tend to exhibit different levels of activity variation: irregular activity variations in fast rotating young stars, cyclic activity in comparatively older slowly rotating solar-type stars, and a possible Maunder-minimum in some stars (Baliunas et al., 1995). Our investigation of chromospheric activity cycles of Mount Wilson (Baliunas et al., 1995) and HARPS (Lovis et al., 2011) stars has also confirmed that solar-like cycles are more likely for slow rotating stars than for fast rotating stars (Boro Saikia et al., 2016b). A further analysis of the Maunder-minimum candidates from the Mt Wilson survey by Schröder et al. (2013) reveals them to be slightly more evolved than the Sun. Coronal activity of cool stars, on the other hand is not intensively monitored compared to their chromospheric activity. Analysis by Hempelmann et al. (1996) produced weak statistical evidence of coronal cycles in cool stars, and since then coronal activity cycles have been detected for a few selected G and K dwarfs. For example, Favata et al. (2008) reported the presence of a coronal activity cycle for the binary system HD81809. Cyclic X-ray activity was also detected for our target star 61 Cyg A (Robrade et al., 2012) and the K1 dwarf  $\alpha$  Cen B (Ayres, 2015, Robrade et al., 2012). The shortest coronal activity cycle of 1.6 years was reported for the young active Sun  $\iota$  Horologii (Sanz-Forcada et al., 2013), where the coronal activity cycle is in phase with its short chromospheric activity cycle.

Although these indirect proxies are reliable indicators of magnetic activity in cool stars, they do not provide any direct information on the strength or orientation of the large-scale magnetic field. Direct measurements of the surface magnetic field rely on the Zeeman effect. By measuring the broadening of spectral lines caused by the Zeeman effect acting on unpolarised spectra (Reiners & Basri, 2006, Robinson, 1980, Saar, 1996), the integrated unsigned magnetic flux, averaged over the entire disk of the star, can be measured. One advantage of this technique is that the small-scale magnetic features also contribute to the total field measurements. This technique does not provide information on the large-scale magnetic field geometry. However, the tomographic technique Zeeman Doppler imaging (ZDI) (Donati et al., 1997, Semel, 1989) uses spectropolarimetric observations to reconstruct the stellar surface magnetic field geometry. Due to cancellation effects this technique is insensi-

tive to small-scale multipolar features, as the overall polarisation signatures of the multipolar field are cancelled out and only the large-scale field is reconstructed. As the ZDI technique provides information about the vector magnetic field, it can provide invaluable insights into the large-scale field geometry as well as the temporal evolution and polarity reversals of the large-scale field.

The large-scale magnetic field of several solar-type stars reconstructed using ZDI over multiple epochs, has revealed their strongly varying magnetic geometry. For the G7 dwarf  $\xi$  Bootis A ( $0.86 M_{\odot}$ ,  $T_{\text{eff}} = 5551$  K) (Morgenthaler et al., 2012), the K2 dwarf  $\varepsilon$  Eridani ( $0.856 M_{\odot}$ ,  $T_{\text{eff}} = 5146$  K) (Jeffers et al., 2014), and the G0 dwarf HN Peg ( $1.085 M_{\odot}$ ,  $T_{\text{eff}} = 5974$  K) (Boro Saikia et al., 2015) rapidly varying field geometry was detected, with surprising appearances and disappearances of the azimuthal field for HN Peg and  $\varepsilon$  Eridani. A two-year magnetic cycle was revealed for the planet hosting F7 dwarf  $\tau$  Bootis ( $1.42 M_{\odot}$ ,  $T_{\text{eff}} = 6360$  K) (Donati et al., 2008, Fares et al., 2009).  $\tau$  Boo is a hot Jupiter host where the planet is orbiting at 0.049 AU. No correlation was detected between the large-scale polarity switch and its chromospheric activity (Fares et al., 2009). Further monitoring of  $\tau$  Boo over three epochs by Fares et al. (2013) has confirmed the previously determined two-year magnetic cycle. Recent new analysis of  $\tau$  Boo polarised spectra (Mengel et al., 2016) shows a 3:1 ratio between the magnetic and chromospheric cycles. A magnetic cycle was also detected for the G0 dwarf HD 78366 ( $1.34 M_{\odot}$ ,  $T_{\text{eff}} = 6014$  K) (Morgenthaler et al., 2011), where the radial component of the magnetic field exhibits polarity reversals indicating a possible three-year cycle. Polarity reversals were observed in the large-scale field of the G2 dwarf HD 190771 ( $0.96 M_{\odot}$ ,  $T_{\text{eff}} = 5834$  K) (Morgenthaler et al., 2011, Petit et al., 2009). However, the variability of the large-scale field of HD 190771 is more complex as the polarity reversal in the azimuthal field reported by Petit et al. (2009) is not detected in subsequent epochs. Instead polarity reversal is reported in the radial component of the magnetic field in the subsequent epochs as shown by Morgenthaler et al. (2011). Polarity reversals of the large-scale field have been detected only for a select few cool stars, out of which none exhibit a magnetic cycle period equivalent to the star's chromospheric cycle period.

This chapter investigates the variability of the large-scale magnetic field geometry of the solar-type K5 dwarf 61 Cyg A, using a time series of spectropolarimetric observations over nine years. We also investigate the correlation between its mean magnetic field, chromospheric activity, and coronal activity. The stellar parameters of 61 Cyg A are discussed in Section 4.2, followed by instrumental setup and data reduction in Section 4.3. Section 4.4 covers both direct and indirect field detection. The large-scale magnetic geometry is discussed in Section 4.5, followed by the long-term evolution of the magnetic and activity cycle in Section 4.6. The results are discussed in Section 4.7 and finally the summary in Section 4.8.

### 4.3. Physical properties of 61 Cyg A

A solar-type dwarf of spectral type K5, 61 Cyg A forms the well known visual binary 61 Cyg together with the K7 dwarf 61 Cyg B. The binary 61 Cyg is a northern system with a

**Table 4.1.:** Summary of the physical parameters of 61 Cyg A.

Parameters	HD 201091	References
Effective temperature, $T_{\text{eff}}(\text{K})$	$4545 \pm 40$	this work
Spectral type	K5V	1
$\log g$	$4.75 \pm 0.10$	this work
Radius, $R_{\odot}$	$0.665 \pm 0.005$	1
Mass, $M_{\odot}$	0.66	1
Rotation period, days	$35.7 \pm 1.9$	this work
..	$34.2 \pm 3.7$	this work
inclination	$70^{\circ}$	this work
B-V	1.069	2
Age, Gyr	6.0	3
..	3.6	4
..	2.0	5
..	1.331	6

**References** (1) Kervella et al. (2008); (2) Perryman et al. (1997); (3) Kervella et al. (2008); (4) Mamajek & Hillenbrand (2008); (5) Barnes (2007); (6) Marsden et al. (2014). The rotation period of  $35.7 \pm 1.9$  is derived from chromospheric activity measurements and the period of  $34.2 \pm 3.7$  is derived from ZDI (See text for more details).

semi-major axis of approximately  $24''$  (Malkov et al., 2012). It is the first stellar object to have its parallax measured (Bessel, 1838). 61 Cyg A has a parallax of  $287.13 \pm 1.51$  mas (Perryman et al., 1997) and is at a distance of approximately 3.5 pc. It is a slow rotator with a rotation period of  $35.7 \pm 1.9$  days as shown in Table 4.1, where the rotation period is obtained from long-term chromospheric activity measurements. We also derive a rotation period of  $34.2 \pm 3.7$  days using ZDI (see Section 4.5.3 for more details). 61 Cyg A has a radius of  $0.665 \pm 0.005 R_{\odot}$  (Kervella et al., 2008), where the radius was determined using interferometric data, and is in agreement with the radius of  $0.62 R_{\odot}$  (Takeda et al., 2007) calculated by using a stellar evolution code. Using the same code and stellar evolutionary tracks, Takeda et al. (2007) also determined a mass of  $0.660 M_{\odot}$ . The angular diameter of  $1.775 \pm 0.013$  mas (Kervella et al., 2008) and the bolometric flux of  $0.3844 \times 10^{-9}$  (Mann et al., 2013) can be used to determine a  $T_{\text{eff}}$  of 4374 K. Applying to the highest S/N spectra an automatic spectral classification tool,<sup>1</sup> the photosphere temperature, logarithmic gravity, and metallicity of 61 Cyg A are respectively equal to  $4545 \pm 40$  K,  $4.75 \pm 0.10$ , and  $-0.18 \pm 0.05$ . The  $T_{\text{eff}}$  from this analysis agrees with the literature value of  $4525 \pm 140$  K (Takeda et al., 2007) with improved accuracy. Using the radius and rotation period from Table 4.1, an equatorial  $v_e$  of  $0.94 \text{ km s}^{-1}$  is determined. This suggests that the  $v \sin i$  of 61 Cyg A should be  $\leq 0.94 \text{ km s}^{-1}$ . A chromospheric age of 1.331 Gyr was determined by Marsden et al. (2014) from the activity age relationship of Wright et al. (2004). Using chromospheric activity and rotation relation, Mamajek & Hillenbrand (2008) determine an age of 3.6 Gyr. In contrast,

<sup>1</sup>The spectral classification tool developed by J. F. Donati, is inspired from that of Valenti & Fischer (2005) and is discussed in a previous paper (Donati et al., 2012)

Kervella et al. (2008) predicted an age of approximately 6 Gyr using evolutionary models combined with interferometric radius measurements. The age estimates of 61 Cyg A from gyrochronology puts its age at approximately 2 Gyr (Barnes, 2007). The stellar parameters of 61 Cyg A are summarised in Table 4.1.

61 Cyg A is a moderately active star and was included in the long-term Mount Wilson survey (Duncan et al., 1991). It was discovered to exhibit an activity cycle of  $7.3 \pm 0.1$  yrs (Baliunas et al., 1995). 61 Cyg A was also included in the Lowell Observatory long-term survey, where it was classified as a star with solar-type variability (Hall et al., 2007, Lockwood et al., 2007). A coronal activity cycle of approximately seven years has also been detected for 61 Cyg A (Robrade et al., 2012) using X-ray observations, where the coronal activity cycle is in phase with the chromospheric activity cycle.

## 4.4. Instrumental setup and data reduction

### 4.4.1. Optical data

The spectropolarimetric data was collected as part of the BCOOL collaboration<sup>2</sup> using the NARVAL spectropolarimeter, at the 2.0 m Telescope Bernard Lyot at Pic du Midi Observatory. NARVAL is equipped with a cross dispersed echelle spectrograph, which is a twin of the ESPaDOnS spectropolarimeter (Donati, 2003) at the 3.6 m Canada-France-Hawaii telescope (CFHT). It covers the full optical wavelength range from 370 nm to 1000 nm, with a resolving power of approximately 65,000 (Aurière, 2003). The spectropolarimetric observations of 61 Cyg A were obtained by combining four successive sub-exposures, taken with different half wave rhomb angles. The data is reduced on-site by using a fully automated reduction package, Libre-ESPRIT, which generates both intensity (Stokes  $I$ ) and circularly polarised (Stokes  $V$ ) spectra. Libre-ESPRIT is based on the reduction pipeline ESPRIT developed by Donati et al. (1997). The reduction package also calculates a diagnostic Null profile, which is a control profile, by combining the four sub-exposures in such a way that any polarisation signal is cancelled out. The output from the reduction pipeline is continuum normalised. Table A.3 shows the journal of observations of 61 Cyg A.

Seven data sets comprising seven epochs spanning nine years of both Stokes  $I$  and  $V$  spectra, were obtained covering epochs 2007.59, 2008.64, 2010.55, 2012.54, 2013.61, 2014.61, and 2015.54. Each epoch contains between nine and sixteen spectra. The spectropolarimetric data from the 2012.54 epoch was discarded due to polarisation anomalies in one of the polarisation rhombs at NARVAL during 2011-2012<sup>3</sup>. The azimuthal angle of the rhomb was wrong during that epoch, leading to incorrect polarisation measurements.

For active cool stars, Zeeman-induced circular polarisation has too low an amplitude to be detected in individual spectral lines. Hence, the technique of least square deconvolution

---

<sup>2</sup><http://bcool.ast.obs-mip.fr/Bcool>

<sup>3</sup><http://spiptbl.bagn.obs-mip.fr/Actualites/Anomalies-de-mesures>

(LSD) is applied to the spectra of 61 Cyg A. LSD is a multiline technique which assumes a similar line profile for all magnetically sensitive lines in a spectra and generates an averaged line profile by deconvolving the stellar spectra to a line mask (Donati et al., 1997, Kochukhov et al., 2010). We use a K5 mask consisting of approximately 12,000 lines to compute the LSD Stokes  $I$  and Stokes  $V$  profiles of 61 Cyg A. The LSD technique used in this chapter is detailed in Marsden et al. (2014).

#### 4.4.2. X-ray data

61 Cyg A is a strong X-ray source and has been continuously monitored with *XMM-Newton* since 2002 with a cadence of two observations a year (see e.g. Hempelmann et al. (2006) and Robrade et al. (2012)). Therefore, in order to check for periodicity in X-ray luminosity all public data sets from the *XMM-Newton* Science Archive was obtained. Data reduction was performed with the *XMM-Newton* Science Analysis System version 10.0, and XSPEC 12.7.1. In order to avoid contamination from 61 Cyg B, source photons were extracted with a  $15''$  aperture, while background levels were estimated with a  $45''$  aperture in source-free regions. Time intervals during which obvious flaring occurred were omitted. The spectra of all three EPIC detectors (MOS 1&2 and PN) were then fitted simultaneously in the 0.2-2.0 keV range with a three-temperature APEC model.

### 4.5. Magnetic field detection: direct and indirect approach

#### 4.5.1. Mean longitudinal magnetic field

We measure the line-of-sight component of the magnetic field, averaged over the stellar surface, using Stokes  $V$  and Stokes  $I$  LSD profile. The mean longitudinal field is measured from the Stokes  $V$  and  $I$  profile (Donati et al., 1997) as shown in equation 4.1.

$$B_l(\text{G}) = -2.14 \times 10^{11} \frac{\int vV(v)dv}{\lambda_0 g c \int (I_c - I(v))dv} \quad (4.1)$$

where  $B_l$  represents the mean longitudinal magnetic field of 61 Cyg A in Gauss,  $\lambda_0 = 630$  nm is the central wavelength of the LSD profile,  $g = 1.22$  is the Landé factor of the line list,  $c$  is the speed of light in  $\text{kms}^{-1}$ ,  $v$  is the radial velocity in  $\text{kms}^{-1}$ , and  $I_c$  is the normalised continuum intensity. A velocity range of  $\pm 20 \text{ kms}^{-1}$  from the line centre was used. The velocity window was selected so that the entire signal could be included. If a smaller integration window is used, then the wings of the signal are ignored which may result in an underestimated value of  $B_l$ . The magnetic field in the Null profile ( $N_l$ ) was also calculated. The error estimates were made by propagating the uncertainties calculated by the reduction pipeline, as mentioned in Marsden et al. (2014). Table A.4 shows the values of  $B_l$ ,  $N_l$ , and the associated uncertainties for each observation.

#### 4. A solar-like magnetic cycle on the mature K-dwarf 61 Cygni A (HD 201091)

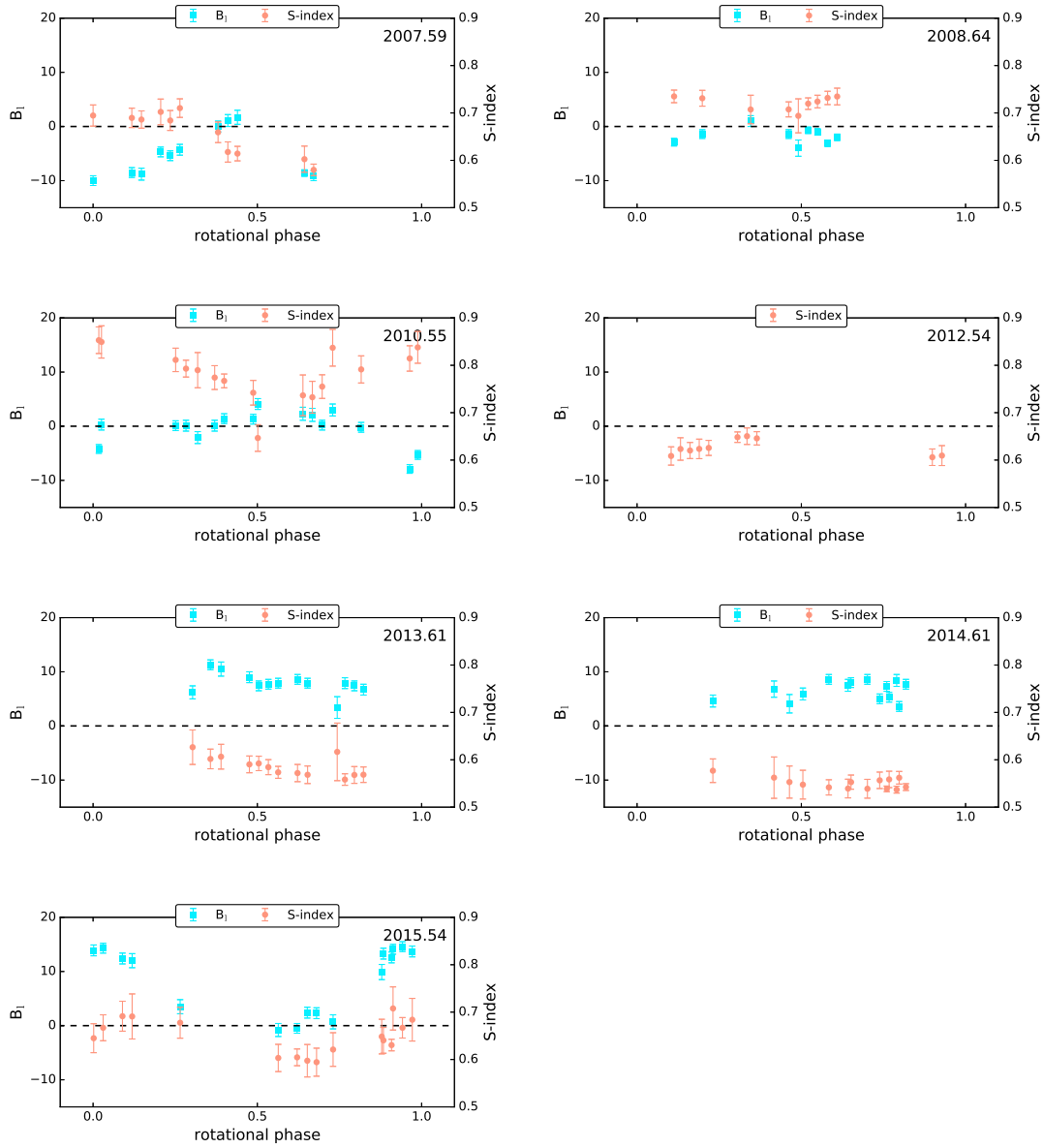


**Figure 4.1.:** Variability of the longitudinal field ( $B_l$ ) (Left y-axis) and S-index (Right y-axis) as a function of rotational phase for each epoch (2007.59, 2008.64, 2010.55, 2012.54, 2013.61, 2014.61 and 2015.54). For epoch 2012.54 only the S-index is plotted, as the Stokes  $V$  observations were not available (see Section 4.3.1). The subplots are all on the same scale for easier comparison between epochs, and the dashed line represents  $B_l=0$ . The scale was chosen based on the minimum and maximum value.

#### 4.5.2. Chromospheric activity as a proxy of magnetic activity

61 Cyg A is known to exhibit cyclic chromospheric activity of approximately seven years (Baliunas et al., 1995). In order to investigate the chromospheric activity of 61 Cyg A, we

monitored the fluxes in three chromospheric indicators: Ca II H&K, H $\alpha$  and the Ca II infrared triplet. These three chromospheric indicators are well known proxies of stellar activity, where the different indicators have different sensitivities to the various chromospheric features such as plages, networks, flares and filaments (Meunier & Delfosse, 2009). Hence, it is important to explore the different chromospheric tracers to obtain as complete a picture as possible of the chromosphere of an active cool star.

### S-index

The S-index has been one of the most widely used proxies of magnetic activity since its introduction in the long-term Mount Wilson survey (Baliunas et al., 1995, Duncan et al., 1991, Wilson, 1978). The S-index of 61 Cyg A is measured by using two triangular band passes with a FWHM of 0.1 nm, centred at the line cores of the Ca II K and H line at 393.3663 nm and 396.8469 nm respectively. The fluxes in the nearby continuum are measured by using two 2 nm wide rectangular band passes at the blue and red side of the K and H lines at 390.107 nm and 400.107 nm respectively (Duncan et al., 1991, Wright et al., 2004). In order to calibrate our measurements to the original Mount Wilson scale, we use the calibration coefficients calculated by Marsden et al. (2014), which is used in the S-index formula as shown in equation 4.2,

$$\text{S-index} = \frac{\alpha F_H + \beta F_K}{\gamma F_R + \delta F_V} + \phi \quad (4.2)$$

where  $F_H$ ,  $F_K$ ,  $F_V$ , and  $F_R$  are the flux in H, K, R, and V bands and  $\alpha = 12.873$ ,  $\beta = 2.502$ ,  $\gamma = 8.877$ ,  $\delta = 4.271$ , and  $\phi = 1.183\text{e-}03$  are the calibration coefficients respectively. The uncertainties associated with the S-index measurements are obtained by carrying out error propagation and are tabulated in Table A.4.

Fig. 4.1 shows the rotational variability of both the  $B_l$  and the S-index as a function of the rotational phase for each epoch, to study variability on the rotation timescale. Overall, 61 Cyg A exhibits a stronger rotational variability in its longitudinal magnetic field during epochs 2007.59, 2010.55 and 2015.54 compared to epochs 2008.64, 2013.61 and 2014.61. During the entire observational time span, the longitudinal field  $B_l$  shows a change in sign which indicates that the field is non-axisymmetric. Except in epochs 2013.61 and 2014.61, which show signs of a more axisymmetric field. The S-index exhibits low rotational dependence, indicating a simple magnetic geometry. However, one should be careful in interpreting the results because the rotational variations might be hidden due to poor phase coverage in certain epochs such as 2012.54. The longitudinal field could not be measured for epoch 2012.54, due to the unavailability of Stokes V observations as already mentioned in the previous Section.

61 Cyg A was part of the original Mount Wilson survey and was observed for three decades at the Mount Wilson observatory from 1961 to 1991 (Baliunas et al., 1995). A continuation of the Mount Wilson survey is being currently carried out at the Lowell observatory (Hall et al., 2007) and all available S-index data of 61 Cyg A together with NARVAL measurements are shown in Fig. 4.2. It shows the temporal variation of the S-index of 61 Cyg A

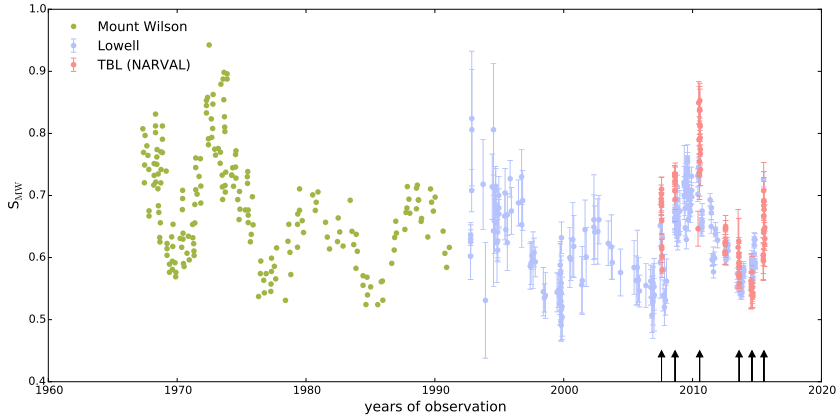


**Figure 4.2.:** Long-term chromospheric activity of 61 Cyg A shown as S-index, which is calibrated to the Mount Wilson S-index. The arrow marks represent epochs for which the large-scale field map is reconstructed using ZDI.

calibrated to the Mount Wilson scale over a time span of 48 years. At the beginning of the observational data in epoch 2007.59, 61 Cyg A exhibits low activity and it increases to its maximum during epoch 2010.55. The chromospheric activity is low in epoch 2013.61, which indicates it is close to activity minimum. The activity in epoch 2014.61 is also very low but it increases again during epoch 2015.54. An activity cycle period of  $7.2 \pm 1.3$  yrs was measured by taking a generalised Lomb-Scargle periodogram (Lomb, 1976, Scargle, 1982, Zechmeister & Kürster, 2009) on all available S-index data. This cycle period agrees with the activity cycle period of  $7.3 \pm 0.1$  yrs, measured using only the Mount Wilson data (Baliunas et al., 1995).

### H $\alpha$ -index

We measured the variability of the chromospheric activity of 61 Cyg A using H $\alpha$  as an activity tracer for each epoch of this analysis. We employed the technique of Gizis et al. (2002), where a rectangular band pass of 0.36 nm width was used at the H $\alpha$  line at 656.285 nm. Two rectangular band passes  $N_{H\alpha\text{blue}}$  and  $N_{H\alpha\text{red}}$  of 0.22 nm width were used to measure the nearby continuum, as shown in equation ??,

$$\text{H}\alpha\text{-index} = \frac{H_{\alpha}}{H_{\text{blue}} + H_{\text{red}}} \quad (4.3)$$

where  $H_{\alpha}$ ,  $H_{\text{blue}}$ , and  $H_{\text{red}}$  refers to different band passes used.

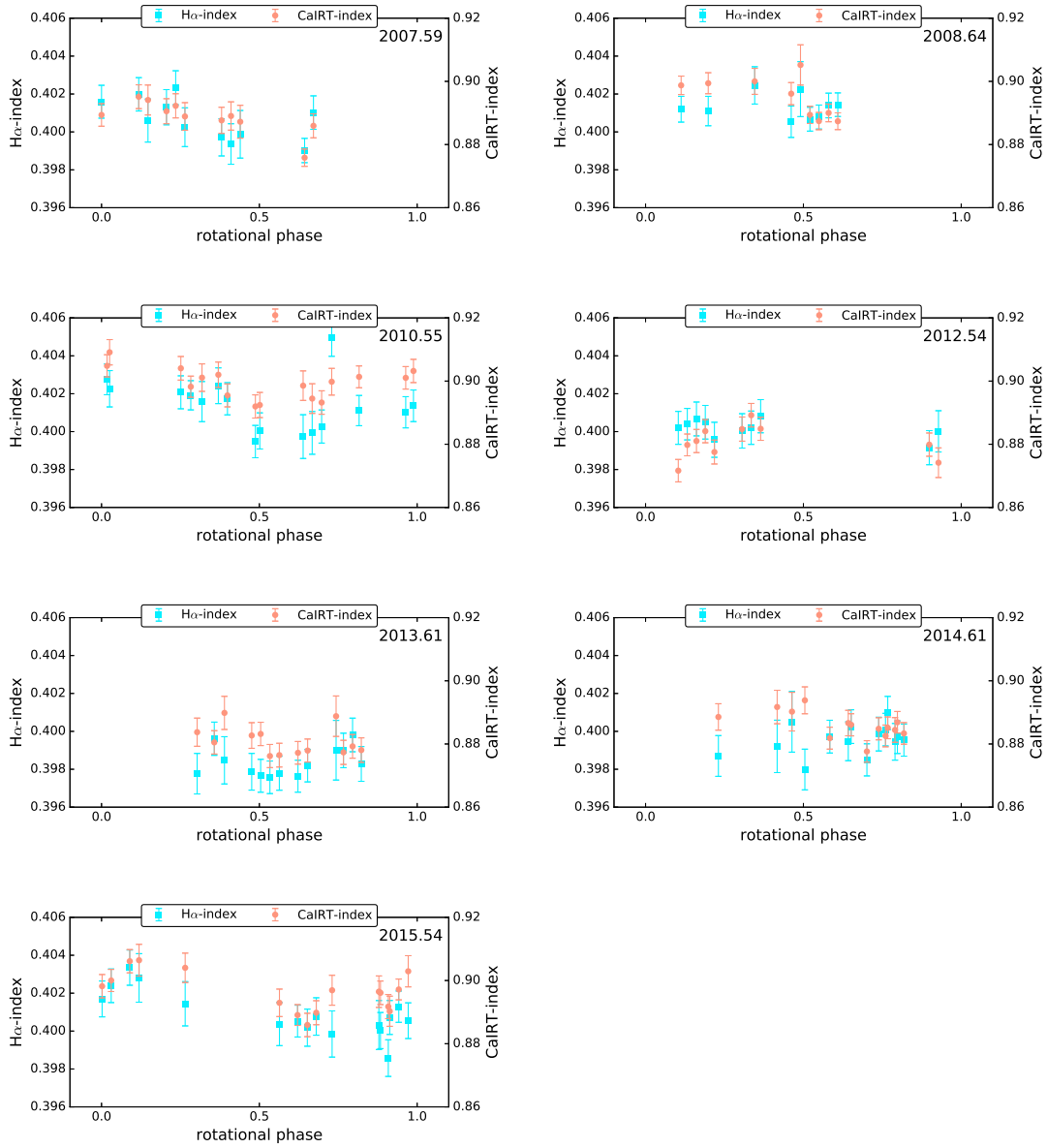


**Figure 4.3.:** Same as Fig. 4.1 for  $H\alpha$ -index (Left y-axis) and CaIRT-index (Right y-axis). The scales are chosen based on the minimum and maximum value.

### CaIRT-index

The CaIRT-index of 61 Cyg A was measured by taking 0.2 nm wide rectangular band passes centred at the Ca II triplet lines at 849.8023 nm, 854.2091 nm, and 866.241 nm respectively. The nearby continuum is measured by taking two 0.5 nm band passes  $N_{\text{IRred}}$ , and  $N_{\text{IRblue}}$  at 870.49 nm, and 847.58 nm respectively (Marsden et al., 2014), as shown in equation 4.4,

$$\text{CaIRT-index} = \frac{\text{IR1} + \text{IR2} + \text{IR3}}{\text{IR}_{\text{red}} + \text{IR}_{\text{blue}}} \quad (4.4)$$

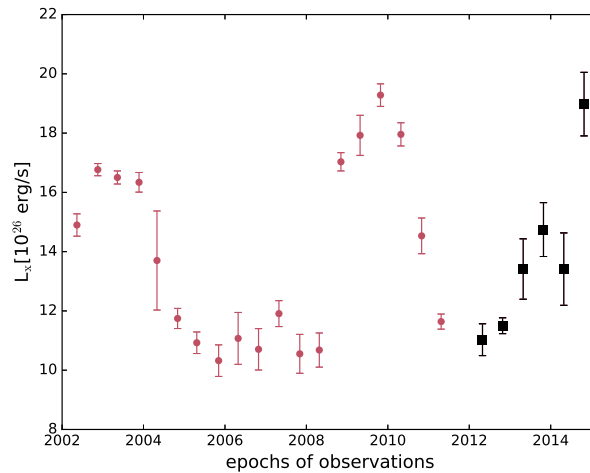


**Figure 4.4.:** Variation of X-ray luminosity of 61 Cyg A determined through *XMM-Newton* observations. The black squares show new previously unpublished results.

where IR1, IR2, IR3 represent flux in the Ca II infra-red triplet lines, The continuum flux is represented by IR<sub>red</sub> and IR<sub>blue</sub> respectively.

The H $\alpha$  and Ca IRT lines are in absorption throughout the entire observational period. The H $\alpha$ -index variability as a function of the rotational phase is shown in Fig. 4.3. The rotational variability of the CaIRT-index is also shown in Fig. 4.3. Surprisingly the H $\alpha$  and Ca II IRT indices do not show the strong variations shown by the S-index. This might indicate that the magnetic field is not strong enough for these lines to go into emission explaining such low variations as compared to the S-index. The uncertainties are obtained by carrying out error propagation and are shown in Table A.4.

### Coronal activity

The X-ray luminosity variation of 61 Cyg A is shown in Fig. 4.4, where the data up to end of 2011 were previously published by Robrade et al. (2012) and the results from 2012 onward are derived for the first time here. While comparison to the results of Robrade et al. (2012) yields minor discrepancies caused by the different data fitting approaches, the overall picture is consistent. A clear cyclic variation in the X-ray luminosity is recovered with a cycle period of  $6.6 \pm 0.5$  years. This is in good agreement with the chromospheric cycle of  $7.2 \pm 1.3$  years.

### Correlation between activity indicators and longitudinal field

As shown in Fig. 4.5, a possible weak anti-correlation between the absolute value of the longitudinal magnetic field  $|B_l|$  and the S-index is detected. The absolute values of  $B_l$  are the weakest in epoch 2010.55, when the chromospheric activity is at a maximum and are the strongest close to minimum chromospheric activity. The average of the absolute longitudinal

magnetic field ( $|B_l|$ ) per epoch is strongest in epoch 2015.54 with  $9.3 \pm 5.9$  G, and is weakest in epoch 2010.55 with  $0.6 \pm 3.1$  G. On the contrary, strong correlation is detected between the three chromospheric activity indicators as shown in Fig. 4.5. The CaIRT-index exhibits a slightly stronger correlation with the S-index ( $r=0.7$ ) compared to the  $H\alpha$ -index ( $r=0.6$ ), which is not surprising as those two indicators are sensitive to similar chromospheric features. A strong correlation between the S-index and the CaIRT-index was detected for HN Peg, as shown in Chapter 3. Similar strong correlations were also detected for the G dwarf  $\xi$  Bootis A by Morgenthaler et al. (2012). Correlation between the  $\log R'_{HK}$  and CaIRT-index was also studied for 170 solar-type stars as part of the BCool snapshot survey Marsden et al. (2014). The  $\log R'_{HK}$  is also an indicator of stellar activity where the photospheric contribution is corrected for the S-index Wright et al. (2004).

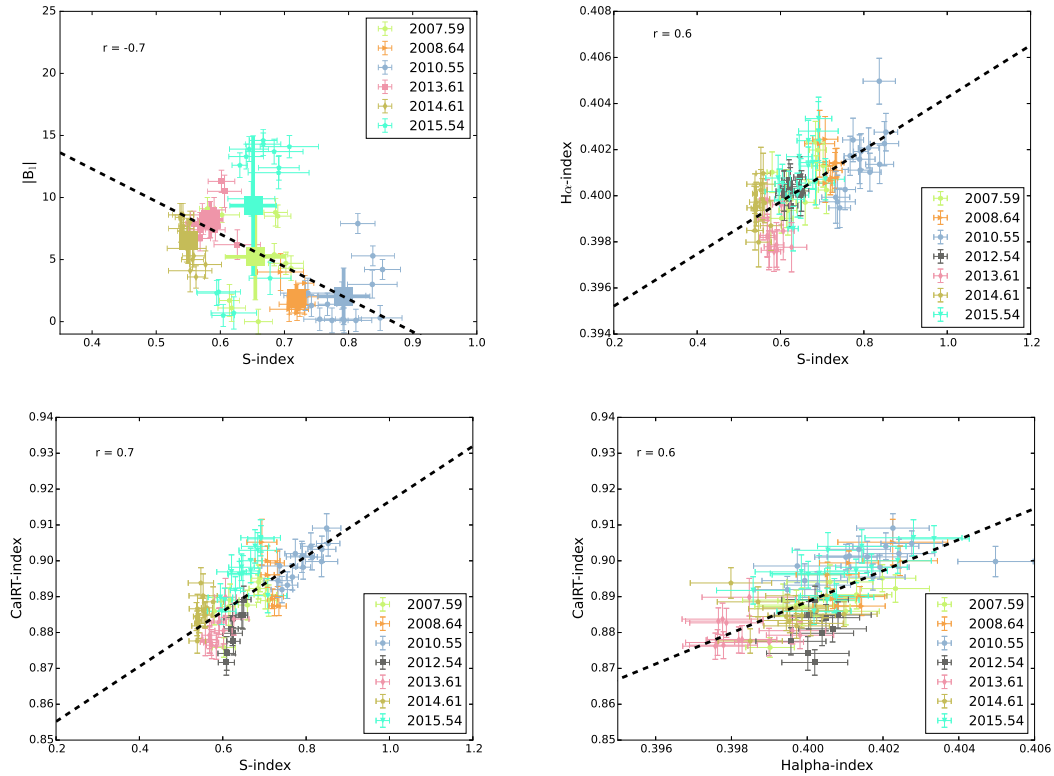


**Figure 4.5.:** Correlation between the different activity indicators and the longitudinal field  $|B_l|$ , where the dashed line represents least square fit to the data and the Pearson's  $r$  is shown in the plot. *Top Left:* Anti-correlation between S-index and  $|B_l|$  over six epochs of observations. The bold crosses represent the mean and standard deviation as dispersion. Only the mean values are included in the fit. *Top Right:* Plot showing the correlation between S-index and  $H\alpha$ -index over seven epochs of observations. *Bottom Left:* Correlation between S-index and CaIRT-index over seven epochs of data. *Bottom Right:* Correlation between  $H\alpha$ -index and CaIRT-index over seven epochs of data.

## 4.6. Large-scale magnetic field geometry

The large-scale surface magnetic geometry of 61 Cyg A is reconstructed using the ZDI technique. ZDI is an inverse tomographic technique which reconstructs the stellar magnetic geometry from a time series of Stokes  $V$  LSD profiles using maximum entropy as a regularisation technique (Skilling & Bryan, 1984). The ZDI version used in this chapter reconstructs the magnetic geometry into its poloidal (potential field) and toroidal (non-potential field) components expressed as spherical harmonic decomposition (see Donati et al., 2006).

If the total surface magnetic field is a combination of poloidal and toroidal field, it can be formalised into three field components  $B_r$ ,  $B_\theta$ , and  $B_\phi$ .  $B_r$  is the radial component of the field and is entirely poloidal, described by the spherical harmonics coefficient  $\alpha_{l,m}$ , where  $l$  and  $m$  are the order and degree respectively.  $B_\theta$  is the meridional component of the total field and  $B_\phi$  is the azimuthal component of the total field.  $B_\theta$  and  $B_\phi$  can be described by a combination of the spherical harmonics coefficients  $\beta_{l,m}$  and  $\gamma_{l,m}$  (Donati et al., 2006, see Section 5.1). The order of the spherical harmonics coefficients determines if the field is simple dipolar or complex, and the degree determines if the field is axisymmetric or non-axisymmetric. For example,  $l = 1, m = 0$  denotes the axisymmetric dipolar field. The quadrupolar and octopolar modes are denoted by higher order  $l = 2$  and  $l = 3$  respectively. The surface magnetic map and the associated Stokes  $V$  spectra of a star can be derived using the spherical harmonics coefficients. ZDI tackles the inverse problem and reconstructs the large-scale surface magnetic field geometry by comparing model Stokes  $V$  spectra to the observed Stokes  $V$  spectra.

For 61 Cyg A a stellar model of 5000 grid points was used, where each grid point is associated with both a local Stokes  $V$  and Stokes  $I$  profile. A solar-type limb darkening law is used in the stellar model and synthetic Stokes  $V$  profiles are computed for all rotational phases. Each of these local Stokes  $V$  profiles are calculated under the weak field assumption and a uniform Stokes  $I$  profile is assumed over the entire photosphere. Using maximum entropy as a regularisation scheme (Skilling & Bryan, 1984), ZDI reconstructs  $\alpha_{l,m}$ ,  $\beta_{l,m}$ , and  $\gamma_{l,m}$  by iteratively comparing the synthetic Stokes  $V$  profiles to the observed Stokes  $V$  profiles.

### 4.6.1. Vector magnetic field

61 Cyg A exhibits chromospheric variability on rotational timescales, indicating a high stellar inclination. An inclination angle of  $70^\circ$  is chosen, which together with a rotation period of 34.2 days and a stellar radius of  $0.665 R_\odot$ , results in a  $v \sin i$  of  $0.92 \text{ kms}^{-1}$ . This  $v \sin i$  is consistent with the  $v_e$  of  $0.94 \text{ kms}^{-1}$  mentioned in Section 4.2. We therefore use the  $v \sin i$  of  $0.92 \text{ kms}^{-1}$  and an inclination angle of  $70^\circ$  in our magnetic field reconstructions. A range of spherical harmonics orders  $l_{\max}=5,7,9,11$  were tested to reconstruct the magnetic maps. For all epochs except 2010.55 and 2015.54, the target  $\chi^2$  was achieved for  $l_{\max} = 7$ . Using  $l_{\max} \geq 7$  does not improve the  $\chi^2$  or the fit to the spectra at epochs 2007.59, 2008.64, 2013.61, and 2014.61. However, for epochs 2010.55 and 2015.54, the best  $\chi^2$  fit was obtained for

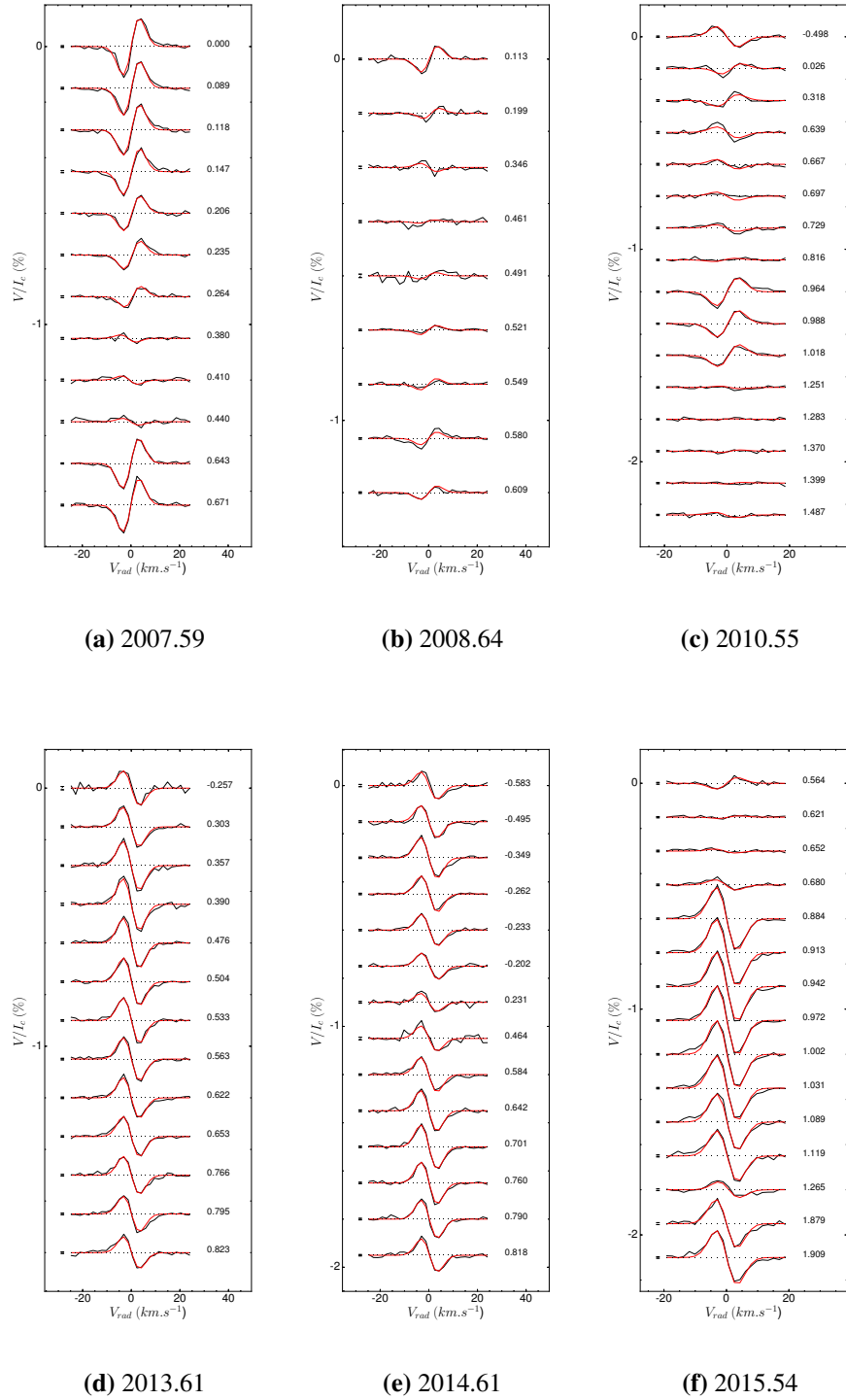


**Figure 4.6.:** Time series of LSD Stokes  $V$  spectra of 61 Cyg A, where Top row (from left to right) represents epochs 2007.59, 2008.64, and 2010.55, and the bottom row shows (left to right) epochs 2013.61, 2014.61, and 2015.54. The observed spectra is shown in black and the corresponding fit is shown in red. For each observed spectra, the phase of the rotational cycle is shown on the right, and on the left side of each plot  $1\sigma$  error is shown. For the purpose of clarity successive Stokes  $V$  profiles are shifted vertically and the scale is expanded by a factor of two.

$l_{\max} \geq 11$ . To make comparisons between the epochs the  $l_{\max}$  was set to 11 throughout the analysis. Differential rotation was also included in the large-scale field reconstructions (see Section 4.5.3 for more details).

Figure 4.6 shows the Stokes  $V$  LSD time series of 61 Cyg A for the entire observational time span. The fit between the model Stokes  $V$  profiles and observed Stokes  $V$  profiles was obtained with a reduced  $\chi^2$  of 1.0 for epoch 2007.59. A reduced  $\chi^2$  of 1.1 was achieved for epochs 2008.64, 2013.61, and 2014.61. For epochs 2010.55 and 2015.54 the observed fit was obtained with a reduced  $\chi^2$  of 1.2 and 1.5 respectively. It is evident from Fig. 4.6 that during epoch 2007.59, which is around activity minimum, the time series of Stokes  $V$  profiles is dominated by a single sign. The Stokes  $V$  profiles in epoch 2010.55 are not dominated by a single orientation. The high variability shown by the Stokes  $V$  profile in 2010.55 is caused by a complex magnetic field geometry. This complexity of the field is likely to make the impact of differential rotation more apparent in this epoch. In the following three epochs (2013.61, 2014.61, and 2015.54) the Stokes  $V$  profiles flip sign and are dominated again by a single orientation. This evolution of the Stokes  $V$  time series indicates that the surface magnetic field geometry is strongly evolving, with a single polarity field during low activity and a more complex field during strong activity.

Since the maximum entropy reconstruction does not allow error calculations of our magnetic maps, we employ the technique described by [Petit et al. \(2008\)](#), where a range of magnetic maps were calculated for the wide range of input stellar parameters used in our ZDI code. These input parameters are varied within their error bars and the resulting dispersion is taken as error bars, as shown in Table 4.2.

### Epoch 2007.59

The large-scale surface magnetic field of 61 Cyg A at epoch 2007.59 exhibits a simple dipolar magnetic geometry. Figure 4.7 shows this large-scale magnetic field geometry reconstructed into three components: radial, azimuthal and meridional. The radial component of the magnetic field exhibits strong negative-polarity magnetic regions at higher latitudes and positive-polarity magnetic field at lower latitudes. On the other hand, the azimuthal field component is dominated by two positive polarity magnetic field regions between the pole and lower latitudes. The  $B_{\text{mean}}$ , which is the average of the surface magnetic field from the reconstructed maps, is  $12 \pm 3$  G. The poloidal magnetic field dominates, accounting for  $93 \pm 5$  % of the magnetic energy seen in Stokes  $V$ . The fraction of the magnetic energy in other field components is shown in Table 4.2. As shown in Fig. 4.8, almost 100% of the poloidal magnetic energy is stored in the lower order spherical harmonics modes,  $l \leq 3$ .

### Epoch 2008.64

In epoch 2008.64 the large-scale magnetic field in the radial component exhibits a similar magnetic geometry as reconstructed for epoch 2007.59, shown in Fig. 4.7. However, the mean magnetic field ( $B_{\text{mean}}$ ) is weaker than in the previous epoch, as shown in Table 4.2,

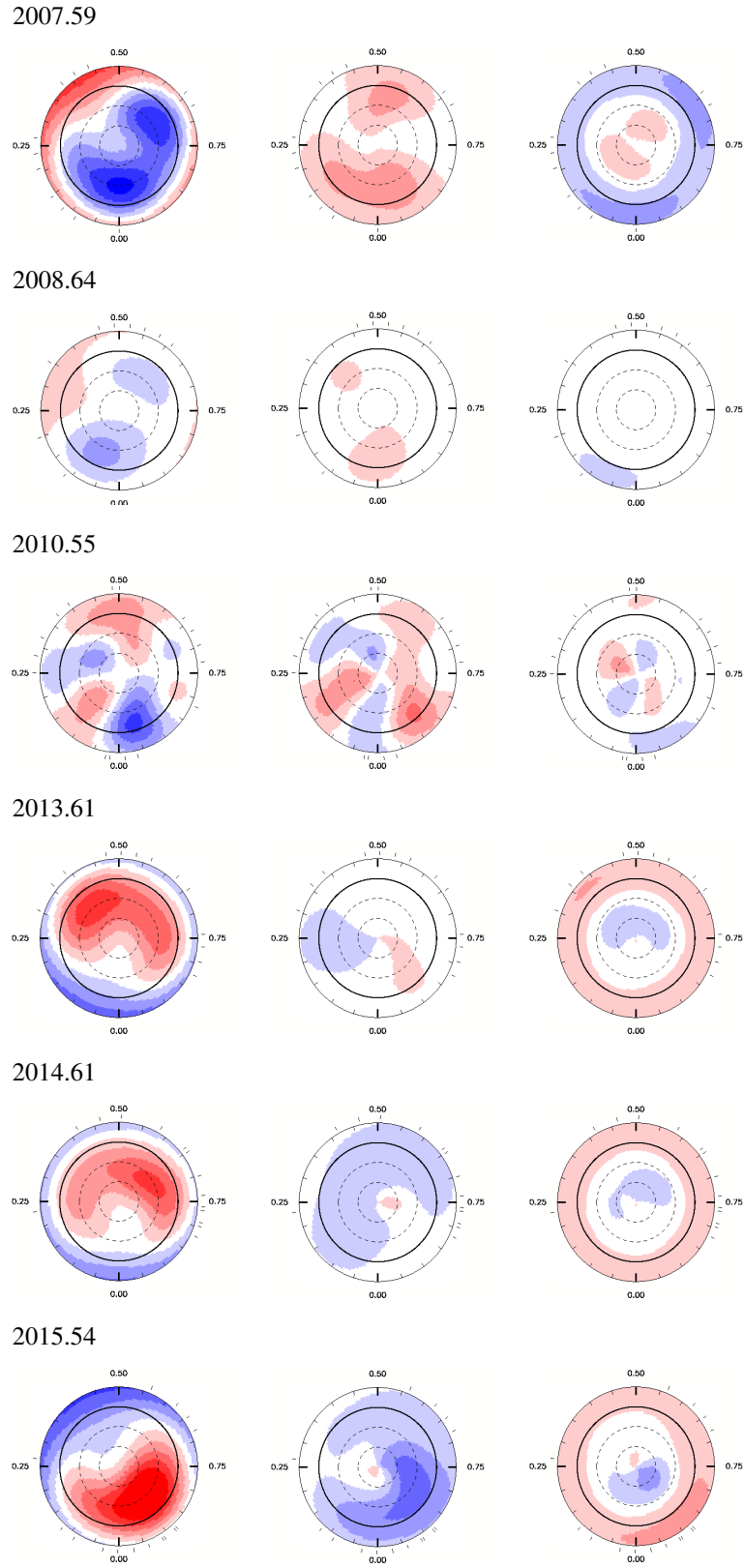


**Figure 4.7.:** Surface magnetic geometry of 61 Cyg A over six observational epochs (2007.59, 2008.64, 2010.55, 2013.61, 2014.61 and 2015.54). The three columns represent the radial, azimuthal, and the meridional component of the large-scale field. The star is shown in flattened polar projection down to latitudes of  $-30^\circ$ , where the dark line depicts the stellar equator.

where  $B_{\text{mean}}$  is  $3 \pm 1$  G. In the azimuthal field component the positive polarity magnetic regions seen in the previous epoch are almost non-existent, as shown in Fig. 4.7. The magnetic field is predominantly poloidal, constituting  $92 \pm 2$  % of the magnetic energy. The dipolar component of the poloidal field accounts for  $56 \pm 5$  % of the poloidal magnetic energy. As in the previous epoch, the lower order modes ( $l \leq 3$ ) account for almost 100% of the poloidal magnetic energy budget as shown in Fig. 4.8.

#### Epoch 2010.55

The large-scale magnetic field of 61 Cyg A changes dramatically in epoch 2010.55. The high-latitude negative polarity field reconstructed in epoch 2007.59 is absent from this epoch and the radial field component is dominated by a more complex magnetic geometry between the equator and the poles, as shown in Fig. 4.7. The azimuthal field component also exhibits a more complex geometry compared to previous epochs as shown in Fig 4.7. The averaged  $B_{\text{mean}}$  for epoch 2010.55 is  $5 \pm 2$  G, which is still weaker than epoch 2007.59, as shown in Table 4.2. The poloidal field dominates and constitutes  $87 \pm 3$  % of the magnetic energy. Only  $19 \pm 6$  % of the poloidal field is dipolar,  $21 \pm 5$  % is quadrupolar and  $44 \pm 13$  % of the poloidal field is reconstructed into its octopolar component, as shown in Table 4.2. The field is also the least axisymmetric in this epoch. Unlike previous epochs, a few % of the poloidal magnetic field is also distributed in the higher order spherical harmonics modes, as shown in Fig. 4.8. The percentage of the magnetic field reconstructed into its toroidal component is higher at this epoch when compared to the previous epochs.

#### Epoch 2013.61

The large-scale magnetic field geometry at epoch 2013.61 is shown in Fig. 4.7, where higher latitude magnetic regions are reconstructed in the radial field component with opposite polarity, as seen in epochs 2007.59 and 2008.64. The azimuthal field component exhibits mixed polarity but it is weak and almost non-existent, as shown in Fig. 4.7. The mean magnetic field derived from the magnetic maps ( $B_{\text{mean}} = 9 \pm 6$  G) is stronger than the previous two epochs. The poloidal component comprises  $99^{+1}_{-3}$  % of the magnetic energy, as shown in Table 4.2. The poloidal magnetic field is  $80 \pm 9$  % dipolar. The distribution of the magnetic field is primarily concentrated at the lower spherical harmonics modes (dipolar, quadrupolar, and octopolar) as shown in Fig. 4.8.

#### Epoch 2014.61

The strong positive field in epoch 2013.61 is also reconstructed in the radial component in epoch 2014.61, as shown in Fig. 4.7. The azimuthal field as shown in Fig. 4.7, is reconstructed as a band of negative-polarity magnetic field at the surface of the star, where the field is of opposite polarity, as seen in epoch 2007.59. Table 4.2 shows the mean magnetic field  $B_{\text{mean}}$  of epoch 2014.61, where the field strength is  $8 \pm 4$  G. The fraction of the magnetic field distributed into the different field components is shown in Table 4.2, where  $93 \pm 4$  % of the magnetic field is reconstructed into its poloidal component.  $78 \pm 8$  % of the poloidal field

**Table 4.2.:** Magnetic properties of 61 Cyg A extracted from the ZDI maps. The columns represent fractional dates, number of observations, radial velocity ( $v_r$ ), mean magnetic field strength ( $B_{\text{mean}}$ ), fraction of magnetic energy reconstructed as the poloidal component, and fraction of poloidal magnetic field stored as dipole, quadrupole, and octopole modes. Finally it also shows the fraction of the total magnetic energy in the axisymmetric component of the magnetic field, and the poloidal axisymmetric fraction (for  $m \leq \frac{l}{2}$ ). The differential rotation parameters  $\Omega_{\text{eq}}$  and  $d\Omega$  are also shown in the last two columns.

Dates	no of obs	$v_r$ (km s $^{-1}$ )	$B_{\text{mean}}$ (G)	poloidal (%tot)	dipole (%pol)	quad (%pol)	oct (%pol)	axi (%tot)	axi (%pol)	$\Omega_{\text{eq}}$ (rad d $^{-1}$ )	$d\Omega$ (rad d $^{-1}$ )
2007.59	12	-65.47 $\pm$ 0.05	12 $\pm$ 3	93 $\pm$ 5	77 $\pm$ 9	17 $\pm$ 7	5 $\pm$ 3	80 $\pm$ 13	80 $\pm$ 17		
2008.64	9	-65.48 $\pm$ 0.05	3 $\pm$ 1	92 $\pm$ 2	56 $\pm$ 5	36 $\pm$ 5	8 $\pm$ 2	56 $\pm$ 10	53 $\pm$ 11		
2010.55	16	-65.48 $\pm$ 0.05	5 $\pm$ 2	87 $\pm$ 3	19 $\pm$ 6	21 $\pm$ 5	44 $\pm$ 13	7 $\pm$ 2	2 $\pm$ 4	0.18 $\pm$ 0.03	0.04 $\pm$ 0.02
2013.61	13	-65.49 $\pm$ 0.05	9 $\pm$ 6	99 $^{+1}_{-3}$	80 $\pm$ 9	16 $\pm$ 7	3 $\pm$ 1	77 $\pm$ 6	77 $\pm$ 6		
2014.61	14	-65.50 $\pm$ 0.05	8 $\pm$ 4	93 $\pm$ 4	78 $\pm$ 8	18 $\pm$ 6	4 $\pm$ 3	81 $\pm$ 7	81 $\pm$ 9		
2015.54	15	-65.52 $\pm$ 0.05	12 $\pm$ 5	87 $\pm$ 5	85 $\pm$ 9	12 $\pm$ 6	2 $\pm$ 1	59 $\pm$ 12	55 $\pm$ 20		

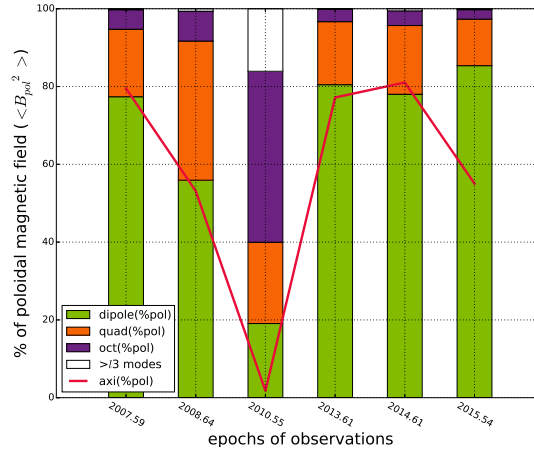


**Figure 4.8.:** Poloidal magnetic field distribution of 61 Cyg A for six epoch of observations.

is in its dipolar component. The magnetic energy budget is spread across the lower spherical harmonics mode  $l \leq 3$ , as shown in Fig. 4.8.

### Epoch 2015.54

During epoch 2015.54 the radial field component exhibits a positive polarity magnetic region between the poles and the equator, together with a negative polarity magnetic field at the equator, as shown in Fig. 4.7. A band of negative polarity magnetic field is reconstructed in the azimuthal component of the magnetic field, as shown in Fig. 4.7. The mean magnetic field  $B_{\text{mean}}$  of  $12 \pm 5$  G is similar to that measured in epoch 2007.59.  $87 \pm 5$  % of the magnetic field is in the poloidal component, as shown in Table 4.2. The percentage of the poloidal field reconstructed into the dipolar component is  $85 \pm 9$  % and, as shown in Fig. 4.8 the poloidal field is distributed across the lower spherical harmonics modes.

### 4.6.2. Evolution of the different multipolar modes over the magnetic cycle

In order to assess the long-term variability of the magnetic field of 61 Cyg A, we consider several ways of paraphrasing the reconstructed magnetic field. First, we measure the vector component of the magnetic field for each epoch, averaged over the stellar surface. The vector radial field component, as mentioned earlier in this Section, is entirely poloidal in nature and the signed value of this component is shown in Fig. 4.9. The field is averaged over the stellar surface for co-latitudes less than 30, which is close to the rotational pole. Here co-latitudes are surface co-latitudes relative to the stellar rotational pole in spherical co-ordinates. The vector azimuthal field, on the other hand, is comprised of both poloidal and toroidal field components in this case. Therefore, the signed azimuthal poloidal field and the signed azimuthal toroidal field are treated separately and calculated by averaging the surface for co-latitudes less than 30. As seen in Fig. 4.9, the poloidal field strength  $B_{\text{pol}}$  in the radial component is weakest in epoch 2010.55 and is stronger during epochs of low

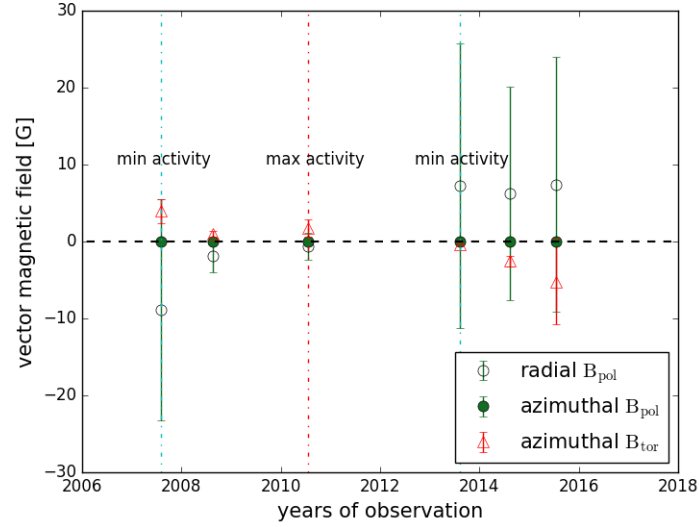


**Figure 4.9.:** Vector component of the poloidal and toroidal magnetic field strength averaged over the stellar surface. The field strengths in the radial and azimuthal components are shown. The horizontal dashed line shows where the field strength is 0. The cyan vertical dashed lines show the epochs with minimum activity and the red vertical dashed line shows the epoch with maximum chromospheric activity.

chromospheric activity. The poloidal component of the azimuthal field is almost negligible for the total azimuthal field. From Fig. 4.9 it is clear that the poloidal field strength on the stellar surface, for co-latitudes  $\leq 30^\circ$ , is mostly radial. The toroidal field strength  $B_{\text{tor}}$  exhibits weak anti correlation to the radial field strength  $B_{\text{pol}}$ .

Since the axisymmetric modes are of great interest for existing dynamo models, we investigate the time evolution of both even and odd axisymmetric modes ( $m = 0$ ) for  $l = 1, 2, 3, 4$ . Figure 4.10 shows the field strength, at the pole of the axisymmetric modes of the poloidal field, for the first four orders of spherical harmonics. The poloidal field strength in the axisymmetric modes is the signed (radial) field strength at the visible rotational pole of the star. The first odd mode  $l=1$ , which is the dipolar mode, exhibits similar behaviour to the full averaged  $B_{\text{pol}}$  in Fig. 4.9. The quadrupolar  $l=2$  mode is anti-correlated with the dipolar mode. The octopolar mode ( $l=3$ ) exhibits correlation with the quadrupolar mode.

Figure 4.11 shows the field strength of only the lowest order ( $l = 1$ ) axisymmetric ( $m = 0$ ) poloidal and toroidal modes. The poloidal field strength is the same as that shown in Fig. 4.10, but only the dipolar mode is plotted. The evolution of the dipolar field is consistent with the polarity reversals of the large-scale radial field shown in Fig. 4.7 and shows strong correlation with the averaged radial poloidal field strength in Fig. 4.9. The signed toroidal field strength is calculated by measuring the strength of the azimuthal component of the toroidal ( $l = 0, m = 0$ ) field, evaluated at the maximum of the toroidal band. The toroidal field strength is anti-correlated with the poloidal field strength in Fig. 4.11.

The uncertainties were estimated using the same technique as described in Section 4.5.1.

### 4.6.3. Differential rotation

Each epoch spanned over multiple weeks; we therefore investigated the effect of differential rotation on the data. In order to investigate the differential rotation parameters of 61 Cyg A, a simple solar-type differential rotation law was incorporated into the ZDI code, as described by [Petit et al. \(2002\)](#),

$$\Omega(l) = \Omega_{\text{eq}} - d\Omega \sin^2 l \quad (4.5)$$

where  $\Omega(l)$  represents the stellar rotation at latitude  $l$ ,  $\Omega_{\text{eq}}$  is the equatorial rotation rate, and  $d\Omega$  is the difference between the rotation rate at the equator and the poles.

We set the  $\chi^2$  to a fixed value and carry out ZDI reconstruction for a wide range of differential rotation parameters  $\Omega_{\text{eq}}$  and  $d\Omega$  in a 2D parameter space. The set of differential rotation parameters for which the minimum information is achieved is then selected, as shown in Fig. 4.12. The uncertainties were calculated by the bootstrap technique, where the input stellar parameters were varied within their error bars and the differential rotation was measured for this wide range of input parameters. The resulting dispersion in the obtained values is considered as the associated uncertainties and is shown in Table 4.2.

To obtain reliable differential rotation parameters, it is necessary to have observations with good phase coverage spread over multiple rotation periods of the star ([Morgenthaler et al., 2012](#), [Petit et al., 2002](#)). Consequently, the differential parameters for 61 Cyg A could only be obtained for epoch 2010.55, as shown in Table 4.2. For epoch 2010.55 a  $\Omega_{\text{eq}}=0.18 \text{ rad d}^{-1}$  and  $d\Omega = 0.04 \text{ rad d}^{-1}$  was obtained. A rotation period  $P_{\text{rot}}$  of  $34.2 \pm 3.7$  days was determined from the differential rotation parameters. This rotation period is in agreement with the rotation period obtained from chromospheric measurements, which is shown in Table 4.1. This  $d\Omega$  and  $\Omega$  value results in a relative horizontal shear ( $\alpha$ ) of 0.2 which is equivalent to the  $\alpha_{\odot} = 0.2$ .

Since the phase coverage of the other epochs was sparse, differential rotation measurements as reliable as those in epoch 2010.55 could not be obtained. The magnetic field geometry is also simple with single polarity dominating the surface in all epochs except 2010.55, making it harder to determine the differential rotation for those epochs. Hence, the differential rotation parameters of 2010.55 was adopted for the rest of the observational epochs.

## 4.7. Long-term evolution of the magnetic and activity cycle

The long-term evolution of the chromospheric indicators and the magnetic field strength is shown in Fig. 4.13. The average value of the different chromospheric activity indicators

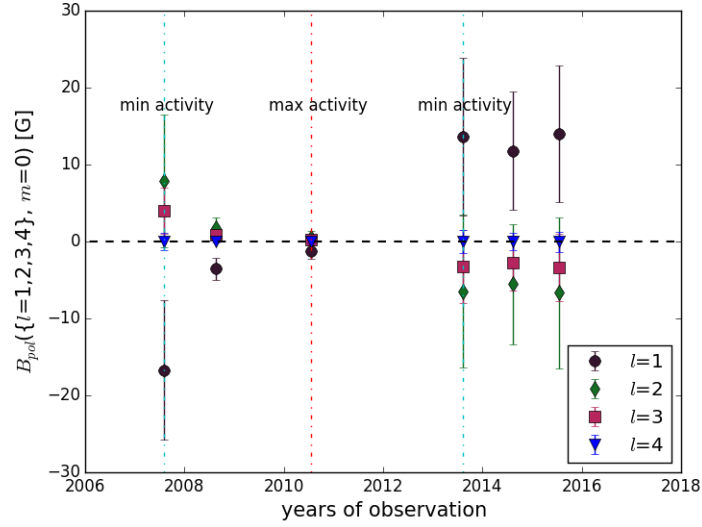


**Figure 4.10.:** Magnetic field strength  $B_r$  at the magnetic pole for the different axisymmetric modes ( $l = \{1, 2, 3\}$ ). The horizontal dashed line represents  $B_r = 0$ , and the vertical dashed lines represents the epochs with minimum and maximum activity as shown in Fig. 4.9.

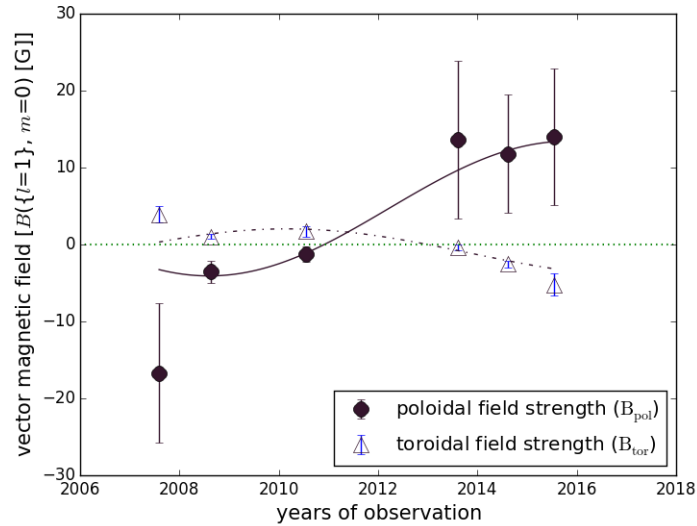


**Figure 4.11.:** Magnetic field strength ( $B$ ) at the magnetic pole for the axisymmetric  $l=1$  mode for the poloidal component, which is similar to  $l=1$  in Fig. 4.10. For the toroidal component,  $B$  represents the strength of the latitudinal or azimuthal field. The green horizontal dashed line represents  $B=0$ . The fits are obtained with a magnetic cycle period of 14.4 years which is twice the activity cycle period of 7.2 years.

exhibits good correlation over a long timescale. Figure 4.13 also shows the mean longitudinal magnetic field of 61 Cyg A averaged over each epoch, where the error bars represent the standard deviation in  $B_l$  per observational epoch. Strong temporal variations are detected for the average longitudinal field, with stronger field strength in epochs 2007.59, 2013.61, 2014.61 and 2015.54. The field strength is the weakest in epochs 2008.64 and 2010.55. However, epochs 2007.59 and 2010.55 exhibit stronger dispersion in  $B_l$  compared to the other epochs. Long-term observations of 61 Cyg A exhibits a weak anti-correlation between the mean magnetic field strength and the different chromospheric activity indicators.

The mean magnetic field obtained from the reconstructed ZDI maps averaged over each epoch is also shown in Fig. 4.13.  $B_{\text{mean}}$  follows a similar trend to  $B_l$ ; however,  $B_{\text{mean}}$  is weakest in epoch 2008.64 and does not show any pronounced anti-correlation with the S-index.

## 4.8. Discussion

The large-scale magnetic field geometry of the solar-type K5 dwarf 61 Cyg A was reconstructed using ZDI for six observational epoch spread over nine years, covering a complete chromospheric activity cycle. It exhibits clear polarity reversals of its large-scale magnetic field geometry.

### 4.8.1. Large-scale magnetic field

#### Polarity reversal of the large-scale field

We report polarity reversals of the large-scale magnetic field of 61 Cyg A, where, for the first time, a strong correlation is detected between the magnetic cycle and the chromospheric activity cycle. Polarity reversals have been previously detected in the large-scale magnetic field reconstructions of several cool stars such as  $\tau$  Boo, HD 190771, and HD 78366. However, the polarity reversals detected in previous targets do not exhibit any correlation with the star's chromospheric activity cycle.

The  $v \sin i$  of 61 Cyg A is lower than other ZDI targets. A previous numerical study by Kochukhov & Piskunov (2002) has shown that although reconstructions of the surface geometry from spectropolarimetric data can be carried out for slow rotators, the resolution of the surface reconstruction decreases with lower  $v \sin i$ . Since 61 Cyg A is a slow rotator, one can only resolve down the surface elements into the lower order spherical harmonics modes. In spite of this shortcoming, the polarity reversal of 61 Cyg A is clearly seen in the Stokes V spectra itself. Figure 4.6 clearly demonstrates that the Stokes V profiles change with rotational phase and also change with the chromospheric activity cycle. As shown in Fig. 4.6, the form of the Stokes V profile in epoch 2007.59 flips in epoch 2013.61, indicating that the large-scale field also flips polarity. The lack of any dominant Stokes V shape in epoch 2010.55 also indicates that the large-scale field is more complex during that epoch. The time

series of Stokes  $V$  profiles reconfirms that the polarity reversals of the large-scale field are in fact independent of any artefact.

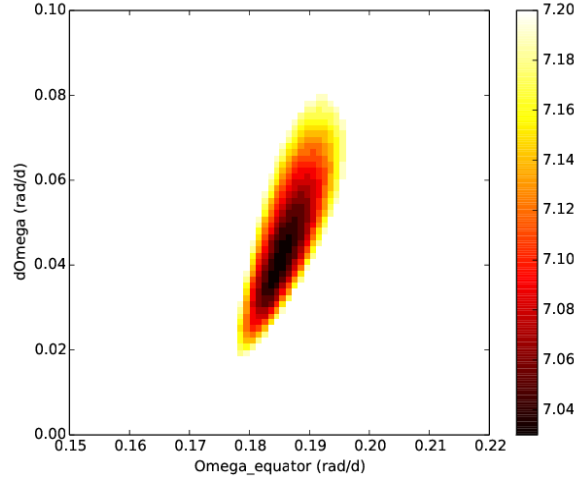


**Figure 4.12.:** Best fit  $B_{\text{mean}}$  map obtained by varying the differential parameters for epoch 2010.55. The  $\Omega_{\text{eq}}$  and  $d\Omega$  values obtained from this map are  $0.184 \text{ rad d}^{-1}$  and  $0.04 \text{ rad d}^{-1}$  respectively. <sup>4</sup>

### Evolution of the multipolar modes of the large-scale field

The magnetic field of 61 Cyg A's large-scale field is strongly poloidal at all epochs of observations, which can be quantified through energy fractions ( $\langle B^2 \rangle$ ). Particularly at epoch 2013.61, which is the epoch around which the field geometry flips polarity, the poloidal magnetic field constitutes 99% of the total magnetic energy budget as seen in Stokes  $V$ . During epoch 2010.55 which is coincidentally the chromospheric activity maximum, the percentage of the toroidal magnetic field increases in comparison to other epochs. The axisymmetry of the poloidal field component also reaches its minimum in epoch 2010.55, as shown in Fig. 4.8. It indicates that the field is complex during activity maximum, in a similar way to the Sun. The poloidal field is dominated by the dipolar component except during activity maximum, when the other higher order modes dominate.

We investigate the lower order spherical harmonics modes of the star and interpret the results in the context of the Sun. Throughout our observational time span, the vector magnetic field averaged over the surface, is stronger in the poloidal component except during epoch 2010.55. During activity maximum the vector component of the both the poloidal and toroidal field averaged over the surface of the star is close to zero. During epochs of minimum activity, a weak anti-correlation is detected between the poloidal and toroidal field.

<sup>4</sup> $B_{\text{mean}}$  is obtained by keeping the  $\chi^2$  constant and minimising the information content for epoch 2010.55 (where the colour bar represents  $B_{\text{mean}}$ ).

The low order axisymmetric modes of the poloidal field indicate that the dipolar component is strongest compared to the quadrupolar and octopolar modes. The poloidal dipolar component ( $l=1$ ) is strongest during epochs of low activity and is almost negligible during activity maximum in epoch 2010.55. The other higher order modes are almost negligible throughout the observations. The large-scale solar magnetic field of the Sun is also more dipolar during epochs of low activity (DeRosa et al., 2012). The quadrupolar component of the solar large-scale field dominates during activity maximum which is not seen in 61 Cyg A. One explanation for this disparity between the modes of 61 Cyg A might be caused by cross-talk between the odd and even sets of modes. To investigate that we suppressed the even modes and measured the field coefficients again. Although the odd modes are favoured no improvements were detected. An alternative explanation might be that the ZDI reconstruction technique has different sensitivities to the different spherical harmonics.

### 4.8.2. Chromospheric activity

The chromospheric activity of 61 Cyg A was determined by using three activity proxies: the Ca II H&K, H $\alpha$ , and Ca II IRT lines. From the combined S-index data, we measure a cycle period of  $7.2 \pm 1.3$  years. An activity cycle period of  $7.3 \pm 0.1$  years was also previously determined by the long-term Mount Wilson survey (Baliunas et al., 1995).

A correlation is detected between the S-index and H $\alpha$ -index of 61 Cyg A as shown in Fig. 4.5. Such correlation is also observed in the Sun, where the correlation between the two indices follows the activity cycle (Livingston et al., 2007). Correlations were also observed for other BCool targets such as  $\xi$  Boo A (Morgenthaler et al., 2012) and HN Peg (Boro Saikia et al., 2015). The correlation between the fluxes in Ca II H&K lines and the H $\alpha$  lines was investigated by Cincunegui et al. (2007) for 109 cool stars. They observed strong dispersion in correlations with both positive and negative correlations. They also suggested that the correlation does not depend on activity and spectral type but on stellar colour.

The correlation between a star's S-index and H $\alpha$ -index has been further studied by Meunier & Delfosse (2009), who suggest that one of the main factors affecting the correlation of these two indices is the filling factor of plages and filaments on the stellar surfaces. Since plages affect both Ca II H&K and H $\alpha$  lines, and filaments are mostly observed as absorption in H $\alpha$ , they claim that the correlations depended strongly on the spatial and temporal distribution of filaments on the stellar surface. They also observe an activity dependence on the correlations, where stronger correlation was observed near the cycle maxima. They also suggest that the correlations might also depend on time span of the observations and stellar inclination.

A correlation was also observed between 61 Cyg A's S-index and IRT-index and between H $\alpha$ -index and IRT-index (both shown in Fig. 4.5). A stronger correlation is observed between the S-index and the IRT-index. This is not surprising as the Ca II IRT lines also arise from plage dominated areas on the stellar surface (Andretta et al., 2005, Busà et al., 2007).

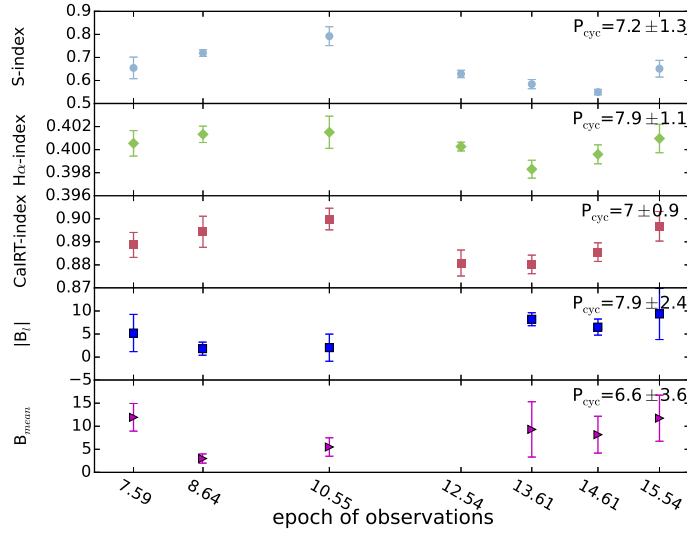


**Figure 4.13.:** Long-term evolution of the average values of the activity indices, the average longitudinal field, and the mean magnetic field measured from the ZDI maps of 61 Cyg A.

In the BCool snapshot study [Marsden et al. \(2014\)](#) also reports a good correlation between these two indices.

A weak anti-correlation was observed between the S-index and the longitudinal magnetic field. In previous ZDI targets no correlation was observed between the chromospheric activity and longitudinal magnetic field  $B_l$ , for example, in  $\xi$  Boo A ([Morgenthaler et al., 2012](#)) and HN Peg ([Boro Saikia et al., 2015](#)). The lack of correlation is expected due to the cancellation of small scale magnetic features in the mean field measurements. However, for 61 Cyg A the longitudinal magnetic field  $B_l$  is weaker during activity maximum and stronger during activity minimum. No anti-correlation was detected, however, between the chromospheric S-index and the mean magnetic field ( $B_{\text{mean}}$ ) measured from the magnetic maps. The chromospheric activity of 61 Cyg A shows good agreement with its coronal activity cycle which is also seen in the Sun.

## 4.9. Summary

In this chapter we reconstruct the large-scale surface geometry of 61 Cyg A for six epochs over nine years of observations. We report the presence of a possible magnetic cycle which is twice the length of the activity cycle. This is the first detection of a cool star, apart from the Sun, where the magnetic cycle is in phase with its chromospheric cycle. The large-scale surface magnetic field geometry of 61 Cyg A flips its polarity and is highly variable, with the radial field showing strong polar field during activity minimum and a complex field during activity maximum. Throughout our observations, the large-scale field of 61 Cyg A is strongly poloidal except during activity minimum when the poloidal field is relatively weaker. The dipolar component of the poloidal field is strongest close to activity minimum

#### *4. A solar-like magnetic cycle on the mature K-dwarf 61 Cygni A (HD 201091)*

---

and is weakest during activity maximum. During activity maximum, higher order modes such as quadrupolar and octopolar modes dominate over the dipolar mode. The evolution of the large-scale field of 61 Cyg A over the activity cycle shows close resemblance to the solar large-scale field, which has never been seen before in cool stars.

# 5. Göttingen chromospheric activity catalogue: questioning the Active branch of stellar activity cycles \*

## Contents

<b>5.1. Abstract</b>	<b>89</b>
<b>5.2. Introduction</b>	<b>90</b>
<b>5.3. Data analysis</b>	<b>92</b>
<b>5.4. Chromospheric activity</b>	<b>94</b>
5.4.1. S-index	94
5.4.2. Chromospheric Ca II H and K	96
5.4.3. Vaughan-Preston gap	97
<b>5.5. Long-term evolution of chromospheric activity vs rotation</b>	<b>98</b>
<b>5.6. Conclusions</b>	<b>104</b>

## 5.1. Abstract

The long-term monitoring of chromospheric activity in cool stars provides important information for understanding the operation of the underlying dynamo in these stars. We aim to understand chromospheric activity of cool stars and also investigate their activity cycles, from early F to mid M dwarfs. We develop a chromospheric activity database of Mount Wilson S-index and R0 values for 5258 main sequence stars. We also investigate the activity cycle of 54 cool stars as a function of stellar rotation to study the Active and Inactive branches of activity cycles. The activity cycle periods are determined using Generalised Lomb-Scargle

---

\*This Chapter is submitted for publication in the journal *Astronomy and Astrophysics* (Boro Saikia, S., Marvin, C. J., Jeffers, S. V., Reiners, A., Cameron R., Marsden, S. C., Petit, P., Warnecke, J., Yadav, A. P., A&A (submitted)). The results included in this Chapter are taken from a collaborative project between Sudeshna Boro Saikia (S.B.S) and another PhD student, Christopher J Marvin (C.J.M). The catalogue was developed by S.B.S and C.J.M. The analysis of activity cycles was also carried out by S.B.S and C.J.M. S.B.S collected all the archived data from *Vizier*. The S-index of the HARPS spectra was analysed by C.J.M. S. V. Jeffers and A. Reiners supervised the project. A. P. Yadav digitised the Mount Wilson data used here. The actual Mount Wilson spectra is not publicly available. The other co-authors provided their expertise in solar and stellar magnetic fields and helped in interpreting the results. The work was carried out as part of project A4 and A16, which was supported by SFB963/DFG.

periodograms. The bimodality of chromospheric activity resulting in the Vaughan-Preston gap is less significant than previous studies, and is heavily weighted towards weak activity for early-type stars. Our periodic analysis shows that sinusoidal activity cycles, mostly seen in slowly rotating stars, are located in the Inactive branch. The activity cycles of fast rotating stars are mostly chaotic and they show multiple periodicities. The Active branch is not as distinct as the Inactive branch. The high density of weak activity in F and G dwarfs is most likely due to stars spinning down and settling at their minimum activity level also known as the basal flux. On the activity cycles vs rotation domain, the presence of multiple cycles in some stars is probably caused by the complexity of their magnetic field, stellar inclination, epoch of observations, or a combination of the three.

## 5.2. Introduction

The non-thermal emission in the line cores of certain chromospheric lines such as the Ca II H&K, Mg II, H $\alpha$  and Ca II infra red triplet lines is widely used as an indicator of surface magnetic activity in cool stars. The first successful measurement of emission in stellar chromospheric lines was carried out by Eberhard & Schwarzschild (1913). Arguably the most famous study of stellar chromospheric emission was the Mount Wilson program that measured chromospheric activity of hundreds of stars, which lasted for more than four decades (Baliunas et al., 1995, Duncan et al., 1991, Wilson, 1968). The Mount Wilson survey appear to indicate that stellar activity can categorise stars as either active or inactive, with a lack of stars with intermediate activity. This lack of stars in the intermediate activity region is famously known as the Vaughan-Preston gap (Vaughan & Preston, 1980). Pace et al. (2009) explains the existence of the gap due to stars crossing the intermediate activity region at faster timescales. Although some authors such as Durney et al. (1981) provide an alternate explanation, where two different dynamo processes act on either side of the gap.

With observations spanning multiple decades the chromospheric activity cycles of the Mount Wilson stars were first investigated by Baliunas et al. (1995). These authors reported the presence of three different kinds of activity cycles: solar-like cyclic activity, highly variable non cyclic activity, and flat activity. Observations of cyclic chromospheric activity on the Mount Wilson sample (Baliunas et al., 1995) suggests that solar-like chromospheric activity is not uncommon and is exhibited by multiple other cool dwarfs. The mechanisms behind the dynamo driven activity cycle was investigated by multiple groups (Baliunas et al., 1985, Böhm-Vitense, 2007, Brandenburg et al., 1998, Noyes et al., 1984b, Saar & Brandenburg, 1999). For old stars with clear cyclic behaviour Noyes et al. (1984b) reported a possible correlation between activity cycle period  $P_{\text{cyc}}$  and Rossby number,  $Ro$ , where  $Ro$  is the ratio of the rotation period to the convective overturn time ( $P_{\text{rot}}/\tau_c$ ). However Baliunas et al. (1985) did not find any correlation between activity cycle period  $P_{\text{cyc}}$ , rotation period  $P_{\text{rot}}$ ,  $Ro$  and other stellar properties.

The well-constrained activity cycles in the Mount Wilson sample were re-investigated by Saar & Baliunas (1992), where they reported that stellar activity cycles form two distinct two branches when plotted as a function of rotation. They classified them as Active (A) and

Inactive (I) branch. The young active stars were in the Active branch and the old inactive stars were in the Inactive branch. The presence of these two branches were also confirmed by Brandenburg et al. (1998), Saar & Brandenburg (1999). Both Brandenburg et al. (1998), Saar & Brandenburg (1999) investigated the dependence of the  $\alpha$ -effect on magnetic field ( $B$ ) for stars with known chromospheric activity cycle <sup>2</sup>. The  $\alpha$ -effect is caused by the convective up-flows and down-flows of the Sun, which are responsible for twisting of the surface field lines from azimuthal to meridional configuration (See Ossendrijver (2003) for a detailed review). Together with the  $\Omega$ -effect it has been successful in reproducing different aspects of the solar magnetic cycle under the mean-field dynamo models. However, the assumptions used in such models are simple. When it comes to certain conditions such as the models dependence on magnetic field in the non-linear regime, there are still a lot unknowns. Hence to provide observational constraints for existing dynamo models Brandenburg et al. (1998), Saar & Brandenburg (1999) used the ratio of activity cycle and rotation frequency ( $\omega_{\text{cyc}}/\Omega = P_{\text{rot}}/P_{\text{cyc}}$ ) and defined Ro as  $1/2\Omega\tau_c = P_{\text{rot}}/4\pi\tau_c$ . In this definition  $\omega_{\text{cyc}}/\Omega$  is proportional to the  $\alpha$  effect in mean-field dynamo theory (Steenbeck et al., 1966). One key result was that stars in both branches show evidence of a dynamo where  $\alpha$  increases linearly with the magnetic field strength  $B$ , instead of the theory that  $\alpha \propto B^{-2}$ . Saar & Brandenburg (1999) also reported the presence of multiple cycles, where stars from the Active branch could have a second cycle in the Inactive branch and vice versa. However, they also noted that the classification of stars into two branches based on their activity and the evolution of the cycles from one branch to another might be more complex than the clear distinction reported in their work. The presence of multiple cycles and migration of stars from one branch to another was also reported by Böhm-Vitense (2007) on a separate model independent study, where cycle periods vs rotation period was investigated.

After the discontinuation of the Mount Wilson program the Lowell observatory continued long-term monitoring of the Mount Wilson targets (Hall et al., 2009, 2007, Lockwood et al., 2007). Multiple other activity surveys have also been carried out since then, such as the survey of southern hemisphere stars (Gray et al., 2006, Henry et al., 1996), and the Magellan survey (Arriagada, 2011). Chromospheric activity of thousands of potential planet host stars were also monitored as part of planet search programs, such as the California and Carnegie planet search program (Isaacson & Fischer, 2010, Wright et al., 2004) and the HARPS radial velocity survey (Lovis et al., 2011). Since the last study of stellar activity cycles by Saar & Brandenburg (1999), the number of stars with chromospheric activity measurements have significantly increased. So has stars with long-term monitoring, enabling us to investigate chromospheric activity cycles for a larger sample compared to previous work.

This chapter includes results from the collaborative research project *Goettingen chromospheric activity catalogue*. The catalogue was created by combining archival data sets available in VizieR <sup>3</sup>, together with digitised data from the Mount Wilson survey (Baliunas et al., 1995) and 110 M dwarfs taken from Marvin et al. 2016 (in prep) (Here after M16). We also analysed thousands of high-resolution spectra of F, G, K and M stars, which are part of the

<sup>2</sup>Saar & Brandenburg (1999) is a continuation of Brandenburg et al. (1998) with a bigger sample size

<sup>3</sup><http://vizier.u-strasbg.fr/viz-bin/VizieR>

HARPS radial velocity survey (Bonfils et al., 2013, Lovis et al., 2011) and calculated their S-index and  $R'_{\text{HK}}$ . One key motivation behind the catalogue was to investigate the Vaughan-Preston gap for available chromospheric activity measurements, which increases the sample size considerably when compared to previous studies. The other motivation was to monitor long-term variability of cool stars and examine trends in stellar activity as a function of physical properties such as rotation. This chapter is organised as follows: In Section 5.2 the archival data is described, followed by an introduction to the catalogue in Section 5.3. The chromospheric activity of the stars in the catalogue are discussed in this section, including the S-index to  $R'_{\text{HK}}$  conversion used. The relation between the long-term activity cycles and rotation is investigated in Section 5.4, followed by the conclusions in Section 5.5.

### 5.3. Data analysis

The data included in the catalogue comes from multiple sources. A brief description of individual sources is as follows: (i) The original Mount Wilson survey (Baliunas et al., 1995), taken from the 111 stars published in Baliunas et al. (1995). The data was digitised using *PlotDigitizer*<sup>4</sup>. The mean S-index ( $S_{\text{mean}}$ ) and median S-index ( $S_{\text{med}}$ ) are calculated from the long-term measurements. (ii) The Magellan survey (Arriagada, 2011), which includes 686 stars observed over a time baseline of 6 years. For individual stars the  $S_{\text{med}}$  is calibrated to the Mount Wilson scale. Only the median S-index is publicly available for this survey. (iii) The majority of stars come from the California and Carnegie planet search program (Isaacson & Fischer, 2010, Wright et al., 2004). Select stars in Wright et al. (2004) were observed multiple times and both  $S_{\text{med}}$  and  $S_{\text{mean}}$  are calculated from archival data. However many stars were observed only once or twice and their  $S_{\text{mean}}$  is included. Isaacson & Fischer (2010) carried out activity measurements of thousands of stars from the California Planet search program and only the  $S_{\text{med}}$  is available. (iv) A survey of southern solar-type stars carried out by Gray et al. (2006), Henry et al. (1996). The southern sample of stars in Henry et al. (1996) consists of stars within 50 pc of the solar neighbourhood. The majority of these stars were observed only once. For the stars that were observed multiple times  $S_{\text{mean}}$  is taken. The  $S_{\text{mean}}$  of a few hundred southern stars were also taken from Gray et al. (2006). (v) A limited sample from the Lowell observatory Solar and Stellar activity program (Hall et al., 2009), where a few solar-like stars were observed for over 14 years, and both  $S_{\text{mean}}$  and  $S_{\text{med}}$  are calculated. (vi) High resolution archival spectra was obtained for a few hundred HARPS radial velocity targets (Bonfils et al., 2013, Lovis et al., 2011). We analyse the spectra and calculate the S-index calibrated to the Mount Wilson S-index based on the technique used by M16. The stars included in the catalogue and their sources is listed in Table 5.1.

The total number of stars in the catalogue is 7259. We are only interested in main sequence (MS) cool stars for our analysis. Only the stars in Gray et al. (2006) have  $\log g$  information. For the list of stars which do not have  $\log g$  measurements we took a two step approach: (i) We obtained the spectral class information of all stars from *SIMBAD* and flagged stars not

---

<sup>4</sup><http://plotdigitizer.sourceforge.net/>. The digitisation was carried out as part of A. P. Yadav's Master's Thesis

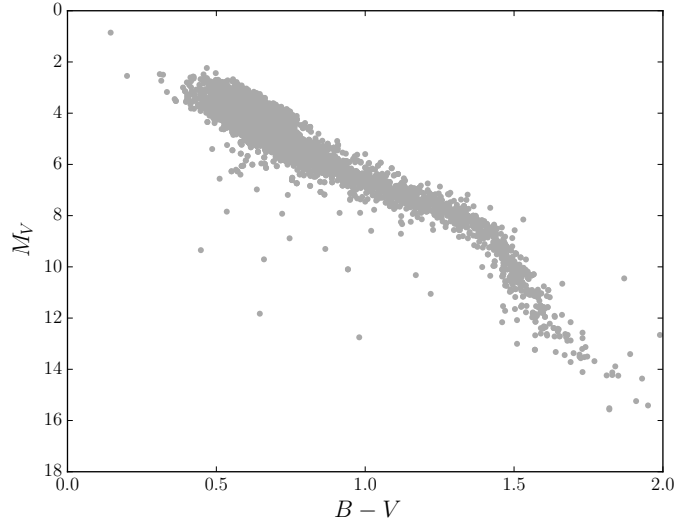


**Figure 5.1.:** HR diagram of the MS stars in the activity catalogue.

**Table 5.1.:** Table of archival surveys and the number of stars corresponding to each survey including the references.

No	survey	Total no. of stars	No. of MS stars	$S_{\text{mean}}$	$S_{\text{med}}$	Reference
(i)	Mount Wilson	111	83	Yes	Yes	1
(ii)	Magellan	686	541	No	Yes	2
(iii)	CPS	808	667	Yes	Yes	3
		401	300	Yes	No	3
		2620	1570	No	Yes	4
(iv)	Southern stars	825	522	Yes	No	5
		1359	1186	Yes	No	6
(v)	Lowell	28	25	Yes	Yes	7
(vi)	HARPS	311	254	Yes	Yes	8
		110	110			9

**References** (1) [Baliunas et al. \(1995\)](#); (2) [Arriagada \(2011\)](#); (3) [Wright et al. \(2004\)](#); (4) [Isaacson & Fischer \(2010\)](#); (5) [Henry et al. \(1996\)](#); (6) [Gray et al. \(2006\)](#); (7) [Hall et al. \(2009\)](#); (8) [Lovis et al. \(2011\)](#); (9) [Bonfils et al. \(2013\)](#). See Section 2 for more details on the type of S-index measurements.

classified as dwarfs. (2) We also make a linear fit to the MS and ignore all stars that lie at a distance of  $2\sigma$  from the fit from the analysis. This two step approach results in 5258 MS cool stars, shown in the HR diagram in Fig 5.1. The number of MS stars corresponding to different surveys including references are shown in Table 5.1 <sup>5</sup>.

## 5.4. Chromospheric activity

### 5.4.1. S-index

The majority of our data comes from archives where the measured S-index is calibrated to the Mount Wilson S-index. We denote the S-index on the Mount Wilson scale as  $S_{\text{MW}}$ . For some surveys, only the mean  $S_{\text{MW}}$  is published, while for other surveys, only the median  $S_{\text{MW}}$  is published. Specifically for the HARPS observations, we measure  $S_{\text{MW}}$  and calculate the mean and the median.

For HARPS spectra, we follow the prescription of [Duncan et al. \(1991\)](#) to mimic the response of the Mount Wilson HKP-2 spectrophotometer. We take a triangular bandpass at the core of the H and K lines at 396.847 nm and 393.3664 nm, respectively, and two 2.0 nm wide rectangular bandpasses to measure the nearby continuum;  $V$  centered on 390.107 nm and  $R$  centered on 400.107 nm. The equation is given as

$$S_{\text{HARPS}} = 8\alpha \frac{N_{\text{H}} + N_{\text{K}}}{N_{\text{V}} + N_{\text{R}}}, \quad (5.1)$$

where  $N_{\text{H}}$ ,  $N_{\text{K}}$ ,  $N_{\text{V}}$ , and  $N_{\text{R}}$  are the counts of the respective bandpasses, 8 is a correction factor for the longer exposure times of the  $V$  and  $R$  bandpasses of the HKP-2 instrument, and  $\alpha$  is a proportionality constant, usually taken to be  $\alpha = 2.4$ . Similar to [Lovis et al. \(2011\)](#), we calibrate  $S_{\text{HARPS}}$  to  $S_{\text{MW}}$  by performing a linear regression on stars common in both surveys so that

$$S_{\text{MW}} = aS_{\text{HARPS}} + b, \quad (5.2)$$

where  $a = 1.1159$  and  $b = 0.0343$ . The common stars are listed in Table 5.2.

---

<sup>5</sup>The full catalogue will be available in *Vizier*

**Table 5.2.:** Common stars for HARPS S-index calibration to the Mount Wilson scale

Star	$S_{\text{MW}}$	$S_{\text{HARPS}}$
HD10700	0.171	0.181
HD115617	0.164	0.172
HD152391	0.386	0.408
HD160346	0.305	0.305
HD16160	0.222	0.233
HD216385	0.142	0.154
HD23249	0.138	0.146
HD26965	0.208	0.195

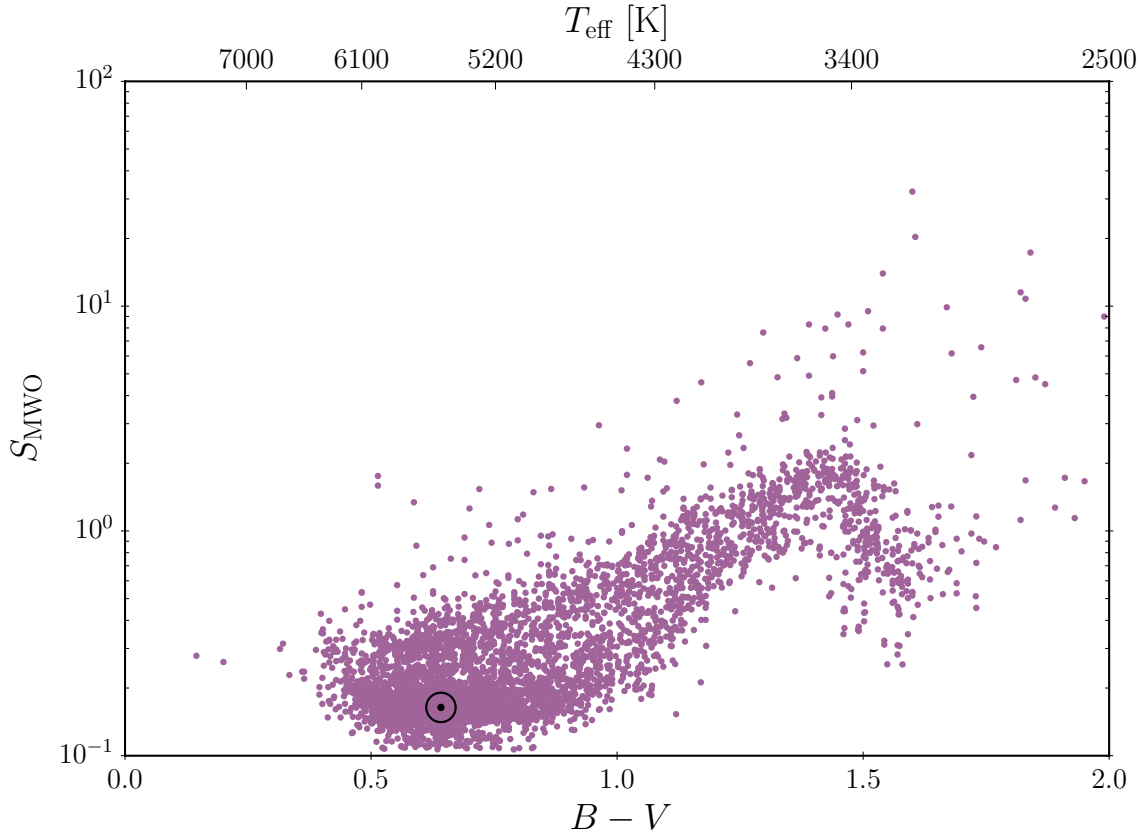
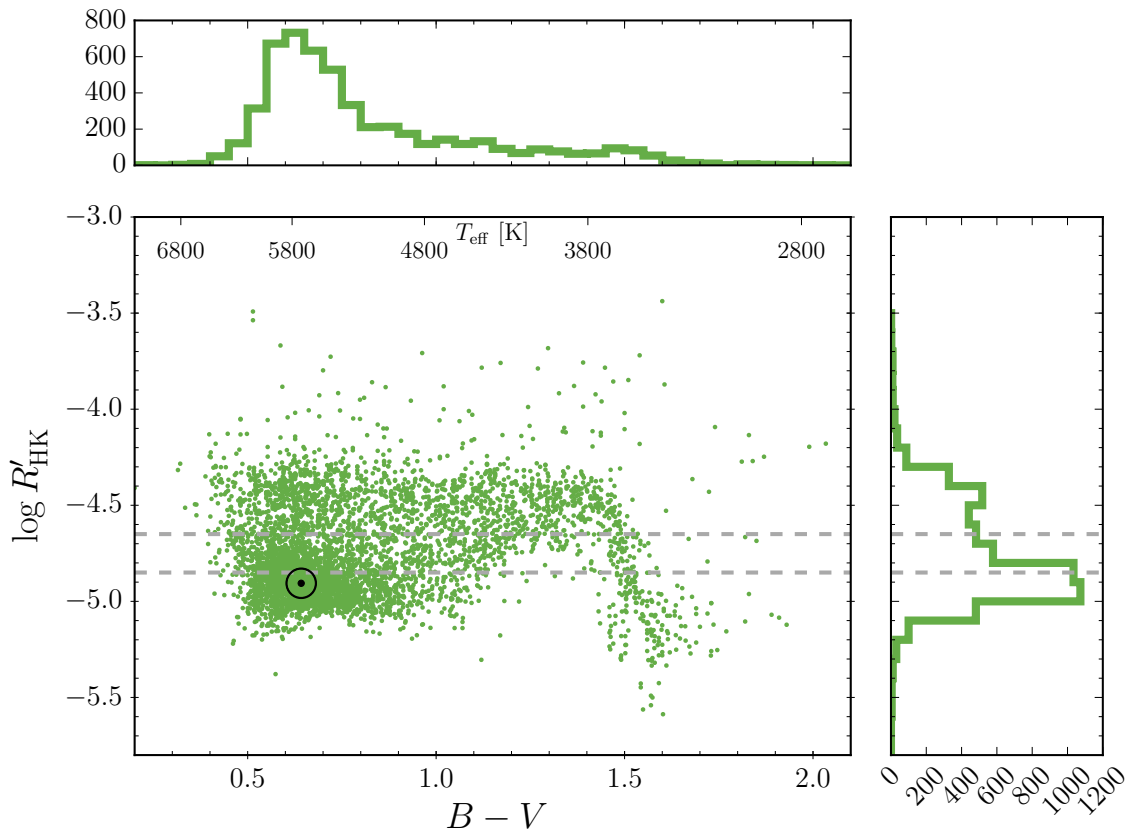
**Figure 5.2.:**  $S_{\text{MW}}$  (calibrated to the Mount Wilson scale) vs.  $B - V$  of 5258 main sequence stars. The Sun at minimum activity is shown by the  $\odot$  symbol.

Figure 5.2 shows  $S_{\text{MW}}$  on a log scale of all available S-index data listed in Table 5.1 as a function of  $B - V$ . We use the median  $S_{\text{MW}}$ ,  $S_{\text{med}}$  whenever available. If not the mean  $S_{\text{MW}}$ ,  $S_{\text{mean}}$  is used. In total, there are 5258 main sequence stars. For  $B - V \lesssim 0.93$ , the lower boundary of activity stays nearly constant. From  $0.93 \lesssim B - V \lesssim 1.4$ , the lower boundary of  $S_{\text{MW}}$  increases towards later spectral types. For  $B - V \gtrsim 1.40$ , the lower boundary of activity begins to drop towards later spectral types. Over the entire  $B - V$  range, the highest levels

of activity rises towards later spectral types. This colour-dependence of activity is consistent with previous S-index surveys, for example [Mittag et al. \(2013\)](#), [Vaughan & Preston \(1980\)](#). While  $S_{\text{MW}}$  gives a measure of Ca II H and K emission for a relative comparison of stars of similar spectral types, its colour-dependence makes it unsuitable to compare stars of different spectral types. Towards later-type stars, the flux in the  $V$  and  $R$  channels decreases as the bulk of radiation moves towards longer wavelengths. This results in a typical K or M dwarf having a much higher  $S_{\text{MW}}$  than a typical F or G star.

### 5.4.2. Chromospheric Ca II H and K



**Figure 5.3.:** Ratio of chromospheric Ca II H and K flux to bolometric flux,  $\log R'_{\text{HK}}$ , vs.  $B - V$  of 5258 main sequence stars. The Sun at minimum activity is shown by the  $\odot$  symbol. Distributions are shown by their respective axes. The dashed grey lines trace the Vaughan-Preston gap, as seen in Fig. 2 of [Noyes et al. \(1984a\)](#).

To compare Ca II H and K emission of F, G, K, and M dwarfs on the same scale, the ratio of chromospheric flux to bolometric flux is more suitable. This concept was formalised by [Linsky et al. \(1979\)](#), and is defined as  $R'_{\text{HK}} = (F_{\text{HK}} - F_{\text{phot}})/\sigma T_{\text{eff}}^4$ . Currently, the most ubiquitous method of measuring  $R'_{\text{HK}}$  is that of [Noyes et al. \(1984a\)](#), which requires a measurement of  $S_{\text{MW}}$  and  $B - V$  for a particular star. The dimensionless  $S_{\text{MW}}$  is converted to

the surface flux  $F_{\text{HK}}$ , most commonly by the calibration of [Middelkoop \(1982\)](#) or the improved [Rutten \(1984\)](#) calibration. The photospheric contribution  $R_{\text{phot}} = F_{\text{phot}}/\sigma T_{\text{eff}}^4$  is most commonly found using [Noyes et al. \(1984a\)](#), who use the [Hartmann et al. \(1984\)](#) method. However, this method is valid only for a limited spectral range  $0.44 \leq B - V \leq 0.82$ , yet many stars lie at  $B - V > 0.82$ .

To extend the relation of  $R_{\text{phot}}$  for all the stars in our sample, where  $B - V$  can be as high as 2.0, we use the  $R_{\text{phot}}$  polynomial of M16. Using PHOENIX stellar atmosphere models, M16 calculates  $R_{\text{phot}}$  values down to  $T_{\text{eff}} = 2300$  K, which covers the colour index range of the stars in our sample. To estimate  $T_{\text{eff}}$ , we use the  $B - V$  to  $T_{\text{eff}}$  conversion used in [Noyes et al. \(1984a\)](#). To remain consistent with the relation given by [Noyes et al. \(1984b\)](#), denoted as  $\log R_{\text{phot}, \text{N84}}$ , we scale the relation given by M16, denoted as  $\log R_{\text{phot}, \text{M16}}$ , to  $\log R_{\text{phot}, \text{N84}}$ :

$$\log R_{\text{phot}, \text{N84}} = \log R_{\text{phot}, \text{M16}} - 0.4529. \quad (5.3)$$

The constant 0.4529 was found by a least-squares fit of both relations in the range  $0.44 \leq B - V \leq 0.82$ . This correction ensures that stars which lie in the [Noyes et al. \(1984a\)](#) calibration range still have similar  $R'_{\text{HK}}$  values, while extending the relation to later spectral types K and M. We also use the  $R_{\text{HK}}$  relation given by M16, which is consistent with both [Middelkoop \(1982\)](#) and [Rutten \(1984\)](#).

For HARPS targets, of which we have the spectra, instead of converting  $S_{\text{MW}}$  to  $R'_{\text{HK}}$ , we use the template-model method of M16 to measure  $R'_{\text{HK}}$ . This method consists of measuring the surface flux  $R_{\text{HK}}$  by co-adding all available spectra into a high S/N template spectra using the HARPS-TERRA software ([Anglada-Escudé & Butler, 2012](#)). The template spectra is normalised to a PHOENIX model atmosphere to convert the arbitrary flux to absolute flux units. Then we integrate the flux of the Ca II H and K line cores. The photospheric flux contribution  $R_{\text{phot}}$  is subtracted from  $R_{\text{HK}}$  by subtracting the integrated Ca II H and K line cores of the PHOENIX model atmosphere. For consistency the  $R_{\text{phot}}$  correction in equation 5.3 is also applied to the HARPS targets.

Figure 5.3 shows the ratio of chromospheric Ca II H and K flux to bolometric flux,  $\log R'_{\text{HK}}$  as a function of  $B - V$ . The Sun at minimum activity is shown by a black  $\odot$  symbol. The majority of stars lie in the range  $-5.1 \leq \log R'_{\text{HK}} \leq -4.3$ . The most active stars have  $\log R'_{\text{HK}} \geq -4.3$  and are located at the top of the plot. Whereas there is a concentration of inactive stars close to the solar activity level of  $\log R'_{\text{HK}} \sim -5.0$ .

### 5.4.3. Vaughan-Preston gap

From the distribution of activity levels in the right panel of Fig. 5.3, we can see hints of the bimodal distribution of activity proposed by [Vaughan & Preston \(1980\)](#), although it is less distinct as previously found. [Vaughan & Preston \(1980\)](#) suggest that the bimodal distribution of activity is because of two distinct stellar populations: higher values are young and active stars, while lower values are old and inactive stars. The authors also suggested that the gap could either be a representation of different dynamo mechanisms or a statistical bias due to

their small sample size. According to Middelkoop (1982) and Durney et al. (1981), the gap suggests the presence of two different dynamo modes. Alternatively, the presence of the gap is explained by Noyes et al. (1984a) with three different possibilities: 1) it is not real, 2) there is a true bimodal distribution, but rotation and chromospheric emission decrease smoothly with age, and 3) there is a mass-dependent, critical rotation rate where rapid spin-down occurs. These authors also suggest that the dependence of chromospheric activity on either side of the gap on stellar rotation and spectral type questions the idea of two different dynamos. Similar to Noyes et al. (1984a), Rutten (1987) attributes the gap to be caused by a rapid spin down for stars beyond a certain rotation rate. These authors also remark that the Vaughan-Preston gap is limited to F and G stars and not present in cooler dwarfs. Lastly, the gap might be caused by stars crossing the gap on a very fast timescale of  $\sim 200\text{Myr}$  (Pace et al., 2009).

In order to investigate this bimodality in more detail, we plot the distribution of stellar activity levels for different ranges of  $B - V$  in Fig. 5.4. For stars with  $B - V \leq 0.82$ , which are F and G dwarfs, we detect a high concentration of low activity stars, caused by the decrease in activity as the star spins down, finally arriving at a minimum activity level. This minimum activity is also termed as the basal flux (Schrijver, 1987), which is the minimum level of chromospheric activity present in all cool stars.

For the late G and early K dwarfs in the range of  $0.82 \leq B - V \leq 1.0$ , the Vaughan-Preston gap is not significant. As we move towards late K and early M dwarfs in  $1.0 \leq B - V \leq 1.4$ , the scenario changes quite drastically. We detect a higher concentration of active stars on the active side of the Vaughan-Preston gap and there is a significantly lower number of less active stars. This lack of low activity K dwarfs was also noticed by Mittag et al. (2013). It is unsurprising given that many of the stars in Mittag et al. (2013) are the same as in this study. One explanation is that K dwarfs are in general more active than F and G dwarfs, and their minimum activity level or their basal flux is higher than F and G dwarfs. Whether the lack of inactive K stars is because they exhibit high basal flux or because of other physical origin is unclear. It is interesting to note that as we go further into the M dwarf regime,  $1.4 \leq B - V \leq 2.0$ , the chromospheric activity level decreases (for a more detailed analysis on the M dwarf activity level please refer to M16).

## 5.5. Long-term evolution of chromospheric activity vs rotation

Out of the 5258 MS dwarfs in the catalogue only few of them have S-index measurements spanning multiple years which include data from the Mount Wilson and HARPS surveys. For the rest of the surveys multiple epoch data was not publicly available. To investigate the long-term evolution of activity cycles we used a generalised Lomb-Scargle periodogram (Zechmeister & Kürster, 2009). Apart from cyclic S-index variations, some Mount Wilson stars also showed a decreasing trend in their S-index data. This decreasing trend might be an indication of a long-term activity cycle, with cycle periods much longer than the length of

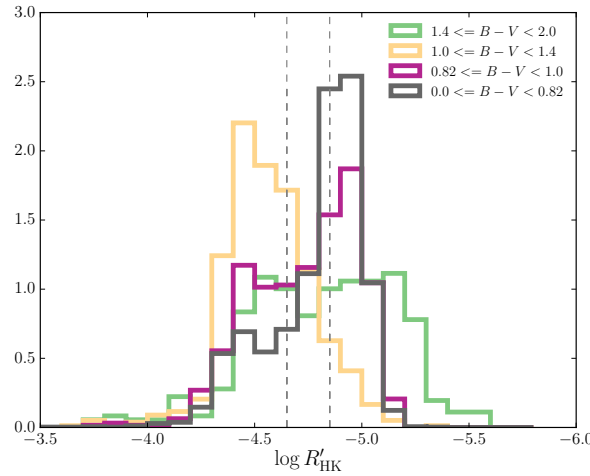


**Figure 5.4.:** Normalised distribution of stellar activity for different ranges of  $B - V$ , where the area under each distribution is normalised to 1. The vertical dashed lines indicate the approximate position of the Vaughan-Preston gap.

the observations. However it might also be an instrumental effect. To account for this trend we treated the data by taking a linear fit and subtracting the fit from the data. There is a possibility that by removing the long-term trend we might be losing information on any longer cycle period. However we do not have enough observations to confirm if the variability is in fact an activity cycle. Hence we remove this long-term trend from our analysis. During the digitisation process the actual error bars on the Mount Wilson stars could not be recovered. Hence we assume that the uncertainty in the S-index measurements is not more than 0.005. The actual errors are most likely lower than our estimate. No de-trending was performed for the HARPS stars.

Determining the presence of an activity cycle based only on the period search algorithm is not entirely without caveats. Since the only robust point of reference of an activity cycle is the solar cycle we assume the stellar activity cycle to be sinusoidal. However in reality this might not be the case and there may be multiple cycles instead of one clear activity cycle (Baliunas et al., 1995, Böhm-Vitense, 2007, Saar & Brandenburg, 1999). To minimise these effects and to be consistent with previous studies we assign False Alarm Probability ( $FAP$ ) grades ranging from excellent to poor to the measured cycle periods. The  $FAP$  was determined using the method described by Zechmeister & Kürster (2009), using the Horne & Baliunas (1986) normalisation. We classify the activity cycles based on their  $FAP$  using the same convention as Baliunas et al. (1995). Activity cycles with  $FAP \leq 10^{-9}$  is assigned an excellent grade,  $10^{-9} < FAP \leq 10^{-5}$  is assigned grade good,  $10^{-5} < FAP \leq 10^{-2}$  is grade fair and for  $FAP \leq 10^{-2}$  it is grade poor. For our purposes we also perform a ‘visual selection’ where we carefully inspect each time series and only include stars with observations spanning at least 6 years and a  $FAP$  grade of fair or above. Based on our selection criteria we divided the activity cycles into three categories: Class A (CA), Class B (CB), and Class C (CC), as listed in Table A.5. Any cycle length longer than 25 years is excluded, as that

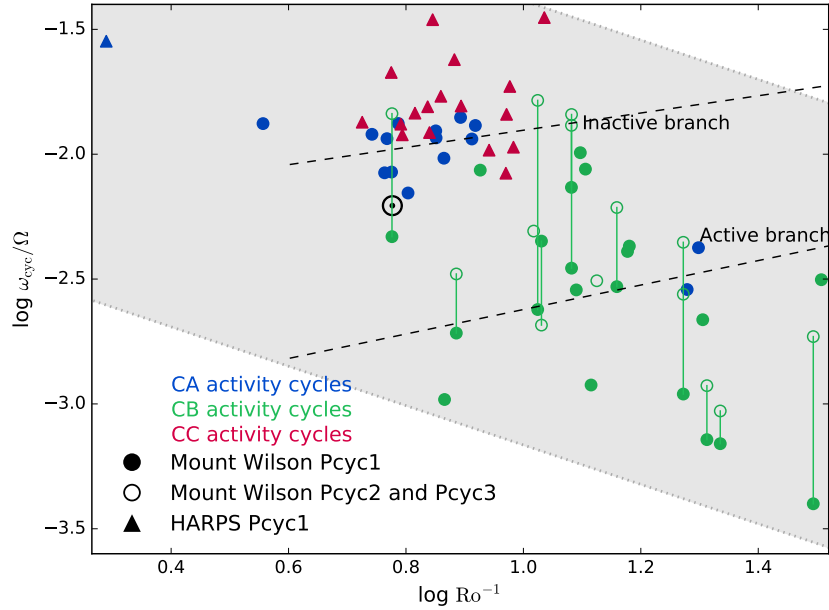


**Figure 5.5.:** Plot showing  $\omega_{\text{cyc}}/\Omega$  vs  $Ro^{-1}$  for the carefully selected group of stars in Table A.5, shown in  $\log$  scale. The blue symbols are activity cycles classified as CA, green symbols are activity cycles classified as CB, and the pink symbols are cycles classified as CC. The circles are Mount Wilson stars and triangles are HARPS stars. The filled symbols are cycle periods with the strongest peak in our analysis (Pcyc1). In the presence of multiple cycles the second and the third cycle periods (Pcyc2 and Pcyc3) are shown as open symbols, which are connected to the filled symbols by a horizontal line. The Sun is shown as a  $\odot$  symbol. The Active and Inactive branch from Saar & Brandenburg (1999) is shown as black dotted lines. The grey area between the two dotted lines show our cycle detection boundary. The stars with cycle periods more than 25 years and less than 2 years fall outside this grey area. (see Section 5.4 for details on the selection criteria.)

is limit of a full cycle recovery based on our observational time span. We also ignore cycle periods less than 2 years because as the period length gets shorter it is tricky to distinguish the rotation period from the activity cycle period.

**CA: Stars with well defined cycles** The stars which show a clear solar-like sinusoidal activity cycle are included in this category. The majority of these stars are slowly rotating stars with rotation periods equivalent to the solar rotation period or longer. Only two of these stars HD115043 and HD152391 have rotation periods less than 12 days. These two stars are the only ones not classified as Inactive branch stars by Saar & Brandenburg (1999). The time-series and corresponding fit from the period search for these well-defined cycles are shown in Fig A.1.

**CB: Stars with multiple or chaotic cycles** This group of stars show chaotic or multiple cycles and are shown in Fig A.2. HD78366, HD101501, HD149661 exhibit activity cycles transitioning from one cycle period to another. Stars such as HD206860, HD39587, HD161239, HD114710 show simultaneous multiple cycles as shown in Fig A.2. An exception is the young active star HD20630 ( $\kappa$  Ceti) which shows a long-term  $23.1 \pm 5.2$  year cycle period co-existing with shorter periods. At the start of the observations this long-term period is simultaneous with a possible  $9.2 \pm 0.3$  period. Towards the next half of the observations this star exhibits a shorter  $5.7 \pm 0.1$  year cycle. This shorter 5.7 year period can be clearly seen in Fig A.2. The rest of the sample indicate the presence of a more chaotic and less clear solar-like cycle.

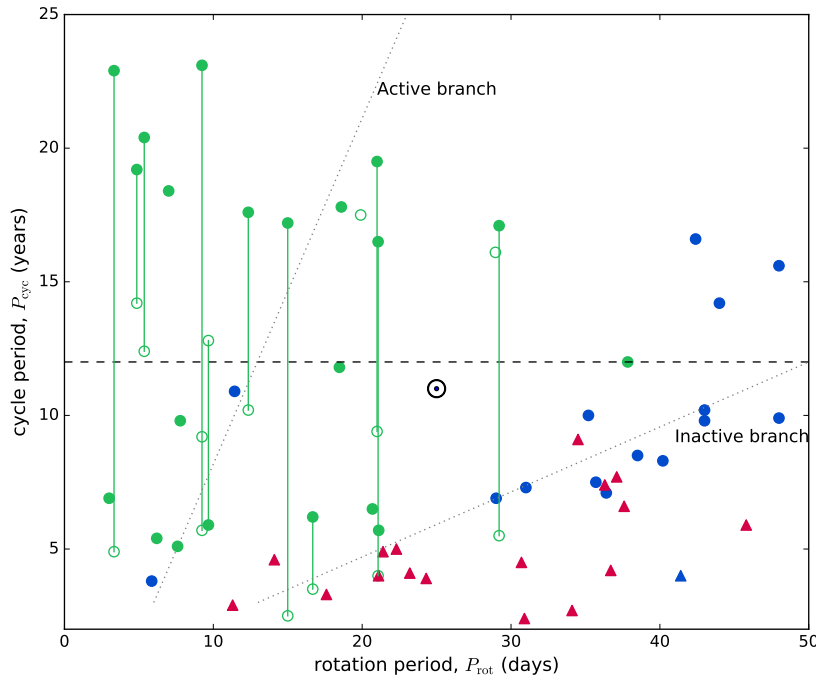


**Figure 5.6.:** Activity cycle period in years as a function of rotation period in days for stars in Table A.5. The symbols are as same as Fig 5.5. The black dotted lines show the Active and Inactive branch according to Böhm-Vitense (2007). The black horizontal line marks the midpoint of the maximum cycle length of 25 years. The Sun is shown as a  $\odot$  symbol.

**CC: Stars with probable cycles** The stars that belong to this category are all HARPS stars. The phase coverage and amplitude of most of these stars are poor resulting in an ambiguity in the nature of the cycle as shown in Fig A.3. Further observations are required to confirm the nature of these activity cycles.

Based on the Mount Wilson long-term survey, previous work investigating activity cycles in cool stars has shown that stars are segregated into two branches Active (A) and Inactive (I) branch (Böhm-Vitense, 2007, Brandenburg et al., 1998, Saar & Brandenburg, 1999). The

young active stars lie on the Active branch where as the old inactive stars lie on the Inactive branch. These authors also noted that there is a clear lack of stars in between these two branch. To investigate the rotation vs activity cycle period relation we plot our stars in Table A.5 in the  $\omega_{cyc}/\Omega$  vs  $Ro^{-1}$  plane similar to Fig 1 in Saar & Brandenburg (1999). Following the definition of Noyes et al. (1984a), the  $Ro$  number used here is determined using an empirically determined  $\tau_c$ . The  $\tau_c$  used by Saar & Brandenburg (1999) in their analysis is not empirically determined. Instead they use a theoretically determined  $\tau_c$  but the exact relation is not specified in the paper. Since the empirical  $\tau_c$  of Noyes et al. (1984a) and theoretical  $\tau_c$  of Saar & Brandenburg (1999) are in good agreement (see Fig 3. in Saar & Brandenburg (1999)), we chose to use the Noyes et al. (1984a) definition.

It is worth noting that the following stars from Saar & Brandenburg (1999) are not included in our analysis: HD98230B is excluded due to in availability of data, HD190406, HD187691, and HD100180 are excluded due to lack of significant variability in their S-index values, and HD26913 and HD154417 were excluded as their measured cycle periods fall outside of our selection boundary. On the other hand few of the Mount Wilson stars which were not included in the analysis of Saar & Brandenburg (1999) are included in our sample. The stars marked with a † symbol in table A.5 are the stars previously published by Saar & Brandenburg (1999).<sup>6</sup> The cycle periods of some of our common stars vary from the periods in Table 1 of Saar & Brandenburg (1999). This discrepancy is most likely caused due to difference in the data used as Saar & Brandenburg (1999) also use results from Radick et al. (1998), which is not included in our analysis. Overall our results are consistent with Baliunas et al. (1995) except for a few stars with chaotic activity cycles<sup>7</sup>.

Fig 5.5 shows that stars with clear activity cycles, including our Sun, all lie on the Inactive branch. Almost all stars with clear well defined cycles have  $\log Ro \leq 1$ . For majority of the stars with  $\log Ro \geq 1$  the activity cycles are more variable and are quasi-periodic. For the stars that do not exhibit well defined cycles, they mostly lie in the region close to the Active branch. The primary cycle, which is the cycle with the strongest peak in the power spectrum, of these stars also populate the intermediate area between the Inactive and Active branch. Fig 5.5 also shows that  $\log \omega_{cyc}/\Omega$  decreases with increasing  $\log Ro^{-1}$ . This linear trend is not a physical effect and is caused by the selection bias. Based on our selection criteria the stars with cycle periods less than 2 years and greater than 25 years were not included in our analysis. This creates this effect as shown by the grey shaded area in Fig 5.5, where stars which do not fall in our criteria lie outside the grey shaded area.

In order to investigate the activity cycles vs rotation relation independent of any empirical trend, we plot activity cycle period as a function of rotation period, as shown in Fig 5.6. It shows that the well defined cycles, classified as CA, mostly lie on the Inactive branch of

<sup>6</sup>All the entries in Table 1 of Saar & Brandenburg (1999) were not included in their analysis. These authors state that they only include stars with weights greater than 0.

<sup>7</sup>In this version of the ‘generalised’ Lomb-Scargle periodogram, measurement errors are weighted and an offset is introduced to account for the floating mean. These modifications make it a more robust algorithm than the periodogram (Scargle, 1982) used in Baliunas et al. (1995)

stellar cycles. However the Active branch of stellar cycles is not as prominent as previously thought. Majority of the fast rotating stars, which are expected to populate the Active branch, exhibit the presence of multiple stellar cycles. Similar work by [Böhm-Vitense \(2007\)](#) indicated that activity cycles of stars in the Active branch can migrate to the Inactive branch. Our results show that this is not the case for most of the stars with multiple cycle periods. Stellar activity cycles do not necessarily migrate from one branch to another and activity cycles are not restricted to Inactive and Active branch. This brings forward the question if classification of stellar activity cycles into two branches is the true representation of their long-term evolution.

The Sun as shown in Fig. 5.6 does not lie in any particular branch and can be mistaken as an outlier. The solar cycle used here is the 11 year sunspot cycle. Long-term monitoring of solar activity has shown that although the solar-cycle is cyclic in nature it is not purely periodic. The Sun also exhibits multiple cycles which are not as dominant as the 11 year cycle (see [Solanki et al., 2006](#), for more details on solar activity). For example, long-term modulation of the sunspot numbers also indicate the presence of a 80 year cycle known as the Gleissberg cycle. The evolution of the Sun's complex magnetic field geometry also results in multiple cycle periods. Multiple cycle periods are seen on the Sun due to the north-south difference in sunspot appearance. These multiple cycle periods are also governed by the underlying dynamo and are comparatively weaker than the 11 year cycle period. But depending on the epoch of observation, these multiple cycle periods might get stronger. It has been shown that these multiple periods were much more dominant on the Sun in the past compared to current observations. If the Sun is observed as a star with an inclination angle, during the time when these frequencies are stronger, then the integrated chromospheric activity of the Sun might also indicate multiple periods in its power spectrum.

The multiple cycles observed in Fig 5.6 is most likely caused by various factors: inclination, complex magnetic field geometry, observational epoch, or any combination of the three. Multiple cycles are mostly observed on fast rotating stars than slow rotating stars. Since young stars are known to exhibit complex magnetic geometry it is not surprising that fast rotating stars exhibit multiple cycles. It is quite interesting that majority of the slowly rotating stars exhibit one dominant solar-like cycle. Slow rotators tend to have simple solar-like magnetic geometry. The magnetic field geometry of solar-like stars with activity cycles was recently investigated by [See et al. \(2016\)](#). They find that the magnetic field geometry of Inactive branch stars, that rotate slowly, appear to remain dominantly poloidal throughout their whole activity cycle. On the other hand, the stars that lie close to the Active branch regime, that are rapidly rotating, show significant toroidal components with large temporal variations in their toroidal energy fractions. The stars with highly variable toroidal field components are also likely to show chaotic chromospheric activity variations. For example, HD206860 and HD20630 are both young active stars which exhibit complex magnetic field geometry with significant toroidal component, and chaotic multiple chromospheric activity cycles. However recent study on a sample of active young stars by [Hackman et al. \(2016\)](#), [Rosén et al. \(2016\)](#) show that, although majority of the fast young rotating stars exhibit a toroidal field geometry there are quite a few exceptions, with some young stars exhibiting

significant poloidal magnetic field component.

## 5.6. Conclusions

In this chapter we introduce a chromospheric activity catalogue of 5258 cool stars. Our main conclusions are as follows:

- We converted the Mount Wilson S-index,  $S_{\text{MW}}$  to the chromospheric flux ratio  $\log R'_{\text{HK}}$  for the entire cool star spectral range F, G, K and M. This is the first time that the calibration for  $\log R'_{\text{HK}}$  is extended to late K and M dwarfs, enabling direct comparison between F, G, K and M dwarfs. The chromospheric flux to bolometric flux ratio  $\log R'_{\text{HK}}$  as a function of  $B - V$  shows that the Vaughan-Preston gap is present but it is not as significant as previously detected. One explanation for the presence of the gap is that main sequence stars begin their lifetime with strong activity and as they spin down they become less active, finally settling down with a quiescent activity level or the basal flux. This is more clear for F and G stars, where they migrate from high activity to low activity and settle when they reach their basal flux. K star activity also migrate from high to low as the star spins down. But their lowest level of activity is much higher than F and G stars. However it is unclear if K stars have a high basal flux or it is caused by some other physical mechanism.
- We determined chromospheric cycle periods for stars with long-term chromospheric activity measurements, and investigated the cycle period-rotation relation. Our results show that the stars with well-defined clear activity cycles, cycles classified as CA, mostly lie on the Inactive branch. Stars with multiple cycles, most of which are rapid rotators compared to the Sun, do not necessarily lie on the Active branch. Rapidly rotating stars, both with and without multiple cycle, are more randomly distributed in the cycle period-rotation plane. The rapidly rotating stars occupy an Active region rather than an Active branch. Multiple cycles are observed for stars which lie close to the Active region. The Sun also exhibits multiple cycles, but they are not as strong as its 11 and 22 year solar cycle. A likely explanation of multiple cycles in cool stars is a combination of their complex magnetic field geometry, the inclination of the star or epoch of observation.

## 6. The relation between stellar magnetic field geometry and chromospheric activity cycles: the complex field of $\epsilon$ Eridani at activity minimum \*

### Contents

<b>6.1. Abstract</b>	<b>105</b>
<b>6.2. Introduction</b>	<b>106</b>
<b>6.3. Observations and Data Analysis</b>	<b>106</b>
6.3.1. Least Squares Deconvolution	107
6.3.2. Chromospheric emission - Ca II H&K	107
<b>6.4. Large-scale magnetic field geometry</b>	<b>107</b>
6.4.1. Magnetic maps	108
6.4.2. Magnetic energy	109
<b>6.5. Discussion</b>	<b>110</b>
<b>6.6. Conclusions</b>	<b>113</b>

### 6.1. Abstract

The young and magnetically active K dwarf Eridani exhibits a chromospheric activity cycle of about 3 years. Previous reconstructions of its large-scale magnetic field show strong variations at yearly epochs. To understand how Epsilon Eridani's large-scale magnetic field geometry evolves over its activity cycle we focus on high cadence observations spanning 5 months at its activity minimum. For each month we reconstruct sectionIntroduction Eridani's large-scale magnetic field using the tomographic technique of Zeeman Doppler Imaging. The results show that Epsilon Eridani's large-scale field is complex with a surprisingly rapid

---

\*This chapter will be submitted for publication in the journal MNRAS (Jeffers, S.V., **Boro Saikia**, S., Barnes, J. R., Petit, P., Marsden, S. C., and the BCoolest collaboration, MNRAS (to be submitted in November)). S.B.S contribute to this work by measuring the differential rotation and the S-index. S.B.S also produced Figure 6.3 and contributed to the text in the Discussion section. The paper is written by S.V.J and the other co-authors provided their expert insights and helped in the interpretation of the results. The work was carried out as part of project A16, which was supported by SFB963/DFG.

**Table 6.1.:** Stellar Parameters

Parameter	Value	Reference
Magnitude	V=3.7	
Spectral Type	K2V	Valenti & Fischer (2005)
Distance	3.2 pc	van Leeuwen (2007)
Effective Temperature	5146 <sup>+31</sup> <sub>-31</sub> K	Valenti & Fischer (2005)
Mass ( $M_{\odot}$ )	0.856 <sup>+0.006</sup> <sub>-0.008</sub>	Valenti & Fischer (2005)
Radius ( $R_{\odot}$ )	0.74 $\pm$ 0.01	Baines & Armstrong (2012)
$v \sin i$ (km s <sup>-1</sup> )	2.4 <sup>+0.04</sup> <sub>-0.04</sub>	Valenti & Fischer (2005)
P <sub>rot</sub> (day)	11.68	Rueddi et al. (1997)
Inclination	46 $\pm$ 2°	this work
Age	440 Myr	Barnes (2007)

toroidal field regeneration over the epochs of this analysis. This complex structure is in contrast to the simple dipolar structure of the Sun's and 61 Cyg A's large-scale field at activity minimum. Our results show that all stars do not necessarily exhibit the same field topology as the Sun will be an important constraint for the dynamo models of active solar-type stars.

## 6.2. Introduction

The young bright K-dwarf  $\epsilon$  Eridani is well known to be magnetically active and as a potentially exoplanet hosting star. Its magnetic activity is established notably from direct measurements of its magnetic field (Rueddi et al., 1997) and the long-term monitoring of activity proxies such as the cores of Ca II H&K lines that show variable cyclic behaviour of currently 2.95 years (Metcalf et al., 2013). In Jeffers et al. (2014) the large-scale magnetic field geometry of  $\epsilon$  Eridani was reconstructed, to understand how the photospheric large-scale magnetic field geometry of  $\epsilon$  Eridani varies over its S-index cycle. These observations comprised six epochs spanning nearly seven years or approximately two S-index cycles. The work of Jeffers et al. (2014) showed that each map has evolved dramatically from one epoch to the next, and that they clearly reconstruct the weakest magnetic field structures at its Ca II H&K (or S-index) minimum. The motivation for this work is to investigate the evolution of  $\epsilon$  Eridani's large-scale magnetic field with a higher cadence of observations over its S-index minimum. To achieve this, we obtained spectropolarimetric observations every night, weather permitting, over a period of five months. This chapter is organised as follows: we present our observations and data reduction methods in Section 6.2. The reconstructions of the large-scale magnetic field are presented in Section 6.3 and we discuss our results in Section 6.4.

## 6.3. Observations and Data Analysis

The observations of  $\epsilon$  Eridani were secured using the high-resolution echelle spectrograph NARVAL at the Telescope Bernard Lyot, France (Aurière, 2003). The observations in this

analysis use NARVAL in spectropolarimetric mode. The instrumental setup, observing and data reduction procedure has previously been described in detail by [Petit et al. \(2008\)](#). We observed  $\epsilon$  Eridani over a time span of five months from September 2014 to January 2015. The total data set comprises 40 spectra which were obtained every night with acceptable observational conditions. The data set was divided into three observational epochs, 2014.71, 2014.84 and 2014.98 (details in Section 6.3.1). The observations are summarised in Table A.6. The data were reduced using the automatic data reduction package LIBRE-ESPRIT which has been specifically adapted to reducing both Stokes  $I$  (unpolarised) and Stokes  $V$  (circularly polarised) NARVAL data. More details can be found in the previous work on  $\epsilon$  Eridani by [Jeffers et al. \(2014\)](#).

### 6.3.1. Least Squares Deconvolution

All Stokes  $I$  and Stokes  $V$  reduced spectra were processed using LSD ([Donati et al., 1997](#)) (see Section 2.2.3 for more details) to enable recovery of the weak signatures in the presence of noise. The multi-line technique LSD extracts the information contained in each spectral line, resulting in one high signal-to-noise spectral profile for each observation. The line mask was downloaded from the VALD atomic database for a star with:  $T_{\text{eff}} = 5000\text{K}$ ,  $\log g = 4.5$ , a depth threshold of 0.1 and  $\log(M/H) = 0.1$  and containing 12220 lines. This line mask was applied to each spectrum resulting in a step size of  $1.8 \text{ km s}^{-1}$  in the LSD profile, matching NARVAL's detector pixel resolution. More details on the application of LSD to the BCoolest sample is provided by [Marsden et al. \(2014\)](#). The observed and modelled Stokes  $V$  profiles for our three observational epochs are shown in Fig. 6.1.

### 6.3.2. Chromospheric emission - Ca II H&K

To determine the Ca II H&K values we use the same method described in [Jeffers et al. \(2014\)](#), where the S-index values calculated using NARVAL spectra are calibrated to the values from the Mount Wilson S-index survey by [Marsden et al. \(2014\)](#).

## 6.4. Large-scale magnetic field geometry

The large-scale magnetic field geometry is reconstructed using the tomographic technique of Zeeman-Doppler imaging which incorporates the maximum entropy algorithm described by [Skilling & Bryan \(1984\)](#). This method uses the stellar parameters shown in Table 1 to model local Stokes  $V$  profiles sampled over the stellar surface from which a disk integrated synthetic Stokes  $V$  profile is computed. This is then used to iteratively fit the model Stokes  $V$  profiles to the observed Stokes  $V$  profiles. The tomographic images of the large-scale magnetic field topology of  $\epsilon$  Eridani are reconstructed by assuming that the field geometry is projected onto a spherical harmonics frame ([Donati et al., 2006](#)), where the magnetic field is decomposed into poloidal and toroidal components. A spherical harmonics expansion with  $\ell_{\text{max}} = 10$  was used as there was no improvement to the fits using larger values.

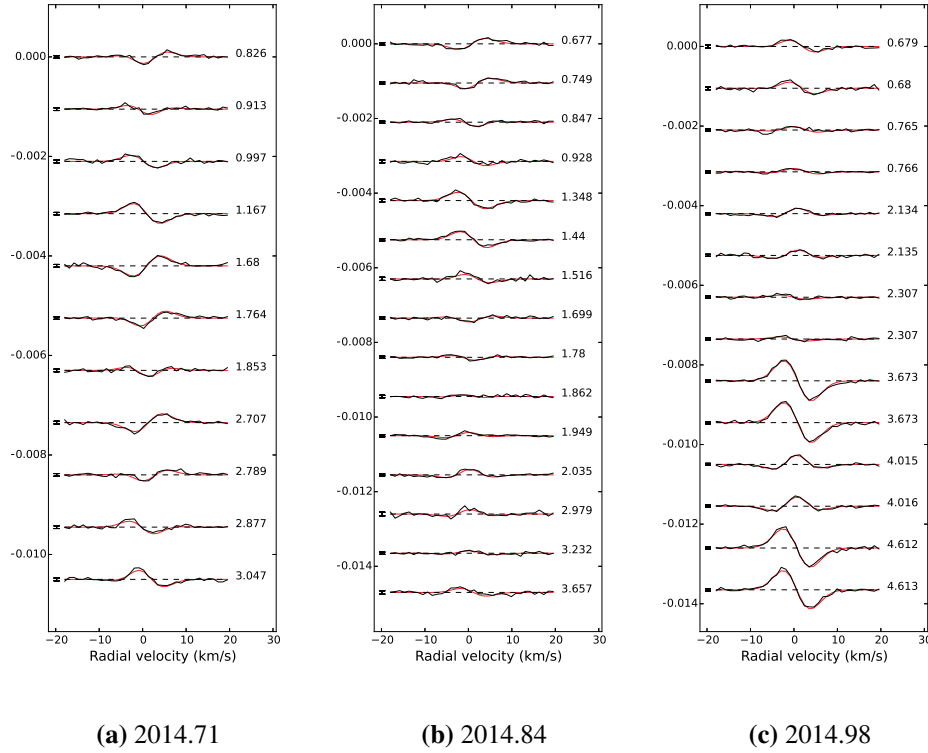


**Figure 6.1.:** Time series of Stokes  $V$  profiles of  $\epsilon$  Eridani for 2014.71, 2014.84 and 2014.98. The black is the observed profile and the red is the fit. The Stokes  $V$  profiles are separated by a constant value for clarity.

#### 6.4.1. Magnetic maps

The reconstructed large scale magnetic field is shown in Figure 6.2. Over the five month timespan of the observations there is a significant evolution of the large-scale magnetic field topology of  $\epsilon$  Eridani. The total observations were divided up into three epochs to avoid the presence of large gaps without observations, resulting from poor weather conditions. The division of the observations into the maps was tested for different combinations of observations (e.g. five maps versus three maps) and the result was comparable to the maps presented in Figure 6.2. We extensively tested the phase coverage of the maps by assigning random phases to the epochs of observation which resulted in a very similar configuration of magnetic features. For the first two maps we determine the differential rotation of the star. The differential rotation was determined using a solar-like differential rotation law and the differential rotation parameters are shown in Table 6.2 (the differential rotation was determined using the technique described in 3.5.3). The differential rotation could not be determined for the third epoch due to low phase coverage. The differential rotation parameters of map 2 are used for map 3. Even though the phase coverage of the last map is not optimal, we note that there is significant evolution of the Stokes  $V$  profiles between the same rotation phase (phase 0.67), which can be taken into account when differential rotation is included in the

reconstruction of the maps. Additionally, for map 3, we note that the Stokes  $V$  profiles have the largest amplitudes and that a simple magnetic field topology is expected. There is a negligible contribution from the meridional component due to cross talk between the radial and azimuthal components and it is not discussed here.

### Radial component

The radial component of  $\epsilon$  Eridani's large-scale magnetic field is dominated by a persistent and large polar magnetic spot<sup>2</sup> of positive polarity which varies in strength and shape. The strength of the region is highest in 2014.98 (map 3), and weakest in 2014.84 (map 2) while the global shape typically ranges in latitude from  $60^\circ$  (2014.98) to  $30^\circ$  (2014.98). The strongest evolution of the magnetic field is at epoch 2014.98 (map 3) where the polar spot has evolved into a large spot that extends to much lower latitudes. This evolution of magnetic features is also evident in the corresponding Stokes  $V$  profiles. Additionally, there are weaker magnetic spots with negative polarity that are likely to be evolving from one epoch to the next. The strength of the negative regions is highest at epochs 2014.98 (map 3) and 2014.71 (map 1) and very weak in 2014.84 (map 2).

### Azimuthal component

The azimuthal component of  $\epsilon$  Eridani's large-scale field appears only very weakly with small hints of magnetic spots at epochs 2014.71 (map 1) and 2014.98 (map 3). The azimuthal field is highest at epoch 2014.84 (map 2) with a large magnetic spot of negative polarity extending from phases 0 to 0.3.

## 6.4.2. Magnetic energy

To further investigate the evolution of  $\epsilon$  Eridani's large-scale field during S-index minimum we determine the magnetic energy in its poloidal and toroidal components of the magnetic field. In this consideration, the radial magnetic field is only poloidal, whereas the azimuthal field is both poloidal and toroidal. The magnetic energy in a component is calculated as being proportional to the square of that component integrated over the stellar surface. The poloidal component is defined by  $\alpha$  and  $\beta$  terms [Donati et al. \(2006\)](#) (equations 2 to 4) and the axisymmetric component is defined by spherical harmonics with  $m = 0$  modes. The results are shown in Figure 6.3 with the individual parameters listed in Table 6.2.

Over a period of approximately five months,  $\epsilon$  Eridani's large-scale field evolves from predominately poloidal to having a notable toroidal component that climbs steadily (as shown in Fig. 6.3 and Table 6.2) with decreasing S-index. This is indicated by the colour of the points in Fig. 6.3 changing from red in 2014.71 (map 1) to orange in 2014.98 (map 3). The field is notably complex at all epochs with significant amounts of the magnetic energy being contained in higher order modes. The poloidal component is approximately 50% dipolar

<sup>1</sup>the term spot here does not refer to a stellar spot but rather a small magnetic region. In reality it can be one spot or a cluster of spots, which can not be resolved using ZDI.

(with values ranging from 43% in 2014.71 to 56% in 2014.84), with additional contributions from the quadrupolar (with an average of 20%) the octopolar component (which are typically of the order of 20%) and higher order modes  $l > 3$ . The axisymmetry of the large-scale field is quite constant with an average value of 35%.

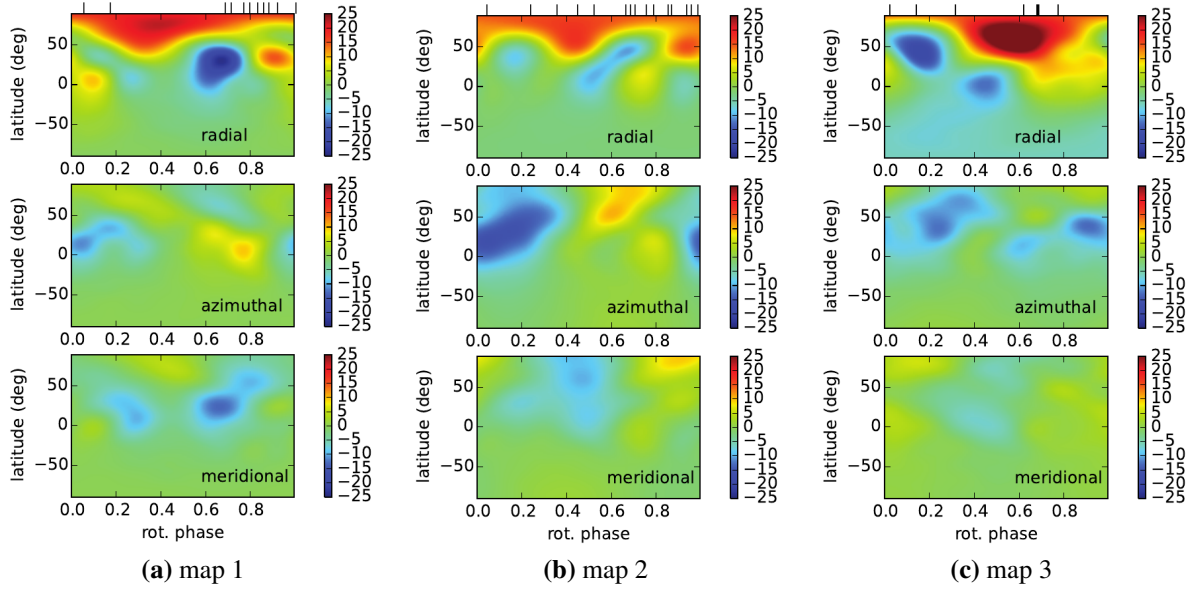


**Figure 6.2.:** Magnetic field maps of  $\epsilon$  Eridani reconstructed for 2014.71 (map1), 2014.84 (map2) and 2014.98 (map3) (ordered left to right). For each image the magnetic field projection is shown in terms of radial (upper), azimuthal (middle), and meridional (lower) field components, where red indicates positive polarity and blue negative polarity. The magnetic field strength is in Gauss where for each map the scale is identical ( $B_{\max} = 25$  G). The tick marks at the top of each poloidal field map indicate the observational phases used to reconstruct the large-scale magnetic field geometry.

## 6.5. Discussion

ZDI reconstructions of cool star generally lack the high cadence that are found in solar observations. Observations of the magnetic geometry evolution of cool stars over their activity cycle can provide valuable information about the cyclic dynamo process. So far, our only point of reference is the Sun. More observational constraints are required for solar and stellar dynamo theory. In this work, the large-scale magnetic field evolution of an active star  $\epsilon$  Eridani is monitored over 5 months of its chromospheric activity cycle minimum (its chromospheric cycle period is approximately 3 years). This is the first dedicated observing campaign of a cool star in its chromospheric activity minimum.

The large-scale magnetic field geometry of  $\epsilon$  Eridani has been shown to be highly variable over its 2.95 year chromospheric activity cycle when observed at yearly epochs (Jeffers et al.,

**Table 6.2.:** The fraction of the large-scale magnetic energy reconstructed in the toroidal and poloidal field components; the fraction of the poloidal field in the dipolar ( $\ell=1$ ), quadrupolar ( $\ell=2$ ) and octupolar ( $\ell=3$ ) components; and the fraction of the energy stored in the axisymmetric component ( $m=0$ ). The parameters for map 2015.01 are not included due to its poor phase coverage.

Epoch	Bmean (G)	Bmax (G)	Toroidal (% tot)	Poloidal (% tot)	Dipolar (% pol)	Quadrupolar (% pol)	Octupolar (% pol)	$l > 3$ (% pol)	Axisymmetric (% tot)	Poloidal (% axi)	Toroidal (% axi)
2014.75	$8 \pm 1$	28	16	84	43	25	19	13	35	41	5
2014.8	$8 \pm 1$	20	23	77	56	14	14	16	32	28	43
2014.9	$10 \pm 1$	33	26	74	50	19	22	9	40	29	72

2014). To investigate the evolution on shorter timescales of the magnetic field geometry of  $\epsilon$  Eridani, we secured observations over a period of five successive months, from September 2014 to January 2015, spanning  $\epsilon$  Eridani's chromospheric activity minimum. The large-scale magnetic field is shown to vary on a timescale of months with the first magnetic map reconstructed for epoch 2014.71 (map 1) showing significant evolution compared to the final map reconstructed for epoch 2014.98 (map 3). Although the complexity of the field geometry changes at minimum chromospheric activity, the mean field strength remains almost constant.

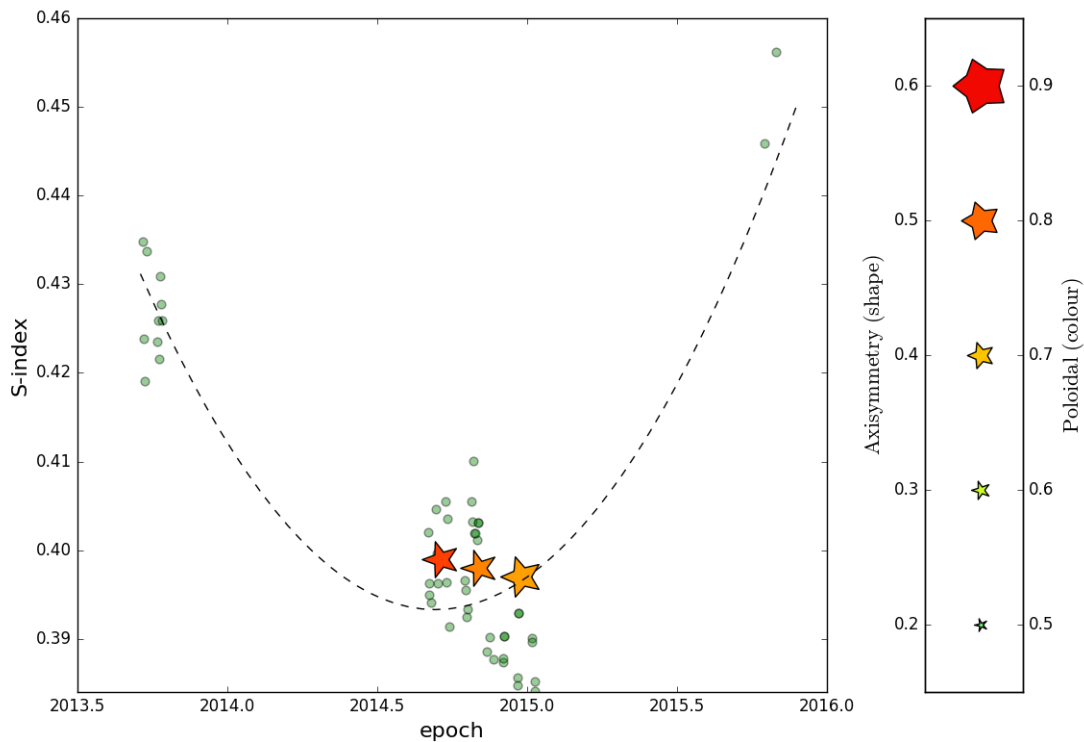


**Figure 6.3.:** Evolution of  $\epsilon$  Eridani's large-scale field during S-index minimum. The symbol shape indicates the axisymmetry of the field (non axisymmetric by pointed star shape and axisymmetric by decagon), the colour of the symbol indicates the fraction of the poloidal components of the field (decreasing strength of the poloidal field is represented by the change in colour from red to orange) and the symbol size indicates the magnetic field strength. Additionally, S-index points before and after the activity minimum are included as circular points. The black dashed line is a fit to all of the S-index points.

The large-scale magnetic field geometry has a strong poloidal component throughout  $\epsilon$  Eridani's activity minimum. Although the toroidal fraction shows a steady increase in the second and the third epoch, it is not as dominant as in Jeffers et al. (2014). The toroidal component of  $\epsilon$  Eridani in Jeffers et al. (2014) was strongest outside minimum activity. Our results show that the poloidal field at chromospheric activity minimum is not a simple dipole. The poloidal field is quite complex with significant fractions in higher order modes such as

quadrupolar and octopolar modes.

The reconstructed complex poloidal field is in contrast to the Sun where its large-scale field is a simple dipole at activity minimum and becomes complex at activity maximum (DeRosa et al., 2012). Another star that has been monitored as part of the BCoolest survey and that has stellar parameters very similar to  $\epsilon$  Eridani is 61 Cyg A (Boro Saikia et al., 2016a), which also exhibits a solar-like magnetic cycle. At activity minimum, the large-scale field of 61 Cyg A is also a simple dipole like the solar case. The poloidal field of  $\epsilon$  Eridani is more complex at activity minimum compared to 61 Cyg A and to the Sun. The stellar parameters of 61 Cyg A are more similar to  $\epsilon$  Eridani than the Sun's. The mass of 61 Cyg A is  $0.66 M_{\odot}$  (Kervella et al., 2008) which is slightly smaller than  $\epsilon$  Eridani's mass of  $0.7 M_{\odot}$  and given their low  $v \sin i$  values, the ZDI technique has a similar resolving power for both stars. The evolutionary state of the two stars is very similar with  $\epsilon$  Eridani having an age that is approximately 7% of its main-sequence lifetime compared to 14% for 61 Cyg A (calculated using the stellar evolution models of Pols et al., 1998). However,  $\epsilon$  Eridani (440 Myr) is much younger than 61 Cyg A (2.12 Gyr), where the ages were determined from gyrochronology (Barnes, 2007). The main difference is the rotation periods of the two stars, with 61 Cyg A having a rotation period that is approximately three times as long, 35.4 days compared to  $\epsilon$  Eridani's 11.68 days. Our results hint that rapidly rotating cool stars might have a different magnetic field evolution over the chromospheric activity cycle when compared to the Sun, providing valuable constraints for stellar dynamo models.

The maximum magnetic field strength of  $\epsilon$  Eridani measured in this work is much lower than previous measured in Jeffers et al. (2014) where the values were almost a factor of two larger. Additionally, previous observations of  $\epsilon$  Eridani by Jeffers et al. (2014) have one measurement at activity minimum at epoch 2011.81, where the large-scale field geometry is predominantly poloidal (74%) and axisymmetric (63%). A total of 65% of the poloidal field is in the form of a dipole resulting in a slightly less complex magnetic field than reconstructed here. In general, the large-scale field from epoch 2011.81 is quite similar to the results of this analysis and could be the first indication of a magnetic field cycle. However further observations, including observations at activity maximum, are need to confirm this.

## 6.6. Conclusions

The high cadence observations of  $\epsilon$  Eridani's large-scale magnetic field geometry shows that the large-scale magnetic field geometry evolves on a timescale of months. It also shows a predominantly poloidal component that is complex. The complexity changes together with the gradual increase of the toroidal field component. However, the mean magnetic field strength remains almost constant. Our results show that the magnetic field of solar-type stars can be quite different from the Sun even when they exhibit clear chromospheric activity cycles, which can provide valuable constraints for theoretical models of the dynamo actions in cool stars. We conclude that this difference appears to be related to the rotation period of the star and future work will investigate this further.



## 7. Summary and conclusions

Magnetic field generation and amplification in cool stars is a complex mechanism which is governed by the dynamo process. In the case of our nearest cool star the Sun, detailed magnetic field observations and theoretical modelling has been carried out over multiple decades. It has greatly improved our understanding of the dynamo process operating in the Sun. Observations of cool stars, which have the same internal structure as the Sun, can provide valuable information about their magnetic field generation. A detailed investigation of the magnetic and activity cycles of cool stars over a range of stellar properties can improve our understanding of the dynamo and its dependence on basic stellar parameters such as rotation and mass.

One of the most prominent manifestation of the solar dynamo is the cyclic generation of magnetic fields which results in the 11 year activity cycle and the 22 year magnetic cycle. Cool stars with similar dynamo process as the Sun are also expected to exhibit cyclic magnetic field variations. However, cool stars are point sources and they lack the surface resolution of the Sun. Detection of cycles in cool stars require dedicated long-term observing programs. The first clear evidence of activity cycles in cool stars other than the Sun was obtained by the Mount Wilson project (Baliunas et al., 1995). This long-term monitoring project detected a wide variety of chromospheric activity cycles in cool stars. Out of which only a few stars showed cyclic chromospheric activity. Multiple stars exhibited highly variable chromospheric activity and some stars were relatively inactive with negligible variability. Chromospheric activity is an proxy of magnetic activity. The activity cycles determined by Baliunas et al. (1995) does not provide any information about the large-scale magnetic geometry evolution or the presence of magnetic cycles in cool stars.

Direct observations of the magnetic cycle in cool stars were only possible in the last two decades with the development of the Zeeman Doppler Imaging (ZDI) technique (Brown et al., 1991, Donati & Brown, 1997, Semel, 1989) and with the development of high-resolution spectropolarimeters (NARVAL, ESPaDOnS, HARPS-pol). ZDI reconstructs the large-scale magnetic geometry of cool stars from circularly polarised spectra. In the Sun cyclic polarity reversal of the polar magnetic field is one of the key observable of the magnetic cycle. Hence, any polarity flips in the magnetic geometry of cool stars will indicate the presence of a magnetic cycle. The first detection of a magnetic cycle in a cool star other than the Sun is  $\tau$  Boo (Fares et al., 2009, Mengel et al., 2016).  $\tau$  Boo has a magnetic cycle period of less than 2 years. Unlike the Sun, the magnetic cycle of this star is not in phase with its chromospheric cycle. The chromospheric cycle period of  $\tau$  Boo is approximately 11 years which is much

longer than its magnetic cycle period. Polarity reversals of magnetic field geometry has been only detected in two other cool stars, HD78366 (Morgenthaler et al., 2011) and HD190771 (Morgenthaler et al., 2011, Petit et al., 2009). But they are not as well studied as  $\tau$  Boo and they need more observations to confirm their magnetic cycle. The polarity reversals in these two stars are also not in phase with the stars' chromospheric cycle.

Observations of the solar magnetic field has provided valuable information about the solar magnetic and activity cycle. As for cool stars, activity and magnetic cycles are not as well studied as the solar case. Chromospheric activity cycles have been detected in multiple stars but it does not provide any information on the magnetic field evolution during the cycle. Observations of magnetic cycles in cool stars using ZDI has been performed for a handful of stars. None of which exhibit any correlation with the stars' chromospheric activity. The aim of this thesis is to investigate the magnetic and activity cycles in cool stars by combining both direct and indirect field detection techniques. A brief summary of the results are as follows,

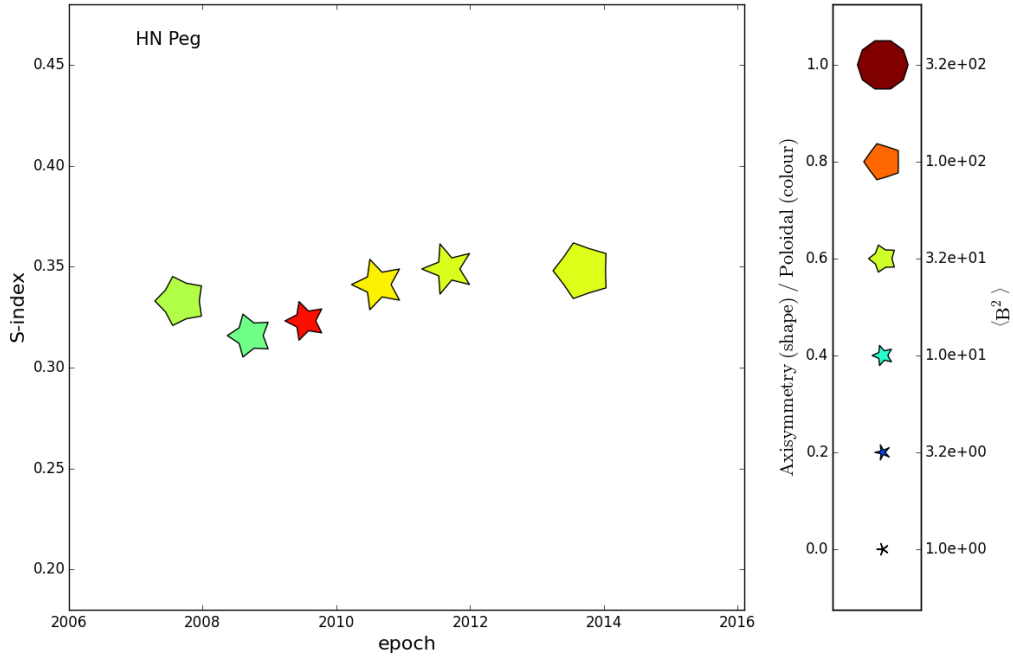


**Figure 7.1.:** Evolution of magnetic field geometry of HN Peg. The x-axis is time and y-axis is chromospheric activity (S-index). The colours represent the axisymmetry of the field and the shapes represent the fraction of the poloidal field. Axisymmetry increases from pointed star to decagon. The poloidal percentage increases from blue to red.

### 7.0.1. Variable magnetic geometry of the young sun HN Pegasi (HD206860)

The large-scale magnetic field geometry of the young solar-type star HN Peg was reconstructed over multiple epochs of observations. HN Peg is a variable young dwarf with a

---

complex magnetic geometry, where the radial magnetic field exhibits stable positive polarity polar magnetic field regions. In contrast, the azimuthal field exhibits a highly variable geometry where a band of positive polarity field is observed in the first epoch of observation followed by a negligible field two years later in epoch 2009.54. The azimuthal band emerges again one year later in epoch 2010.62 which is stable in the later epochs 2011.67 and 2013.68. HN Peg exhibits a highly varying magnetic geometry with no visible polarity reversals. Significant toroidal fractions are detected, where the percentage of the toroidal field changes with time, as shown in Fig 7.1 <sup>1</sup>. The field is also mostly non-axisymmetric throughout the observations. The magnetic geometry evolution of HN Peg does not resemble the solar case. In the Sun, the large-scale magnetic field is strongly poloidal (Vidotto, 2016), which evolve from simple dipolar at minimum activity to more a complex geometry at activity maximum. The multi-epoch magnetic geometry reconstructions of HN Peg brings us a step closer in understanding the complex nature of magnetic field evolution in cool stars.

### **7.0.2. A solar-like magnetic cycle on the mature K dwarf 61 Cygni A (HD201091)**

The large-scale surface geometry of 61 Cyg A was reconstructed for six epochs over nine years of observations. The large-scale surface magnetic field geometry of 61 Cyg A flips its polarity from one activity minimum to the next. The magnetic field exhibits a strong polar magnetic field during activity minimum and a complex field during activity maximum. Throughout the observations the large-scale field of 61 Cyg A is strongly poloidal. The evolution of the large-scale field of 61 Cyg A over the activity cycle shows close resemblance to the solar large-scale field, which has never been seen before in cool stars. Figure 7.2 shows the evolution of the magnetic geometry of 61 Cyg A <sup>2</sup>. The magnetic field geometry is strongly poloidal when compared to HN Peg. Such strong poloidal field is also detected in the Sun. The evolution of the solar poloidal field is similar to 61 Cyg A. At minimum activity the field is simple dipolar and at maximum it is complex. 61 Cyg A is the first detection of a solar-like magnetic cycle in any cool star, other than the Sun.

### **7.0.3. Göttingen chromospheric activity catalogue: questioning the Active branch of stellar activity cycles**

A chromospheric activity catalogue was created consisting of 5258 cool stars. Since the Mount Wilson project (Baliunas et al., 1995, Duncan et al., 1991), multiple long-term surveys of chromospheric activity have been carried out. Publicly available data from long-term surveys were combined to create a chromospheric catalogue. The majority of the data comes from archives, which consists of S-index measurements. Additionally, high-resolution spectra were taken from the HARPS archive. The spectra were analysed to measure the chromospheric activity, S-index. The S-index is not suitable for stars with an wide range of spectral

---

<sup>1</sup>This figure summarises the results in Table 3.2 of Boro Saikia et al. (2015) although it is was not included in the original publication.

<sup>2</sup>This figure summarises the results in Table 4.2 of Boro Saikia et al. (2016a) although it is was not included in the original publication.

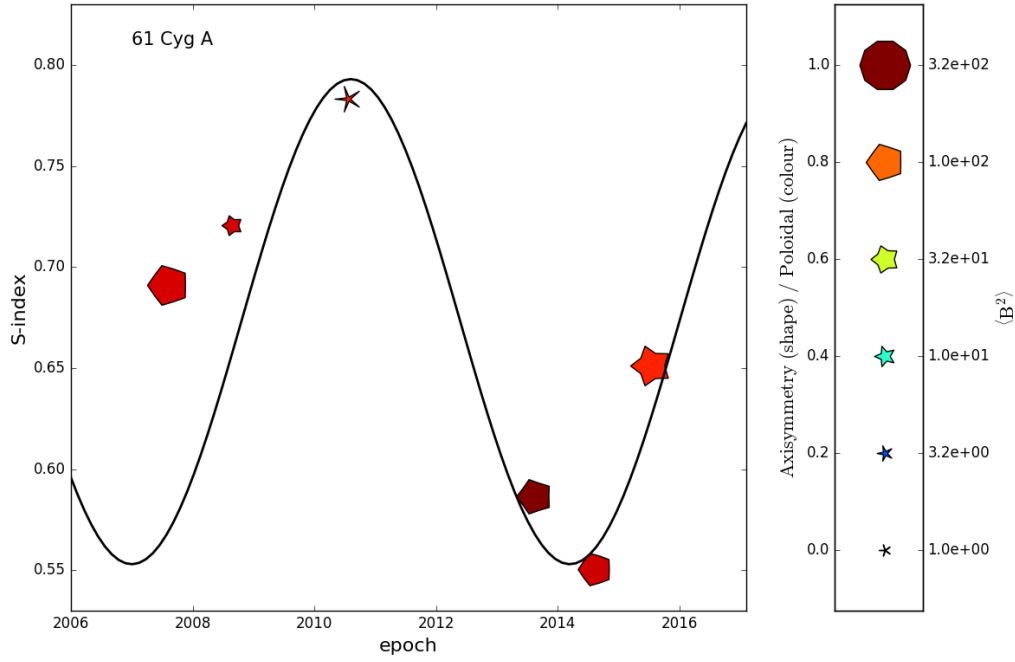


**Figure 7.2.:** Magnetic geometry evolution of 61 Cyg A. Axes and symbol descriptions are same as Fig. 7.1. The black sine curve represents the 7.3 year chromospheric cycle period.

type and it also includes photospheric contribution in its measurement. Hence the S-index was converted to the chromospheric flux ratio  $\log R'_{\text{HK}}$ , which is the physical representation of chromospheric activity. The  $\log R'_{\text{HK}}$  conversion was calibrated for the entire cool star spectral range, F, G, K and M. Until now calibration of  $\log R'_{\text{HK}}$  was only available from F to K dwarfs. This new calibration will allow direct comparison of chromospheric activity of cool stars from F to M.

Chromospheric activity cycles were also determined for stars with long-term measurements, where both cyclic and chaotic activity cycles were detected. The activity cycle periods were plotted as a function of the rotation period of the stars, to investigate the Active and Inactive branch of stellar activity cycles. Slowly rotating stars with cyclic activity cycles show a possible dependence on rotation. These stars lie on the Inactive branch of [Böhm-Vitense \(2007\)](#), [Saar & Brandenburg \(1999\)](#). Multiple cycles are also observed for some stars. Surprisingly, most of which are rapidly rotating stars. These stars do not necessarily lie on the Active branch of [Böhm-Vitense \(2007\)](#), [Saar & Brandenburg \(1999\)](#). Instead they exhibit a more random distribution in the rotation-cycle period plane. Multiple cycles are also seen on the Sun but they are not as dominant as the 22 year and 11 year solar cycle. One possible explanation for existence of multiple cycles in some cool stars is any combination of the star's complex magnetic field geometry, the inclination and epoch of observation.

#### 7.0.4. The relationship between stellar magnetic field geometry and chromospheric activity cycles: the complex field of $\epsilon$ Eridani at activity minimum

The young and magnetically active K dwarf  $\epsilon$  Eridani exhibits a chromospheric activity cycle of about 2.95 years (Metcalf et al., 2013). Previous reconstructions of its large-scale magnetic field by Jeffers et al. (2014) show strong variations at yearly epochs. High cadence observations spanning 5 months was taken at  $\epsilon$  Eridani's activity minimum, where the observations were split into three epochs. We reconstructed its large-scale magnetic field using the tomographic technique of ZDI. The results show that  $\epsilon$  Eridani's large-scale field is complex with a surprisingly toroidal field evolution over the epochs of this analysis. Despite this rapid evolution of its complex magnetic field, the mean field strength is almost constant. The complex magnetic geometry of  $\epsilon$  Eridani and its notable evolution of the toroidal field is in contrast to the simple dipolar structure of the Sun's and 61 Cyg A's large-scale field at activity minimum. The stellar properties of  $\epsilon$  Eridani are similar to 61 Cyg A except the rotation period.  $\epsilon$  Eridani rotates much faster than 61 Cyg A, indicating that rotation might be dominant property affecting its magnetic geometry evolution. Our results show that all stars do not necessarily exhibit the same field topology as the Sun, which can be an important constraint for the dynamo models of active solar-type stars.

### 7.1. Ongoing and future work

In the past two decades ZDI of cool stars has revealed a wide range of magnetic geometries in cool stars. In this thesis, a solar-like magnetic cycle has been detected for the first time for any cool star other than the Sun. Only a few other stars show the presence of magnetic cycles. None of which show solar-like 2:1 relation between the magnetic and chromospheric activity cycle other than 61 Cyg A. On the other hand, rapidly rotating cool stars such as HN Peg (Boro Saikia et al., 2015) exhibit strong azimuthal magnetic field which is not seen in the Sun.

One major difference between the ZDI observations and the Sun is the resolution. ZDI maps only reveal the large-scale features on the star's surface. In order to make reliable comparison with the Sun, we have to either increase the resolution of stellar observations or decrease the resolution of the solar observations. Unfortunately stars are point sources and their resolution is limited by the stellar  $v \sin i$ . So the only option is to decrease the resolution of the solar observations. Recently, Vidotto (2016) performed spherical harmonics decomposition of the radial magnetic field of the Sun. The spherical harmonics decomposition carried out by Vidotto (2016) is comparable to the decomposition in ZDI. The field is decomposed into the poloidal and toroidal components providing easier comparison with the ZDI reconstructions of cool stars.

The global magnetic field of the Sun is known to exhibit a 'Butterfly' shape when observed over multiple years, as shown in Fig. 1.7. However the pattern made by its large-scale field is

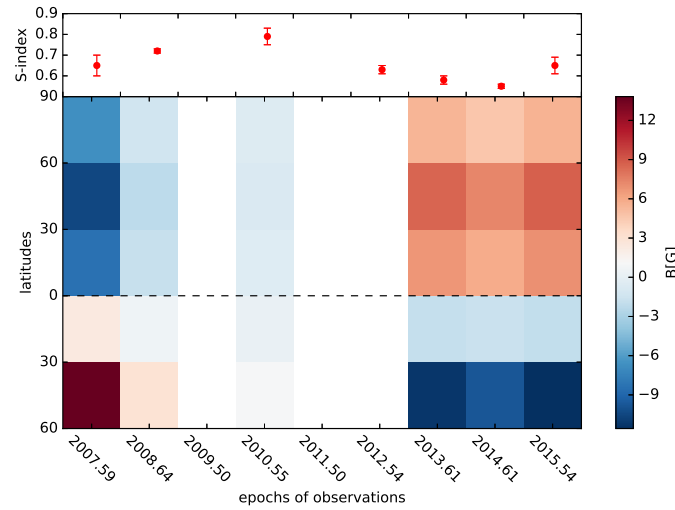


**Figure 7.3.:** Latitudinal distribution of the average radial field of 61 Cyg A for each epoch for nine years of observations. The average radial field for each  $30^\circ$  latitude range is shown. For the southern hemisphere only latitudes up to  $60^\circ$  is shown as the star’s inclination is  $70^\circ$ , the higher latitudes on the southern hemisphere are not reliable measurements. The equator is shown as a black dashed line and the epochs with no observations are left as blank spaces.

not yet investigated. In an ongoing project, the large-scale ‘Butterfly’ diagram of stars with known magnetic activity cycles including the Sun is investigated.

In order to plot a large-scale ‘Butterfly’ diagram of 61 Cyg A, the stellar surface is divided into latitude bands of  $30^\circ$ . For each of these latitude bands the average radial field strength on the surface is picked. Latitude bands of only up to  $60^\circ$  is included for the southern hemisphere in the calculation. Because the stellar inclination is  $70^\circ$  the entire disk of the star is not visible, limiting the latitude range. Figure 7.3 shows the latitudinal distribution of the large-scale radial field of 61 Cyg A (large-scale ‘Butterfly’ diagram). The chromospheric activity cycle is also shown on the top panel. Although the characteristics butterfly shape is lost due to poor resolution, it reconfirms the polarity reversal of the radial magnetic field near the poles. During low activity at the start of the observations a strong magnetic field with a single polarity is seen in each hemisphere near the poles, with opposite polarities in opposite hemispheres. The field strength is stronger in the latitude band of  $30^\circ$ - $60^\circ$  in the northern hemisphere. This is not surprising as the magnetic field is concentrated around that latitude as shown by the ZDI maps (See Fig 4.7). On the other hand a weak field strength is detected near the equator which is most likely caused by the complex magnetic structure at equatorial latitudes. During epoch of maximum activity (2010.55), the field strength is almost negligible. The lack of a dominating polarity in both hemispheres during this epoch can be explained by the presence of mixed polarities which cancel out leaving a very weak field. During the next minimum activity period, the field strength gets stronger and single dominating polarities emerge at higher latitudes but now with switched polarities. However, we don’t see a clear progression of magnetic strength from high to low latitudes, over the course of a couple years out side of reversal (e.g. from 2013.61-2015.54). This is most likely

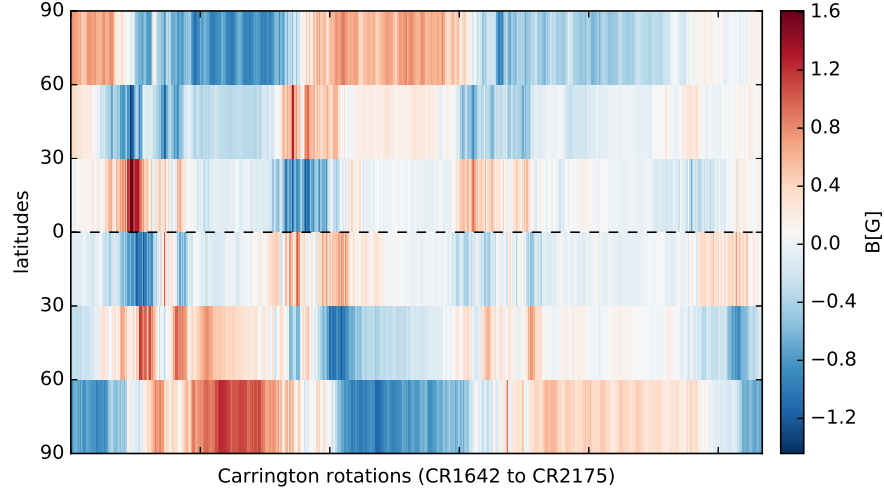


**Figure 7.4.:** The latitudinal distribution of the large-scale magnetic field of the Sun. The Y-axis shows latitude bands of  $30^\circ$  each. The X-axis is the Carrington rotation from CR1642 to CR2175 (534 in total). The equator is shown by the black dashed line.

caused by the lower resolution of the stellar observations.

The large-scale ‘Butterfly’ diagram of the Sun is reconstructed for 534 Carrington rotations. The data was taken from [Vidotto \(2016\)](#) and spans from 1976 to early 2016. The lower order harmonics mode of  $l_{\max}=10$  is used to be consistent with stellar observations. The solar large-scale ‘Butterfly’ is shown in Fig. 7.4, where the average magnetic field per latitude band of  $30^\circ$  is shown for each Carrington rotation. Figure 7.4 was created using the same  $30^\circ$  latitudinal bands as in 61 Cyg A. We detect similarities between the large-scale patterns in Figs. 7.3 and 7.4. The polarity reversals in Fig. 7.4 agree with the sunspot cycle and the global magnetic cycle of the Sun. The decreasing strength of the large-scale field towards the later half of the plot is reflective of the decreasing number of sunspots in recent years. Fig 7.4 shows that in spite of the lowered resolution of the solar ‘Butterfly’ diagram, the polarity reversals in the polar fields are reconstructed without fail. Figure 7.4 is the first step towards investigating the solar cycle from a stellar physics perspective. The next step will be to lower the temporal resolution in combination with the lower order harmonics to make comparisons with other cool stars.

In the upcoming years my research will focus on magnetic field evolution in sun-like stars as seen in different layers of the stellar atmosphere, the photosphere, the chromosphere and the corona. Both activity and magnetic cycle will be investigated in this project (a Marie Skłodowska Curie individual fellowship application has been submitted). The magnetic cy-

cle will be monitored using magnetic field reconstructions using ZDI. This will provide information about the photospheric magnetic field. Chromospheric activity will be determined simultaneously to record the chromospheric cycle. Additionally, X-ray observations of the corona will be carried out to investigate the presence of coronal activity cycles. The coronal activity observations will also be complemented by stellar winds modelling. It is the coronal magnetic fields which can interact with the magnetosphere of planets. In the Sun the solar winds heavily influence space weather conditions. But little is known about the evolution of stellar winds in other cool stars. This project will combine observing techniques with theoretical models providing valuable information about the magnetic field evolution of the stars at different atmospheric heights, and its possible impact on the space weather of exoplanets.

# Bibliography

- ANDRETTA, V., BUSÀ, I., GOMEZ, M. T. & TERRANEGRA, L. (2005) The Ca II Infrared Triplet as a stellar activity diagnostic . I. Non-LTE photospheric profiles and definition of the  $R_{IRT}$  indicator. *A&A*, **430**, 669–677.
- ANGLADA-ESCUDE, G. & BUTLER, R. P. (2012) The HARPS-TERRA Project. I. Description of the Algorithms, Performance, and New Measurements on a Few Remarkable Stars Observed by HARPS. *ApJS*, **200**, 15.
- ARRIAGADA, P. (2011) Chromospheric Activity of Southern Stars from the Magellan Planet Search Program. *ApJ*, **734**, 70.
- AURIÈRE, M. (2003) Stellar Polarimetry with NARVAL. In *EAS Publications Series*, edited by J. Arnaud & N. Meunier, vol. 9 of *EAS Publications Series*.
- AYRES, T. R. (2015) The Far-Ultraviolet Ups and Downs of Alpha Centauri. *AJ*, **149**, 58.
- BABCOCK, H. W. (1961) The Topology of the Sun’s Magnetic Field and the 22-YEAR Cycle. *ApJ*, **133**, 572.
- BAINES, E. K. & ARMSTRONG, J. T. (2012) Confirming Fundamental Properties of the Exoplanet Host Star epsilon Eridani Using the Navy Optical Interferometer. *ApJ*, **744**, 138.
- BALIUNAS, S. L., DONAHUE, R. A., SOON, W. H., HORNE, J. H., FRAZER, J., WOODARD-EKLUND, L., BRADFORD, M., RAO, L. M. ET AL. (1995) Chromospheric variations in main-sequence stars. *ApJ*, **438**, 269–287, doi:10.1086/175072.
- BALIUNAS, S. L., HORNE, J. H., PORTER, A., DUNCAN, D. K., FRAZER, J., LANING, H., MISCH, A., MUELLER, J. ET AL. (1985) Time-series measurements of chromospheric CA II H and K emission in cool stars and the search for differential rotation. *ApJ*, **294**, 310–325.
- BARNES, S. A. (2007) Ages for Illustrative Field Stars Using Gyrochronology: Viability, Limitations, and Errors. *ApJ*, **669**, 1167–1189.
- BASRI, G., WALKOWICZ, L. M. & REINERS, A. (2013) Comparison of Kepler Photometric Variability with the Sun on Different Timescales. *ApJ*, **769**, 37.
- BESSEL, F. W. (1838) On the parallax of 61 Cygni. *MNRAS*, **4**, 152–161.
- BINGHAM, R. G. (1979) Grating spectrometers and spectrographs re-examined. *QJRAS*, **20**, 395–421.

- BOEHM-VITENSE, E. (1989) *Introduction to stellar astrophysics. Volume 1 - Basic stellar observations and data. Volume 2 - Stellar atmospheres.*
- BÖHM-VITENSE, E. (2007) Chromospheric Activity in G and K Main-Sequence Stars, and What It Tells Us about Stellar Dynamos. *ApJ*, **657**, 486–493, doi: 10.1086/510482.
- BONFILS, X., DELFOSSE, X., UDRY, S., FORVEILLE, T., MAYOR, M., PERRIER, C., BOUCHY, F., GILLON, M. ET AL. (2013) The HARPS search for southern extra-solar planets. XXXI. The M-dwarf sample. *A&A*, **549**, A109.
- BORO SAIKIA, S., JEFFERS, S. V., MORIN, J., PETIT, P., FOLSOM, C. P., MARSDEN, S. C., DONATI, J.-F., CAMERON, R. ET AL. (2016a) A solar-like magnetic cycle on the mature K-dwarf 61 Cyg A (HD 201091). *ArXiv e-prints*.
- BORO SAIKIA, S., JEFFERS, S. V., PETIT, P., MARSDEN, S., MORIN, J. & FOLSOM, C. P. (2015) Variable magnetic field geometry of the young sun HN Pegasi (HD 206860). *A&A*, **573**, A17.
- BORO SAIKIA, S., MARVIN, C. J., JEFFERS, S. V., REINERS, A., MARSDEN, S. C., CAMERON, R., PETIT, P., WARNECKE, J. ET AL. (2016b) Göttingen chromospheric activity catalogue: Questioning the Active branch of stellar activity cycles. *A&A(submitted)*.
- BRANDENBURG, A., SAAR, S. H. & TURPIN, C. R. (1998) Time Evolution of the Magnetic Activity Cycle Period. *ApJ*, **498**, L51–L54.
- BRANDENBURG, A. & SUBRAMANIAN, K. (2005) Astrophysical magnetic fields and non-linear dynamo theory. *Phys. Rep.*, **417**, 1–209.
- BROWN, B. P., BROWNING, M. K., BRUN, A. S., MIESCH, M. S. & TOOMRE, J. (2010) Persistent Magnetic Wreaths in a Rapidly Rotating Sun. *ApJ*, **711**, 424–438.
- BROWN, S. F., DONATI, J.-F., REES, D. E. & SEMEL, M. (1991) Zeeman-Doppler imaging of solar-type and AP stars. IV - Maximum entropy reconstruction of 2D magnetic topologies. *A&A*, **250**, 463–474.
- BUSÀ, I., AZNAR CUADRADO, R., TERRANEGRA, L., ANDRETTA, V. & GOMEZ, M. T. (2007) The Ca II infrared triplet as a stellar activity diagnostic. II. Test and calibration with high resolution observations. *A&A*, **466**, 1089–1098.
- CATALA, C., DONATI, J.-F., SHKOLNIK, E., BOHLENDER, D. & ALECIA, E. (2007) The magnetic field of the planet-hosting star  $\tau$  Bootis. *MNRAS*, **374**, L42–L46.
- CHARBONNEAU, P. (2010) Dynamo Models of the Solar Cycle. *Living Reviews in Solar Physics*, **7**, 3.
- CINCUNEGUI, C., DÍAZ, R. F. & MAUAS, P. J. D. (2007)  $H\alpha$  and the Ca II H and K lines as activity proxies for late-type stars. *A&A*, **469**, 309–317.
- CONDON, E. U. & SHORTLEY, G. H. (1963) *The theory of atomic spectra*.

- DEROSA, M. L., BRUN, A. S. & HOEKSEMA, J. T. (2012) Solar Magnetic Field Reversals and the Role of Dynamo Families. *ApJ*, **757**, 96.
- DONATI, J.-F. (2003) ESPaDOnS: An Echelle Spectropolarimetric Device for the Observation of Stars at CFHT. In *Solar Polarization*, edited by J. Trujillo-Bueno & J. Sanchez Almeida, vol. 307 of *Astronomical Society of the Pacific Conference Series*.
- DONATI, J.-F. & BROWN, S. F. (1997) Zeeman-Doppler imaging of active stars. V. Sensitivity of maximum entropy magnetic maps to field orientation. *A&A*, **326**, 1135–1142.
- DONATI, J.-F. & COLLIER CAMERON, A. (1997) Differential rotation and magnetic polarity patterns on AB Doradus. *MNRAS*, **291**, 1–19.
- DONATI, J.-F., COLLIER CAMERON, A., SEMEL, M., HUSSAIN, G. A. J., PETIT, P., CARTER, B. D., MARSDEN, S. C., MENGEL, M. ET AL. (2003) Dynamo processes and activity cycles of the active stars AB Doradus, LQ Hydrae and HR 1099. *MNRAS*, **345**, 1145–1186.
- DONATI, J.-F., GREGORY, S. G., ALENCAR, S. H. P., HUSSAIN, G., BOUVIER, J., DOUGADOS, C., JARDINE, M. M., MÉNARD, F. ET AL. (2012) Magnetometry of the classical T Tauri star GQ Lup: non-stationary dynamos and spin evolution of young Suns. *MNRAS*, **425**, 2948–2963.
- DONATI, J.-F., HOWARTH, I. D., JARDINE, M. M., PETIT, P., CATALA, C., LANDSTREET, J. D., BOURET, J.-C., ALECIAN, E. ET AL. (2006) The surprising magnetic topology of  $\tau$  Sco: fossil remnant or dynamo output? *MNRAS*, **370**, 629–644.
- DONATI, J.-F. & LANDSTREET, J. D. (2009) Magnetic Fields of Nondegenerate Stars. *ARA&A*, **47**, 333–370.
- DONATI, J.-F., MENGEL, M., CARTER, B. D., MARSDEN, S., COLLIER CAMERON, A. & WICHMANN, R. (2000) Surface differential rotation and prominences of the Lupus post T Tauri star RX J1508.6-4423. *MNRAS*, **316**, 699–715.
- DONATI, J.-F., MOUTOU, C., FARÈS, R., BOHLENDER, D., CATALA, C., DELEUIL, M., SHKOLNIK, E., COLLIER CAMERON, A. ET AL. (2008) Magnetic cycles of the planet-hosting star  $\tau$  Bootis. *MNRAS*, **385**, 1179–1185.
- DONATI, J.-F., SEMEL, M., CARTER, B. D., REES, D. E. & COLLIER CAMERON, A. (1997) Spectropolarimetric observations of active stars. *MNRAS*, **291**, 658.
- DONATI, J.-F., SEMEL, M. & REES, D. E. (1992) Circularly polarized spectroscopic observations of RS CVn systems. *A&A*, **265**, 669–681.
- DUNCAN, D. K., VAUGHAN, A. H., WILSON, O. C., PRESTON, G. W., FRAZER, J., LANNING, H., MISCH, A., MUELLER, J. ET AL. (1991) CA II H and K measurements made at Mount Wilson Observatory, 1966-1983. *ApJS*, **76**, 383–430.

- DURNEY, B. R., MIHALAS, D. & ROBINSON, R. D. (1981) A preliminary interpretation of stellar chromospheric CA II emission variations within the framework of stellar dynamo theory. *PASP*, **93**, 537–543.
- EBERHARD, G. & SCHWARZSCHILD, K. (1913) On the reversal of the calcium lines H and K in stellar spectra. *ApJ*, **38**.
- EISENBEISS, T., AMMLER-VON EIFF, M., ROELL, T., MUGRAUER, M., ADAM, C., NEUHÄUSER, R., SCHMIDT, T. O. B. & BEDALOV, A. (2013) The Hercules-Lyra association revisited. New age estimation and multiplicity study. *A&A*, **556**, A53.
- ERTEL, S., WOLF, S., MARSHALL, J. P., EIROA, C., AUGEREAU, J.-C., KRIVOV, A. V., LÖHNE, T., ABSIL, O. ET AL. (2012) A peculiar class of debris disks from Herschel/DUNES. A steep fall off in the far infrared. *A&A*, **541**, A148.
- FARES, R., DONATI, J.-F., MOUTOU, C., BOHLENDER, D., CATALA, C., DELEUIL, M., SHKOLNIK, E., COLLIER CAMERON, A. ET AL. (2009) Magnetic cycles of the planet-hosting star  $\tau$  Bootis - II. A second magnetic polarity reversal. *MNRAS*, **398**, 1383–1391.
- FARES, R., DONATI, J.-F., MOUTOU, C., JARDINE, M., CAMERON, A. C., LANZA, A. F., BOHLENDER, D., DIETERS, S. ET AL. (2012) Magnetic field, differential rotation and activity of the hot-Jupiter-hosting star HD 179949. *MNRAS*, **423**, 1006–1017.
- FARES, R., DONATI, J.-F., MOUTOU, C., JARDINE, M. M., GRIESSMEIER, J.-M., ZARKA, P., SHKOLNIK, E. L., BOHLENDER, D. ET AL. (2010) Searching for star-planet interactions within the magnetosphere of HD189733. *MNRAS*, **406**, 409–419.
- FARES, R., MOUTOU, C., DONATI, J.-F., CATALA, C., SHKOLNIK, E. L., JARDINE, M. M., CAMERON, A. C. & DELEUIL, M. (2013) A small survey of the magnetic fields of planet-host stars. *MNRAS*, **435**, 1451–1462.
- FAVATA, F., MICELA, G., ORLANDO, S., SCHMITT, J. H. M. M., SCIORTINO, S. & HALL, J. (2008) The X-ray cycle in the solar-type star HD 81809. XMM-Newton observations and implications for the coronal structure. *A&A*, **490**, 1121–1126.
- FOLSOM, C. P., PETIT, P., BOUVIER, J., LÈBRE, A., AMARD, L., PALACIOS, A., MORIN, J., DONATI, J.-F. ET AL. (2016) The evolution of surface magnetic fields in young solar-type stars - I. The first 250 Myr. *MNRAS*, **457**, 580–607.
- FRASCA, A., FREIRE FERRERO, R., MARILLI, E. & CATALANO, S. (2000) Spots and plagues on a young main-sequence solar-type star: HD 206860. *A&A*, **364**, 179–190.
- FUHRMANN, K. (2004) Nearby stars of the Galactic disk and halo. III. *Astronomische Nachrichten*, **325**, 3–80.
- GAIDOS, E. J. (1998) Nearby Young Solar Analogs. I. Catalog and Stellar Characteristics. *PASP*, **110**, 1259–1276.

- GIZIS, J. E., REID, I. N. & HAWLEY, S. L. (2002) The Palomar/MSU Nearby Star Spectroscopic Survey. III. Chromospheric Activity, M Dwarf Ages, and the Local Star Formation History. *AJ*, **123**, 3356–3369.
- GOMES DA SILVA, J., SANTOS, N. C., BOISSE, I., DUMUSQUE, X. & LOVIS, C. (2013) On the long-term correlation between the flux in the Ca II H and K and H $\alpha$  lines for FGK stars. *ArXiv e-prints*.
- GRAY, R. O., CORBALLY, C. J., GARRISON, R. F., MCFADDEN, M. T., BUBAR, E. J., MCGAHEE, C. E., O'DONOGHUE, A. A. & KNOX, E. R. (2006) Contributions to the Nearby Stars (NStars) Project: Spectroscopy of Stars Earlier than M0 within 40 pc-The Southern Sample. *AJ*, **132**, 161–170.
- GÜDEL, M. (2004) X-ray astronomy of stellar coronae. *A&A Rev.*, **12**, 71–237.
- HACKMAN, T., LEHTINEN, J., ROSÉN, L., KOCHUKHOV, O. & KÄPYLÄ, M. J. (2016) Zeeman-Doppler imaging of active young solar-type stars. *A&A*, **587**, A28.
- HALE, G. E. (1908) On the Probable Existence of a Magnetic Field in Sun-Spots. *ApJ*, **28**, 315.
- HALL, J. C. (2008) Stellar Chromospheric Activity. *Living Reviews in Solar Physics*, **5**(2), URL <http://www.livingreviews.org/lrsp-2008-2>.
- HALL, J. C., HENRY, G. W., LOCKWOOD, G. W., SKIFF, B. A. & SAAR, S. H. (2009) The Activity and Variability of the Sun and Sun-Like Stars. II. Contemporaneous Photometry and Spectroscopy of Bright Solar Analogs. *AJ*, **138**, 312–322.
- HALL, J. C., LOCKWOOD, G. W. & SKIFF, B. A. (2007) The Activity and Variability of the Sun and Sun-like Stars. I. Synoptic Ca II H and K Observations. *AJ*, **133**, 862–881.
- HARTMANN, L., SODERBLOM, D. R., NOYES, R. W., BURNHAM, N. & VAUGHAN, A. H. (1984) An analysis of the Vaughan-Preston survey of chromospheric emission. *ApJ*, **276**, 254–265.
- HATHAWAY, D. H. (2010) The Solar Cycle. *Living Reviews in Solar Physics*, **7**, 1.
- HEMPELMANN, A., ROBRADÉ, J., SCHMITT, J. H. M. M., FAVATA, F., BALIUNAS, S. L. & HALL, J. C. (2006) Coronal activity cycles in 61 Cygni. *A&A*, **460**, 261–267.
- HEMPELMANN, A., SCHMITT, J. H. M. M. & STĘPIEŃ, K. (1996) Coronal X-ray emission of cool stars in relation to chromospheric activity and magnetic cycles. *A&A*, **305**, 284.
- HENRY, T. J., SODERBLOM, D. R., DONAHUE, R. A. & BALIUNAS, S. L. (1996) A Survey of Ca II H and K Chromospheric Emission in Southern Solar-Type Stars. *AJ*, **111**, 439.
- HORNE, J. H. & BALIUNAS, S. L. (1986) A prescription for period analysis of unevenly sampled time series. *ApJ*, **302**, 757–763.

- ISAACSON, H. & FISCHER, D. (2010) Chromospheric Activity and Jitter Measurements for 2630 Stars on the California Planet Search. *ApJ*, **725**, 875–885.
- JEFFERIES, J. T. & THOMAS, R. N. (1959) Source Function in a Non-Equilibrium Atmosphere. III. The Influence of a Chromosphere. *ApJ*, **129**, 401.
- JEFFERS, S. V. & DONATI, J.-F. (2008) High levels of surface differential rotation on the young G0 dwarf HD171488. *MNRAS*, **390**, 635–644.
- JEFFERS, S. V., PETIT, P., MARSDEN, S. C., MORIN, J., DONATI, J.-F. & FOLSOM, C. P. (2014)  $\epsilon$  Eridani: an active K dwarf and a planet hosting star?. The variability of its large-scale magnetic field topology. *A&A*, **569**, A79.
- KERVELLA, P., MÉRAND, A., PICHON, B., THÉVENIN, F., HEITER, U., BIGOT, L., TEN BRUMMELAAR, T. A., MCALISTER, H. A. ET AL. (2008) The radii of the nearby K5V and K7V stars 61 Cygni A and B. CHARA/FLUOR interferometry and CESAM2k modeling. *A&A*, **488**, 667–674.
- KOCHUKHOV, O., MAKAGANIUK, V. & PISKUNOV, N. (2010) Least-squares deconvolution of the stellar intensity and polarization spectra. *A&A*, **524**, A5.
- KOCHUKHOV, O. & PISKUNOV, N. (2002) Doppler Imaging of stellar magnetic fields. II. Numerical experiments. *A&A*, **388**, 868–888.
- KRAUSE, F. & RAEDLER, K.-H. (1980) *Mean-field magnetohydrodynamics and dynamo theory*.
- LANDI DEGL'INNOCENTI, E. & LANDOLFI, M. (eds.) (2004) *Polarization in Spectral Lines*, vol. 307 of *Astrophysics and Space Science Library*.
- LANDIN, N. R., MENDES, L. T. S. & VAZ, L. P. R. (2010) Theoretical values of convective turnover times and Rossby numbers for solar-like, pre-main sequence stars. *A&A*, **510**, A46.
- LEGGETT, S. K., SAUMON, D., ALBERT, L., CUSHING, M. C., LIU, M. C., LUHMAN, K. L., MARLEY, M. S., KIRKPATRICK, J. D. ET AL. (2008) HN Peg B: A Test of Models of the L to T Dwarf Transition. *ApJ*, **682**, 1256–1263.
- LEIGHTON, R. B. (1964) Transport of Magnetic Fields on the Sun. *ApJ*, **140**, 1547.
- LEIGHTON, R. B. (1969) A Magneto-Kinematic Model of the Solar Cycle. *ApJ*, **156**, 1.
- LINSKY, J. L., MCCLINTOCK, W., ROBERTSON, R. M. & WORDEN, S. P. (1979) Stellar model chromospheres. X - High-resolution, absolute flux profiles of the CA II H and K lines in stars of spectral types F0-M2. *ApJS*, **41**, 47–74.
- LIVINGSTON, W., WALLACE, L., WHITE, O. R. & GIAMPAPA, M. S. (2007) Sun-as-a-Star Spectrum Variations 1974-2006. *ApJ*, **657**, 1137–1149.

- LOCKWOOD, G. W., SKIFF, B. A., HENRY, G. W., HENRY, S., RADICK, R. R., BALIUNAS, S. L., DONAHUE, R. A. & SOON, W. (2007) Patterns of Photometric and Chromospheric Variation among Sun-like Stars: A 20 Year Perspective. *ApJS*, **171**, 260–303.
- LOMB, N. R. (1976) Least-squares frequency analysis of unequally spaced data. *Ap&SS*, **39**, 447–462.
- LÓPEZ-SANTIAGO, J., MONTES, D., CRESPO-CHACÓN, I. & FERNÁNDEZ-FIGUEROA, M. J. (2006) The Nearest Young Moving Groups. *ApJ*, **643**, 1160–1165.
- LOVIS, C., DUMUSQUE, X., SANTOS, N. C., BOUCHY, F., MAYOR, M., PEPE, F., QUELOZ, D., SÉGRANSAN, D. ET AL. (2011) The HARPS search for southern extra-solar planets. XXXI. Magnetic activity cycles in solar-type stars: statistics and impact on precise radial velocities. *A&A*.
- LUHMAN, K. L., PATTEN, B. M., MARENGO, M., SCHUSTER, M. T., HORA, J. L., ELLIS, R. G., STAUFFER, J. R., SONNETT, S. M. ET AL. (2007) Discovery of Two T Dwarf Companions with the Spitzer Space Telescope. *ApJ*, **654**, 570–579.
- LUNDIN, R., LAMMER, H. & RIBAS, I. (2007) Planetary Magnetic Fields and Solar Forcing: Implications for Atmospheric Evolution. *Space Sci. Rev.*, **129**, 245–278.
- MALKOV, O. Y., TAMAZIAN, V. S., DOCOBO, J. A. & CHULKOV, D. A. (2012) Dynamical masses of a selected sample of orbital binaries. *A&A*, **546**, A69.
- MAMAJEK, E. E. & HILLENBRAND, L. A. (2008) Improved Age Estimation for Solar-Type Dwarfs Using Activity-Rotation Diagnostics. *ApJ*, **687**, 1264–1293.
- MANN, A. W., GAIDOS, E. & ANSDELL, M. (2013) Spectro-thermometry of M Dwarfs and Their Candidate Planets: Too Hot, Too Cool, or Just Right? *ApJ*, **779**, 188.
- MARSDEN, S. C., PETIT, P., JEFFERS, S. V., MORIN, J., FARES, R., REINERS, A., DO NASCIMENTO, J.-D., AURIÈRE, M. ET AL. (2014) A BCool magnetic snapshot survey of solar-type stars. *MNRAS*, **444**, 3517–3536.
- MARSDEN, S. C., WAITE, I. A., CARTER, B. D. & DONATI, J.-F. (2004) Doppler imaging of G-dwarfs in two young open clusters. *Astronomische Nachrichten*, **325**, 246–246.
- MASSEY, P. & HANSON, M. M. (2013) *Astronomical Spectroscopy*.
- MAUNDER, E. W. (1904) Note on the distribution of sun-spots in heliographic latitude, 1874-1902. *MNRAS*, **64**, 747–761.
- MENGEL, M. W., FARES, R., MARSDEN, S. C., CARTER, B. D., JEFFERS, S. V., PETIT, P., DONATI, J.-F., FOLSOM, C. P. ET AL. (2016) The Evolving Magnetic Topology of  $\tau$  Bo<sup>o</sup>tis. *ArXiv e-prints*.
- MESSINA, S. & GUINAN, E. F. (2002) Magnetic activity of six young solar analogues I. Starspot cycles from long-term photometry. *A&A*, **393**, 225–237.

- MESSINA, S. & GUINAN, E. F. (2003) Magnetic activity of six young solar analogues II. Surface Differential Rotation from long-term photometry. *A&A*, **409**, 1017–1030.
- METCALFE, T. S., BUCCINO, A. P., BROWN, B. P., MATHUR, S., SODERBLOM, D. R., HENRY, T. J., MAUAS, P. J. D., PETRUCCI, R. ET AL. (2013) Magnetic Activity Cycles in the Exoplanet Host Star epsilon Eridani. *ApJ*, **763**, L26.
- MEUNIER, N. & DELFOSSE, X. (2009) On the correlation between Ca and H $\alpha$  solar emission and consequences for stellar activity observations. *A&A*, **501**, 1103–1112.
- MIDDELKOOP, F. (1982) Magnetic structure in cool stars. IV - Rotation and CA II H and K emission of main-sequence stars. *A&A*, **107**, 31–35.
- MITTAG, M., SCHMITT, J. H. M. M. & SCHRÖDER, K.-P. (2013) Ca II H+K fluxes from S-indices of large samples: a reliable and consistent conversion based on PHOENIX model atmospheres. *A&A*, **549**, A117.
- MORGENTHALER, A., PETIT, P., MORIN, J., AURIÈRE, M., DINTRANS, B., KONSTANTINOVA-ANTOVA, R. & MARSDEN, S. (2011) Direct observation of magnetic cycles in Sun-like stars. *Astronomische Nachrichten*, **332**, 866.
- MORGENTHALER, A., PETIT, P., SAAR, S., SOLANKI, S. K., MORIN, J., MARSDEN, S. C., AURIÈRE, M., DINTRANS, B. ET AL. (2012) Long-term magnetic field monitoring of the Sun-like star  $\xi$  Bootis A. *A&A*, **540**, A138.
- NOYES, R. W., HARTMANN, L. W., BALIUNAS, S. L., DUNCAN, D. K. & VAUGHAN, A. H. (1984a) Rotation, convection, and magnetic activity in lower main-sequence stars. *ApJ*, **279**, 763–777.
- NOYES, R. W., WEISS, N. O. & VAUGHAN, A. H. (1984b) The relation between stellar rotation rate and activity cycle periods. *ApJ*, **287**, 769–773.
- ORLANDO, S., PERES, G. & REALE, F. (2001) The Sun as an X-Ray Star. IV. The Contribution of Different Regions of the Corona to Its X-Ray Spectrum. *ApJ*, **560**, 499–513.
- OSSENDRIJVER, M. (2003) The solar dynamo. *A&A Rev.*, **11**, 287–367.
- PACE, G., MELENDEZ, J., PASQUINI, L., CARRARO, G., DANZIGER, J., FRANÇOIS, P., MATTEUCCI, F. & SANTOS, N. C. (2009) An investigation of chromospheric activity spanning the Vaughan-Preston gap: impact on stellar ages. *A&A*, **499**, L9–L12.
- PARKER, E. N. (1955) Hydromagnetic Dynamo Models. *ApJ*, **122**, 293.
- PERRYMAN, M. A. C., LINDEGREN, L., KOVALEVSKY, J., HOEG, E., BASTIAN, U., BERNACCA, P. L., CRÉZÉ, M., DONATI, F. ET AL. (1997) The HIPPARCOS Catalogue. *A&A*, **323**, L49–L52.

- PETIT, P., AURIÈRE, M., KONSTANTINOVA-ANTOVA, R., MORGENTHALER, A., PERIN, G., ROUDIER, T. & DONATI, J.-F. (2013) Magnetic Fields and Convection in the Cool Supergiant Betelgeuse. In *Lecture Notes in Physics, Berlin Springer Verlag*, vol. 857 of *Lecture Notes in Physics, Berlin Springer Verlag*.
- PETIT, P., DINTRANS, B., MORGENTHALER, A., VAN GROOTEL, V., MORIN, J., LANOUX, J., AURIÈRE, M. & KONSTANTINOVA-ANTOVA, R. (2009) A polarity reversal in the large-scale magnetic field of the rapidly rotating sun HD 190771. *A&A*, **508**, L9–L12.
- PETIT, P., DINTRANS, B., SOLANKI, S. K., DONATI, J.-F., AURIÈRE, M., LIGNIÈRES, F., MORIN, J., PALETOU, F. ET AL. (2008) Toroidal versus poloidal magnetic fields in Sun-like stars: a rotation threshold. *MNRAS*, **388**, 80–88.
- PETIT, P., DONATI, J.-F. & COLLIER CAMERON, A. (2002) Differential rotation of cool active stars: the case of intermediate rotators. *MNRAS*, **334**, 374–382.
- PEVTSOV, A. A., FISHER, G. H., ACTON, L. W., LONGCOPE, D. W., JOHNS-KRULL, C. M., KANKELBORG, C. C. & METCALF, T. R. (2003) The Relationship Between X-Ray Radiance and Magnetic Flux. *ApJ*, **598**, 1387–1391, doi: 10.1086/378944.
- PISKUNOV, N. & KOCHUKHOV, O. (2002) Doppler Imaging of stellar magnetic fields. I. Techniques. *A&A*, **381**, 736–756.
- POLS, O. R., SCHRÖDER, K.-P., HURLEY, J. R., TOUT, C. A. & EGGLETON, P. P. (1998) Stellar evolution models for  $Z = 0.0001$  to  $0.03$ . *MNRAS*, **298**, 525–536.
- RADICK, R. R., LOCKWOOD, G. W., SKIFF, B. A. & BALIUNAS, S. L. (1998) Patterns of Variation among Sun-like Stars. *ApJS*, **118**, 239–258.
- REES, D. E. & SEMEL, M. D. (1979) Line formation in an unresolved magnetic element - A test of the centre of gravity method. *A&A*, **74**, 1–5.
- REINERS, A. (2012) Observations of Cool-Star Magnetic Fields. *Living Reviews in Solar Physics*, **9**.
- REINERS, A. & BASRI, G. (2006) Measuring Magnetic Fields in Ultracool Stars and Brown Dwarfs. *ApJ*, **644**, 497–509.
- REINERS, A. & SCHMITT, J. H. M. M. (2003) Rotation and differential rotation in field F- and G-type stars. *A&A*, **398**, 647–661.
- ROBINSON, JR., R. D. (1980) Magnetic field measurements on stellar sources - A new method. *ApJ*, **239**, 961–967.
- ROBRADÉ, J., SCHMITT, J. H. M. M. & FAVATA, F. (2012) Coronal activity cycles in nearby G and K stars. XMM-Newton monitoring of 61 Cygni and  $\alpha$  Centauri. *A&A*, **543**, A84.

- ROSÉN, L., KOCHUKHOV, O., HACKMAN, T. & LEHTINEN, J. (2016) Magnetic fields of young solar twins. *A&A*.
- ROSÉN, L., KOCHUKHOV, O. & WADE, G. A. (2015) First Zeeman Doppler Imaging of a Cool Star Using all Four Stokes Parameters. *ApJ*, **805**, 169.
- RUEEDI, I., SOLANKI, S. K., MATHYS, G. & SAAR, S. H. (1997) Magnetic field measurements on moderately active cool dwarfs. *A&A*, **318**, 429–442.
- RUTTEN, R. G. M. (1984) Magnetic structure in cool stars. VII - Absolute surface flux in CA II H and K line cores. *A&A*, **130**, 353–360.
- RUTTEN, R. G. M. (1987) Magnetic structure in cool stars. XII - Chromospheric activity and rotation of giants and dwarfs. *A&A*, **177**, 131–142.
- SAAR, S. H. (1988) Improved methods for the measurement and analysis of stellar magnetic fields. *ApJ*, **324**, 441–465.
- SAAR, S. H. (1996) Recent magnetic fields measurements of stellar. In *Stellar Surface Structure*, edited by K. G. Strassmeier & J. L. Linsky, vol. 176 of *IAU Symposium*.
- SAAR, S. H. & BALIUNAS, S. L. (1992) Recent Advances in Stellar Cycle Research. In *The Solar Cycle*, edited by K. L. Harvey, vol. 27 of *Astronomical Society of the Pacific Conference Series*.
- SAAR, S. H. & BRANDENBURG, A. (1999) Time Evolution of the Magnetic Activity Cycle Period. II. Results for an Expanded Stellar Sample. *ApJ*, **524**, 295–310, doi: 10.1086/307794.
- SAAR, S. H. & LINSKY, J. L. (1985) The photospheric magnetic field of the dM3.5e flare star AD Leonis. *ApJ*, **299**, L47–L50.
- SANDERSON, T. R., APPOURCHAUX, T., HOEKSEMA, J. T. & HARVEY, K. L. (2003) Observations of the Sun’s magnetic field during the recent solar maximum. *Journal of Geophysical Research (Space Physics)*, **108**, 1035.
- SANZ-FORCADA, J., STELZER, B. & METCALFE, T. S. (2013) *t*Horologi, the first coronal activity cycle in a young solar-like star. *A&A*, **553**, L6.
- SCARGLE, J. D. (1982) Studies in astronomical time series analysis. II - Statistical aspects of spectral analysis of unevenly spaced data. *ApJ*, **263**, 835–853.
- SCHRIJVER, C. J. (1987) Magnetic structure in cool stars. XI - Relations between radiative fluxes measuring stellar activity, and evidence for two components in stellar chromospheres. *A&A*, **172**, 111–123.
- SCHRIJVER, C. J., COTE, J., ZWAAN, C. & SAAR, S. H. (1989) Relations between the photospheric magnetic field and the emission from the outer atmospheres of cool stars. I - The solar CA II K line core emission. *ApJ*, **337**, 964–976.

- SCHRÖDER, K.-P., MITTAG, M., HEMPELMANN, A., GONZÁLEZ-PÉREZ, J. N. & SCHMITT, J. H. M. M. (2013) What do the Mt. Wilson stars tell us about solar activity? *A&A*, **554**, A50.
- SCHWABE, M. (1844) Sonnenbeobachtungen im Jahre 1843. Von Herrn Hofrath Schwabe in Dessau. *Astronomische Nachrichten*, **21**, 233.
- SEE, V., JARDINE, M., VIDOTTO, A. A., DONATI, J.-F., BORO SAIKIA, S., BOUVIER, J., FARES, R., FOLSOM, C. P. ET AL. (2016) The connection between stellar activity cycles and magnetic field topology. *MNRAS*, **462**, 4442–4450.
- SEMEL, M. (1989) Zeeman-Doppler imaging of active stars. I - Basic principles. *A&A*, **225**, 456–466.
- SKILLING, J. & BRYAN, R. K. (1984) Maximum Entropy Image Reconstruction - General Algorithm. *MNRAS*, **211**, 111.
- SOLANKI, S. K., INHESTER, B. & SCHÜSSLER, M. (2006) The solar magnetic field. *Reports on Progress in Physics*, **69**, 563–668.
- STEENBECK, M., KRAUSE, F. & RÄDLER, K.-H. (1966) Berechnung der mittleren LORENTZ-Feldstärke  $\langle E \rangle$  für ein elektrisch leitendes Medium in turbulenter, durch CORIOLIS-Kräfte beeinflusster Bewegung. *Zeitschrift Naturforschung Teil A*, **21**, 369.
- STOKES, G. G. (1852) On the Change of Refrangibility of Light. *Philosophical Transactions of the Royal Society of London Series I*, **142**, 463–562.
- TAKEDA, G., FORD, E. B., SILLS, A., RASIO, F. A., FISCHER, D. A. & VALENTI, J. A. (2007) Structure and Evolution of Nearby Stars with Planets. II. Physical Properties of ~1000 Cool Stars from the SPOCS Catalog. *ApJS*, **168**, 297–318.
- VALENTI, J. A. & FISCHER, D. A. (2005) Spectroscopic Properties of Cool Stars (SPOCS). I. 1040 F, G, and K Dwarfs from Keck, Lick, and AAT Planet Search Programs. *ApJS*, **159**, 141–166.
- VAN LEEUWEN, F. (2007) Validation of the new Hipparcos reduction. *A&A*, **474**, 653–664.
- VAUGHAN, A. H. & PRESTON, G. W. (1980) A survey of chromospheric CA II H and K emission in field stars of the solar neighborhood. *PASP*, **92**, 385–391.
- VERNAZZA, J. E., AVRETT, E. H. & LOESER, R. (1981) Structure of the solar chromosphere. III - Models of the EUV brightness components of the quiet-sun. *ApJS*, **45**, 635–725, doi: 10.1086/190731.
- VIDOTTO, A. A. (2016) The magnetic field vector of the Sun-as-a-star. *MNRAS*, **459**, 1533–1542.
- VOGT, S. S. & PENROD, G. D. (1983) Doppler Imaging of spotted stars - Application to the RS Canum Venaticorum star HR 1099. *PASP*, **95**, 565–576.

- WADE, G. A., DONATI, J.-F., LANDSTREET, J. D. & SHORLIN, S. L. S. (2000) Spectropolarimetric measurements of magnetic Ap and Bp stars in all four Stokes parameters. *MNRAS*, **313**, 823–850.
- WAITE, I., MARSDEN, S. C., CARTER, B. C., PETIT, P., DONATI, J. F., JEFFERS, S. V. & BORO SAIKIA, S. (2014) Magnetic fields on young, moderately rotating Sun-like stars I: HD 35296 and HD 29615. *MNRAS*, *submitted*.
- WANG, Y.-M., NASH, A. G. & SHEELEY, JR., N. R. (1989) Magnetic flux transport on the sun. *Science*, **245**, 712–718.
- WILSON, O. C. (1968) Flux Measurements at the Centers of Stellar h- and K-Lines. *ApJ*, **153**, 221.
- WILSON, O. C. (1978) Chromospheric variations in main-sequence stars. *ApJ*, **226**, 379–396.
- WRIGHT, J. T., MARCY, G. W., BUTLER, R. P. & VOGT, S. S. (2004) Chromospheric Ca II Emission in Nearby F, G, K, and M Stars. *ApJS*, **152**, 261–295.
- ZECHMEISTER, M. & KÜRSTER, M. (2009) The generalised Lomb-Scargle periodogram. A new formalism for the floating-mean and Keplerian periodograms. *A&A*, **496**, 577–584.
- ZEEMAN, P. (1897) On the Influence of Magnetism on the Nature of the Light Emitted by a Substance. *ApJ*, **5**, 332.
- ZUCKERMAN, B. & SONG, I. (2009) The minimum Jeans mass, brown dwarf companion IMF, and predictions for detection of Y-type dwarfs. *A&A*, **493**, 1149–1154.

## A. appendix

**Table A.1.:** Journal of observations of HN Peg for seven epochs(2007-2013). Column 1 represents the year and date of observations, column 2 is the Heliocentric Julian date, column 3 is the exposure time, column 4 is the signal-to-noise ratio of each Stokes V LSD profile and column 5 represents the error bars in Stokes V LSD profile.

Date	Julian date (2454000+)	Exposure time	S/N	$\sigma_{\text{LSD}}$ $10^{-5}I_c$
2007 July 27	309.595010	2400	33888	2.9509
2007 July 28	310.602470	1200	24226	4.1279
2007 July 29	311.560380	1200	22030	4.5393
2007 July 30	312.547230	1200	23060	4.3366
2007 July 31	313.548380	1200	17034	5.8706
2007 August 2	315.554720	1200	21801	4.5871
2007 August 3	316.551130	1200	21899	4.5664
2007 August 4	317.552700	1200	17688	5.6536
2007 August 8	321.525450	1200	20126	4.9688
2007 August 9	322.545370	1200	12680	7.8868
2007 August 10	323.545440	1200	15856	6.3068
2007 August 13	326.520920	1200	2225	0.0004
2007 August 14	327.534930	1200	19289	5.1843
2007 August 17	330.524710	1200	21711	4.6061
2007 August 18	331.481500	1200	22426	4.4592
2007 August 26	339.432390	1200	3523	0.0003
2008 August 10	689.532480	1200	20933	4.7772
2008 August 12	691.512640	1200	22440	4.4563
2008 August 17	696.541340	1200	14770	6.7706
2008 August 19	698.608480	1200	19645	5.0903
2008 August 20	699.569970	1200	22309	4.4826
2008 August 21	700.499080	1200	16068	6.2235
2008 August 21	700.51924	1200	4218	0.0002
2008 August 22	701.454560	1200	11621	8.6048
2008 August 23	702.529090	1200	26050	3.8388
2008 August 24	703.500480	1200	26143	3.8251
2008 August 25	704.553140	1200	25206	3.9673
2009 June 1	984.634140	1200	18628	5.3684
2009 June 2	985.633550	1200	20178	4.9560
2009 June 3	986.630640	1200	20354	4.9131
2009 June 12	995.615700	1200	6753	0.0001
2009 June 18	1001.610390	1200	2183	0.0005

---

continued.

Date	Julian date (2454000+)	Exposure time	S/N	$\sigma_{\text{LSD}}$ $10^{-5} \text{I}_c$
2009 June 19	1002.632590	1200	7840	0.0001
2009 June 22	1005.639920	1200	18545	5.3923
2009 June 23	1006.610200	1200	16505	6.0586
2009 June 27	1010.568540	1200	17878	5.5936
2009 June 30	1013.598260	1200	18632	5.3672
2009 July 5	1018.658940	1200	10351	9.6608
2010 June 21	1369.590720	1200	18367	5.4444
2010 July 4	1382.615660	1200	23145	4.3206
2010 July 6	1384.584890	1200	23052	4.3381
2010 July 7	1385.533040	1200	22897	4.3674
2010 July 10	1388.555690	1200	19426	5.1477
2010 July 12	1390.561220	1200	15164	6.5946
2010 July 13	1391.543670	1200	13473	7.4222
2010 July 14	1392.566570	1200	19724	5.0700
2010 July 18	1396.485880	1200	22411	4.4621
2010 July 23	1401.561040	1200	23969	4.1721
2010 August 2	1411.510430	1200	19422	5.1488
2010 August 7	1416.561860	1200	21276	4.7002
2010 August 20	1429.547050	1200	15018	6.6587
2011 July 11	1754.590060	1200	15272	6.5481
2011 July 21	1764.613990	1200	21317	4.6911
2011 July 22	1765.579850	1200	21091	4.7414
2011 August 8	1782.512460	1200	17905	5.5850
2011 August 10	1784.515440	1200	17964	5.5668
2011 August 11	1785.571320	1200	19745	5.0646
2011 August 15	1789.590600	1200	18044	5.5420
2011 August 16	1790.530870	1200	19198	5.2088
2011 August 17	1791.472450	1200	—	—
2011 August 18	1792.535280	1200	—	—
2012 June 21	2100.610620	1200	—	—
2012 June 22	2101.635920	1200	—	—
2012 June 23	2102.612400	1200	—	—
2012 June 24	2103.529510	1200	—	—
2012 July 9	2118.614210	1200	—	—
2012 July 15	2124.664630	1200	—	—
2012 July 16	2125.639690	1200	—	—
2012 July 17	2126.631180	1200	—	—
2012 July 18	2127.593570	1200	—	—
2012 July 19	2128.578110	1200	—	—
2012 July 22	2131.572610	1200	—	—
2012 July 23	2132.561810	1200	—	—
2012 July 24	2133.592020	1200	—	—
2012 August 6	2146.566500	1200	—	—

---

---

continued.				
Date	Julian date (2454000+)	Exposure time	S/N	$\sigma_{\text{LSD}}$ $10^{-5}I_c$
2012 August 7	2147.537680	1200	–	–
2013 July 8	2482.556520	1200	21586	4.6327
2013 July 11	2485.512210	1200	14989	6.6715
2013 August 2	2507.629120	1200	16687	5.9928
2013 August 4	2509.533370	1200	21228	4.7107
2013 August 5	2510.636070	1200	17799	5.6183
2013 August 8	2513.550070	1200	17224	5.8058
2013 August 9	2514.559260	1200	20757	4.8178
2013 August 10	2515.562810	1200	21317	4.6912
2013 August 11	2516.582590	1200	21314	4.6917
2013 August 13	2518.601950	1200	21551	4.6401
2013 August 15	2520.501260	1200	20952	4.7728
2013 August 18	2523.532240	1200	20357	4.9122
2013 August 19	2524.518410	1200	22046	4.5360
2013 August 20	2525.463280	1200	21075	4.7450
2013 August 21	2526.533220	1200	19830	5.0429
<sup>1</sup>				

---



---

<sup>1</sup>The spectropolarimetric observations are not included for 2012.61 and parts of 2011.67 epoch due to instrumental defects at NARVAL. See Sect. 3.3 for details.

**Table A.2.:** Chromospheric activity measurements and magnetic field measurements of HN Peg for seven epochs (2007.67, 2008.71, 2009.54, 2010.62, 2011.67, 2012.61 and 2013.68). From left to right it represents: Julian date, rotational phase, S-index, uncertainty in S-index ( $\sigma_{\text{CaHK}}$ ), H $\alpha$ -index, uncertainty in H $\alpha$ -index ( $\sigma_{\text{H}\alpha}$ ), CaIRT-index, uncertainty in CaIRT-index ( $\sigma_{\text{CaIRT}}$ ), longitudinal magnetic field ( $B_l$ ) and magnetic field of the Null profile ( $N_l$ ).

Julian date (2454000+)	rot.phase	S-index	H $\alpha$ -index	CaIRT-index	$B_l$	$N_l$
309.595010	0.000000	0.3092 $\pm$ 0.0032	0.3234 $\pm$ 0.0008	0.9297 $\pm$ 0.0044	1.8 $\pm$ 0.5	-0.4 $\pm$ 0.5
310.602470	0.219490	0.3158 $\pm$ 0.0044	0.3276 $\pm$ 0.0011	0.9384 $\pm$ 0.0062	-1.6 $\pm$ 0.7	0.8 $\pm$ 0.7
311.560380	0.428185	0.3088 $\pm$ 0.0048	0.3263 $\pm$ 0.0012	0.9301 $\pm$ 0.0067	12.7 $\pm$ 0.8	0.0 $\pm$ 0.8
312.547230	0.643185	0.3106 $\pm$ 0.0045	0.3262 $\pm$ 0.0012	0.9312 $\pm$ 0.0065	5.1 $\pm$ 0.7	-1.1 $\pm$ 0.7
313.548380	0.861301	0.3099 $\pm$ 0.0065	0.3248 $\pm$ 0.0015	0.9286 $\pm$ 0.0083	3.6 $\pm$ 1.5	0.7 $\pm$ 1.5
315.554720	0.298412	0.3162 $\pm$ 0.0052	0.3273 $\pm$ 0.0012	0.9341 $\pm$ 0.0068	1.6 $\pm$ 1.9	0.7 $\pm$ 1.9
316.551130	0.515495	0.3104 $\pm$ 0.0051	0.3255 $\pm$ 0.0012	0.9287 $\pm$ 0.0067	11.1 $\pm$ 0.8	0.0 $\pm$ 0.8
317.552700	0.733702	0.3086 $\pm$ 0.0063	0.3248 $\pm$ 0.0015	0.9237 $\pm$ 0.0084	7.4 $\pm$ 1.3	-0.5 $\pm$ 1.3
321.525450	0.599224	0.3082 $\pm$ 0.0056	0.3254 $\pm$ 0.0013	0.9287 $\pm$ 0.0072	7.9 $\pm$ 0.8	0.7 $\pm$ 0.8
322.545370	0.821429	0.3045 $\pm$ 0.0086	0.3263 $\pm$ 0.0020	0.9241 $\pm$ 0.0112	4.7 $\pm$ 1.3	0.9 $\pm$ 1.3
323.545440	0.039309	0.3097 $\pm$ 0.0072	0.3282 $\pm$ 0.0016	0.9284 $\pm$ 0.0088	2.6 $\pm$ 1.1	-0.4 $\pm$ 1.1
327.534930	0.908479	0.4618 $\pm$ 0.1629	0.3402 $\pm$ 0.0118	0.9293 $\pm$ 0.0633	3.8 $\pm$ 0.9	1.2 $\pm$ 0.9
330.524710	0.559847	0.3102 $\pm$ 0.0062	0.3252 $\pm$ 0.0014	0.9293 $\pm$ 0.0075	12.2 $\pm$ 0.8	0.5 $\pm$ 0.8
331.481500	0.768298	0.3112 $\pm$ 0.0051	0.3252 $\pm$ 0.0012	0.9230 $\pm$ 0.0067	1.8 $\pm$ 1.2	0.7 $\pm$ 1.2
689.532480	0.775048	0.3076 $\pm$ 0.0048	0.3259 $\pm$ 0.0012	0.9220 $\pm$ 0.0065	-2.4 $\pm$ 0.8	-0.7 $\pm$ 0.8
691.512640	0.206455	0.3508 $\pm$ 0.0689	0.3271 $\pm$ 0.0073	0.7714 $\pm$ 0.0437	-2.6 $\pm$ 0.8	1.0 $\pm$ 0.8
696.541340	0.302033	0.3080 $\pm$ 0.0053	0.3216 $\pm$ 0.0012	0.9110 $\pm$ 0.0068	2.3 $\pm$ 1.1	0.6 $\pm$ 1.1
698.608480	0.752390	0.3285 $\pm$ 0.0051	0.3269 $\pm$ 0.0012	0.9254 $\pm$ 0.0065	6.0 $\pm$ 0.9	-1.0 $\pm$ 0.9
699.569970	0.961865	0.3299 $\pm$ 0.0085	0.3265 $\pm$ 0.0017	0.9228 $\pm$ 0.0092	7.0 $\pm$ 0.8	-0.8 $\pm$ 0.8
700.499080	0.164285	0.3145 $\pm$ 0.0062	0.3244 $\pm$ 0.0013	0.9129 $\pm$ 0.0067	4.1 $\pm$ 4.7	1.8 $\pm$ 1.2
700.519240	0.168678	0.3075 $\pm$ 0.0051	0.3233 $\pm$ 0.0012	0.9069 $\pm$ 0.0064	8.4 $\pm$ 1.2	-5.3 $\pm$ 4.7
701.454560	0.372451	0.3122 $\pm$ 0.0692	0.3225 $\pm$ 0.0015	0.9249 $\pm$ 0.0084	-3.7 $\pm$ 3.6	4.5 $\pm$ 3.6
702.529090	0.606553	0.3041 $\pm$ 0.0163	0.3230 $\pm$ 0.0030	0.9304 $\pm$ 0.0165	-1.3 $\pm$ 1.1	-0.2 $\pm$ 1.1
703.500480	0.818185	0.3233 $\pm$ 0.0098	0.3275 $\pm$ 0.0021	0.9201 $\pm$ 0.0117	3.1 $\pm$ 0.6	-0.4 $\pm$ 0.6
704.553140	0.047523	0.3213 $\pm$ 0.0043	0.3243 $\pm$ 0.0010	0.9109 $\pm$ 0.0056	3.7 $\pm$ 0.7	0.9 $\pm$ 0.7
984.634100	0.067340	0.3144 $\pm$ 0.0042	0.3231 $\pm$ 0.0010	0.9077 $\pm$ 0.0056	5.3 $\pm$ 0.9	0.1 $\pm$ 0.9
985.633550	0.285085	0.3075 $\pm$ 0.0043	0.3230 $\pm$ 0.0011	0.9016 $\pm$ 0.0058	1.7 $\pm$ 0.8	0.3 $\pm$ 0.8
986.630640	0.502316	0.3228 $\pm$ 0.0063	0.3306 $\pm$ 0.0013	0.9189 $\pm$ 0.0070	5.1 $\pm$ 1.6	2.6 $\pm$ 1.6
995.615700	0.459845	0.3155 $\pm$ 0.0056	0.3290 $\pm$ 0.0012	0.9158 $\pm$ 0.0065	8.5 $\pm$ 4.4	-10.9 $\pm$ 4.5
1001.610390	0.765878	0.3303 $\pm$ 0.0059	0.3255 $\pm$ 0.0012	0.9230 $\pm$ 0.0066	-14.0 $\pm$ 7.8	-17.7 $\pm$ 7.8
1002.632590	0.988580	0.3036 $\pm$ 0.0206	0.3245 $\pm$ 0.0031	0.9098 $\pm$ 0.0158	7.9 $\pm$ 2.5	-0.7 $\pm$ 2.5
1005.639920	0.643771	0.3107 $\pm$ 0.0202	0.3250 $\pm$ 0.0033	0.9318 $\pm$ 0.0175	3.5 $\pm$ 2.0	2.6 $\pm$ 2.0
1006.610200	0.855161	0.3209 $\pm$ 0.0180	0.3259 $\pm$ 0.0029	0.9319 $\pm$ 0.0154	5.9 $\pm$ 1.0	-0.1 $\pm$ 1.0
1010.568540	0.717545	0.3326 $\pm$ 0.0080	0.3260 $\pm$ 0.0013	0.9327 $\pm$ 0.0072	-2.0 $\pm$ 2.1	-1.5 $\pm$ 2.1
1013.598260	0.377614	0.3338 $\pm$ 0.0084	0.3271 $\pm$ 0.0015	0.9259 $\pm$ 0.0080	-4.5 $\pm$ 1.8	-0.0 $\pm$ 1.8
1018.658940	0.480159	0.3381 $\pm$ 0.0072	0.3252 $\pm$ 0.0014	0.9332 $\pm$ 0.0072	3.1 $\pm$ 1.7	-3.5 $\pm$ 1.7
1369.590720	0.935885	0.3212 $\pm$ 0.0074	0.3230 $\pm$ 0.0013	0.9292 $\pm$ 0.0068	13.9 $\pm$ 0.9	0.3 $\pm$ 0.9
1382.615660	0.773562	0.3193 $\pm$ 0.0081	0.3251 $\pm$ 0.0019	0.9147 $\pm$ 0.0096	7.3 $\pm$ 0.7	-0.7 $\pm$ 0.7
1384.584890	0.202588	0.3577 $\pm$ 0.0073	0.3291 $\pm$ 0.0013	0.9423 $\pm$ 0.0069	4.7 $\pm$ 0.7	-0.7 $\pm$ 0.7

continued.						
Julian date (2454000+)	rot.phase	S-index	H $\alpha$ -index	CaIRT-index	B <sub>I</sub>	N <sub>I</sub>
1385.533000	0.409148	0.3323 $\pm$ 0.0051	0.3255 $\pm$ 0.0011	0.9265 $\pm$ 0.0061	6.1 $\pm$ 0.7	0.5 $\pm$ 0.7
1388.555690	0.067686	0.3493 $\pm$ 0.0057	0.3284 $\pm$ 0.0011	0.9325 $\pm$ 0.0062	9.5 $\pm$ 1.0	-0.8 $\pm$ 1.0
1390.561220	0.504621	0.3474 $\pm$ 0.0056	0.3264 $\pm$ 0.0011	0.9293 $\pm$ 0.0062	3.2 $\pm$ 1.1	0.9 $\pm$ 1.1
1391.543670	0.718662	0.3446 $\pm$ 0.0067	0.3256 $\pm$ 0.0013	0.9293 $\pm$ 0.0068	4.7 $\pm$ 2.8	-0.8 $\pm$ 2.8
1392.566500	0.941501	0.3370 $\pm$ 0.0090	0.3262 $\pm$ 0.0016	0.9263 $\pm$ 0.0080	-4.6 $\pm$ 1.0	2.1 $\pm$ 1.0
1396.485880	0.795397	0.3290 $\pm$ 0.0100	0.3244 $\pm$ 0.0018	0.9133 $\pm$ 0.0096	4.4 $\pm$ 0.9	1.0 $\pm$ 0.9
1401.561040	0.901096	0.3358 $\pm$ 0.0061	0.3248 $\pm$ 0.0013	0.9214 $\pm$ 0.0068	10.0 $\pm$ 0.7	1.1 $\pm$ 0.7
1411.510430	0.068719	0.3314 $\pm$ 0.0062	0.3264 $\pm$ 0.0011	0.9156 $\pm$ 0.0062	8.4 $\pm$ 1.0	-0.3 $\pm$ 1.0
1416.561860	0.169248	0.3302 $\pm$ 0.0052	0.3262 $\pm$ 0.0011	0.9155 $\pm$ 0.0059	5.5 $\pm$ 0.8	0.8 $\pm$ 0.8
1429.547050	0.998266	0.3474 $\pm$ 0.0072	0.3289 $\pm$ 0.0013	0.9177 $\pm$ 0.0069	8.1 $\pm$ 1.5	0.1 $\pm$ 1.5
1754.590060	0.813736	0.3520 $\pm$ 0.0068	0.3287 $\pm$ 0.0012	0.9170 $\pm$ 0.0064	-2.3 $\pm$ 1.1	-0.4 $\pm$ 1.1
1764.613990	0.997599	0.3397 $\pm$ 0.0135	0.3264 $\pm$ 0.0017	0.9093 $\pm$ 0.0095	-2.4 $\pm$ 0.9	-0.1 $\pm$ 0.9
1765.579850	0.208026	0.3392 $\pm$ 0.0075	0.3281 $\pm$ 0.0016	0.9445 $\pm$ 0.0088	6.1 $\pm$ 0.8	0.5 $\pm$ 0.8
1782.512460	0.897048	0.3445 $\pm$ 0.0040	0.3286 $\pm$ 0.0012	0.9421 $\pm$ 0.0068	-6.4 $\pm$ 1.9	0.1 $\pm$ 1.9
1784.515440	0.333427	0.3398 $\pm$ 0.0048	0.3285 $\pm$ 0.0012	0.9415 $\pm$ 0.0068	4.3 $\pm$ 2.1	1.4 $\pm$ 2.1
1785.571320	0.563466	0.3475 $\pm$ 0.0056	0.3289 $\pm$ 0.0014	0.9458 $\pm$ 0.0079	12.8 $\pm$ 0.8	-1.0 $\pm$ 0.8
1789.590600	0.439126	0.3292 $\pm$ 0.0072	0.3278 $\pm$ 0.0014	0.9324 $\pm$ 0.0078	3.7 $\pm$ 1.1	-0.3 $\pm$ 1.1
1790.530870	0.643978	0.3674 $\pm$ 0.0056	0.3344 $\pm$ 0.0013	0.9572 $\pm$ 0.0073	6.1 $\pm$ 0.9	0.1 $\pm$ 0.9
1791.472450	0.849115	0.3313 $\pm$ 0.0070	0.3277 $\pm$ 0.0014	0.9453 $\pm$ 0.0076	—	—
1792.535280	0.080669	0.3808 $\pm$ 0.0084	0.3328 $\pm$ 0.0013	0.9579 $\pm$ 0.0073	—	—
2100.610620	0.199479	0.3737 $\pm$ 0.0071	0.3319 $\pm$ 0.0014	0.9606 $\pm$ 0.0075	—	—
2101.635920	0.422856	0.3344 $\pm$ 0.0096	0.3253 $\pm$ 0.0018	0.9335 $\pm$ 0.0110	—	—
2102.612400	0.635597	0.3560 $\pm$ 0.0069	0.3281 $\pm$ 0.0015	0.9344 $\pm$ 0.0082	—	—
2103.529510	0.835403	0.3419 $\pm$ 0.0054	0.3260 $\pm$ 0.0013	0.9280 $\pm$ 0.0074	—	—
2118.614210	0.121830	0.3514 $\pm$ 0.0057	0.3265 $\pm$ 0.0014	0.9339 $\pm$ 0.0081	—	—
2124.664630	0.440004	0.3407 $\pm$ 0.0082	0.3278 $\pm$ 0.0017	0.9361 $\pm$ 0.0092	—	—
2125.639690	0.652436	0.3459 $\pm$ 0.0051	0.3293 $\pm$ 0.0015	0.9290 $\pm$ 0.0085	—	—
2126.631180	0.868447	0.3374 $\pm$ 0.0062	0.3273 $\pm$ 0.0012	0.9252 $\pm$ 0.0069	—	—
2127.593570	0.078118	0.3511 $\pm$ 0.0049	0.3288 $\pm$ 0.0012	0.9401 $\pm$ 0.0067	—	—
2128.578110	0.292614	0.3490 $\pm$ 0.0058	0.3300 $\pm$ 0.0012	0.9457 $\pm$ 0.0069	—	—
2131.572610	0.945011	0.3451 $\pm$ 0.0044	0.3273 $\pm$ 0.0012	0.9412 $\pm$ 0.0070	—	—
2132.561810	0.160523	0.3361 $\pm$ 0.0061	0.3270 $\pm$ 0.0013	0.9302 $\pm$ 0.0072	—	—
2133.592020	0.384969	0.3523 $\pm$ 0.0055	0.3290 $\pm$ 0.0012	0.9444 $\pm$ 0.0072	—	—
2146.566500	0.211654	0.3467 $\pm$ 0.0059	0.3298 $\pm$ 0.0013	0.9401 $\pm$ 0.0075	—	—
2147.537680	0.423240	0.3357 $\pm$ 0.0055	0.3283 $\pm$ 0.0013	0.9288 $\pm$ 0.0076	—	—
2482.556520	0.412094	0.3507 $\pm$ 0.0064	0.3285 $\pm$ 0.0011	0.9437 $\pm$ 0.0063	2.8 $\pm$ 0.8	-0.2 $\pm$ 0.8
2485.512210	0.056035	0.3385 $\pm$ 0.0083	0.3261 $\pm$ 0.0014	0.9330 $\pm$ 0.0076	12.7 $\pm$ 1.1	-2.4 $\pm$ 1.1
2507.629120	0.874534	0.3404 $\pm$ 0.0054	0.3272 $\pm$ 0.0012	0.9341 $\pm$ 0.0066	4.1 $\pm$ 2.5	-3.3 $\pm$ 2.5
2509.533370	0.289403	0.3384 $\pm$ 0.0068	0.3263 $\pm$ 0.0016	0.9330 $\pm$ 0.0090	6.2 $\pm$ 0.8	0.5 $\pm$ 0.8
2510.636070	0.529643	0.3367 $\pm$ 0.0070	0.3249 $\pm$ 0.0015	0.9287 $\pm$ 0.0083	6.1 $\pm$ 0.9	0.3 $\pm$ 0.9
2513.550070	0.164501	0.3520 $\pm$ 0.0064	0.3293 $\pm$ 0.0012	0.9430 $\pm$ 0.0068	10.3 $\pm$ 1.0	0.3 $\pm$ 1.0
2514.559260	0.384368	0.3520 $\pm$ 0.0080	0.3288 $\pm$ 0.0014	0.9452 $\pm$ 0.0078	5.4 $\pm$ 0.8	0.6 $\pm$ 0.8
2515.562810	0.603007	0.3414 $\pm$ 0.0079	0.3278 $\pm$ 0.0014	0.9384 $\pm$ 0.0079	4.8 $\pm$ 0.8	0.3 $\pm$ 0.8
2516.582590	0.825181	0.3515 $\pm$ 0.0062	0.3278 $\pm$ 0.0012	0.9422 $\pm$ 0.0069	3.4 $\pm$ 0.8	-0.1 $\pm$ 0.8

continued.						
Julian date (2454000+)	rot.phase	S-index	H $\alpha$ -index	CaIRT-index	B <sub>I</sub>	N <sub>I</sub>
2518.601950	0.265129	0.3535 $\pm$ 0.0052	0.3275 $\pm$ 0.0012	0.9367 $\pm$ 0.0067	8.4 $\pm$ 0.8	0.2 $\pm$ 0.8
2520.501260	0.678922	0.3498 $\pm$ 0.0060	0.3280 $\pm$ 0.0012	0.9407 $\pm$ 0.0066	2.8 $\pm$ 0.8	0.2 $\pm$ 0.8
2523.532240	0.339266	0.3505 $\pm$ 0.0058	0.3293 $\pm$ 0.0012	0.9390 $\pm$ 0.0065	5.0 $\pm$ 0.8	-0.6 $\pm$ 0.8
2524.518410	0.554118	0.3548 $\pm$ 0.0056	0.3288 $\pm$ 0.0012	0.9402 $\pm$ 0.0067	7.7 $\pm$ 0.9	-0.7 $\pm$ 0.9
2525.463280	0.759972	0.3547 $\pm$ 0.0073	0.3282 $\pm$ 0.0012	0.9402 $\pm$ 0.0068	1.8 $\pm$ 0.8	-0.0 $\pm$ 0.8
2526.533220	0.993074	0.3545 $\pm$ 0.0065	0.3281 $\pm$ 0.0012	0.9412 $\pm$ 0.0065	5.9 $\pm$ 0.8	-0.2 $\pm$ 0.8
<sup>2</sup>						

---

<sup>2</sup>The longitudinal magnetic field measurements are not included for 2012.61 and parts of 2011.67 epochs due to spectropolarimetric errors at NARVAL. See Sect. 3.3 for details.

**Table A.3.:** Journal of observations of 61 Cyg A for seven epochs (2007.59, 2008.64, 2010.55, 2012.54, 2013.61, 2014.61, and 2015.54). Column 1 represents the year and date of observations, column 2 is the Julian date, column 3 is the exposure time, column 4 is the signal-to-noise ratio of each Stokes V LSD profile, and column 5 represents the error bars in the Stokes V LSD profile.

Date	Julian date (2450000+)	Exposure time (s)	S/N	$\sigma_{\text{LSD}}$ ( $10^{-5}I_c$ )
2007 July 26	4308.49809	1200	35765	2.7960
2007 July 30	4312.52989	800	35807	2.7928
2007 July 31	4313.53121	800	27096	3.6905
2007 August 02	4315.53608	800	33873	2.9522
2007 August 03	4316.53315	800	35102	2.8489
2007 August 04	4317.53462	800	30572	3.2710
2007 August 08	4321.50738	800	31550	3.1696
2007 August 09	4322.52760	800	28744	3.4790
2007 August 10	4323.52773	800	24362	4.1048
2007 August 17	4330.50089	1600	48802	2.0491
2007 August 18	4331.46147	800	35561	2.8121
2008 August 09	4688.54994	1200	46210	2.1641
2008 August 12	4691.48653	1200	40079	2.4951
2008 August 17	4696.52126	1200	31218	3.2033
2008 August 21	4700.47785	1200	36751	2.7210
2008 August 22	4701.48433	1200	21527	4.6454
2008 August 23	4702.50793	1200	50016	1.999
2008 August 24	4703.47966	1200	49602	2.0161
2008 August 25	4704.53225	1200	48263	2.0720
2008 August 26	4705.52953	1200	49904	2.0039
2010 June 03	5351.64786	900	32082	3.1171
2010 June 21	5369.57210	900	31021	3.2236
2010 July 01	5379.58460	900	27037	3.6987
2010 July 12	5390.54209	900	25343	3.9458
2010 July 13	5391.52388	900	26541	3.7678
2010 July 14	5392.54747	900	34955	2.8608
2010 July 15	5393.63958	900	31139	3.2114
2010 July 18	5396.60809	900	38824	2.5757
2010 July 23	5401.65920	900	37562	2.6623
2010 July 24	5402.49800	900	37471	2.6687
2010 July 25	5403.49549	900	37945	2.6354
2010 August 02	5411.49161	900	35432	2.8224
2010 August 03	5412.56953	900	40189	2.4883
2010 August 06	5415.55556	900	32469	3.0799
2010 August 07	5416.54320	900	36301	2.7548
2010 August 10	5419.56875	900	36220	2.7610
2012 July 08	6117.63676	900	33129	..
2012 July 09	6118.63476	900	28811	..
2012 July 15	6124.64113	900	35051	..

---

continued.

Date	Julian date (2450000+)	Exposure time (s)	S/N	$\sigma_{\text{LSD}}$ ( $10^{-5}I_c$ )
2012 July 16	6125.61827	900	36914	..
2012 July 17	6126.61222	900	34327	..
2012 July 18	6127.56778	900	34221	..
2012 July 19	6128.55829	900	32787	..
2012 July 22	6131.55361	900	34150	..
2012 July 23	6132.54263	900	35066	..
2012 July 24	6133.56659	900	34955	..
2013 July 14	6488.51321	800	15411	6.4889
2013 August 02	6507.65889	800	28131	3.5548
2013 August 04	6509.51420	800	34901	2.8653
2013 August 05	6510.61746	800	24113	4.1472
2013 August 08	6513.57114	800	31163	3.2090
2013 August 09	6514.54087	800	35398	2.8251
2013 August 10	6515.54442	800	35718	2.7997
2013 August 11	6516.56402	800	33745	2.9634
2013 August 13	6518.58190	800	36075	2.7720
2013 August 14	6519.62914	800	35479	2.8186
2013 August 18	6523.51294	800	33442	2.9903
2013 August 19	6524.49914	800	34439	2.9036
2013 August 20	6525.44457	800	33347	2.9988
2014 July 14	6853.55493	800	21642	4.6207
2014 July 17	6856.55743	800	28094	3.5596
2014 July 22	6861.57410	800	34595	2.8906
2014 July 25	6864.55546	800	34374	2.9092
2014 July 26	6865.53839	800	35150	2.8449
2014 July 27	6866.58350	800	35645	2.8055
2014 August 11	6881.38890	800	27850	3.5907
2014 August 19	6889.36216	800	18535	5.3954
2014 August 23	6893.46397	800	35628	2.8068
2014 August 25	6895.46092	800	29424	3.3987
2014 August 27	6897.47963	800	36306	2.7544
2014 August 29	6899.49512	800	35859	2.7888
2014 August 30	6900.52575	800	31814	3.1433
2014 August 31	6901.48870	800	36408	2.7467
2015 June 26	7200.57599	900	26403	3.7874
2015 June 28	7202.53874	900	36708	2.7242
2015 June 29	7203.59939	900	30539	3.2745
2015 June 30	7204.56304	900	30669	3.2607
2015 July 07	7211.52277	900	31832	3.1415
2015 July 08	7212.52460	900	34962	2.8603
2015 July 09	7213.50574	900	37205	2.6878
2015 July 10	7214.52800	900	33875	2.9521
2015 July 11	7215.56071	900	32176	3.1080
2015 July 12	716.54418	900	34501	2.8985

---

---

continued.

Date	Julian date (2450000+)	Exposure time (s)	S/N	$\sigma_{\text{LSD}}$ ( $10^{-5}I_c$ )
2015 July 14	7218.55681	900	32888	3.0407
2015 July 15	7219.56343	900	23679	4.2233
2015 July 20	7224.56050	900	25336	3.9469
2015 August 05	7240.48208	900	24468	4.0871
2015 August 10	7245.54843	900	22931	4.3610
2015 August 11	7246.57034	900	31250	3.2000

**Table A.4.:** The chromospheric activity and longitudinal field measurements of 61 Cyg A for six epochs (2007.59, 2008.64, 2010.55, 2012.54, 2013.61, 2014.61, and 2015.54). From left to right it represents: Julian date, rotational phase, S-index,  $H\alpha$ -index, CaIRT-index, longitudinal magnetic field ( $B_l$ ), and magnetic field of the Null profile ( $N_l$ ).

Epoch	Julian date (2454000+)	rot.phase	S-index	$H\alpha$ -index	CaIRT-index	$B_l$ (G)	$N_l$ (G)
2007.59	4308.49809	0.00000	$0.69 \pm 0.02$	$0.402 \pm 0.001$	$0.889 \pm 0.003$	$-10.0 \pm 0.9$	$-0.8 \pm 0.9$
	4312.52989	0.11789	$0.69 \pm 0.02$	$0.402 \pm 0.001$	$0.895 \pm 0.003$	$-8.5 \pm 0.9$	$-0.0 \pm 0.9$
	4313.53121	0.14717	$0.69 \pm 0.01$	$0.401 \pm 0.001$	$0.894 \pm 0.004$	$-8.8 \pm 1.1$	$-1.1 \pm 1.1$
	4315.53608	0.20579	$0.70 \pm 0.02$	$0.401 \pm 0.001$	$0.891 \pm 0.003$	$-4.7 \pm 0.9$	$0.1 \pm 0.9$
	4316.53315	0.23494	$0.68 \pm 0.02$	$0.402 \pm 0.001$	$0.892 \pm 0.003$	$-5.4 \pm 0.9$	$0.1 \pm 0.9$
	4317.53462	0.26423	$0.71 \pm 0.01$	$0.400 \pm 0.001$	$0.889 \pm 0.004$	$-4.3 \pm 1.0$	$0.6 \pm 1.0$
	4321.50738	0.38039	$0.66 \pm 0.02$	$0.399 \pm 0.001$	$0.888 \pm 0.004$	$0.0 \pm 1.0$	$-0.2 \pm 1.0$
	4322.52760	0.41022	$0.62 \pm 0.02$	$0.399 \pm 0.001$	$0.889 \pm 0.004$	$1.1 \pm 1.1$	$-0.6 \pm 1.1$
	4323.52773	0.43946	$0.61 \pm 0.01$	$0.400 \pm 0.001$	$0.887 \pm 0.005$	$1.7 \pm 1.3$	$0.6 \pm 1.3$
	4330.50089	0.64336	$0.60 \pm 0.02$	$0.399 \pm 0.001$	$0.876 \pm 0.002$	$-8.6 \pm 0.6$	$-0.4 \pm 0.6$
2008.64	4331.46147	0.67144	$0.58 \pm 0.01$	$0.401 \pm 0.001$	$0.886 \pm 0.003$	$-9.1 \pm 0.9$	$0.4 \pm 0.9$
	4688.54994	0.11263	$0.73 \pm 0.01$	$0.401 \pm 0.001$	$0.898 \pm 0.003$	$-2.9 \pm 0.7$	$0.3 \pm 0.7$
	4691.48653	0.19849	$0.73 \pm 0.02$	$0.401 \pm 0.001$	$0.899 \pm 0.003$	$-1.4 \pm 0.8$	$-0.9 \pm 0.8$
	4696.52126	0.34571	$0.71 \pm 0.03$	$0.402 \pm 0.001$	$0.900 \pm 0.004$	$1.0 \pm 1.0$	$0.4 \pm 1.0$
	4700.47785	0.46140	$0.71 \pm 0.02$	$0.400 \pm 0.001$	$0.896 \pm 0.004$	$-1.4 \pm 0.8$	$0.2 \pm 0.8$
	4701.48433	0.49083	$0.69 \pm 0.04$	$0.402 \pm 0.002$	$0.905 \pm 0.006$	$-4.0 \pm 1.5$	$-0.3 \pm 1.5$
	4702.50793	0.52076	$0.72 \pm 0.01$	$0.400 \pm 0.001$	$0.889 \pm 0.003$	$-0.7 \pm 0.6$	$0.4 \pm 0.6$
	4703.47966	0.54917	$0.72 \pm 0.01$	$0.401 \pm 0.001$	$0.887 \pm 0.003$	$-1.0 \pm 0.6$	$1.1 \pm 0.6$
	4704.53225	0.57995	$0.73 \pm 0.01$	$0.401 \pm 0.001$	$0.890 \pm 0.003$	$-3.1 \pm 0.6$	$-0.1 \pm 0.6$
	4705.52953	0.60911	$0.73 \pm 0.02$	$0.401 \pm 0.001$	$0.887 \pm 0.003$	$-2.0 \pm 0.6$	$0.2 \pm 0.6$
2010.55	5351.64786	0.50146	$0.65 \pm 0.03$	$0.400 \pm 0.001$	$0.892 \pm 0.004$	$4.1 \pm 1.0$	$-0.8 \pm 1.0$
	5369.57210	0.02556	$0.85 \pm 0.03$	$0.402 \pm 0.001$	$0.909 \pm 0.004$	$0.3 \pm 1.0$	$-0.6 \pm 1.0$
	5379.58460	0.31832	$0.79 \pm 0.04$	$0.402 \pm 0.001$	$0.901 \pm 0.004$	$-2.1 \pm 1.1$	$-1.9 \pm 1.1$
	5390.54209	0.63871	$0.74 \pm 0.04$	$0.400 \pm 0.001$	$0.899 \pm 0.005$	$2.3 \pm 1.2$	$1.4 \pm 1.2$
	5391.52388	0.66742	$0.73 \pm 0.03$	$0.399 \pm 0.001$	$0.894 \pm 0.005$	$2.1 \pm 1.2$	$1.6 \pm 1.2$
	5392.54747	0.69735	$0.76 \pm 0.02$	$0.400 \pm 0.001$	$0.893 \pm 0.004$	$0.2 \pm 0.9$	$1.0 \pm 0.9$
	5393.63958	0.72928	$0.84 \pm 0.04$	$0.405 \pm 0.001$	$0.900 \pm 0.004$	$3.0 \pm 1.1$	$-0.8 \pm 1.1$
	5396.60809	0.81608	$0.79 \pm 0.03$	$0.401 \pm 0.001$	$0.901 \pm 0.003$	$-0.2 \pm 0.9$	$-0.7 \pm 0.9$
	5401.65920	0.96378	$0.81 \pm 0.03$	$0.401 \pm 0.001$	$0.901 \pm 0.004$	$-7.9 \pm 0.8$	$0.2 \pm 0.8$
	5402.49800	0.98830	$0.84 \pm 0.03$	$0.401 \pm 0.001$	$0.903 \pm 0.004$	$-5.3 \pm 0.8$	$-0.3 \pm 0.8$
	5403.49549	0.01747	$0.85 \pm 0.03$	$0.403 \pm 0.001$	$0.905 \pm 0.004$	$-4.2 \pm 0.8$	$0.5 \pm 0.8$
	5411.49161	0.25127	$0.81 \pm 0.02$	$0.402 \pm 0.001$	$0.904 \pm 0.004$	$0.1 \pm 0.9$	$-0.3 \pm 0.9$
	5412.56953	0.28279	$0.79 \pm 0.02$	$0.402 \pm 0.001$	$0.898 \pm 0.003$	$0.1 \pm 1.0$	$-0.6 \pm 1.0$
	5415.55556	0.37010	$0.77 \pm 0.03$	$0.402 \pm 0.001$	$0.902 \pm 0.004$	$0.1 \pm 1.0$	$-0.6 \pm 1.0$
	5416.54320	0.39897	$0.77 \pm 0.01$	$0.402 \pm 0.001$	$0.895 \pm 0.004$	$1.4 \pm 0.9$	$-1.5 \pm 0.9$
	5419.56875	0.48745	$0.74 \pm 0.03$	$0.399 \pm 0.001$	$0.892 \pm 0.004$	$1.3 \pm 0.9$	$0.1 \pm 0.9$
2012.54	6117.63676	0.89879	$0.61 \pm 0.02$	$0.399 \pm 0.001$	$0.880 \pm 0.004$	..	..
	6118.63476	0.92797	$0.61 \pm 0.02$	$0.400 \pm 0.001$	$0.874 \pm 0.005$	..	..
	6124.64113	0.10360	$0.61 \pm 0.02$	$0.400 \pm 0.001$	$0.872 \pm 0.004$	..	..
	6125.61827	0.13217	$0.62 \pm 0.02$	$0.400 \pm 0.001$	$0.880 \pm 0.003$	..	..

continued.							
Epoch	Julian date (2450000+)	rot.phase	S-index	H $\alpha$ -index	CaIRT-index	B <sub>I</sub> (G)	N <sub>I</sub> (G)
2012.54	6126.61222	0.16123	0.62 $\pm$ 0.02	0.401 $\pm$ 0.001	0.881 $\pm$ 0.004	..	..
	6127.56778	0.18917	0.62 $\pm$ 0.02	0.400 $\pm$ 0.001	0.884 $\pm$ 0.004	..	..
	6128.55829	0.21813	0.63 $\pm$ 0.02	0.400 $\pm$ 0.001	0.878 $\pm$ 0.004	..	..
	6131.55361	0.30572	0.65 $\pm$ 0.01	0.400 $\pm$ 0.001	0.885 $\pm$ 0.004	..	..
	6132.54263	0.33464	0.65 $\pm$ 0.02	0.400 $\pm$ 0.001	0.889 $\pm$ 0.004	..	..
	6133.56659	0.36458	0.65 $\pm$ 0.01	0.401 $\pm$ 0.001	0.885 $\pm$ 0.004	..	..
2013.61	6488.51321	0.74313	0.62 $\pm$ 0.06	0.399 $\pm$ 0.002	0.889 $\pm$ 0.006	3.4 $\pm$ 2.0	-2.7 $\pm$ 2.1
	6507.65889	0.30295	0.63 $\pm$ 0.04	0.398 $\pm$ 0.001	0.884 $\pm$ 0.004	6.2 $\pm$ 1.2	0.5 $\pm$ 1.2
	6509.51420	0.35720	0.60 $\pm$ 0.02	0.400 $\pm$ 0.001	0.881 $\pm$ 0.004	11.3 $\pm$ 0.9	0.3 $\pm$ 0.9
	6510.61746	0.38946	0.61 $\pm$ 0.03	0.398 $\pm$ 0.001	0.890 $\pm$ 0.005	10.5 $\pm$ 1.3	-0.2 $\pm$ 1.3
	6513.57114	0.47582	0.59 $\pm$ 0.02	0.398 $\pm$ 0.001	0.883 $\pm$ 0.004	9.0 $\pm$ 1.0	-0.1 $\pm$ 1.0
	6514.54087	0.50417	0.59 $\pm$ 0.02	0.398 $\pm$ 0.001	0.883 $\pm$ 0.004	7.4 $\pm$ 0.9	-0.0 $\pm$ 0.9
	6515.54442	0.53352	0.58 $\pm$ 0.02	0.397 $\pm$ 0.001	0.876 $\pm$ 0.004	7.7 $\pm$ 0.9	-0.1 $\pm$ 0.9
	6516.56402	0.56333	0.57 $\pm$ 0.01	0.398 $\pm$ 0.001	0.876 $\pm$ 0.004	7.9 $\pm$ 0.9	0.7 $\pm$ 0.9
	6518.58190	0.62233	0.57 $\pm$ 0.02	0.398 $\pm$ 0.001	0.877 $\pm$ 0.004	8.6 $\pm$ 0.9	0.7 $\pm$ 0.9
	6519.62914	0.65295	0.57 $\pm$ 0.02	0.398 $\pm$ 0.001	0.878 $\pm$ 0.004	7.9 $\pm$ 0.9	-0.2 $\pm$ 0.9
	6523.51294	0.76652	0.56 $\pm$ 0.01	0.398 $\pm$ 0.001	0.877 $\pm$ 0.004	7.9 $\pm$ 1.0	-0.1 $\pm$ 1.0
	6524.49914	0.79535	0.57 $\pm$ 0.02	0.399 $\pm$ 0.001	0.879 $\pm$ 0.004	7.4 $\pm$ 0.9	-1.4 $\pm$ 0.9
	6525.44457	0.82300	0.57 $\pm$ 0.02	0.398 $\pm$ 0.001	0.878 $\pm$ 0.004	6.7 $\pm$ 1.0	-1.1 $\pm$ 1.0
	6853.55493	0.41687	0.56 $\pm$ 0.04	0.399 $\pm$ 0.001	0.892 $\pm$ 0.005	6.8 $\pm$ 1.5	-1.6 $\pm$ 1.5
	6856.55743	0.50466	0.55 $\pm$ 0.03	0.398 $\pm$ 0.001	0.894 $\pm$ 0.004	5.9 $\pm$ 1.1	-1.4 $\pm$ 1.1
2014.61	6861.57410	0.65135	0.55 $\pm$ 0.02	0.400 $\pm$ 0.001	0.886 $\pm$ 0.004	8.0 $\pm$ 0.9	0.4 $\pm$ 0.9
	6864.55546	0.73852	0.56 $\pm$ 0.02	0.400 $\pm$ 0.001	0.885 $\pm$ 0.004	5.0 $\pm$ 0.9	-0.7 $\pm$ 0.9
	6865.53839	0.76726	0.56 $\pm$ 0.02	0.401 $\pm$ 0.001	0.885 $\pm$ 0.003	5.3 $\pm$ 0.9	-1.2 $\pm$ 0.9
	6866.58350	0.79782	0.56 $\pm$ 0.01	0.400 $\pm$ 0.001	0.887 $\pm$ 0.003	3.6 $\pm$ 0.9	1.1 $\pm$ 0.9
	6881.38890	0.23073	0.58 $\pm$ 0.02	0.399 $\pm$ 0.001	0.889 $\pm$ 0.004	4.6 $\pm$ 1.1	1.7 $\pm$ 1.1
	6889.36216	0.46386	0.55 $\pm$ 0.03	0.401 $\pm$ 0.002	0.890 $\pm$ 0.006	4.1 $\pm$ 1.7	0.0 $\pm$ 1.7
	6893.46397	0.58380	0.54 $\pm$ 0.02	0.400 $\pm$ 0.001	0.882 $\pm$ 0.003	8.6 $\pm$ 0.9	1.2 $\pm$ 0.9
	6895.46092	0.64219	0.54 $\pm$ 0.02	0.399 $\pm$ 0.001	0.887 $\pm$ 0.004	7.5 $\pm$ 1.1	0.9 $\pm$ 1.1
	6897.47963	0.70121	0.54 $\pm$ 0.02	0.398 $\pm$ 0.001	0.878 $\pm$ 0.003	8.6 $\pm$ 0.9	-0.3 $\pm$ 0.9
	6899.49512	0.76015	0.54 $\pm$ 0.01	0.400 $\pm$ 0.001	0.883 $\pm$ 0.003	7.3 $\pm$ 0.9	0.7 $\pm$ 0.9
	6900.52575	0.79028	0.54 $\pm$ 0.01	0.399 $\pm$ 0.001	0.884 $\pm$ 0.004	8.4 $\pm$ 1.1	-0.9 $\pm$ 1.1
	6901.48870	0.81844	0.54 $\pm$ 0.01	0.400 $\pm$ 0.001	0.883 $\pm$ 0.003	7.7 $\pm$ 0.9	-1.4 $\pm$ 0.9
2015.54	7200.57599	0.56368	0.60 $\pm$ 0.03	0.400 $\pm$ 0.001	0.893 $\pm$ 0.004	-0.8 $\pm$ 1.2	0.3 $\pm$ 1.2
	7202.53874	0.62107	0.60 $\pm$ 0.02	0.401 $\pm$ 0.001	0.889 $\pm$ 0.003	-0.5 $\pm$ 0.9	-1.1 $\pm$ 0.9
	7203.59939	0.65208	0.59 $\pm$ 0.03	0.400 $\pm$ 0.001	0.886 $\pm$ 0.004	2.4 $\pm$ 1.0	1.0 $\pm$ 1.0
	7204.56304	0.68026	0.59 $\pm$ 0.03	0.401 $\pm$ 0.001	0.890 $\pm$ 0.004	2.3 $\pm$ 1.0	0.4 $\pm$ 1.0
	7211.52277	0.88376	0.64 $\pm$ 0.03	0.400 $\pm$ 0.001	0.896 $\pm$ 0.004	13.3 $\pm$ 1.0	-1.2 $\pm$ 1.0
	7212.52460	0.91306	0.71 $\pm$ 0.05	0.401 $\pm$ 0.001	0.890 $\pm$ 0.005	14.1 $\pm$ 0.9	-0.5 $\pm$ 0.9
	7213.50574	0.94174	0.67 $\pm$ 0.02	0.401 $\pm$ 0.001	0.897 $\pm$ 0.003	14.6 $\pm$ 0.9	0.3 $\pm$ 0.9
	7214.52800	0.97163	0.68 $\pm$ 0.05	0.401 $\pm$ 0.001	0.903 $\pm$ 0.005	13.7 $\pm$ 1.0	1.0 $\pm$ 1.0
	7215.56071	0.00183	0.64 $\pm$ 0.03	0.402 $\pm$ 0.001	0.898 $\pm$ 0.004	13.9 $\pm$ 1.0	-0.7 $\pm$ 1.0
	7216.54418	0.03059	0.67 $\pm$ 0.03	0.402 $\pm$ 0.001	0.900 $\pm$ 0.004	14.3 $\pm$ 0.9	-0.9 $\pm$ 0.9
	7218.55681	0.08943	0.69 $\pm$ 0.03	0.403 $\pm$ 0.001	0.906 $\pm$ 0.004	12.4 $\pm$ 1.0	0.5 $\pm$ 1.0

continued.							
Epoch	Julian date (2450000+)	rot.phase	S-index	H $\alpha$ -index	CaIRT-index	B <sub>l</sub> (G)	N <sub>l</sub> (G)
	7219.56343	0.11887	0.69 $\pm$ 0.05	0.403 $\pm$ 0.001	0.906 $\pm$ 0.005	12.0 $\pm$ 1.3	0.2 $\pm$ 1.3
	7224.56050	0.26498	0.68 $\pm$ 0.03	0.401 $\pm$ 0.001	0.904 $\pm$ 0.005	3.5 $\pm$ 1.3	-0.2 $\pm$ 1.2
	7240.48208	0.73053	0.62 $\pm$ 0.04	0.400 $\pm$ 0.001	0.897 $\pm$ 0.005	0.7 $\pm$ 1.3	1.1 $\pm$ 1.3
	7245.54843	0.87866	0.65 $\pm$ 0.04	0.400 $\pm$ 0.001	0.896 $\pm$ 0.005	9.9 $\pm$ 1.4	0.2 $\pm$ 1.4
	7246.57034	0.90855	0.63 $\pm$ 0.01	0.399 $\pm$ 0.001	0.892 $\pm$ 0.004	12.6 $\pm$ 1.0	0.3 $\pm$ 1.0
<sup>3</sup>							

---

<sup>3</sup>The longitudinal magnetic field measurements are not included for 2012.54 epoch due to spectropolarimetric errors at NARVAL. See Sect. 4.3 for details.

**Table A.5.:** Cool stars with well determined activity cycles are tabulated first, followed by chaotic and multiple cycles, and finally cycles not well constrained due to poor phase coverage or low amplitude. The HD name of the star is shown in column 1, the rotation period in column 2, and columns 3, 4, and 5 show the cycle periods determined in this work. Column 6 is the cycle period taken from [Saar & Brandenburg \(1999\)](#) and column 7 shows the active and inactive branch classification from literature.

name	$P_{\text{rot}}$ days	$P_{\text{cyc1}}$ years	$P_{\text{cyc2}}$ years	$P_{\text{cyc3}}$ years	$P_{\text{cyc}}^{(a)}$	Branch <sup>(b)</sup>	$\tau_c$
CA: Cool stars with clear well defined solar-like activity cycles							
HD4628 <sup>†</sup>	38.5	$8.5 \pm 0.1$	..	..	8.6	I	21.72
HD185144 <sup>†</sup>	29	$6.9 \pm 0.3$	..	..	6.5	I	18.86
HD201091 <sup>†*</sup>	35.7 <sup>(1)</sup>	$7.5 \pm 0.1$	..	..	7.3	I	23.53
HD16160 <sup>†</sup>	48.0	$15.6 \pm 0.6$	..	..	13.2	I	22.16
HD166620 <sup>†</sup>	42.4	$16.6 \pm 0.6$	..	..	15.8	I	21.46
HD10476 <sup>†</sup>	35.2	$10.0 \pm 0.2$	..	..	9.6	I	20.51
HD26965 <sup>†</sup>	43.0	$10.2 \pm 0.2$	..	..	10.1	I	20.04
HD152391 <sup>†</sup>	11.43	$10.9 \pm 0.3$	..	..	10.9	A(Ab)	17.29
HD32147 <sup>†</sup>	48.0	$9.9 \pm 0.2$	..	..	11.1	I	23.38
HD103095 <sup>†</sup>	31.0	$7.3 \pm 0.1$	..	..	7.3	I	17.52
HD81809 <sup>†</sup>	40.2	$8.3 \pm 0.1$	..	..	8.2	I	12.28
HD219834B <sup>†</sup>	43.0	$9.8 \pm 0.2$	..	..	10.0	I	18.89
HD160346 <sup>†</sup>	36.4	$7.1 \pm 0.1$	..	..	7.0	I	8.76
HD115043	5.861 <sup>(2)</sup>	$3.8 \pm 0.3$	..	..	..	..	9.27
HD3651 <sup>†</sup>	44.0	$14.2 \pm 0.6$	..	..	14.6	I	20.88
HD7199	41.4	$4.0 \pm 0.3$	..	..	..	..	6.42
CB: Cool stars with less certain activity cycles							
HD78366 <sup>†</sup>	9.67	$5.9 \pm 0.2$	12.8	..	12.2	A	8.26
HD155885*	21.11	$5.7 \pm 0.1$	..	..	5.7	A	21.00
HD20630 <sup>†</sup>	9.24	$23.1 \pm 5.2$	$9.2 \pm 0.3$	$5.7 \pm 0.1$	5.6	A	13.77
HD101501	16.68	$6.2 \pm 0.3$	$3.5 \pm 0.1$	..	..	..	16.03
HD155886*	20.69	$6.5 \pm 0.2$	..	..	5	A	21.00
HD76151 <sup>†</sup>	15.0	$17.2 \pm 1.3$	$2.5 \pm 0.0$	..	2.52	I	12.62
HD206860	4.86	$19.2 \pm 2.4$	$14.2 \pm 1.6$	..	6.2	A	8.37
HD115383	3.33	$22.9 \pm 6.2$	$4.9 \pm 0.2$	..	4.3	A	8.26
HD18256 <sup>†</sup>	3.0	$6.9 \pm 0.3$	..	..	6.8	A	3.11
HD1835 <sup>†</sup>	7.78	$9.8 \pm 0.8$	..	..	9.1	A	12.51
HD82885	18.6	$17.8 \pm 1.4$	..	..	7.9	A	18.21
HD194012	7.0	$18.4 \pm 1.3$	..	..	16.7	A	4.09
HD39587	5.36	$20.4 \pm 2.4$	$12.4 \pm 1.5$	..	..	..	8.76
HD149661 <sup>†</sup>	21.07	$16.5 \pm 0.9$	$4.0 \pm 0.1$	..	16.2	A(Ab, I)	20.25
HD131156A	6.2 <sup>(3)</sup>	$5.4 \pm 0.1$	..	..	..	..	15.87
HD201092 <sup>†*</sup>	37.84	$12.0 \pm 1.4$	..	..	10.5	I	25.42
HD97334	7.6 <sup>(3)</sup>	$5.1 \pm 0.2$	..	..	..	..	9.10

continued.							
name	$P_{\text{rot}}$ days	$P_{\text{cyc1}}$ years	$P_{\text{cyc2}}$ years	$P_{\text{cyc3}}$ years	$P_{\text{cyc}}^{(a)}$	Branch <sup>(b)</sup>	$\tau_c$
HD161239 <sup>†</sup>	29.2	17.1±1.4	5.5±0.2	..	5.7	I	13.88
HD190007 <sup>†</sup>	28.95	16.1±1.9	..	..	13.7	..	23.98
HD114710 <sup>†</sup>	12.35	17.6±1.1	10.2±0.6	..	16.6	A	7.55
HD165341A <sup>†</sup>	19.9	17.5±1.4	..	..	15.5	A	21.12
HD115404 <sup>†</sup>	18.47	11.8±1.2	..	..	12.4	A	22.27
HD156026 <sup>†</sup>	21.0	19.5±1.9	..	..	21.0	A	24.11
CC: Cool stars with probable activity cycles							
HD20003	37.1	7.7±0.5	..	..	..	..	18.25
HD21693	36.3	7.4±0.3	..	..	..	..	15.35
HD45184	21.4	4.9±0.3	..	..	..	..	10.59
HD82516	36.7	4.2±0.1	..	..	..	..	22.28
HD89454	21.1	4.0±0.8	..	..	..	..	15.72
HD114613	34.1	2.7±0.1	..	..	..	..	19.01
HD157830	24.3	3.9±0.5	..	..	..	..	13.99
HD20619	22.3	5.0±0.2	..	..	..	..	12.28
HD207129	17.6	3.3±0.1	..	..	..	..	9.15
HD209100	37.6	6.6±0.0	..	..	..	..	23.43
HD361	14.1	4.6±0.2	..	..	..	..	10.48
HD12617	30.7	4.5±2.2	..	..	..	..	23.16
HD166724	30.9	2.4±0.2	..	..	..	..	26.69
HD88742	11.3	2.9±0.1	..	..	..	..	8.65
HD154577	45.8	5.9±0.1	..	..	..	..	21.71

**Table A.6.:** Journal of Observations of  $\epsilon$  Eridani. Phase = 0 is defined as 2454101.5 and is used for all epochs, with subsequent epochs taking phase = 0 as an integer number of cycles from this value. The exposure time of all observations is 400s.

Date	Julian Date (-2454000)	UT	Phase	LSD S/N	S-index
Map 1 (2014.71)					
01sep14	2902.67	04:05:45	-1.1737	39478	0.4020
02sep14	2903.68	04:24:48	-1.0870	36435	0.3963
03sep14	2904.67	04:00:01	-1.0029	37224	0.3950
05sep14	2906.65	03:38:55	-0.8329	42847	0.3940
11sep14	2912.65	03:33:12	-0.3195	35636	0.4046
12sep14	2913.62	02:53:49	-0.2362	38801	0.3996
13sep14	2914.66	03:47:37	-0.1474	39293	0.3962
23sep14	2924.64	03:16:40	0.7069	38855	0.4055
24sep14	2925.6	02:19:16	0.7891	36714	0.3964
25sep14	2926.62	02:52:49	0.8767	35734	0.4035
27sep14	2928.61	02:36:02	1.0469	35976	0.3913
Map 2 (2014.84)					
16oct14	2947.65	03:36:25	-1.3227	30832	0.3966
17oct14	2948.49	23:49:35	-1.2506	34626	0.3956
18oct14	2949.63	03:09:04	-1.1531	36745	0.3925
19oct14	2950.58	01:59:09	-1.0717	28518	0.3933
24oct14	2955.48	23:37:39	-0.6520	29839	0.4055
25oct14	2956.56	01:23:13	-0.5601	36520	0.4032
26oct14	2957.44	22:40:33	-0.4842	24285	0.4100
28oct14	2959.59	02:07:25	-0.3006	33182	0.4020
29oct14	2960.53	00:47:06	-0.2198	36670	0.4019
30oct14	2961.49	23:39:16	-0.1382	33682	0.3977
31oct14	2962.51	00:13:05	-0.0506	36824	0.4012
01nov14	2963.51	00:10:47	0.0349	42832	0.4031
12nov14	2974.53	00:45:23	-1.0213	20765	0.3885
15nov14	2977.48	23:38:01	-0.7684	31998	0.3092
20nov14	2982.45	22:45:26	-0.3435	21015	0.3877
Map 3 (2014.98)					
02dec14	2994.39	21:21:14	-2.3211	28400	0.3873
02dec14	2994.40	21:32:10	-2.3204	29646	0.3878
03dec14	2995.40	21:30:49	-2.2349	38856	0.3902
03dec14	2995.40	21:41:47	-2.2342	38417	0.3903
19dec14	3011.39	21:17:49	-0.8658	42049	0.3856
19dec14	3011.39	21:28:46	-0.8652	39688	0.3848
21dec14	3013.40	21:38:44	-0.6933	39051	0.3929
21dec14	3013.41	21:49:41	-0.6927	37356	0.3929
06jan15	3029.36	20:35:57	0.6728	39935	0.3900
06jan15	3029.37	20:46:56	0.6735	39952	0.3896
10jan15	3033.36	20:36:39	1.0153	41780	0.3841
10jan15	3033.37	20:47:36	1.0160	41215	0.3851
17jan15	3040.33	19:56:13	1.6122	31182	0.3803
17jan15	3040.34	20:07:11	1.6129	32611	0.3798

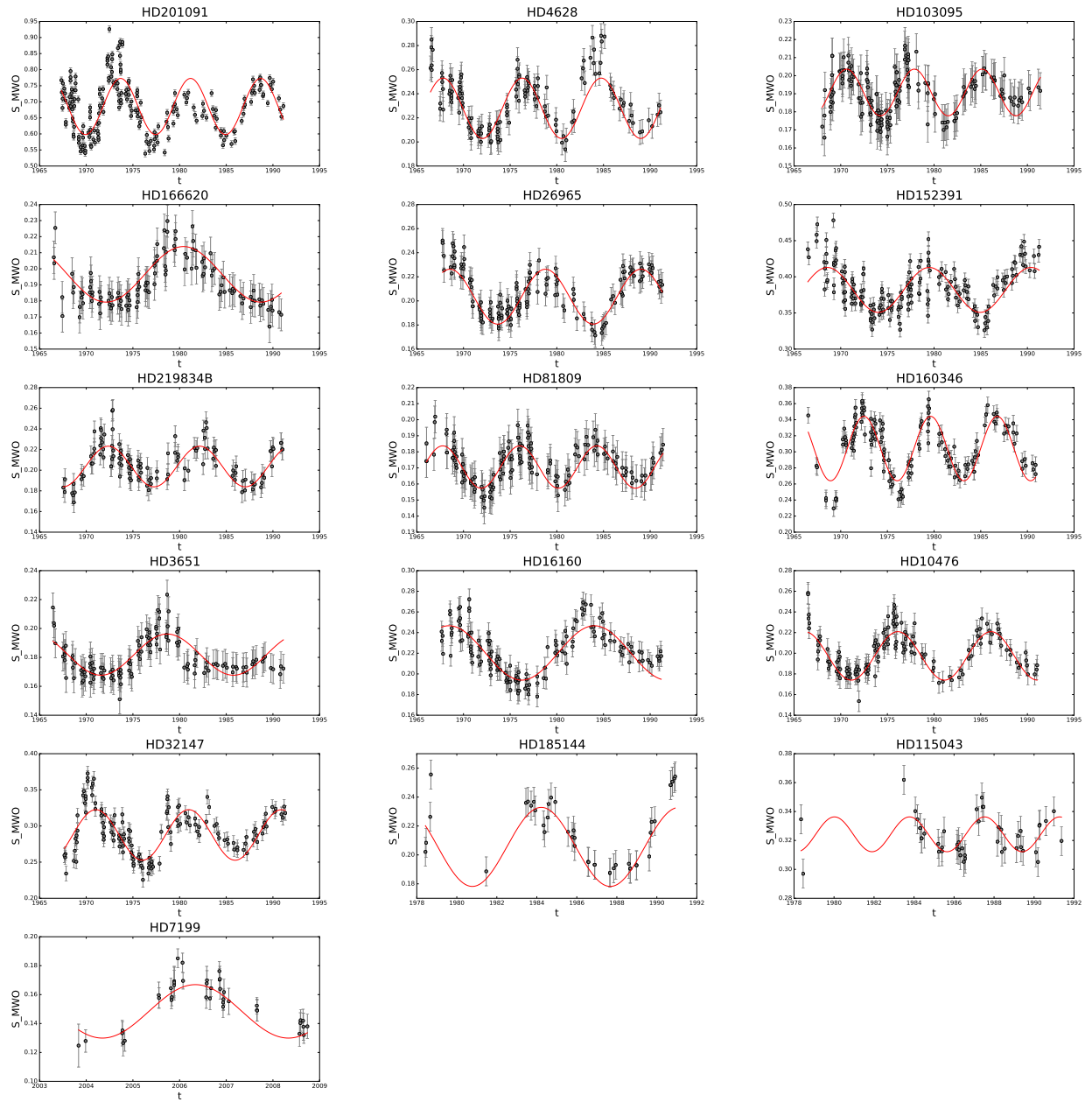


**Figure A.1.:** Cool stars with clear solar-like cycles

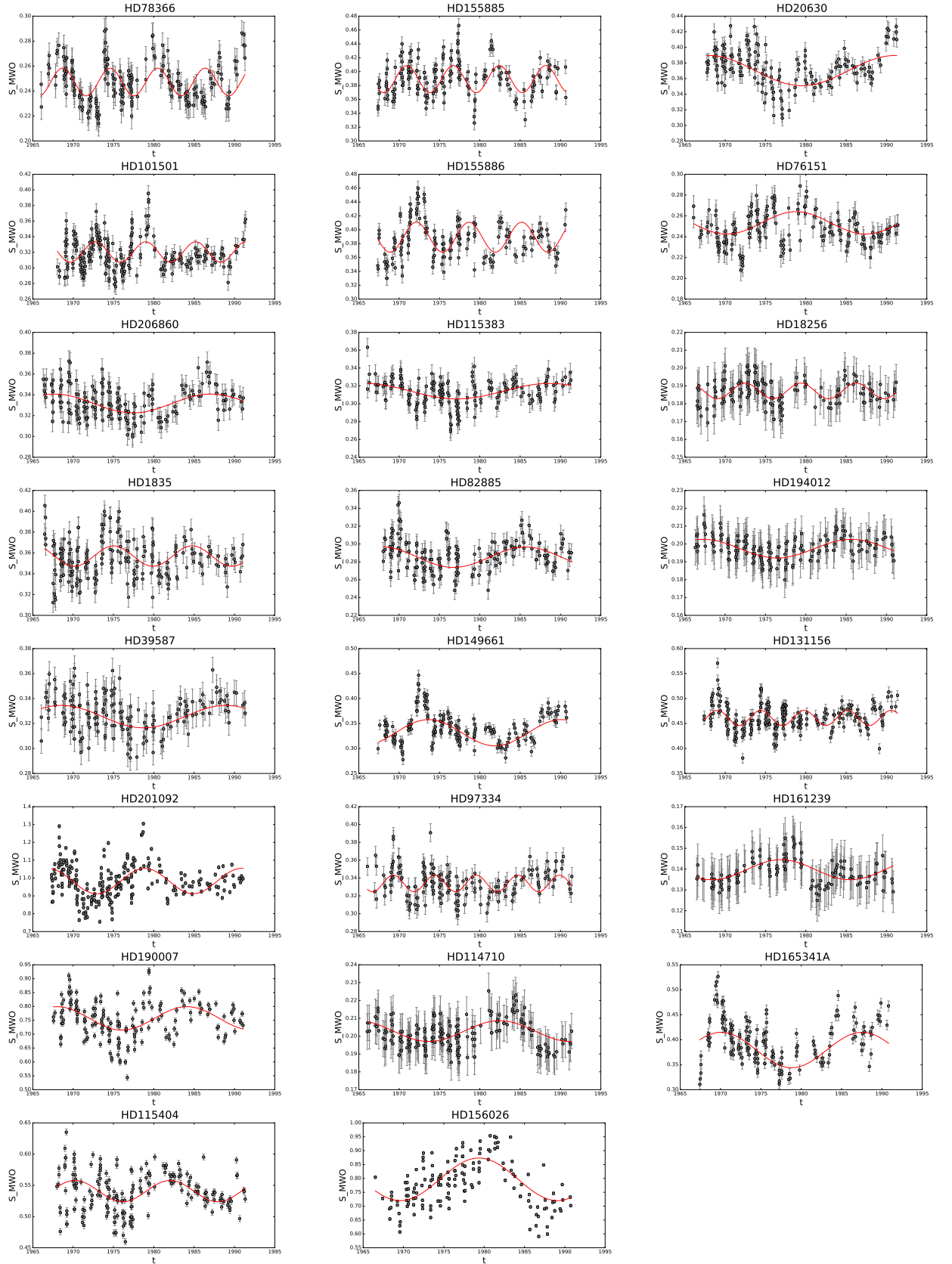


**Figure A.2.:** Cool stars with multiple cycles. The red fit to the data shows the strongest period in the periodogram.

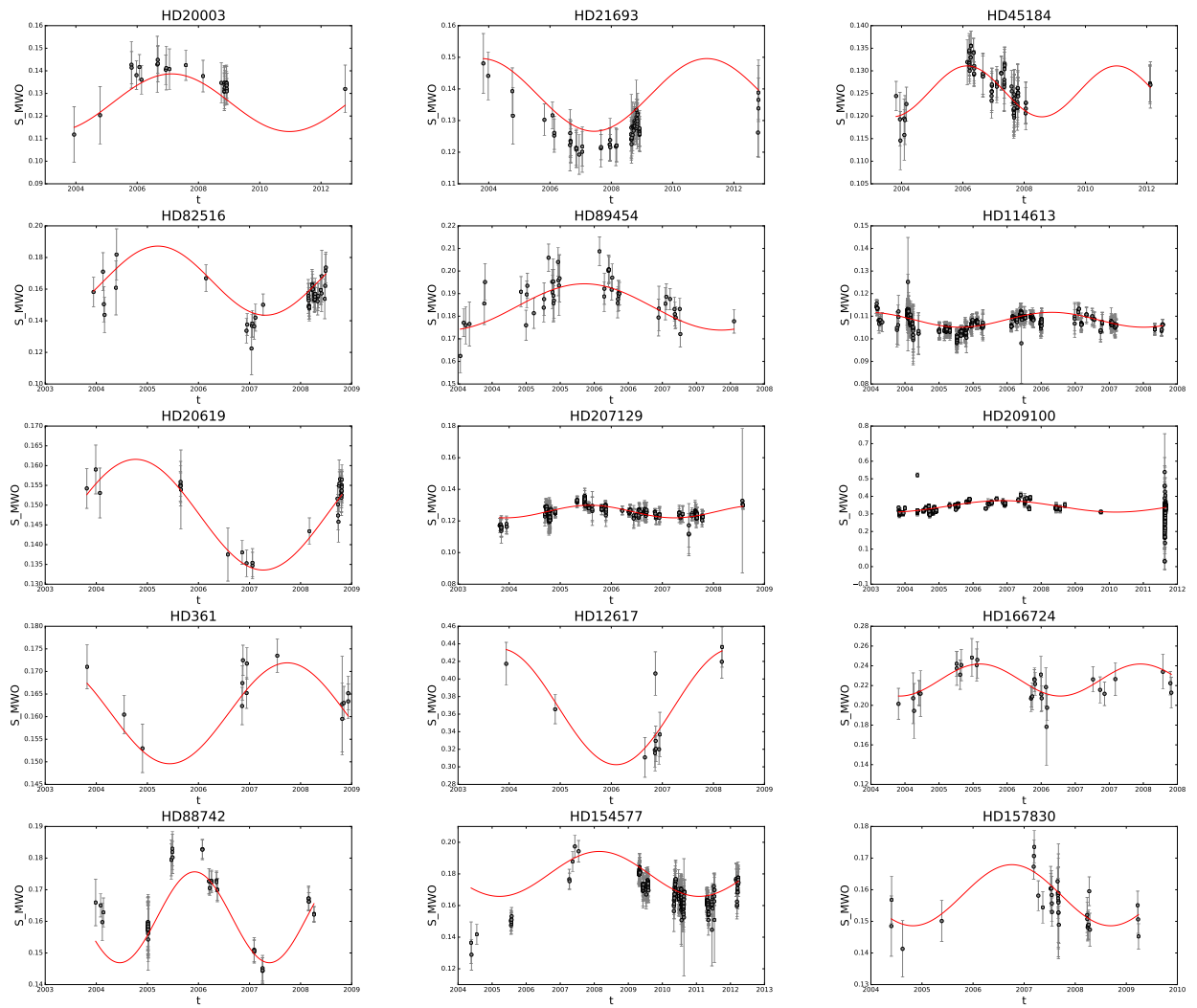


Figure A.3.: Cool stars with probable solar-like cycles.

# Acknowledgements

There are a lot of people to thank without whose support this thesis would not have taken its current shape. Firstly, I would like to thank Sandra and Ansgar for their immense support and guidance during these four years. Special thanks to Sandra for always encouraging me and giving me an extra push to do my best. Thanks to the BCool team: Julien, Colin, Pascal, Stephen and Aline. I would also like to thank the people in our stellar group and the astrophysics institute for creating a fantastic working environment. The secretaries, especially Silke, deserve a special mention. I would like thank my partners in crime (you know who you are), the friends I have gathered over the years in Goettingen and my friend in Dublin. Thanks Christopher Marvin for putting up with me in the office during these four years. I would also like to thank the people who voluntarily read my thesis: Philipp, Denis, Chris, Florian, Luis, Abhay. I must thank my parents for their immense support, you guys are amazing. This project was funded by project A16 SFB963/DFG). The COST Action MP1104 also supported my participation in several conferences and short scientific visits.



# Curriculum Vitae

## Sudeshna Boro Saikia

sudeshna@astro.physik.uni-goettingen.de  
office phone: +495513913826  
Institute for Astrophysics, University of Göttingen  
Friedrich Hund Platz 1, 37077 Göttingen

### Education

2013-2016 (expected)

**PhD, Astrophysics**; University of Göttingen (Göttingen, Germany)

*Thesis: Magnetic and activity cycles of cool stars. Supervisor: Dr Sandra V Jeffers*

2011-2012

**MSc with Merit, Astrophysics**; University of Glasgow (Glasgow, UK)

*Thesis: Gravitational waves from the merger and ring-down of binary black hole systems. Supervisor: Dr Ik Siong Heng*

### Publications

**3** First-author and **5** co-author publications in peer-reviewed journals Total number of publications: **8**, Total number of citations: **21**

#### First-author publications

1. **Boro Saikia, S.**, Marvin, C. J., Jeffers, S. V., Reiners, A., Cameron, R., Marsden, S. C., Petit, P., Warnecke, J., and Yadav, A. P., *Göttingen chromospheric activity catalogue: questioning the Active branch of stellar activity cycles*, A&A, (submitted)

2. **Boro Saikia, S.**, Jeffers, S. V., Morin, J., Petit, P., Folsom, C. P., Marsden, S. C., Donati, J. F., Cameron, R., Hall, J. C., Perdelwitz, V., Reiners, A., and Vidotto, A. A., *A solar-like magnetic cycle on the mature K dwarf 61 Cyg A (HD201091)*, A&A, 2016, 594, 29B

3. **Boro Saikia, S.**, Jeffers, S. V., Petit, P., Marsden, S. C., Morin, J., Folsom, C. P., *Variable magnetic field geometry of the young sun HN Peg (HD 206860)*, A&A, 2015, 573, 17

#### Co-author publications

1. See, V., M., Vidotto, A. A., Donati, J. F., **Boro Saikia, S.**, Fares, R., Hébrard, É. M., Jeffers, S. V., Marsden, S. C., Morin, J., Petit, P., Waite, I., and the BCool collaboration, *Studying stellar spin-down with Zeeman Doppler magnetograms*, MNRAS (submitted)

2. See V., Jardine, M., Vidotto, A. A., Donati, J. F., **Boro Saikia, S.**, Bouvier, J., Fares, R., Folsom, C. P., Gregory, S. G., Hussain, G., Jeffers, S. V., Marsden, S. C., Morin, J., Moutou,

C., do Nascimento Jr, J. D., Petit, P., and Waite, I. A., *The connection between stellar activity cycles and magnetic field topology*, MNRAS, 462, 4442S

3. Vidotto, A. A., Donati, J. F., Jardine, M., See, V., Petit, P., Boisse, I., **Boro Saikia, S.**, Hébrard, E., Jeffers, S. V., Marsden, S. C., and Morin, J., *Could a change in magnetic field geometry cause the break in the wind-activity relation?*, MNRAS, 2016, 455, L52-56

4. Waite, I. A., Marsden, S. C., Carter, B. D., Petit, P., Donati, J. F., Jeffers, S. V., and **Boro Saikia, S.**, *Magnetic fields on young, moderately rotating Sun-like stars I: HD 35296 and HD 29615*, MNRAS, 2015, 449, 8

5. See, V., Jardine, M., Vidotto, A. A., Donati, J. F., Folsom, C. P., **Boro Saikia, S.**, Bouvier, J., Fares, R., Gregory, S. G., Hussain, G., Jeffers, S., Marsden, S., Morin, J., Moutou, C., do Nascimento Jr, J. D., Petit, P., RosÃ©n, L., and Waite, I. A., *The energy budget of stellar magnetic fields*, MNRAS, 2015, 453, 4301S

## Conference talks/Seminars

(I=invited, C=contributed)

IAUS328 Living around active stars, Maresias, Brazil, October 2016 (C)

Fifth BCool meeting, Vienna, Austria, February 2016 (C)

Future of Polarimetry, Brussels, Belgium, October 2015, (I)

Annual meeting of the German Astronomical Society, Splinter session on Solar and Stellar activity, Kiel, Germany, October 2015 (C)

IAU General Assembly, Focus meeting on Brightness variations of the Sun and Sun-like stars, Honolulu, USA, August 2015 (C)

Fourth BCool meeting, Geneva Observatory, Switzerland, February 2015 (C)

Institute for Astrophysics, SFB colloquium, G ttingen, Germany, June 2014 (seminar)

Astronomical Polarimetry, Grenoble, France, May 2014 (C)

Third BCool meeting, St Andrews, UK, January 2014 (C)

Third TOUPIES meeting, Toulouse, France, October 2013 (C)

## Funding

Total grant receive: € 7900

Grant of € 1148 awarded by the University of G ttingen to attend the IAU symposium *Living around active stars* in Brazil to be held in October 2016

Travel grant of € 750 from the COST action *Polarization as a tool to study the Solar-system and beyond*

Travel grant of \$ 750 from the IAU to attend the IAU General assembly in Hawaii, 2015

Grant of € 1400 from the COST action *Polarization as a tool to study the Solar-system and beyond* for a scientific visit to LUPM, University of Montpellier for collaboration with Dr Julien Morin

Travel grant of € 1200 from the COST action *Polarization as a tool to study the Solar-system and beyond*

Travel grant of € 2300 from the COST action *Polarization as a tool to study the Solar-system and beyond*, which also included grant for a scientific visit to IRAP, Toulouse for on going collaboration work with Dr Pascal Petit

IAU travel grant of € 350 to attend the IAU symposium *Magnetic fields throughout stellar evolution*, Biarritz

## Programming language/Tools

Python: Python's numpy, scipy, pandas, astropy, and matplotlib libraries to analyse high-resolution stellar spectra

MATLAB: Experienced in MATLAB's imaging processing tools, analysing solar data taken by NASA's SDO mission. Also experienced in data analysis using MATLAB during Master's thesis on simulated gravitational wave data

LATEX: Experience in preparing documents, presentations, and posters

Git & Github: Extensive use of Github while working on the *Chromospheric activity database* project. The project was carried out together with another PhD student which required the use of Github for version control and tracking

Gimp, Inkscape Used for conference poster design, and image processing

Basic knowledge: C, SQL, HTML/CSS

## Teaching Experience

Tutor *Introduction to Astrophysics and Geophysics* (undergraduate course)

Teaching Assistant *XLAB Summer School on Astrophysics*, the week long summer camp is aimed at high school students

Tutor *Physics I* (undergraduate course)

## Collaborations

2013-present

Active member of the BCool project, which is an international collaboration aimed at investigating magnetic field generation and amplification in cool stars. Member of the science working group on sun-like stars

2015-present

Science working group member of ESA's L class X-ray mission ATHENA. Member of the working group *Solar system and Exoplanets*

2014-present

Science working group member of the UV mission UVMag, proposed to ESA as a M-class mission. Member of the working group on solar-type stars

2013-2015

Active participant in the European COST Action MP1104 *Polarization as a tool to study the solar-system and beyond* Participated in two conferences, one summer school as part of the action, which resulted in expansion of scientific network and form new collaborations in several EU countries. This action also supported my participation in two scientific visits, that resulted in two publications.

